

OBSERVATÓRIO NACIONAL

DOCTORAL THESIS

**Using the Dark Energy Survey
to Explore Galaxy Evolution**

Author:

Julia F. GSCHWEND

Supervisor:

Marcio A. G. MAIA

*A thesis submitted in fulfillment of the requirements
for the degree of Doctor in Astronomy*

November 14, 2019

Disclaimer

This thesis was elaborated based on preliminary and proprietary data from the Dark Energy Survey. The results presented in this work have not passed yet through the whole process of vetting by the collaboration that is required before being published by an academic journal.

©2019

Julia F. GSCHWEND
ALL RIGHTS RESERVED

“Não há saber mais ou saber menos: há saberes diferentes.”

Paulo Freire

Abstract

The Dark Energy Survey (DES) is an ongoing 5-year program that covers $\sim 5000 \text{ deg}^2$ of the sky area in five optical-near infrared photometric bands ($grizY$), designed to measure the dark energy and dark matter densities and the dark energy equation of state by combining multiple probes. The vast dataset generated by DES contains multi-wavelength information about hundreds of million galaxies in an unprecedented combination of area and depth. As a result, DES is a goldmine for a broad list of science cases far beyond the dark energy studies. We present a study of the galaxy luminosity function (LF) evolution using preliminary data from the three first years of DES observations. Here, we discuss and validate a new methodology to be applied at the completion of the survey and also for upcoming projects, as the Large Synoptic Survey Telescope (LSST). We introduce the probability density function of photometric redshifts calculated with the DNF algorithm directly as additional weight in the traditional $1/V_{max}$ estimator. Absolute magnitudes are recomputed for each redshift slice using template-fitting algorithm LePhare, with a unique combination of synthetic SED templates optimized for the DES dataset. We observed dimming of global characteristic luminosity (measured in terms of absolute magnitude, M^*) and luminosity density (j), accompanied by a modest increase in the characteristic number density (ϕ^*) with cosmic time, in agreement with previous results available in the literature. We split the sample into two populations based on morphology and studied their LF evolution separately. We found that bulge-dominated systems increased in number density and in their contribution to the total luminosity density with cosmic time. Our results are compatible with the transformation of part of the disk-dominated population into bulge-dominated galaxies. We also observed pieces of evidence of a “downsizing” effect in galaxy assembly from the lack of evolution at the bright-end of bulge-dominated LF, suggesting that the brightest early-type objects are already in place at $z \sim 1$.

Resumo

O Dark Energy Survey (DES) é um levantamento que cobre ~ 5000 graus quadrados do céu em cinco bandas fotométricas, do óptico ao infravermelho-próximo ($grizY$). O DES foi projetado para medir as densidades de matéria e energia escura e a equação de estado de energia escura combinando múltiplos experimentos. O vasto conjunto de dados gerado pelo DES contém informação sobre centenas de milhões de galáxias com uma combinação de área e profundidade sem precedentes. Como resultado, o DES é uma mina de ouro para uma ampla lista de casos científicos muito além dos estudos sobre energia escura. Neste trabalho apresentamos um estudo da evolução da função de luminosidade de galáxias (LF) usando dados preliminares dos três primeiros anos de observações do DES. Discutimos e validamos as metodologias empregadas que também servirão para os próximos projetos, como o Large Synoptic Survey Telescope (LSST). Introduzimos a função de densidade de probabilidade do redshift fotométrico calculada com o algoritmo DNF diretamente como peso adicional no tradicional estimador $1/V_{max}$. Magnitudes absolutas são recalculadas para cada fatia de redshift usando o algoritmo de ajuste de modelos LePhare com uma combinação inédita de SEDs sintéticas otimizadas para o conjunto de dados do DES. Observamos a diminuição da luminosidade característica global (medida em termos de magnitude absoluta, M^*) e densidade de luminosidade (j), acompanhada por um aumento modesto na densidade numérica característica (ϕ^*) com o tempo cósmico, em concordância com resultados da literatura. Dividimos a amostra em duas populações com base na morfologia e estudamos a evolução de suas LFs. Verificamos que os sistemas dominados por bojo aumentaram em densidade numérica em sua contribuição para a densidade total de luminosidade com o tempo. Nossos resultados são compatíveis com a transformação de parte da população dominada por disco em galáxias dominadas por bojo. Também observamos evidências de um efeito de “downsizing” na formação de galáxias devido à falta de evolução na parte brilhante da LF para sistemas dominados por bojo, sugerindo que os objetos mais brilhantes do tipo early já estão estabelecidos em $z \sim 1$.

Acknowledgements

I would like to express my gratitude for all the people directly and indirectly involved in this project and those who have been giving the necessary support during the last years. First of all, I'd like to say special thanks to my supervisor Dr. Marcio Maia, who inspired me to become a scientist in the first place, back in 2007 (or 2008, I can't remember precisely). At that epoch, I was right in the middle of the college course, getting the degree of a physics teacher in the Universidade do Estado do Rio de Janeiro, when I attended to an outreach seminar given by him about large surveys and the future of astrophysics. Since that day, I never was the same person again. Thanks Marcio for your generosity, patience, assiduity with the thesis, and for continue encouraging to continue when I was almost overcome by tiredness.

Secondly, I'd like to show my appreciation for all the help I got from Dr. Luiz da Costa, the leader of our group, who supported my research in every little aspect I can think of. He offered guidance in science and technology topics, career advice and taught me uncountable values that I will take for the whole life. Thanks to him, I became an active member of a large international collaboration, I got the opportunity to contribute and to be fairly recognized by my efforts with a buildership status in DES.

Thanks to Dr. Paulo Pellegrini for all the support and the fertile discussions on the scientific topics addressed in this work, especially for the hours of phone calls when I disturbed his retirement asking for help. Thanks Dr. Aurelio Carnero and Dr. Ricardo Ogando for making my life easier being always willing to help at the beginning of my masters, when I had no programming skills and, no experience with the Science Portal computational infrastructure at all. Thanks Dr. Adriano Pieres, Dr. Michel Aguena, and Dr. Rodrigo Boufler for the very useful discussions on data handling and for being great partners at work.

Thanks to Dr. Will Hartley for crossing the Atlantic Ocean to spend a week in Rio collaborating with our team, especially focused on my research topic. His pieces of advice were priceless. Thanks Dr. Antonella Palmese and Dr. Carles Sanchez, and Dr. Huan Lin for the leadership and fruitful discussions in DES working groups where I participate.

Special thanks for all the support I received from LIneA's IT-team. I'd like to emphasise my thanks to Carlos Adean, Cristiano Singulani, Guilherme Soares, Lucas Nunes, and Glauber Vila-Verde. Also, great thanks to Dr. Carolina Felicíssimo and Jeferson de Souza from RNP for supporting our research.

Last, but not least, thanks to my family and friends, especially for not being judgmental about my absence in social events during the last year.

This research was made possible by the Ph.D. fellowship number 1530181 provide by CAPES with resources from the MCTIC. Computational resources were provided by LIneA and ON. Participation in national and international scientific events were supported by the INCT e-Universo, DES, and Fermilab.

Funding for the DES Projects has been provided by the U.S. Department of Energy, the U.S. National Science Foundation, the Ministry of Science and Education of Spain, the Science and Technology Facilities Council of the United Kingdom, the Higher Education Funding Council for England, the National Center for Supercomputing Applications at the University of Illinois at Urbana-Champaign, the Kavli Institute of Cosmological Physics at the University of Chicago, the Center for Cosmology and Astro-Particle Physics at the Ohio State University, the Mitchell Institute for Fundamental Physics and Astronomy at Texas A&M University, Financiadora de Estudos e Projetos, Fundação Carlos Chagas Filho de Amparo à Pesquisa do Estado do Rio de Janeiro, Conselho Nacional de Desenvolvimento Científico e Tecnológico and the Ministério da Ciência, Tecnologia e Inovação, the Deutsche Forschungsgemeinschaft and the Collaborating Institutions in the Dark Energy Survey.

The Collaborating Institutions are Argonne National Laboratory, the University of California at Santa Cruz, the University of Cambridge, Centro de Investigaciones Energéticas, Medioambientales y Tecnológicas-Madrid, the University of Chicago, University College London, the DES-Brazil Consortium, the University of Edinburgh, the Eidgenössische Technische Hochschule (ETH) Zürich, Fermi National Accelerator Laboratory, the University of Illinois at Urbana-Champaign, the Institut de Ciències de l'Espai (IEEC/CSIC), the Institut de Física d'Altes Energies, Lawrence Berkeley National Laboratory, the Ludwig-Maximilians Universität München and the associated Excellence Cluster Universe, the University of Michigan, the National Optical Astronomy Observatory, the University of Nottingham,

The Ohio State University, the University of Pennsylvania, the University of Portsmouth, SLAC National Accelerator Laboratory, Stanford University, the University of Sussex, Texas A&M University, and the OzDES Membership Consortium.

Based in part on observations at Cerro Tololo Inter-American Observatory, National Optical Astronomy Observatory, which is operated by the Association of Universities for Research in Astronomy (AURA) under a cooperative agreement with the National Science Foundation.

The DES data management system is supported by the National Science Foundation under Grant Numbers AST-1138766 and AST-1536171. The DES participants from Spanish institutions are partially supported by MINECO under grants AYA2015-71825, ESP2015-66861, FPA2015-68048, SEV-2016-0588, SEV-2016-0597, and MDM-2015-0509, some of which include ERDF funds from the European Union. IFAE is partially funded by the CERCA program of the Generalitat de Catalunya. Research leading to these results has received funding from the European Research Council under the European Union’s Seventh Framework Program (FP7/2007-2013) including ERC grant agreements 240672, 291329, and 306478. We acknowledge support from the Australian Research Council Centre of Excellence for All-sky Astrophysics (CAASTRO), through project number CE110001020, and the Brazilian Instituto Nacional de Ciéncia e Tecnologia (INCT) e-Universo (CNPq grant 465376/2014-2).

Dedicated to Victor. My love, my best friend, and my life partner.

Contents

Disclaimer	iii
Abstract	vii
Resumo	ix
Acknowledgements	xi
1 Introduction	1
2 The Data	7
2.1 The Dark Energy Survey	7
2.1.1 DES Wide	8
2.1.2 DES Deep and Balrog	24
2.2 MICE Simulations	27
3 Photometric Redshifts	31
3.1 Getting redshifts from magnitudes	31
3.1.1 Photo-z methods	31
3.1.2 Photo-z quality metrics	35
3.1.3 Building test samples with DES data	35
3.1.4 Building test samples with MICE simulations	45
3.2 Tests with MICE simulations	46
3.2.1 Evaluating the performance of photo-z methods	46
3.2.2 Using extra magnitudes	50
3.2.3 Do shape parameters improve photo-z estimates?	54
3.2.4 Using photo-z PDFs	58
3.3 Tests with DES real data	61
3.3.1 Using different magnitude types	61
3.3.2 Exploring different magnitude limits	64
3.3.3 Using photo-z PDFs	65
3.4 Photo-zs for DES science sample	69
4 Galaxy Properties	71
4.1 Basic elements to study Galaxy Evolution	71
4.1.1 Spectral Energy Distribution templates	71
4.1.2 K-correction	73
4.1.3 Absolute magnitudes	75
4.2 Tests with MICE simulations	76
4.2.1 Absolute magnitude estimation	77
4.2.2 The impact of input data on absolute magnitude determination	79
4.3 Exploring SED templates	82
4.4 Absolute magnitudes of DES science sample	92

5 Galaxy luminosity function	93
5.1 Luminosity Function	93
5.2 Tests with MICE simulations	100
5.2.1 LF algorithm validation	100
5.2.2 Evaluating sources of errors in the LF determination	102
5.3 Tests with real data	110
5.3.1 Correcting for sample incompleteness	110
5.3.2 Exploring dependence on area	112
5.4 DES Y3 global and galaxy populations LF	114
5.4.1 Global LF	114
5.4.2 LF of galaxy populations	120
6 Summary and conclusions	127
Bibliography	133
A The DES Science Portal	145
A.1 The DES Science Portal	145

List of Figures

2.1	DECam images	8
2.2	DES observing strategy	9
2.3	DECam filters transmission curves.	10
2.4	Distribution of fraction of De Vaucouleurs model	11
2.5	Percentage distribution of quality flags	12
2.6	Star/galaxy classification quality assessment	14
2.7	Percentage distribution of star/galaxy classification flag	14
2.8	$E(B - V)$ map from Schlegel et al. (1998)	15
2.9	Distribution of total extinction	16
2.10	Detection fraction map	17
2.11	Number of images map	18
2.12	Magnitude versus error	18
2.13	Depth map	19
2.14	Magnitude distributions	20
2.15	Bad regions map	20
2.16	Foreground objects mask	21
2.17	Footprint map	22
2.18	Spatial density of DES Y3	23
2.19	Spatial density of DES Y3 medium subsample	24
2.20	<i>i</i> -band number counts	24
2.21	Sky Viewer tool	25
2.22	Spatial distribution (DES Wide versus DES Deep)	26
2.23	Comparison between DES Wide and Deep samples	26
2.24	Selection function of DES Y3	27
2.25	SDSS + DES + VHS filters transmission curves.	28
2.26	MICE apparent magnitude and redshift distributions.	29
3.1	Spatial density of the spec-z sample	36
3.2	Redshift distribution of the spec-z sample	38
3.3	Spatial density and z distribution of matched spec-z sample	39
3.4	Statistics of spec-z sample matched to DES data	40
3.5	Statistics of weighted spec-z sample	42
3.6	Statistics of pruned spec-z sample	43
3.7	Properties of the three subsets for DES Y3: <i>train</i> , <i>valid</i> , and <i>test</i>	44
3.8	Magnitude versus redshifts for the DES Y3 <i>test</i> subset	44
3.9	Properties of MICE representative subsample	45
3.10	Comparison between MICE subsample and total sample	45
3.11	Properties of the three subsets for MICE: <i>train</i> , <i>valid</i> , and <i>test</i>	46
3.12	Magnitude versus redshifts for the MICE <i>test</i> subset	46
3.13	$N(z)$ of MICE <i>test</i> sample by four photo-z algorithms	47
3.14	Photo-zs versus true-zs by four photo-z algorithms	47
3.15	Magnitude versus photo-z by four photo-z algorithms	48

3.16	Global metrics for the four algorithms	49
3.17	Photo-z metrics as a function of redshift for the four algorithms	49
3.18	SEDs and filter transmission curves	51
3.19	$N(z)$ of MICE test sample using extra magnitudes	52
3.20	Photo-zs versus true-zs $N(z)$ using extra magnitudes	53
3.21	Magnitude versus photo-z using extra magnitudes	54
3.22	Global metrics using extra magnitudes	54
3.23	Photo-z metrics as a function of redshift using extra magnitudes	54
3.24	Distributions of MICE input parameters	55
3.25	Normalized redshift distribution of MICE <i>test</i> sample	56
3.26	Photo-zs versus true-zs using shape parameters	57
3.27	Magnitude versus photo-z using shape parameters	57
3.28	Global metrics using shape parameters	58
3.29	Photo-z metrics as a function of redshift using shape parameters	58
3.30	Example of photo-z PDFs for MICE	58
3.31	$N(z)$ of MICE <i>test</i> sample by stacking the photo-z PDFs	59
3.32	Global metric $\Delta N(z)$ using photo-zs PDFs for MICE	59
3.33	$\Delta N(z)$ as a function of redshift for MICE	61
3.34	$N(z)$ of DES Y3 <i>test</i> sample using the three sets of magnitudes	62
3.35	Photo-zs and true-zs using the three sets of magnitudes	63
3.36	Magnitude versus photo-zs using the three sets of magnitudes	63
3.37	Global metrics using the three sets of magnitudes	64
3.38	Photo-z metrics as a function of redshift using the three sets of magnitudes	64
3.39	$N(z)$ of DES Y3 <i>test</i> sample using the three magnitude-limited sets	65
3.40	Photo-zs and true-zs using the three magnitude-limited sets	66
3.41	Global metrics using the three magnitude-limited sets	66
3.42	Photo-z metrics as a function of redshift using the three magnitude-limited sets	67
3.43	Example of photo-z PDFs for DES Y3	67
3.44	$N(z)$ of DES Y3 <i>test</i> sample by stacking the photo-z PDFs	67
3.45	Global metric $\Delta N(z)$ using PDFs for DES Y3	68
3.46	$\Delta N(z)$ as a function of redshift for DES Y3	68
3.47	$N(z)$ of DES Y3 science sample	69
3.48	Spatial distribution of photo-z statistics	70
4.1	COSMOS SEDs	72
4.2	Extinction laws	73
4.3	COSMOS K-corrections as a function of redshift	74
4.4	MICE cosmology	75
4.5	Absolute magnitude residuals for the five methods	77
4.6	Absolute magnitude residuals by reference band	78
4.7	Absolute magnitude metrics for the five methods	78
4.8	Absolute magnitude metrics as a function of redshift for the the five methods	79
4.9	Absolute magnitude residuals using different inputs	80
4.10	Absolute magnitude quality metrics using different inputs	81
4.11	Absolute magnitude metrics using different inputs	81
4.12	Absolute magnitude metrics as a function of redshift using different inputs	82
4.13	COSMOS SEDs coverage of color-redshift space	83
4.14	COSMOS SEDs coverage of color-color space	83
4.15	Median of the residuals for colors using COSMOS SEDs	84
4.16	Median of the residuals for absolute magnitude using COSMOS SEDs	85
4.17	Three examples of SED tracks as a function of redshift	85

4.18	COSMOS SEDs coverage of color-redshift space for DES	86
4.19	COSMOS SEDs coverage of color-color space for DES	86
4.20	Outliers in color-redshift diagram.	87
4.21	COSMOS and MARASTON SEDs coverage of color-redshift space	88
4.22	COSMOS and MARASTON SEDs coverage of color-color space	89
4.23	COSMOS and MARASTON K -corrections as a function of redshift	89
4.24	New templates added to the COSMOS SEDs	90
4.25	Median of the residuals for colors using COSMOS and MARASTON SEDs	91
4.26	Absolute magnitude distributions of DES science sample	92
5.1	Completeness factor $C(m, \mu)$	97
5.2	K-correction and absolute magnitude limits	98
5.3	LF of one HEALPix pixel $NSide = 32$	99
5.4	LF of all pixels combined	100
5.5	MICE LF validation in comparison to SDSS original parameters	101
5.6	MICE LF validation in comparison to SDSS considering absolute magnitude limit	102
5.7	Global LF of MICE test sample using different photo-z methodologies	104
5.8	Evolution of Schechter parameters using different photo-z methodologies	105
5.9	Global LF of MICE test sample using the u -band	106
5.10	Evolution of Schechter parameters using the u -band	107
5.11	Mock $griz$ magnitude errors applied to MICE catalog	107
5.12	Global LF of MICE test sample introducing mock magnitude errors	108
5.13	Evolution of Schechter parameters introducing mock magnitude errors	109
5.14	Global LF of DES Y3 applying the completeness factor	111
5.15	Evolution of Schechter parameters applying the completeness factor	112
5.16	Global LF of DES Y3 samples in three different sizes	113
5.17	Evolution of Schechter parameters in three different sizes	114
5.18	Global LF in comparison with previous results from the literature	116
5.19	Evolution of Schechter parameters in comparison with previous results from the literature	117
5.20	Linear fit of Schechter parameters versus redshift in comparison with previous results from the literature	118
5.21	Color-magnitude diagram of early and late-type galaxies	121
5.22	Color-color diagram of early and late-type galaxies	121
5.23	Distribution of $fracdev$ in redshift intervals	122
5.24	Fraction of early and late-type galaxies as a function of redshift	122
5.25	LF of early and late-type galaxies separately	123
5.26	Evolution of Schechter parameters for early and late-type galaxies separately	124
5.27	Linear fit of Schechter parameters versus redshift for early and late-type galaxies separately	124
5.28	Percentage contribution of early and late-type galaxies to the total j	126
6.1	Luminosity Function at $z < 0.2$ of SDSS, DES, and LSST (simulations)	131
A.1	Components of Portal's infrastructure	145
A.2	Screenshot of Photo-z Compute's configuration tab	146
A.3	Screenshot of Photo-z Training's product log	146
A.4	Flowchart of the DES Science Portal E2E	147

List of Tables

2.1	Wavelength (Å) coverage limits of DECam filters.	10
2.2	Meaning of quality flags.	12
2.3	Bits in the bad regions mask.	20
2.4	Foreground objects mask.	21
3.1	Surveys source of spectroscopic data.	37
3.2	OzDES quality flags definitions	38
3.3	Photo-z quality metrics of four algorithms	48
3.4	Photo-z quality metrics for MICE catalog using distinct set of filters.	52
3.5	MICE photo-z <u>quality</u> metrics considering shape parameters.	56
3.6	Global metric $\Delta N(z)$	59
3.7	Photo-z quality metrics for distinct types of magnitudes in DES real data.	62
3.8	Photo-z <u>quality</u> metrics for distinct magnitude-limited samples in DES real data.	65
3.9	Global metric $\Delta N(z)$	68
4.1	MICE SED templates and extinction laws	73
4.2	Redshift intervals and the respective bands used in LePhare's method 4.	77
4.3	Absolute magnitude quality metrics for MICE using the five methods	78
4.4	Absolute magnitude metrics	81
4.5	COSMOS and MARASTON templates	88
5.1	Double Schechter fit parameters for the LF validation	101
5.2	Schechter fit parameters.	109
5.3	Characteristics of previous works (approximated values).	115
5.4	Double Schechter fit parameters at low z .	118
5.5	Single Schechter fit parameters and luminosity density.	119
5.6	Double Schechter fit parameters.	126
5.7	Schechter fit parameters and luminosity density.	126

List of Abbreviations

2dF	fibre-fed 2-degree-Field
ANNz	Artificial Neural Network
ArborZ	Photometric Redshifts Using Boosted Decision Trees
BDT	Boosted Decision Tree
BPZ	Bayesian Photometric Redshift (Z) Estimation.
DNF	Directional Neighborhood Fitting
CFHTLS	Canada-France-Hawaii Telescope Legacy Survey
CMD	Color-Magnitude Diagram
COSMOS	Cosmic Evolution Survey
CTIO	Cerro Tololo Inter-American Observatory
DECam	Dark Energy Camera
DES	Dark Energy Survey
DESDM	Dark Energy Survey Data Management (System)
DNF	Galaxy photometric redshift by Directional Neighbourhood Fitting
DR1	First Data Release
EAZY	Easy and Accurate Z (photometric redshifts) from Yale
ENF	Euclidean Neighbourhood Fitting
Fermilab	Fermi National Accelerator Laboratory
FGCM	Forward Global Photometric Calibration Method
FWHM	Full Width Half Maximum
FOF	Friends of Friends
GAMA	Galaxy And Mass Assembly
HAM	Halo Abundance Matching
HOD	Halo Occupation Distribution
HEALPix	Hierachical Equal Area isoLatitude Pixelation
HyperZ	SED fitting code for photometric redshift
ICM	Intra-Cluster Medium
IGM	Inter-Galactic Medium
k-NN	k-Nearest Neighbors
KDE	Kernel Density Estimation
LePhare	Le Photometric Analysis for Redshift Estimations
LF	(Galaxy) Luminosity Function
LRG	Luminous Red Galaxies
LSST	Large Synoptic Survey Telescope
MARZ	Manual and Automatic Redshifting Software
MF	(Galaxy) Stellar Mass Function
MICE	Marenostrum Institut de Ciències de l'Espai (dark matter simulations)
MLZ	Machine Learning and photo-Z
MOF	Multi-epoch, multi-band, and multi-Object Fit
MSE	Mean Squared Error
M^*	Characteristic Absolute Magnitude (in galaxy luminosity function)
NCSA	National Center (for) Supercomputing Applications
OzDES	The Australian Dark Energy Survey

PDF	Probability Density Function
PHAT	Photo-z Accuracy Testing (program)
Photo-z	Photometric redshift
Pofz	Photometric redshift using weights to estimate $N(z)$
PSF	Point Spread Function
PSFex	Point Spread Function Extractor
S/N	Signal-toNoise ratio
SB	Starburst
SDSS	Sloan Digital Sky Survey
SED	Spectral Energy Distribution
SExtractor	Source Extractor
SFH	Star Formation History
SFR	Star Formation Rate
SkyNet	Robust Neural Network Training Tool for Machine Learning in Astronomy
SN	SuperNovae
SOMz	Self Organizing Maps and Random Atlas (z)
Spec-z	Spectroscopic redshift (z)
STILTS	Starlink Tables Infrastructure Library Tool Set
S/N	Signal-to-Noise ratio
SV	Science Verification (phase)
TPZ	Trees for Photo-Zs
VHS	VISTA Hemisphere Survey
VIPERS	VIMOS Public Extragalactic Redshift Survey
VVDS	VIMOS VLT Deep Survey
Y1	Year 1
Y2	Year 2
Y3A2	Year 3 Annual Release 2

Chapter 1

Introduction

Galaxies comprise just a small percentage of the total content in the Universe. However, they work as lighthouses, delineating territories in the large-scale structure, providing probes not only about themselves but also about dark components of the Universe. These complex systems exhibit a large variety of properties like size, color, shape, morphology, luminosity, surface brightness, and star-formation activity. Such characteristics are the result of an evolutionary process undergone for billions of years, driven by both internal and external mechanisms. Colors and luminosities tell us about the masses and ages of underlying stellar populations. The mix of morphological components reveals the relative importance of energy dissipation and collisionless processes present in their history (Robertson et al., 2017).

According to the hierarchical paradigm (e.g., White et al., 1978), primordial density fluctuations created gravitational potential wells, assembling dark matter in small halos (Press et al., 1974). These little halos felt the gravitational attraction by their neighbor halos and progressively merged, forming more massive structures, creating increasingly stronger potential wells. The baryonic matter available fell into these wells and formed the proto-galaxies in the center of dark matter halos. Later on, star formation activity in those systems started when smaller cold gas clouds contracted by self-gravity, and eventually, allowed nuclear fusion to happen. If the proto-galaxy cloud had some angular momentum, the young galaxies should present some rotation, which favored the formation of disk-shaped objects (Mo et al., 2010).

Throughout the history of the Universe, large scale structures formed, resulting in overdense regions like galaxy clusters, filaments, and walls, and underdense regions known as cosmic voids. A fraction of the galaxies also merged to form new systems with the mixed content from the progenitors. If the two merging galaxies were similar in mass and size (the so-called major merger), the encounter caused the dissolution of the disk structure (if existent). The new system is sustained by the velocity dispersion of its stars instead of rotation, forming an elliptical galaxy. Otherwise, if the scales of the merging objects were too different, the smaller object may be captured as a satellite, or even incorporated (minor merger). In this case, the morphological aspects of the more massive galaxy would not change drastically (Roukema et al., 1993).

The result of a galaxy merger also depends on the content of the participants. If the two galaxies were gas-poor before the event (“dry” merger), the process is collisionless (given the vast distances between stars), and the stars utterly reorganize. The resulting system preserves the total mass and retains a fossils record of stellar populations (ages and metallicities) from the two progenitors (van Albada, 1982; L. Lin et al., 2008). If the two galaxies were gas-rich before the event (“wet” merger), the gas collision might have triggered a burst of star formation. This episode can consume the gas reservoir quickly, leading to a drastic drop in the star formation rate. The result is a radical change in the color of the remnant system from blue to red.

The transition to a new phase in the galaxy life, where the star formation activity is weak or absent, and the galaxy evolves passively, is known as quenching. Besides wet mergers, other mechanisms are capable of preventing gas cooling either to extinguishing star formation activity and preventing the galaxy from returning to form stars once quenched, e.g., virial shock, ram pressure, or dynamical friction (Man et al., 2018).

Present-day galaxies occupy two distinct regions in color-magnitude space, the so-called red sequence, and blue cloud. Besides the distinction between two populations that differ in color and luminosity, this 2-dimensional distribution is also strongly correlated to morphological components (Strateva et al., 2001). The blue cloud galaxies are predominantly disk or irregular objects, while the red sequence galaxies are mostly spheroidal systems.

Very deep images taken with the Hubble Space Telescope (HST), known as the Hubble Ultra Deep Field (HUDF, Beckwith et al., 2006), showed that the evolution was substantial in the first few billion years of the Universe. The star formation activity was already intense, even less than 1 billion years after the Big Bang. In the early Universe, galaxies were not so well morphologically defined as they are today. At that epoch, the young systems were mostly clumpy and irregular.

As the Universe evolved, galaxies experienced transformations, resulting in populations that share similar physical and structural properties. The goal of galaxy evolution studies is to understand the process responsible for this differentiation. The origin of such transformations can be internal and (or) external, as states the old *cliché* “nature versus nurture”.

Observations have shown that quenched galaxies leave the blue cloud and build-up the red sequence over cosmic time. The scarcity of galaxies with intermediate properties between the red sequence and the blue cloud (the so-called green valley) suggests that the quenching and the subsequent migration in color-magnitude space is a rapid process (e.g., Strateva et al., 2001; Faber et al., 2007; Gonçalves et al., 2012). The evolutionary paths in the color-magnitude diagram, CMD, the physical processes related to these movements, and the epochs when each kind of process is dominant are a vibrant and exciting topic of debate in the literature. It is not yet evident whether galaxies follow strictly the same “bottom-up” pattern, as it is believed for the assembly of dark matter haloes, or whether the red sequence is built, at least in part, in a “top-down” fashion, i.e., with large systems forming first.

The peak of star formation activity in today’s Universe takes place at smaller galaxies compared to the past when it peaked at more massive galaxies (Cowie et al., 1996). This phenomenon is known as *downsizing* of star formation efficiency, and it is related to the evidence that most massive galaxies present older stellar populations. This concept is counter-intuitive within the hierarchical paradigm, where most massive galaxies should appear younger, since they assemble at later times. Faber et al. (2007) proposed a mixed scenario where galaxies with different luminosities migrate to the red sequence at different epochs, mostly after wet mergers, but also due to other processes, in a mass-dependent order. Once they are already in the red sequence, subsequent dry mergers would build-up the most massive red galaxies, without significant changes in color.

Likely, the hierarchical assembly and the passive evolution coexist, and their relative importance depends on the lookback time and the environment (Kormendy, 2013). As the Universe expands, the probability of galaxy encounters decreases. Most objects in low-density regions will continue to evolve passively and will never merge with another galaxy.

Galaxies may exchange energy and matter with the IGM through inflow and outflow processes. They can be modeled as a system composed of hot and cold gas, stars, and a supermassive black hole, SMBH. The energy would flow between these components via known physical processes. Radiative cooling turns the hot gas into cold gas, so it can collapse to form stars. Star formation gives back energy, heating the surrounding gas via UV emission and supernova explosions, which also deliver mass and metals to the interstellar medium, ISM. The accretion of material by the SMBH can trigger an active galactic nucleus, AGN, which also contributes to heat the gas and to eject mass and radiation, even to outside the galaxy, through jet outflows. Hence, the system is not a closed box. It is possible to happen inflow of gas from the IGM, and outflows due to SN and (or) AGN activity. All these processes can be intensified or suppressed if one galaxy eventually merges or interacts with another (Mo et al., 2010).

High-density environments such as galaxy groups and clusters play a role of a catalyst in quenching galaxy star formation. These environments are richer of early-type galaxies, compared to low-density regions. The average fraction of elliptical and lenticular galaxies is $\sim 80\%$ in relaxed clusters, and $\sim 50\%$ in young clusters, while it is $\sim 30\%$ in the field (e.g., Mei et al., 2009; Mo et al., 2010).

Early-type galaxies form a narrow red sequence in the cluster's CMD. The color-magnitude relation can be attributed to age and (or) metallicity. Older galaxies that are redder due to natural stellar evolution would also be the most massive ones because they are assembling mass for longer. On the other hand, massive galaxies are prone to avoid the escape of metals during supernova explosions and stellar winds, due to their stronger gravity field. Hence, the larger the width of the red sequence, the higher the range of ages and metallicities of the stars of cluster members. There is no substantial variation on the slope of the red sequence in CMD in the range from $z \sim 1$ to $z = 0$. The passive evolution of stellar populations in the elliptical galaxies causes a translation of the red sequence to a redder locus in CMD with time (Mei et al., 2009).

There is a strong correlation between the environmental galaxy density and essential characteristics such as morphology and star formation rate (SFR). The densest regions contain predominantly spheroidal galaxies (Dressler, 1980) with the smallest or none star formation (Hashimoto et al., 1998). The morphological segregation alone is not sufficient to explain this lack of star formation in clusters, as there are observations of passive disk galaxies in these high-density regions. These objects can be an intermediate stage between late and early-type galaxies. Infrared observations confirmed the presence of passive spiral galaxies in clusters against the hypothesis of these galaxies to have hidden star formation, obscured by dust (Yamauchi et al., 2004).

Galaxies inside clusters are moving fast in an environment embedded in hot X-ray emitting gas. If the intracluster medium (ICM) gas pressure is larger than the HI pressure in outer regions of a galaxy, this cold gas can be ripped out by ram-pressure stripping. This phenomenon is one of the responsible for enriching the ICM since metals are thrown out from galaxies (Gunn et al., 1972). The same mechanism is also the cause of strangulation, which is the suppression of the star formation activity due to the loss of gas. Under normal conditions, this gas systematically falls in the disk, serving as fuel to maintain active star formation. The loss of a significant amount of gas can explain the rapid quenching and the subsequent transformation of spiral galaxies into lenticular inside clusters (Larson et al., 1980).

In general, the probability of galaxies to merge inside the massive clusters is relatively low, due to the high velocities involved (Binney et al., 1987). Nonetheless, the dynamical friction decreases the galaxy's energy and momentum so that they can fall into the cluster's potential well. If so, the satellite is "swallowed" by the central galaxy. This process, known as cannibalism, can occur repeated times, so the central galaxy becomes more and more bright, massive and large. It increases the difference between the luminosity of the first and the second most luminous galaxies in the cluster. This central galaxy eventually forms a large and diffuse envelope, which can be the result of the accretion of material tidally stripped from the cannibalized galaxies (e.g., Gallagher et al., 1972). These galaxies are known as cD galaxies, and they are exclusively found in the center of galaxy clusters.

The time scale of the transformations undergone by a galaxy is the order of hundreds of millions to billions of years. However, it is possible to receive photons emitted in different epochs and organize the observational data in a timeline. Thus, galaxy evolution studies benefit from statistical tools to characterize galaxy populations at different redshifts, z , frequently under the paradigm of the Λ CDM model. Large samples are demanded to explore the observables with a good representation of galaxy populations and to ensure robust statistics.

To visualize the big picture of the Universe's history, one needs to observe deep, in a large range of redshifts. The so-called "pencil beam" surveys, e.g., the VIMOS VLT Deep Survey (VVDS, Le Fèvre et al., 2004), the redshift Cosmic Evolution Survey (zCOSMOS, Lilly et al., 2007), and Deep Evolutionary Exploratory Probe 2 Galaxy Redshift Survey (DEEP2, Newman et al., 2013), were designed for that purpose.

Nonetheless, since the Universe is homogeneous only in vast scales, to avoid biases introduced by cosmic variance, it is also necessary to cover a large area of the sky. A good combination of area and depth is the ideal observational scenario for galaxy evolution studies. Fortunately, in the last decades, several large surveys have been carried out, as the Sloan Digital Sky Survey (SDSS, York et al., 2000)

and the Canada-France-Hawaii Telescope Legacy Survey (CFHTLS¹). There are ongoing projects, such as the Dark Energy Survey (DES, Flaugher, 2005; Annis et al., 2005) and the SDSS-IV (Dawson et al., 2016), and others are planned for the near future, as Dark Energy Spectroscopic Instrument (DESI, DESI Collaboration et al., 2016), EUCLID (Content et al., 2008), and the Large Synoptic Survey Telescope (LSST, Ivezić et al., 2008). Most of these surveys were designed to investigate dark energy, but they provide a goldmine of data suited for galaxy evolution by the combination of area and depth.

The combination of data from different sources is also a possible strategy to bypass the limitation of individual surveys. For instance, Conselice et al. (2016) used results from 13 works covering different redshift ranges to show that the total number density of galaxies is decreasing over the cosmic time (t), proportionally to t^{-1} . They estimated that the total number of galaxies above $10^6 M_{\odot}$ in the observable Universe is $\sim 2 \times 10^{12}$ (two trillion) up to $z \sim 8$. This number is ten times higher than what would be observable in a full-sky survey with the best current technology available.

Another interesting example is the famous *Lilly-Madau plot* (Lilly et al., 1996; Madau et al., 1998). This plot is a compilation of SFR measurements in different wavelengths, from 14 independent works. It shows that the overall galaxy activity of converting gas into stars increased in the early Universe, reached a peak around $z \sim 1.9$ (3.5 Gyr after the Big Bang), and is exponentially declining recently. With that combination of data, Madau et al. (2014) also inferred that before $z \sim 1.3$, half of the current total stellar mass was already assembled in stars and that there is evidence in favor of the co-evolution of black holes and their host galaxies.

The Luminosity Function (LF), $\Phi(L)$, in successive redshift intervals is a simple but powerful statistical tool to quantify how the demographic properties of galaxy populations evolved over cosmic time. The LF can be parameterized using the Schechter Function (Schechter, 1976), a composite function that combines an exponential decline and a power-law component that are separated by the characteristic coordinates (L^* , ϕ^*). The variation of the parameters ϕ^* and L^* with redshift tells us about the evolution of the characteristic spatial density and intrinsic brightness of galaxy populations. The luminosity density, j (also derived from the LF), brings information about the total light emitted at a given epoch by different types of galaxies. The LF has been used by many authors in the literature using either spectroscopic redshifts (spec-z), photometric redshifts (photo-z), or the combination of both types.

Analogously, the mass function, MF, is also a powerful tool to understand the stellar mass distribution among galaxies populations. Although the mass to be a more fundamental property than luminosity, its determination is an indirect measurement based on several ingredients, each one having their sources of uncertainties. So, the MF is more susceptible to observational and methodological biases than the LF.

The evolution of the luminosity function is still a matter of debate. For each extragalactic survey, there is at least one work focused on the luminosity function of galaxies performed. A few examples are Wolf et al. (2003) and Faber et al. (2007) for the Classifying Objects by Medium-Band Observations in 17 Filters (COMBO-17); Blanton et al. (2003), Nakamura et al. (2003), Blanton et al. (2005b), and Bates et al. (2019) for the Sloan Digital Sky Survey (SDSS); Ilbert et al. (2004), Ilbert et al. (2006), and Zucca et al. (2006) for the VIMOS-VLT Deep Survey (VVDS); Willmer et al. (2006), and Faber et al. (2007) for the Deep Evolutionary Exploratory Probe 2 (DEEP2); Franceschini et al. (2006) for the Great Observatories Origins Deep Survey (GOODS); Ramos et al. (2011) and Sarron et al. (2018) for the Canada–France–Hawaii Telescope Legacy Survey (CFHTLS); Loveday et al. (2012) for the Galaxy and Mass Assembly (GAMA).

An outcome shared by different works is the evolution of the LF faint-end slope. Many authors have found that the parameter α depends strongly on the galaxy type, but not (or not much) on redshift (e.g., Wolf et al., 2003; Ilbert et al., 2006; Zucca et al., 2006; Faber et al., 2007; Ramos et al., 2011). The evolution observed in α values for the global LF is attributed to the mixed type evolution, where the relative contributions of different populations vary with time.

Other result commonly found is the overall fading of the characteristic luminosity with cosmic time (e.g., Ilbert et al., 2005; Willmer et al., 2006; Zucca et al., 2006; Faber et al., 2007; Ramos et al., 2011; Loveday et al., 2012). This behavior is interpreted as an evidence of decreasing star-forming activity and

¹<http://www.cfht.hawaii.edu/Science/CFHTLS>

emergence of old “quiescent” galaxies in the second half of the Universe history, i.e., the last 6–8 Gyrs (e.g., Wolf et al., 2003; Ilbert et al., 2005; Ilbert et al., 2006), which corroborates with the trend present in the Madau-Dickinson plot, but using independent methodology.

The early and late-types LFs unveiled the flux of galaxies from the blue cloud to the red sequence. Several authors have observed the loss in the number of late-types accompanied by an emergence of the early-type galaxies with quiescent stellar populations (e.g., Wolf et al., 2003; Ilbert et al., 2005; Franceschini et al., 2006; Zucca et al., 2009; Loveday et al., 2012). At low- z , early-type dominates the bright-end, and late-type dominates the faint-end (Zucca et al., 2009; Loveday et al., 2012).

Looking back in time, at $z \sim 1$, early and late-type contributions to the bright-end are comparable (Zucca et al., 2009). According to Faber et al. (2007), half of the present-day characteristic spheroidal ($L \sim L^*$) must be visible in the blue galaxy population at $z \sim 1$. Two mechanisms, likely operating together, would explain the intense number density evolution of spheroidal galaxies. First, intermediate objects increasing in stellar mass by merging acquisition and new star-forming activity, migrating to higher mass bins with decreasing redshift. Second, spiral/irregular galaxies relaxing to become spheroidal systems as a consequence of either merger or gas exhaustion (Franceschini et al., 2006).

While there is significant evolution ongoing for ordinary galaxies since $z \sim 1$, apparently, this is not the case for the largest and most massive ones. The brightest red galaxies are already in place at $z \sim 1$, the comoving density increases, being stronger for moderate-mass, but almost absent for high-mass galaxies, a piece of evidence of “downsizing” in galaxy formation (Ilbert et al., 2006; Franceschini et al., 2006).

Recently, Bates et al. (2019) found that the most massive galaxies incorporated most of their mass before $z=0.8$. The transformation would have happened mostly before $z \sim 1$, in overdense regions and still ongoing in underdense regions at lower redshifts (Zucca et al., 2009).

In galaxy clusters, the quenching of central galaxies would have happened first (mostly at $2.5 < z < 3.0$) due to the high concentration of mass (Ilbert et al., 2013). The rapid consumption of gas available to form stars would occur during major merger processes. The quenching of satellite galaxies would happen later, as a result of environmental effects leading to gas starvation (Faber et al., 2007; Ilbert et al., 2013).

Although different works reasonably agree in many aspects, there is still tension between some of their results, and consequently, in their interpretation under the context of the evolution of galaxy populations. For instance, in the B -band, Willmer et al. (2006) measured an increase in the characteristic number density of blue galaxies since $z \sim 1.2$, while Ilbert et al. (2006) and Zucca et al. (2006) measured a significant decrease and Faber et al. (2007) found it to be constant at a similar redshift interval. These inconsistencies are probably related to the differences in the criteria adopted to separate galaxies in red and blue populations.

Inevitably, contradictory results obtained by different surveys can be partially explained by the different conditions and arbitrary choices present in the various experiments. Some of them are: the survey area and depth; the photometric band used; the methods to estimate both redshifts and the LF itself; the cosmological parameters adopted, the redshift range and its binning; the luminosity/absolute magnitude range and its binning; the sample selection criteria; the completeness and contamination; and the definition of galaxy populations.

Some of these elements are indeed relevant for the interpretation of the results. The photometric band, for instance, constrains the wavelength covered by the observations, therefore selecting which stellar populations are predominantly contributing to the LF measurements. LF based on UV brings mostly information about galaxies with a young population of stars, and the results are helpful to trace the evolution of the star formation activity in galaxies. At $z \lesssim 1$, the LF evolution is stronger in bluer bands than in redder ones because the former are more sensitive to changes in star formation history (SFH) (Wolf et al., 2003; Ilbert et al., 2005; Loveday et al., 2012). On the other hand, the LF in redder bands accesses information on the relatively older stellar populations, which is related to the total amount of stellar mass present in the galaxy.

Other elements are not related to the nature of what is being observed but are the result of observational, operational, or even financial limitations, such as the survey area and depth. In general, the larger

the volume of the Universe observed, the better the statistical power of the results. The next-generation surveys will potentially unveil galaxy populations that are significant in number but are hidden by the present observational limitations, such as the low surface brightness galaxies. These are a few examples of reasons to continue measuring the LF nowadays, as we enter the era of Petascale astronomy.

In this work, we use data from the DES to study how the demographic properties of galaxy populations evolved since $z \sim 1$, using the galaxy LF of early and late-type galaxies as the main statistical tool. The steps described in Chapters 3, 4 and 5 were implemented in a complex computing infrastructure, in preparation for the next generation of telescopes, in particular, the LSST.

Chapter 2

The Data

Overview

In this chapter, we describe the data used in this work. We provide information about the Dark Energy Survey, addressing its strategy, operation, and data products. We present the selection criteria to define the science samples used to study galaxy evolution in the next chapters. We also characterize the simulated data selected from the MICE catalog used to validate and improve the methodology.

2.1 The Dark Energy Survey

The Dark Energy Survey¹ (DES, Flaugher, 2005; Abbott et al., 2006) is an international collaborative project whose primary goal is to improve our understanding of the accelerating Universe by measuring the dark energy equation of state parameter, ω , to a statistical precision of $\sim 5\%$. It requires the combination of four independent observational probes: (i) counts of galaxy clustering; (ii) baryon acoustic oscillations; (iii) weak gravitational lensing; (iv) determination of distances of Type Ia supernova (Abbott et al., 2016).

DES expects to observe 300 million galaxies, 30,000 galaxy clusters, 100 million stars, and 2000 Type Ia supernovae (Flaugher, 2005), yielding the largest extragalactic dataset of its epoch, which will, eventually, be overcome by the Large Synoptic Survey Telescope (LSST, Ivezić et al., 2008) in 2022. DES observations finished in January of 2019, but the reduced data and science ready catalogs are expected to be available by December 2019.

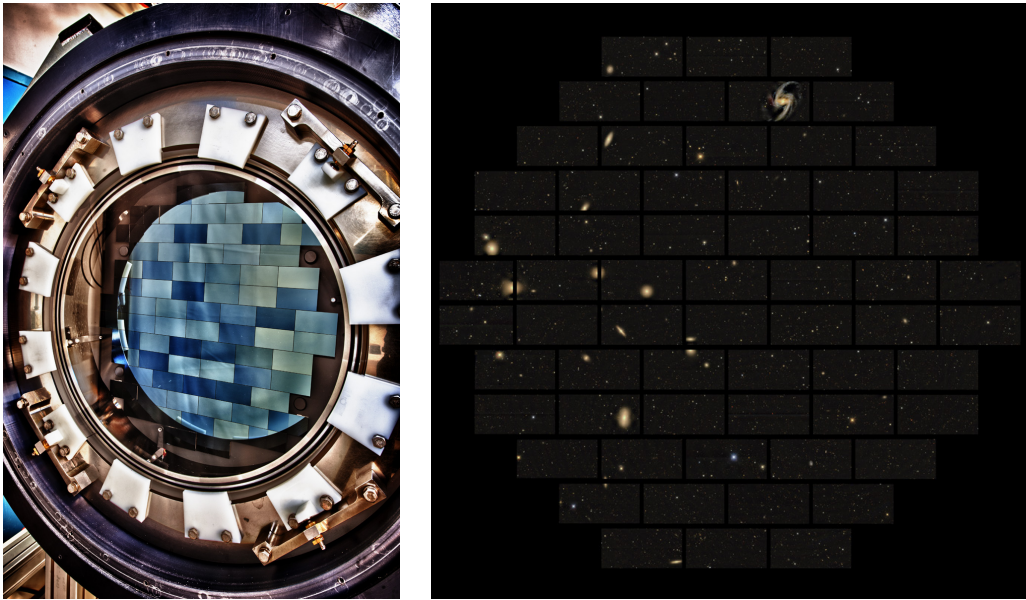
The Dark Energy Camera (DECam) is a three deg² mosaic camera composed of 62 2k×4k CCDs for imaging and 12 2k×2k CCDs for guiding, with a plate scale of $\sim 0.^{\circ}263$ per pixel (see Figure 2.1). The 570-megapixel camera operates at the prime focus of Blanco 4m telescope at the Cerro Tololo Inter-American Observatory (CTIO, Abbott et al., 2006; Honscheid et al., 2008; Flaugher et al., 2015).

The tank-shaped DES footprint covers $\sim 5,000$ deg² of the southern sky. This area was selected intentionally to avoid the galactic plane and to overlap with the South Pole Telescope survey (SPT, Carlstrom et al., 2011) and the SDSS region known as Stripe82 (Abazajian et al., 2009), including the field in between to ensure a contiguous area and enhance calibrations (Abbott et al., 2018b). Furthermore, the DES wide-area overlaps with several photometric and spectroscopic surveys, as shown in Figure 2.2, which is Figure 1 from Abbott et al. (2016). All the coordinates in this work refer to the J2000 epoch.

The target wavelength range spans from optical to near-infrared ($\sim 3,800 < \lambda < \sim 10,700$ Å) in five broad photometric bands, *grizY* (Li et al., 2016; Burke et al., 2018). Concurrently, the search for supernova is part of a deep-survey that covers ~ 30 deg² in four bands (*griz*) with a cadence of about 1 week (Kessler et al., 2015). The DECam also counts with the *u*-band filter, although it is not included in the main observing plan (see filters transmission curves in Figure 2.3 and wavelength ranges in Table 2.1).

The DECam images are processed at the National Center for Supercomputing Applications (NCSA) at the University of Illinois at Urbana-Champaign by the DES data management system (DESDM, Ngeow

¹www.darkenergysurvey.org



^a <https://www.darkenergysurvey.org/wp-content/uploads/2016/05/11-0222-13D.jpg>

^b <http://vms.fnal.gov/asset/detail?recid=1940143>

FIGURE 2.1: DECam images from DES website photo gallery. Left: the DECam focal plane detector (credits: Reidar Hahn^a, Fermilab). Right: Fornax Cluster DECam Full Plane (credits: DES Collaboration^b).

et al., 2006; Mohr et al., 2008; Sevilla et al., 2011; Desai et al., 2012; Mohr et al., 2012; Morganson et al., 2018), where the single-epoch images are stacked to improve the signal-to-noise ratio, leading to coadded images. The source detection and photometric measurements performed by the DESDM pipeline use the software SExtractor (Bertin et al., 1996) to create the so-called coadded catalogs. The bandpass flux measurements have been calibrated using the Forward Global Photometric Calibration method (FGCM, Burke et al., 2018), which takes into account both atmospheric and instrumental components of the system throughput.

The creation and distribution of coadded catalogs within the collaboration occurs approximately annually. At the time of writing this thesis, the latest coadded catalog, and therefore, the main data set used is the Y3A2, which stands for Year 3 Annual Release 2 (hereafter called DES Y3). It is also part of the DES first public data release (DR1, Abbott et al., 2018b). Besides the regular dataset DES Y3, we use products derived from the Y3 Deep Catalog, an ancillary dataset derived from the supernova fields. Both sets of data are detailed below.

2.1.1 DES Wide - Y3 Gold Catalog

The Y3 Gold is a value-added catalog that consists of a validated object catalog derived from the Y3A2 coadded images, added by extra columns and ancillary files. The set of additional columns comprises new magnitude types (not present in SExtractor's outputs), star-galaxy classification, quality control flags, and approximate estimates of photozs. Besides, the catalog contains position-dependent values extracted from ancillary maps and masks, also released in separated files. This complex data set is intended to be the basis for cosmology analyses with DES data and has also been used for other science cases (e.g., Abbott et al., 2016). The Y3 Gold is not public at the time of writing, but the reader can get more details about the catalog construction methodology from the Y1 Gold (Drlica-Wagner et al., 2018), an analogous catalog, but based on the Y1A1 internal release, that was used to obtain the first DES cosmological results (e.g., Abbott et al., 2017; Krause et al., 2017; Chang et al., 2018; Elvin-Poole et al., 2018; Hoyle et al., 2018; Prat et al., 2018; Samuroff et al., 2018; Troxel et al., 2018; Zuntz et al., 2018).

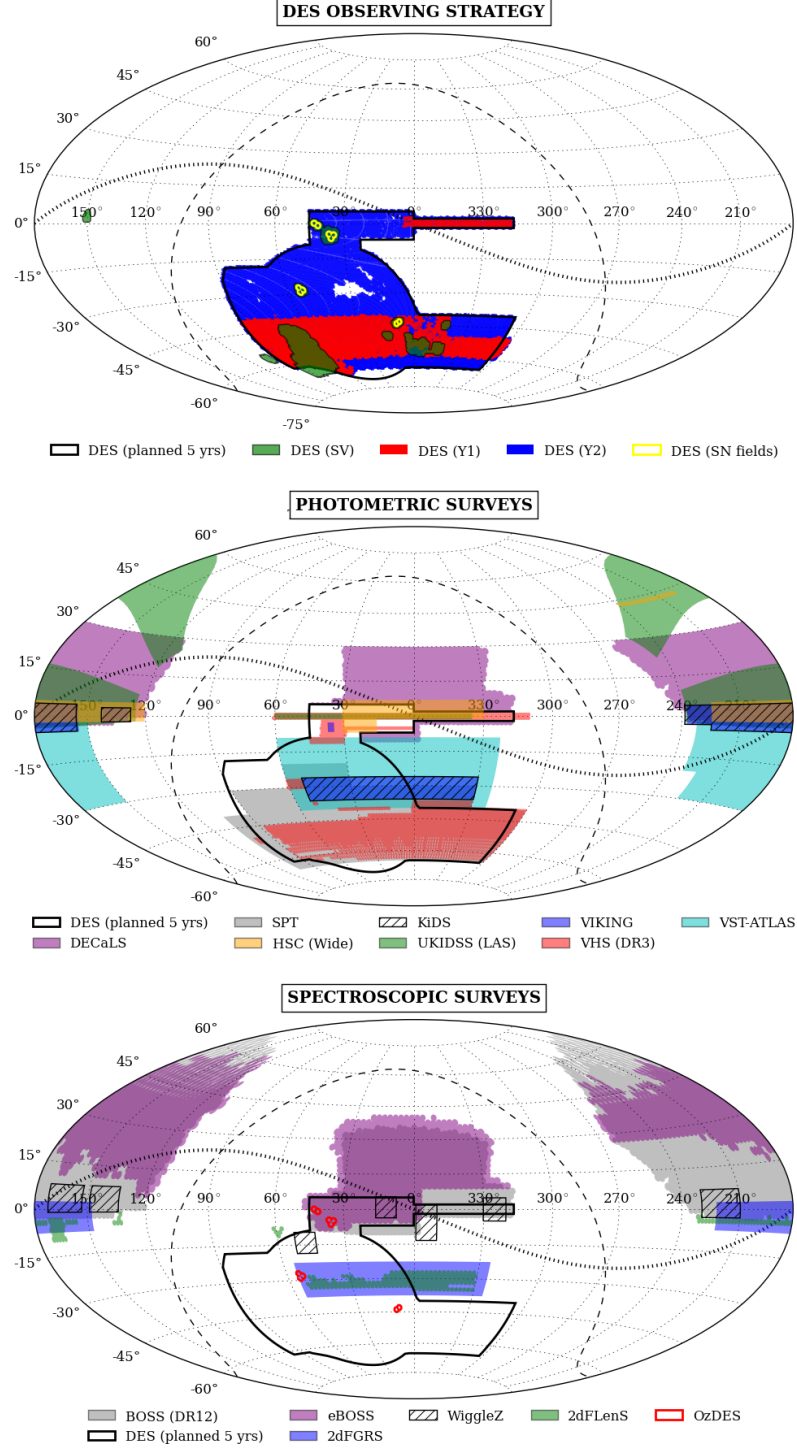


FIGURE 2.2: Upper panel: the DES observing strategy for the five years (solid black line), the science verification phase (SV, green area), the two first years of operation (Y1 and Y2, red and blue areas), and the deep fields for supernova searching (SN, yellow contours). The third year of observations, not shown in this figure, covered the complete area delimited by the black line. Middle and lower panels: photometric and spectroscopic surveys, respectively, that overlap the same region observed by DES. Image credits: Abbott et al. (2016).

The catalog contains measurements of 399,263,026 objects spatially distributed in 10,338 tiles. Tiles are tangent projections of an array equivalent to 5000×5000 CCD pixels, $0.^{\circ}7306$ on each side, or to an

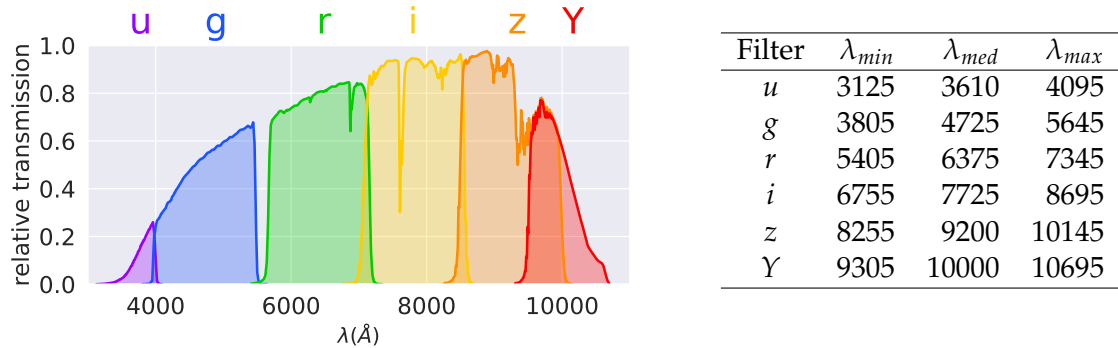


FIGURE 2.3: DECam filters transmission curves.

TABLE 2.1: Wavelength (Å) coverage limits of DECam filters.

area of 0.534 deg^2 (Morganson et al., 2018). The tile is the sky unit area used by DESDM to parcel the DES footprint and organize the coadded outputs (Abbott et al., 2018b). The catalog is also partitioned by Hierarchical Equal Area isoLatitude Pixelation (HEALPix, Górski et al., 2005)² occupying 1,753 pixels of $NSide = 32$ (resolution used in parallel computing photo-zs, see Chapter 3), or 25,573,058 pixels of $NSide = 4096$ (resolution used for ancillary maps, next in this chapter).

Photometry

The Y3 Gold catalog contains 446 columns with the results of the photometric measurements done by the DESDM pipeline. We describe only the quantities that are relevant to our study, either those used directly in the calculations or those used to select a science sample from the raw catalogs.

We use two possible types of apparent magnitudes:

- AUTO (SExtractor’s MAG_AUTO)³ - an estimation of the total magnitude of the object, derived from the flux measured in an elliptical aperture centered at the maximum intensity pixel, taking into account partial pixel fluxes in the perimeter. The ellipse radius is a function of the object’s Kron radius (Kron, 1980), which can vary according to the wavelength range observed. The magnitude errors are estimated from the fluctuations of the background around the sources. Magnitude AUTO is available for all the *grizY* bands in the Y3 Gold catalog.
- MOF (Multi-epoch, multi-band, and multi-object fit) - This is an alternative method of computing the total magnitude that corrects the effects of discontinuous point spread functions (PSF) and correlated noise properties that are introduced by the averaging process of coaddition of multiple images. This method uses PSFEx (Bertin, 2011) to model and interpolates the PSF at the location of each object, and then uses ngmix⁴ code (Sheldon, 2014) in “multi-epoch” mode to simultaneously fit a model to all available epochs and bands. In this mode, a model is convolved by the local PSF in each single-epoch image, and a χ^2 sum is calculated over all pixels. The model used is a composite of a highly constrained bulge (De Vaucouleurs profile, *dev* in Eq. 2.3):

$$I(R) = I_0 \exp \left[-kR^{1/4} \right], \quad (2.1)$$

where I is the surface brightness at the distance R from the center (I_0 is the central brightness and $k=\text{const.}$), plus a disk model (exponential profile, *exp* model in Eq. 2.3):

²<http://healpix.sourceforge.net/index.php>

³<https://media.readthedocs.org/pdf/sExtractor/latest/sExtractor.pdf>

⁴<https://github.com/esheldon/ngmix>

$$I(R) = I_0 \exp \left[\frac{-R}{h_R} \right], \quad (2.2)$$

where h_R is the radius where the brightness is equal to $I_0 e^{-1}$. This procedure is repeated for each epoch and band. The total χ^2 sum is used to find the parameters of the model that maximizes the likelihood. The multi-object analysis is done afterward by identifying groups of objects using a friends-of-friends algorithm. The fit is done again, this time subtracting the light from neighbors using the models from the previous fit. This sophisticated methodology leads to more accurate magnitudes, especially in crowded fields. Moreover, the resulting composite model gives a first approximation of a morphological classification, quantified by the quantity $fracdev$, which is a free parameter to be determined by the fitting process. It means the fraction of De Vaucouleurs model that contributes to the best fit so that $fracdev$ varies from 0 to 1:

$$CM = (fracdev \times dev) + ((1 - fracdev) \times exp), \quad (2.3)$$

where $fracdev=0$ refers to a pure disk galaxy (the large peak in Figure 2.4), $fracdev=1$ refers to pure elliptical galaxies, and an intermediate value of $fracdev$ fit the objects that have both contributions, e.g., a disk with a visible bulge. We will refer to this quantity in Chapter 5 when discussing the partial Luminosity Functions for early and late-type galaxies. The whole process of computing MOF photometry is described in detail by Drlica-Wagner et al. (2018). Due to the low signal-to-noise of Y-band images, magnitude MOF is not available for this filter in the Y3 Gold catalog.

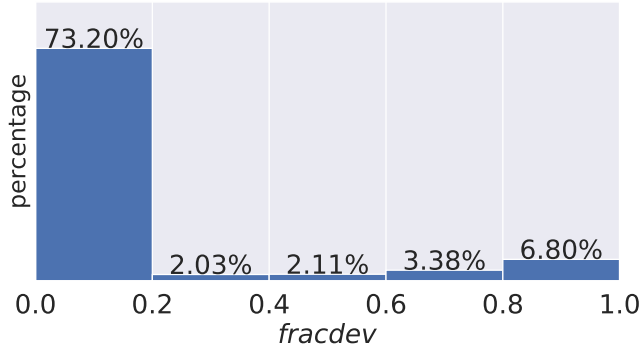


FIGURE 2.4: Percent distribution of fraction of De Vaucouleurs model present in composite model of MOF photometry in DES Y3 Gold catalog.

Quality Flags

The Y3 Gold catalog also provides, for each object, a set of flags regarding the quality of photometry. Two of them are mainly of interest for our science case, one for the i -band magnitude AUTO (SExtractor FLAGS i) and the other for the magnitude MOF $griz$ (FLAGS Gold). Both are 16-bit parameters that contain warnings about the source extraction or flux measurement processes, in order of increasing concern, as detailed in Table 2.2.

The SExtractor FLAGS are obtained directly from the source extraction process, as a regular output of SExtractor software. The FLAGS Gold are a combination of different quality indicators, including quantities from SExtractor, such as the image flags TMAFLAGS_ISO_GRIZ and the magnitude AUTO FLAGS for the five bands.

The acronym SOF stands for Single Object Fitting, a kind of magnitude similar to MOF, but its process of measurement skips the last step that corrects for contamination from neighbors. In this work, we do not use SOF magnitudes in the analysis.

Bit	SExtractor FLAG	Gold FLAG
1	The object has neighbors, bright and close enough to significantly bias the AUTO photometry, or bad pixels (more than 10% of the integrated area affected).	$\text{MOF FLAGS} \neq 0$ or $\text{MOF FLAGS} = \text{NULL}$. Galaxy science with MOF generally wants FLAGS Gold = 0.
2	The object was originally blended with another one.	$\text{SOF FLAGS} \neq 0$. This bit removes SOF galaxy-fit failures. Most bright stars have galaxy fit failures. $\text{SOF FLAGS} = 1$ or $\text{SOF FLAGS} > 2$. Stellar science with SOF generally wants FLAGS Gold < 4. These flags are for PSF fit failures (and worse).
4	At least one pixel of the object is saturated (or very close to).	Any SExtractor $\text{FLAGS_GRIZY} > 3$.
8	The object is truncated (too close to an image boundary).	Any of $\text{IMAFLAGS_ISO_GRIZ} \neq 0$.
16	Object's aperture data are incomplete or corrupted.	Bright Blue Junk (generally contaminated by flux from a very bright neighbor star).
32	Object's isophotal data are incomplete or corrupted.	Bright, crazy color objects, possible transients.
64	A memory overflow occurred during deblending.	
128	A memory overflow occurred during extraction.	

TABLE 2.2: Meaning of quality flags.

The vast majority of the detected objects have $\text{FLAGS} \leq 3$. Precisely, 99.96% for SExtractor FLAGS i and 98.68% for FLAGS Gold, as shown in Figure 2.5.

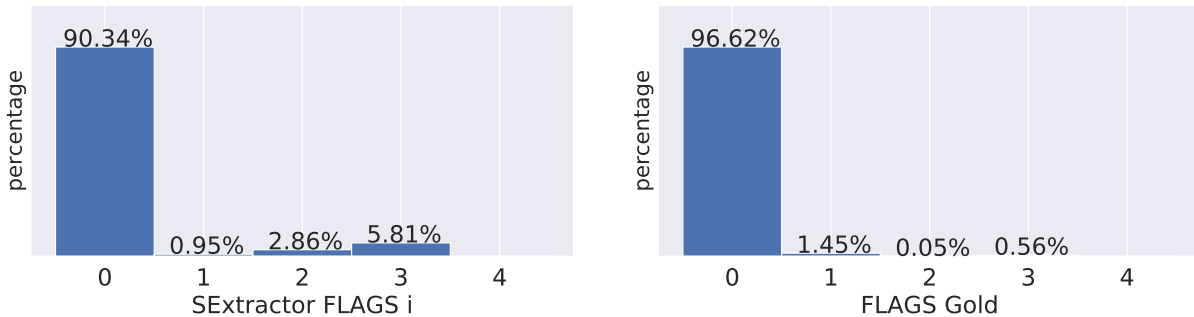


FIGURE 2.5: Percentage distribution of quality flags in Y3 Gold Catalog.

Object Classification

We use the EXTENDED CLASS classifier defined in DES DR1 paper (Abbott et al., 2018b) to remove all point sources from the sample, either stars or QSOs. This quantity is calculated based on the SPREAD MODEL, a linear discriminant-based algorithm available with the SExtractor package. Roughly, the SPREAD MODEL is a non-dimensional quantity that indicates the degree of spread of a detected source. The calculation relies on the best fitting to a local PSF model representing a point source, or to an extended model representing a galaxy, the one that better matches the image data. The RMS error on the SPREAD MODEL (SPREADERR MODEL) is estimated by propagating the uncertainties on individual pixel values (Drlica-Wagner et al., 2018). SPREAD MODEL is explained in details by Sevilla-Noarbe et al. (2018). They present it as one of several star/galaxy classification methods applied to DES Y1 and discuss their efficiency based on results of purity and completeness analysis.

The EXTENDED CLASS comes from the two types of photometry from SExtractor, or MOF. Abbott et al. (2018b), defined the EXTENDED CLASS based on the SExtractor quantity SPREAD MODEL, so-called EXTENDED CLASS COADD, as the independent sum of the Boolean conditions:

$$\begin{aligned}
\text{EXTENDED CLASS COADD} = & \\
& ((\text{SPREAD MODEL} + 3 \times \text{SPREADERR MODEL}) > 0.005) \\
& + ((\text{SPREAD MODEL} + \text{SPREADERR MODEL}) > 0.003) \\
& + ((\text{SPREAD MODEL} - \text{SPREADERR MODEL}) > 0.003)
\end{aligned} \tag{2.4}$$

where the SPREAD MODEL was measured from the i -band coadded images. Analogously, the EXTENDED CLASS can also be defined based on MOF photometry, but using the composite model size squared of the object ($\text{CM_T} = x^2 + y^2$), where x and y are, respectively, semi-major and semi-minor axes of the ellipse corresponding to the best fit composite model used to compute magnitude MOF, as follows:

$$\begin{aligned}
\text{EXTENDED CLASS MOF} = & \\
& ((\text{CM_T} + 3 \times \text{CM_T ERROR}) > 0.1) \\
& + ((\text{CM_T} + \text{CM_T ERROR}) > 0.05) \\
& + ((\text{CM_T} - \text{CM_T ERROR}) > 0.02)
\end{aligned} \tag{2.5}$$

Possible values for the EXTENDED CLASS are 0, 1, 2, or 3, which refer to, respectively, high confidence stars, potential stars, possible galaxies, and high confidence galaxies. The errors of the object classification method influence the completeness and purity of the galaxy sample. At this point, we are not yet discussing the sample incompleteness due to observational effects. We address this subject in Section 2.1.2.

The EXTENDED classifier was tested by members of the collaboration using data from the Hyper Suprime-Cam (HSC, Aihara et al., 2018) as a truth sample of reference. The “takeaways” of the tests are summarized in Figure 2.6.

Results circulated within the DES collaboration indicate that the classifier based on MOF photometry performs better than SOF and COADD, considering completeness and purity of stellar or galaxy samples selected. However, since the EXTENDED MOF uses MOF photometry, which requires a higher signal-to-noise ratio (S/N) threshold than SExtractor, EXTENDED CLASS MOF is not available for the total sample, but $\sim 95\%$. Therefore, we use EXTENDED CLASS MOF when possible, and complete the remaining $\sim 5\%$ with EXTENDED CLASS COADD. Still, there is a non-negligible degeneracy on the object’s classification, especially for magnitudes $i > 23$, where light blue and red points are partially mixed in the top right panel of Figure 2.6. This is a known limitation of our sample.

For simplicity, we present only the results of EXTENDED CLASS MOF classifier in Figure 2.6. The top left panel shows the composite model size CM_T versus i -band magnitude colored by the classification given by the HSC (here assumed as fiducial). The red dots with large values of CM_T ($\text{CM_T} > 0.2$) indicates the existence of stars best fit to models of extended objects, which will make them be classified incorrectly as galaxies. The problem worsens for fainter magnitudes. The comparison with the top left shows that part of these objects receives EXTENDED CLASS MOF=3. The bottom panels provide the translation of the comparison to HSC in numbers. The solid lines represent the efficiency rate, while the dashed lines represent the contamination rate for each selection based on the different values of EXTENDED CLASS MOF. It demonstrates that up to magnitudes $i \sim 22$, the classifier is very robust for a galaxy selection, and the efficiency problem starts to become significant for objects fainter than that. Before cleaning the sample to build a science catalog, approximately $\sim 89\%$ of objects are classified as stars (see left panel of Figure 2.7).

Ancillary Maps

In addition to the main catalog, DESDM also provides ancillary maps and masks of quantities that vary across the sky that are necessary for scientific analysis. Both are released in HEALPix format $NSide = 4096$, NEST schema, equatorial coordinates. In general, maps refer to any quantity distributed

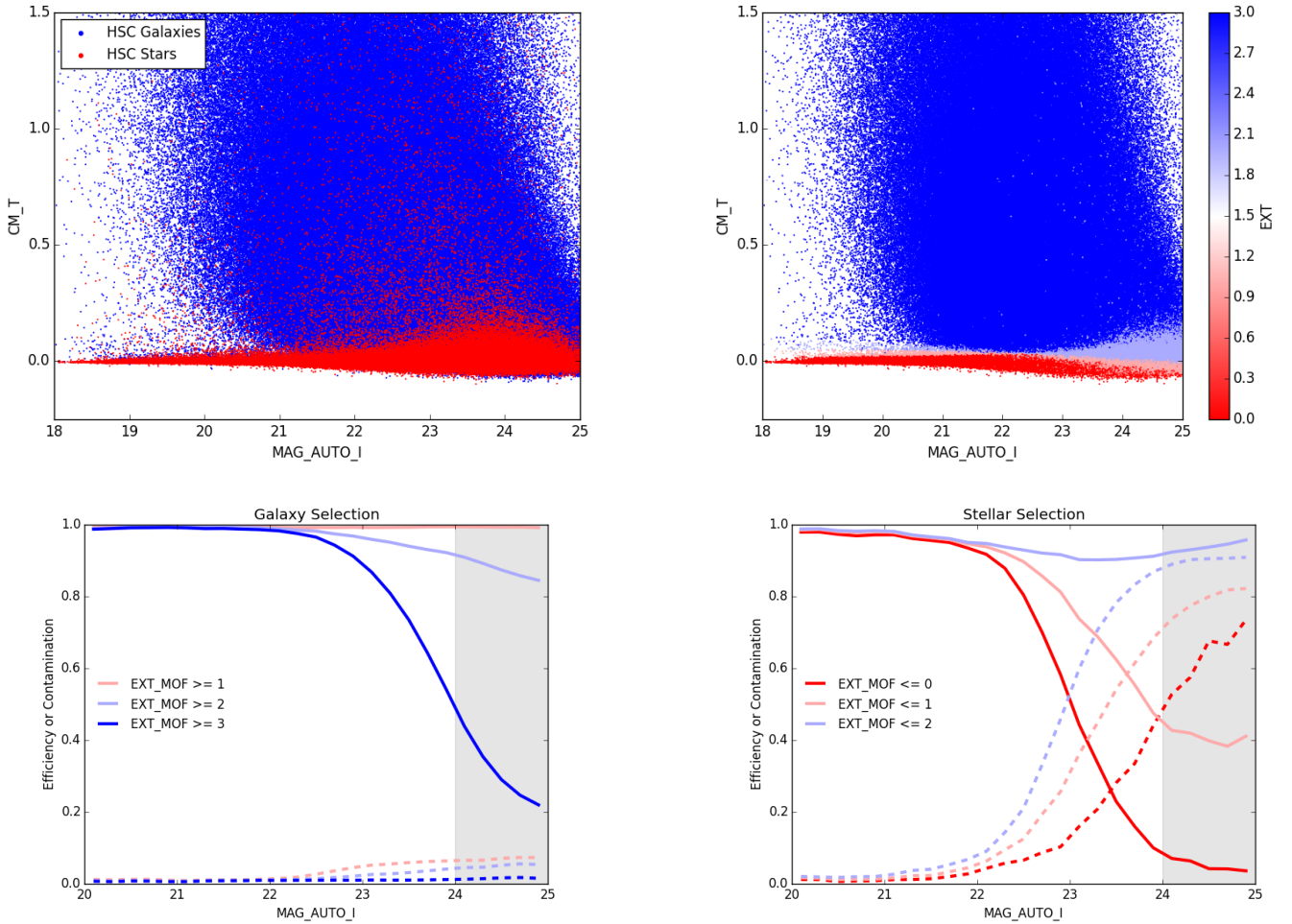


FIGURE 2.6: Results of star/galaxy separation quality assessment in comparison to HSC data. Top panels: composite model size CM_T versus i -band magnitude $AUTO_I$, color-coded by object classification (galaxies in blue, stars in red). Bottom panels: efficiency (solid lines) and contamination (dashed lines) rates depending on the EXTENDED CLASS MOF values for a galaxy selection (left) or stellar selection (right). Figure provided by Dr. Keith Bechtol (private communication).

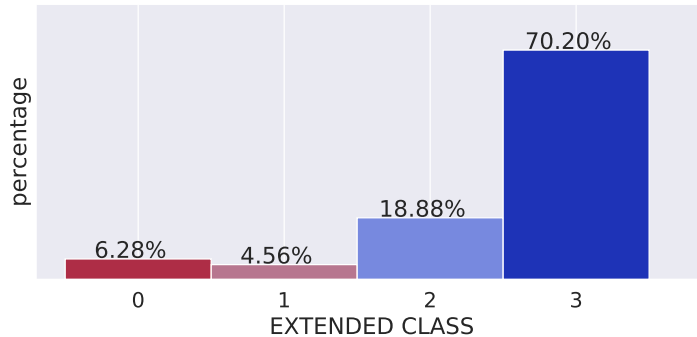


FIGURE 2.7: Percentage distribution of EXTENDED CLASS in Y3 Gold before catalog pruning. In blue, objects classified as galaxies (EXTENDED CLASS = 2 (light), 3 (dark)). In red, objects classified as stars (EXTENDED CLASS = 1 (light), 0 (dark)).

in all pixels which contain DES photometric data, and masks refer to problematic regions of the sky, marked to be removed.

Milky-Way extinction

DES Y3 photometry is not de-reddened by default. The original Zenithal Equal Area projected map of interstellar extinction, $E(B - V)$, from Schlegel et al. (1998) was converted from the original source⁵ to match the format of other DES maps ($NSide = 4096$, NEST schema, equatorial coordinates) by doing linear interpolation to HEALPix pixel centers. As the footprint was chosen to avoid the galactic disk, the $E(B - V)$ values contained inside DES footprint are relatively low. The average $E(B - V)$ is ≈ 0.03 (see Figure 2.8). The conversion of $E(B - V)$ values from the extinction map into magnitude shifts, A , follows the expression:

$$A_{band} = E(B - V) R_{band}, \quad (2.6)$$

where $R = 3.186, 2.140, 1.569, 1.196$, and 1.048 , respectively for $grizY$ (Schlafly et al., 2011). These values were derived using the Fitzpatrick (1999) reddening law ($R_V = 3.1$) and the calibration adjustment from Schlafly et al. (2011) (see Abbott et al., 2018b, for more details). As the footprint avoids the galactic disk, the amplitude of these shifts are small compared to the magnitudes ($\lesssim 0.1$ mag), as reported in Figure 2.9.

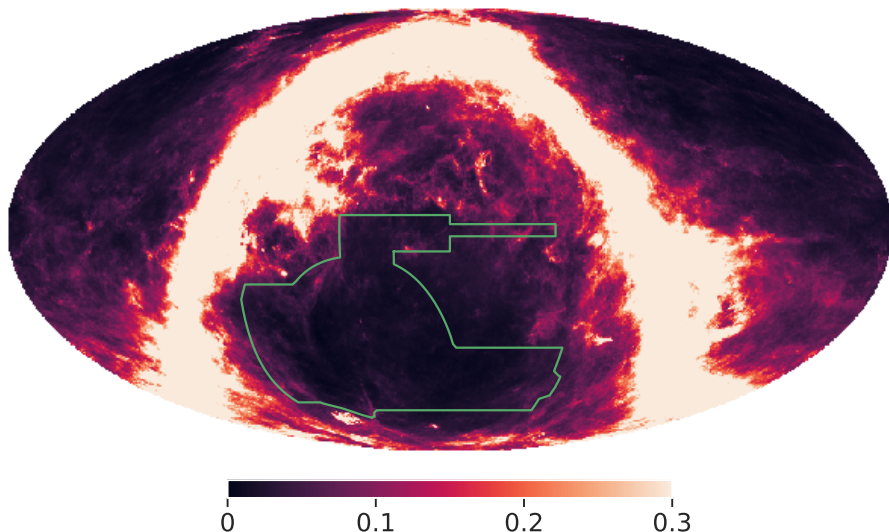


FIGURE 2.8: $E(B - V)$ map from Schlegel et al. (1998) converted into HEALPix format $NSide = 4096$. The green line shows the contour of the survey footprint.

Survey Conditions Maps

The survey conditions maps contain information about the spatial variation of observing conditions, strategy, and instrument configuration. The original maps created by the DESDM pipeline along with the coadded objects tables represent the complex geometry of observed regions through the software package MANGLE (Hamilton et al., 2004; Swanson et al., 2008). The area is split into tiny polygons to guarantee the quantities related to observing conditions are homogeneous within each division. These quantities can vary in time (e.g., seeing, sky brightness) and space (e.g., airmass, CCD response curves). Therefore, the initial maps refer to the observing conditions at the moment when each single-epoch

⁵https://lambda.gsfc.nasa.gov/product/foreground/f_products.cfm

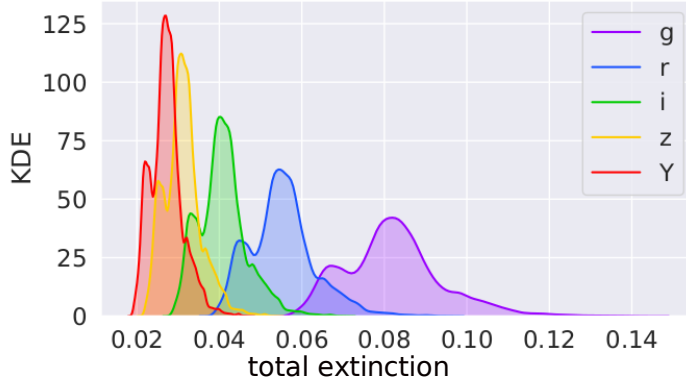


FIGURE 2.9: Distribution of total extinction in the Y3 Gold catalog.

image is taken. A “HEALPixelized” version of $NSide=4096$ is created afterward, referring to combined quantities correspondent to the coadded catalogs. The following paragraphs describe the maps and quantities which are relevant for the selection of a science sample for this work.

- **Detection fraction:** the fraction of the HEALPix pixel area that has been effectively observed in a given band. In general, incomplete pixels are at the edges of the footprint. To minimize the impact of missing magnitude determinations due to the lack of observations, we chose to remove all pixels with detection fraction smaller than 50% in any of *griz* bands from the analyses. The area that fulfills this requirement corresponds to $5,076.64 \text{ deg}^2$. The lack of one or more bands could lead to catastrophic errors in the photo-z and absolute magnitude estimates. We also use the *i*-band detection fraction map (see Figure 2.10) to correct the area that contributes to the LF measurements. The effective area is obtained by multiplying each pixel area by its detection fraction (details below in Section 2.1.1).
- **Number of images:** the number of single-epoch images used to compose the final coadded image for each band. The dark regions in the top panel of Figure 2.11 highlight the SN fields, where the number of exposures is significantly higher than in the regular wide survey. The overall non-homogeneity observed in the maps is a consequence of all the data have not been taken at this stage. As shown in the bottom panel of Figure 2.11, most regions were observed less than five times. After the completion of the five years, the footprint should be covered by an approximately similar number of exposures (expected to be ~ 10), except for the SN fields. In this work, we include in the science sample only regions with at least two images in each one of the *griz* bands. The area that fulfills this condition corresponds to $4,881.69 \text{ deg}^2$.
- **Exposure time:** the time in seconds for exposures in a given filter. For *i*-band, the usual single exposures last 90 seconds for *griz* and 45 seconds for *Y*-band. The cumulative exposure time of a Y3 coadded image sums up to 2160 seconds. These maps also provide the estimate of the effective exposure time, which is weighted with the atmospheric transmission, seeing and sky brightness.
- **Airmass:** the average of the secant of the zenith angle for the observations included in the pixel. The maximum value of airmass for Y3 observations is 1.84.
- **Seeing:** the same classical concept of seeing in astronomy. It measures the sky quality as a blurring of point-like sources. In DES, the full width half maximum (in arcseconds) of the PSF is taken from FWHM_MEAN of the PSF_QA table calculated using PSFEx software Bertin (2011).
- **Sky variance:** the fluctuation of the sky brightness.

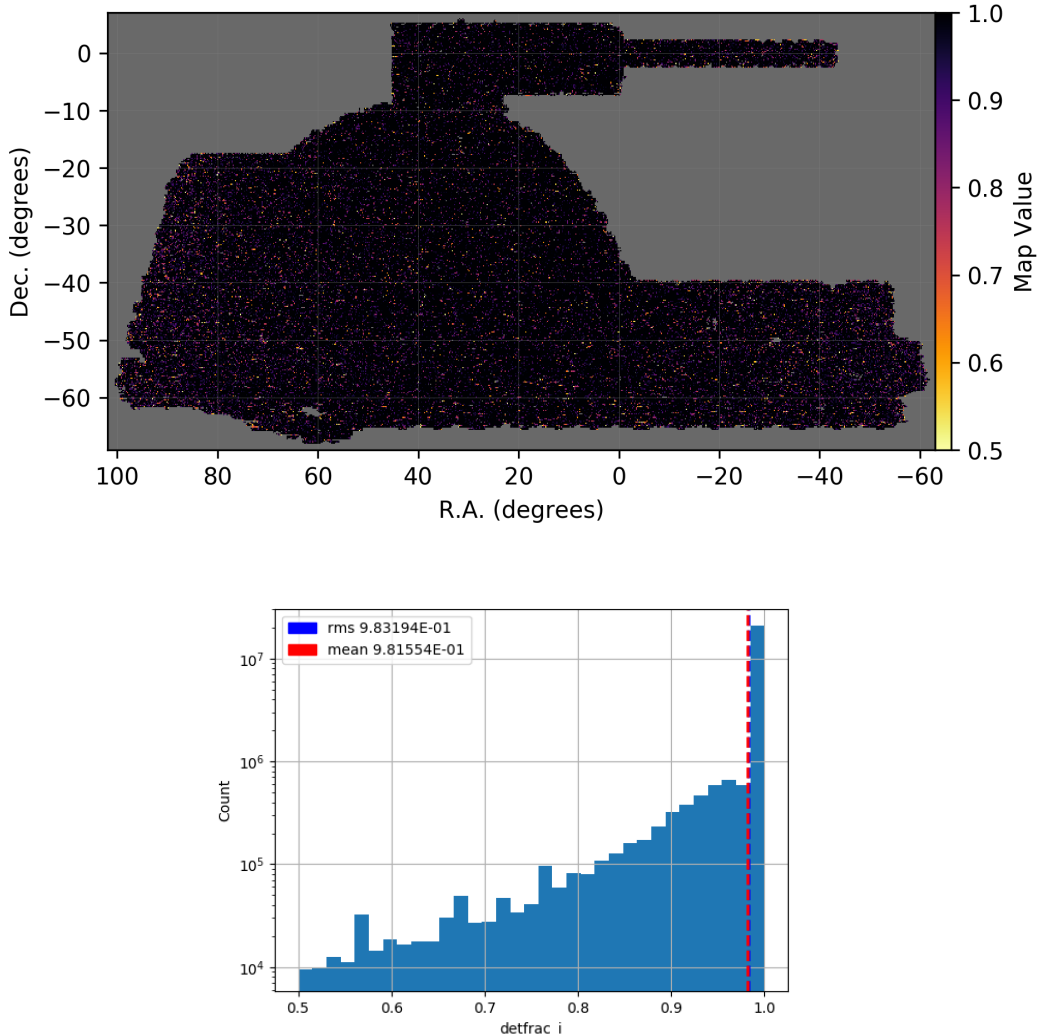


FIGURE 2.10: Top panel: detection fraction map for the i -band. The colors represent the fraction of area effectively measured in each pixel. Bottom panel: distribution of the map values on the logarithmic scale. The vertical lines represent the mean (in red) and the RMS (in blue) values, which are virtually overlapping.

- **Zero point residues:** residual “gray” corrections from Forward Global Calibration Method (FGCM, Burke et al., 2018).
- **Stellar density:** the approximate number of stars used for PSF determination.

We do not apply cuts based on exposure time, airmass, seeing, sky variance, zero-point residues, and stellar density maps. However, these quantities are essential to computing the depth maps.

Depth Maps

The differences in observing conditions combined with the survey strategy (the order of pointing to target regions, including the dithering) result in a non-homogeneous coverage of the sky. The magnitude limit is used to quantify the spatial variation in the survey depth. This quantity is empirically estimated from the distribution of magnitude errors as a function of magnitude for a given S/N threshold, here set to five, as illustrated in Figure 2.12.

In DES, the magnitude limit at each HEALPix pixel is first computed for magnitude APER4, a fixed aperture magnitude recommended for stellar sciences. Then, the magnitude limits are obtained to other

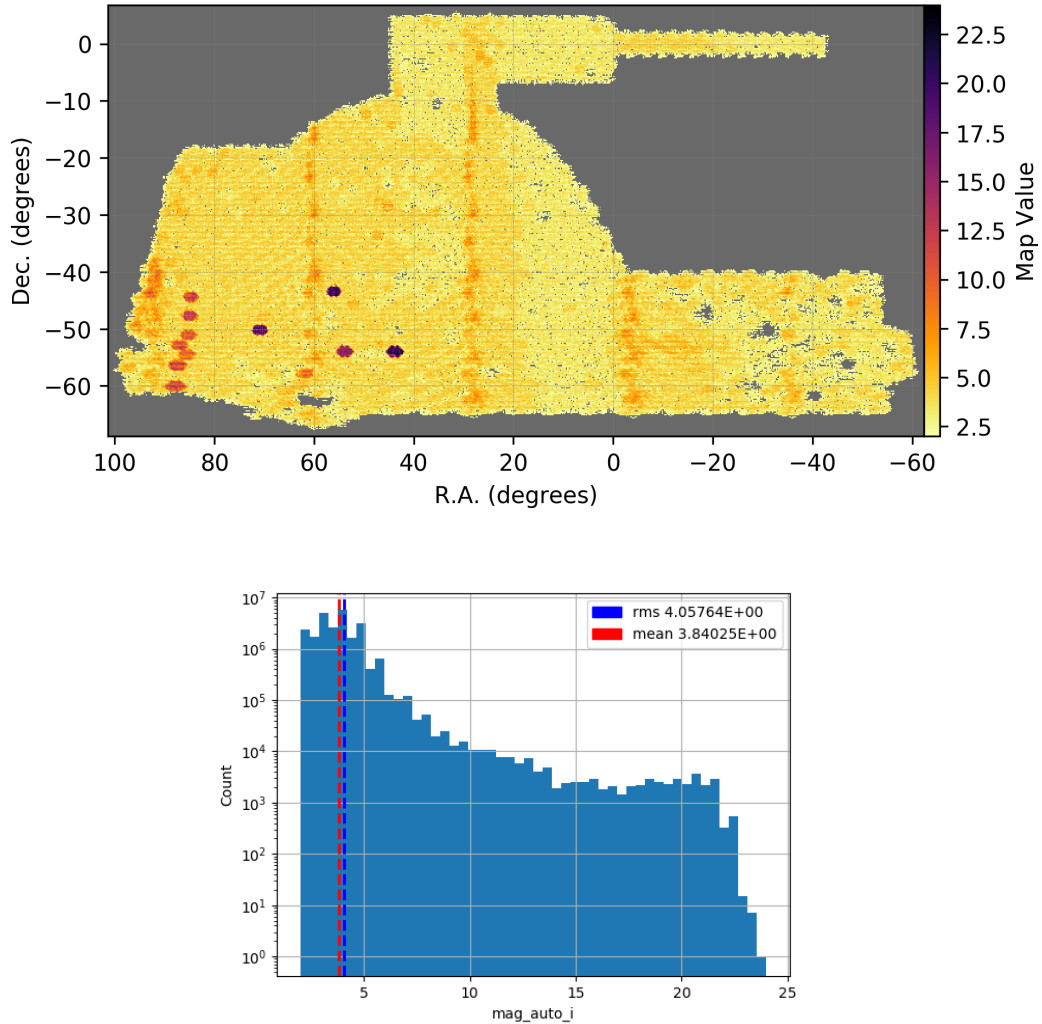


FIGURE 2.11: Top panel: map of number of i -band single-epoch images used to compose the coadded images. Supernova fields are evident in dark regions. Bottom panel: distribution of the map values in logarithmic scale.

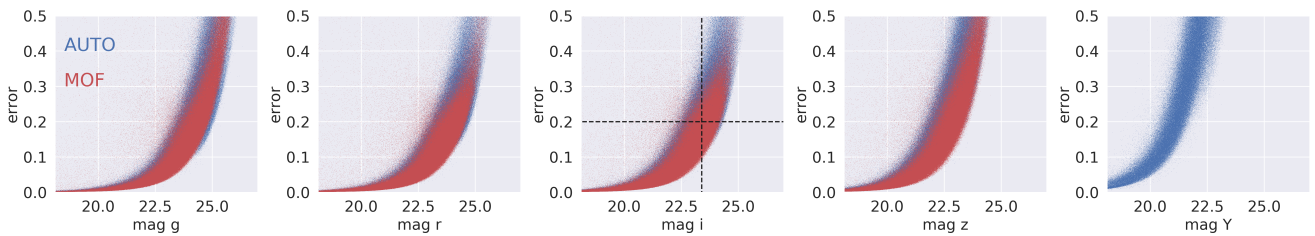


FIGURE 2.12: Magnitude versus error for all DES bands. In blue, magnitudes AUTO. In red, magnitudes MOF. The dashed line locates the S/N threshold of 5σ (approximately the error of ~ 0.2 magnitudes), that corresponds to the average of ~ 23.5 in i -band MOF.

magnitude types, including our two kinds of interest – AUTO, and MOF. This conversion of units is done by a machine learning algorithm that takes into account the original limits (in units of magnitude APER4) and the survey conditions map. The details about converting DES depth maps are explained by Rykoff et al. (2015).

All the depth maps are top-of-the-Galaxy, i.e., they can be used directly with extinction-corrected photometry. As expected, the depth is strongly correlated with the number of exposures for a given band,

which can be observed from the comparison between the top panels of Figure 2.11 (number of images) and Figure 2.13 (magnitude limit map for i -band MOF). For simplicity, we do not show the map for AUTO magnitudes, because its differences from the MOF map are not noticeable by eye.

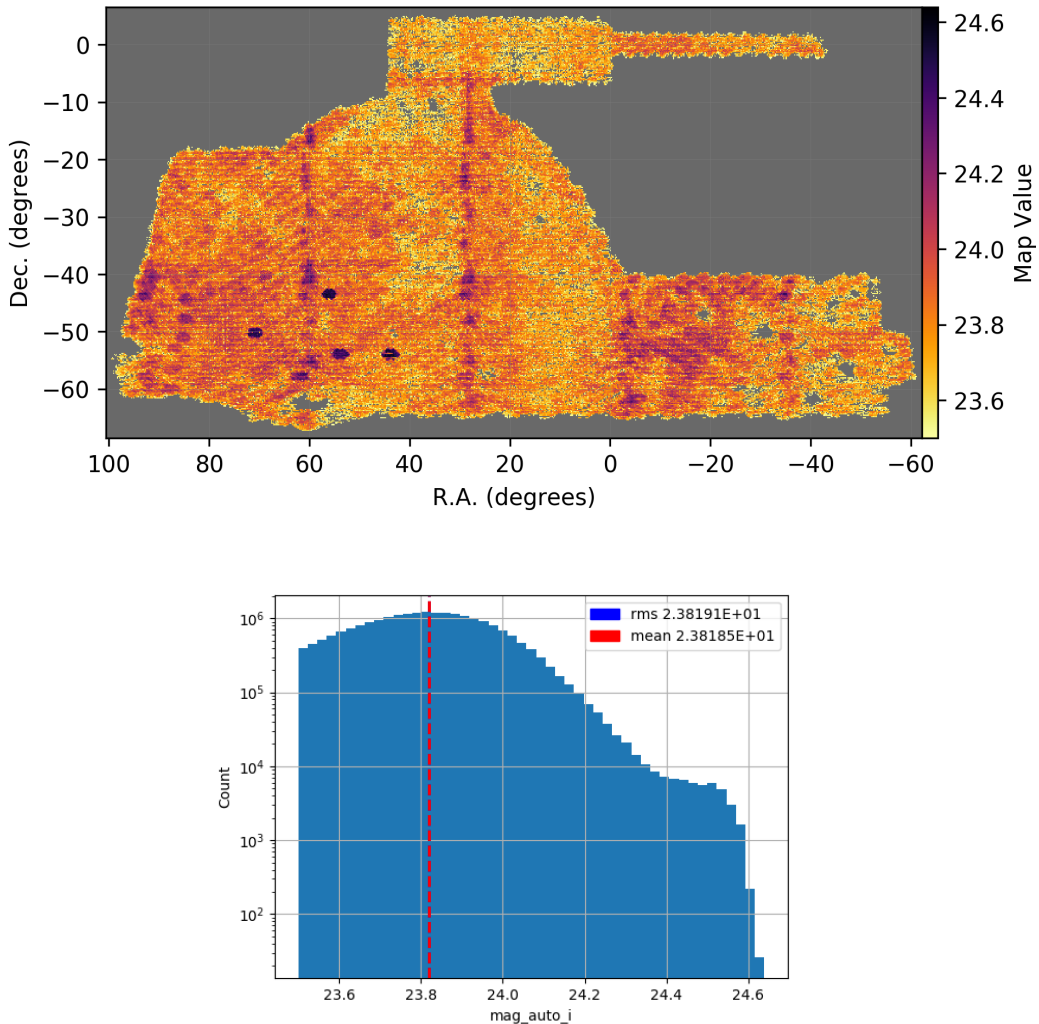


FIGURE 2.13: Top panel: depth map for magnitude MOF in i -band. The colors represent the magnitude limit for a 5σ detection in each pixel. Bottom panel: distribution of the map values in logarithmic scale.

From the magnitude distributions (Figure 2.14), it is evident that beyond magnitude $i \sim 23$ for magnitude AUTO, or $i \sim 23.5$ for MOF, the incompleteness becomes an issue. Therefore, besides applying a completeness correction factor obtained from simulations (details in Section 2.1.2), we establish the region selection criteria based on the i -band MOF depth map as: remove all pixels where the magnitude limit at 5σ is smaller than 23.5. This condition, alone, reduces the area to $4,571.86 \text{ deg}^2$.

Bad Regions Mask

The bad regions mask removes those regions that presented problems in the photometric measurements, usually detected by the presence of a high density of objects with abnormal SExtractor or MOF quantities. There are multiple reasons for a pixel to be classified as a bad region. They are commonly associated with image artifacts, such as detection of cosmic ray, satellite tracks, CCD pixel saturation, etc. The mask has two possible bit values, reflecting the origin of the good/bad classification (see Table 2.3). As a bitmask, the sum of the individual flags means that a given pixel accumulates the two problems.

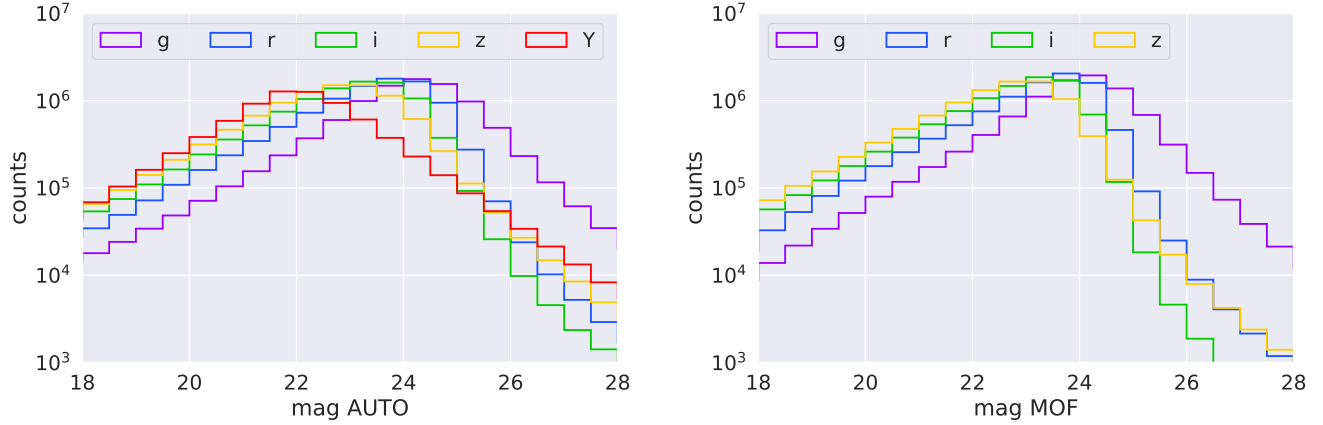


FIGURE 2.14: Magnitude distributions of a random subsample of DES Y3 Gold for AUTO (left panel) and MOF (right panel).

The regions flagged by the bad regions mask are highlighted in yellow, pink, and black in Figure 2.15. For scientific analysis, we removed all pixels with a non-zero flag in the bad regions bitmask.

Mask bit	Meaning	Area removed (deg ²)
1	PSF failure regions	44.53
2	Bad MOF photometry	33.62

TABLE 2.3: Bits in the bad regions mask.

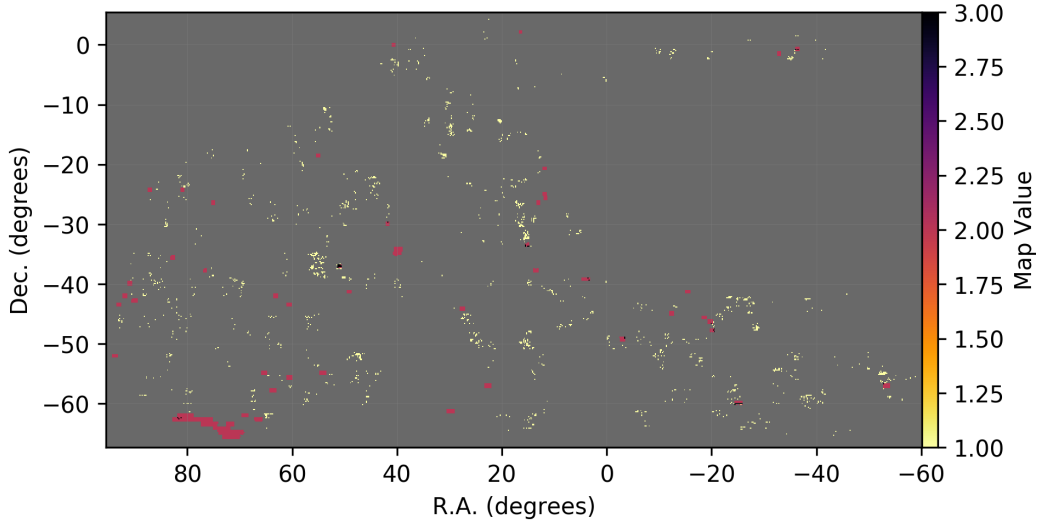


FIGURE 2.15: Bad regions map. In yellow, pink, and black, respectively pixels with bit=1 (PSF failure regions), 2 (Bad MOF photometry), and 3 (1+2).

Foreground Object Masks

The foreground objects mask is beneficial for extragalactic science cases that are not interested in objects in near objects in our “cosmic vicinity”. These objects, as well as the galactic ones, can spoil a large scale extragalactic analysis due to their extension or brightness. They are mapped from external reference catalogs (see Table 2.4) with a suitable radius set around it. The area removed based on the

foreground objects mask is approximately 17% of the total area covered by the survey (regions flagged by the foreground objects mask are highlighted in purple in Figure 2.16). Pixels can accumulate more than one contamination by foreground objects, so the mask value is the sum of individual flags. We also removed all pixels with non-zero flags in the foreground bitmask.

Mask bit	Meaning	Area removed (deg ²)
1	2MASS faint stars ($8 < J < 12$)	255.55
2	Large nearby galaxy (HyperLEDA catalog)	23.26
4	2MASS bright stars ($5 < J < 8$)	100.13
8	Near the LMC	104.19
16	Yale bright stars	91.40
32	Globular clusters	0.55
64	Other bright stars	63.05

TABLE 2.4: Foreground objects mask.

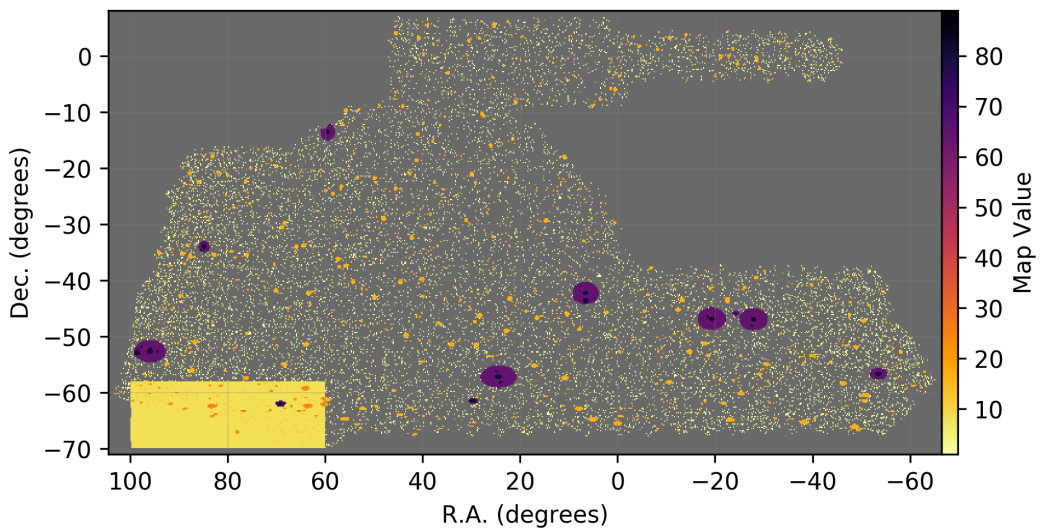


FIGURE 2.16: Foreground objects mask. The color codes are expressed in Table 2.4. The yellow rectangle at the left bottom of the footprint corresponds to the masked region with bit = 8, where the objects are significantly contaminated by Large Magellanic Cloud stars and it can affect the results of star/galaxy classification.

Galaxy evolution science sample

Using the Y3 Gold catalog, we define a scientific sample appropriate to explore the galaxy evolution effects. It means to remove stars and spurious objects, and, in some cases, entire regions, depending on the quality indicators discussed above.

Region Selection - Footprint Map

The selection of the area is made by defining the Footprint Map – the Boolean map that identifies the regions that satisfy all the quality conditions simultaneously:

- minimum of 50% of detection fraction in each one of the *griz*-bands;
- at least two exposures in each one of the *griz*-bands;

- magnitude limit deeper than 23.5 in i -band mag MOF;
- bad regions bitmask flag equal to zero;
- foreground objects bitmask flag equal to zero.

The final footprint is not a contiguous area, as can be seen in Figure 2.17. We use this map, to determine the effective area that contributes to the calculation of cosmic volume for the galaxy LF estimation as:

$$\text{effective area} = \sum_{N_{\text{pixels}}} (\text{detection fraction}) \times 6.24 \times 10^{-8} = 3,437.75 \text{ deg}^2, \quad (2.7)$$

where $6.24 \times 10^{-8} \text{ deg}^2$ is the area of one HEALPix pixel of resolution $NSide = 4096$.

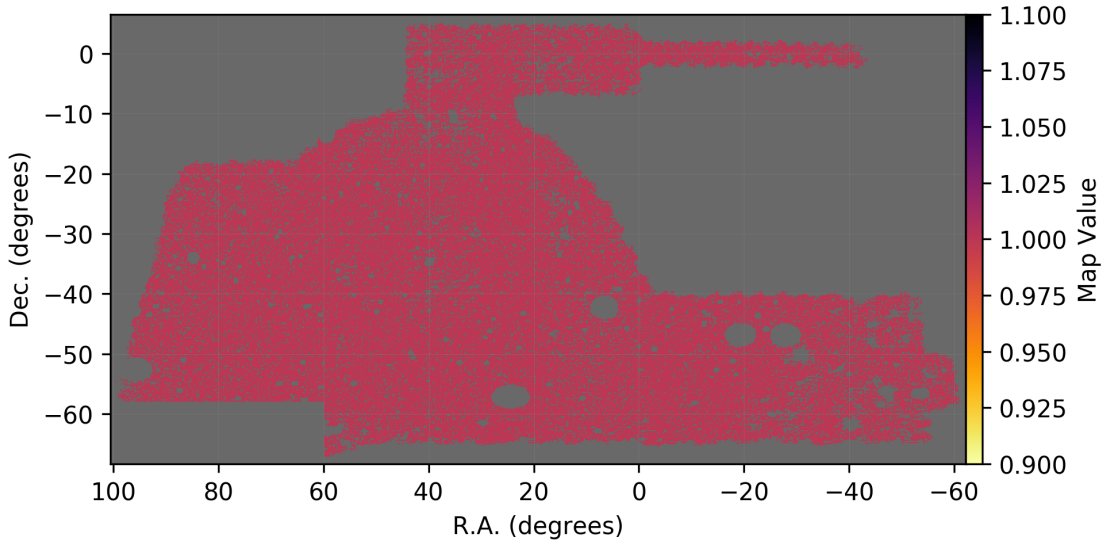


FIGURE 2.17: Footprint map for Y3 Gold catalog: the Boolean map for valid pixels. Valid pixels are in red (map value = 1), the rest in gray (map value = 0).

Object Selection - Pruning the Sample

Once we have defined the valid regions, we then select the objects to create a magnitude-limited galaxy sample free of bad data and nonphysical objects. Objects must satisfy all the criteria below:

- EXTENDED CLASS ≥ 2 ;
- SExtractor FLAG < 4 ;
- FLAG Gold = 0;
- $15.0 < \text{mag MOF} < 23.5$;
- MOF colors in the interval $-2.0 < (g - r), (r - i), (i - z) < 4.0$.

The final selection to be used in the scientific analysis contains 173,054,184 galaxies over a region of $3,437.75 \text{ deg}^2$, resulting in the average number density of 12.3 galaxies/arcmin 2 (Figure 2.18 for the spatial distribution of number density). Hereafter we refer to this sample as *GE science sample*.

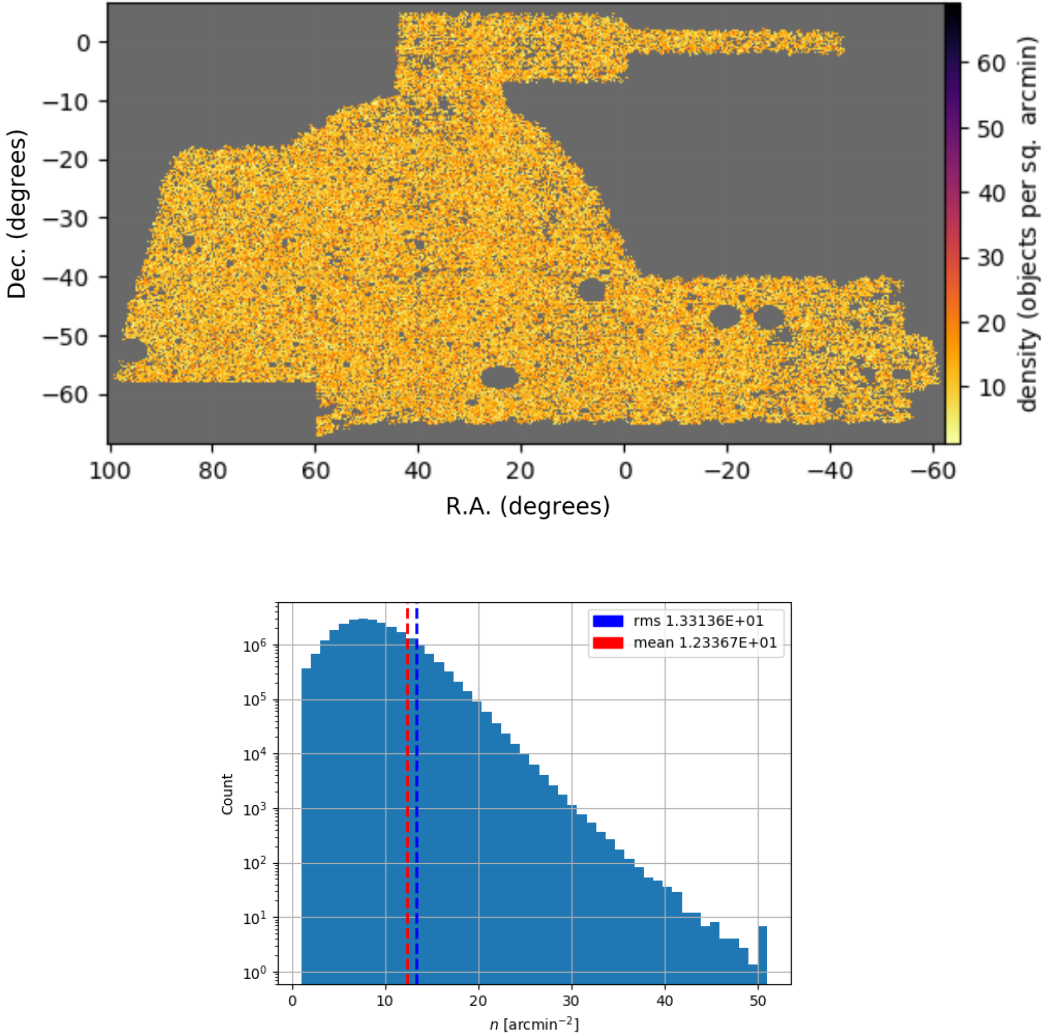


FIGURE 2.18: Top panel: projected spatial density of objects inside the footprint map for Y3 Gold catalog, after all steps of sample cleaning. Bottom panel: distribution of galaxy density, n , for the individual pixels.

To test some aspects of the methodology, we defined a “medium” GE science subsample by selecting a circular region arbitrarily chosen to be far from the footprint edges, centered at the coordinates (RA, Dec) = (35.0, -25.0) and with radius of 10 degrees. The resulting area contains 261.02 deg^2 of valid pixels, with a mean density of 12.5 galaxies/arcmin 2 (see Figure 2.19). Regarding spatial distribution, the comparison between the density distribution in individual pixels in both samples (right panels of Figures 2.18 and 2.19) shows that the medium sample is large enough to preserve reasonably the characteristics of the science sample. For other tests regarding photo-zs and galaxy properties, we define even smaller subsets depending on the test requirements. They are described in the next chapters.

To validate our science sample, in Figure 2.20 we compare the i -band number counts with measurements from previous works: the ESO imaging survey of the Chandra Deep Field South (CDF-S, Arnouts et al., 2001), SDSS (Yasuda et al., 2001), the VIRMOS deep imaging survey (McCracken et al., 2003), Hubble Deep Field North (HDF-N, Capak et al., 2004), the Subaru Deep Field (SDF, Kashikawa et al., 2004), and the COSMOS survey (Capak et al., 2007). Our results (black line) are in good agreement with all works. The slight decrease in the slope at magnitude $i > 22$ raises a hint of possible significant incompleteness at $22.0 < i < 23.5$. We address this issue by applying a completeness correction factor directly in the LF estimates (details in Section 5.1) based on simulations, as described below.

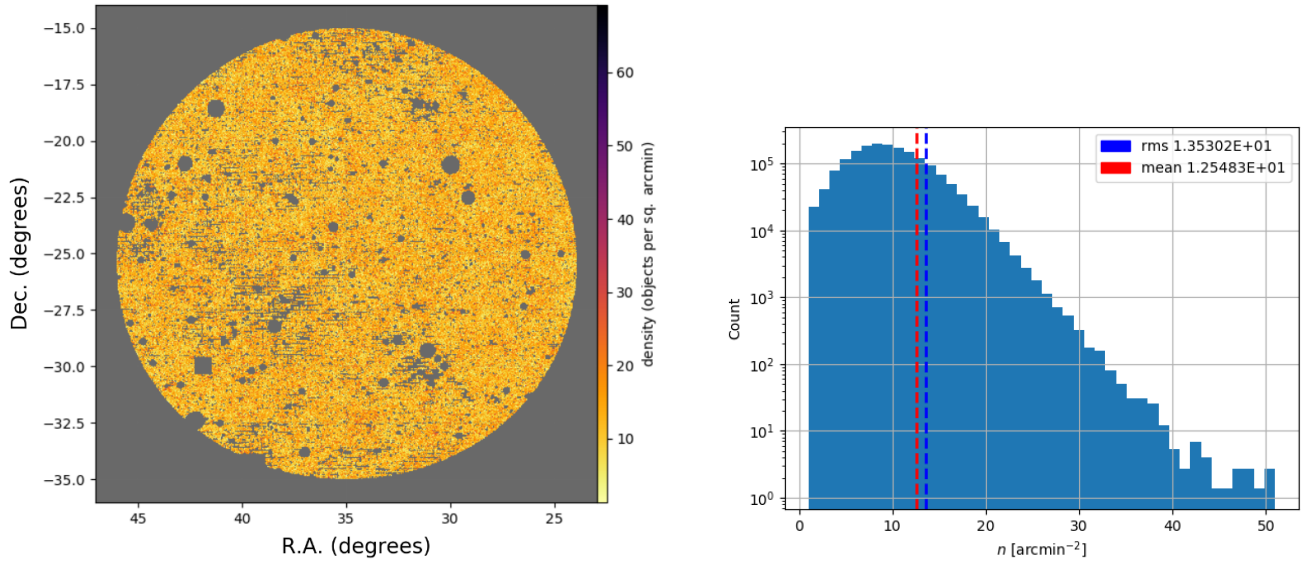


FIGURE 2.19: Left panel: projected spatial density of the “medium” GE science subsample. Right panel: distribution of density in the individual pixels.

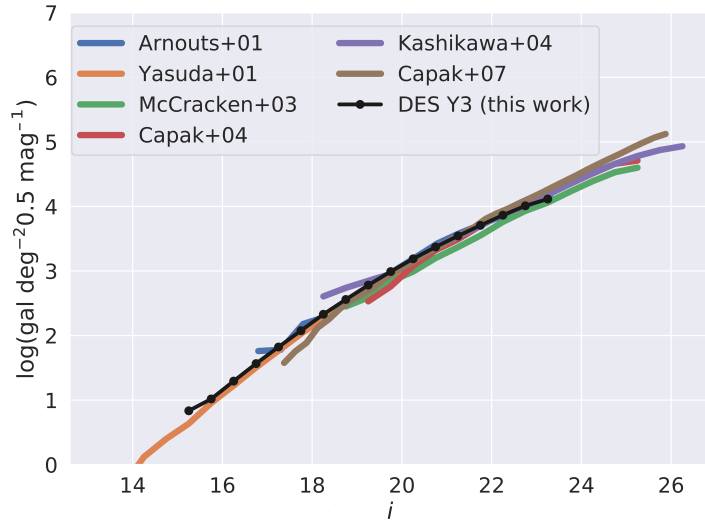


FIGURE 2.20: i -band number counts in logarithmic scale, in comparison with results from other surveys.

2.1.2 DES Y3 Deep Catalog and Balrog Simulations

The Y3 Deep data set is a product of the supernova Ia discovery program. The strategy to detect these objects is to image the same fields repeatedly and look for transients. This observing strategy yields a larger number of images per region than the average in the wide survey. They can be used to produce deeper coadded catalogs. The SN fields cover a non-contiguous region of $\sim 300 \text{ deg}^2$, including the COSMOS field (Scoville et al., 2007), which are outside the wide survey footprint. In Figure 2.21 we show the visualization tool *Sky Viewer*⁶ with SN fields indicated on it.

⁶The tool *Sky Viewer* was developed by LIneA. DES scientists can navigate through the footprint and select individual tiles for visual inspection. On its initial page, the tiles from a given data release are shown in green contours to be selected.



FIGURE 2.21: Screenshot of the *Sky Viewer* tool showing the spatial distribution of DES Y3 Deep tiles (green contours).

The deep fields are observed with no dithering (Yuan et al., 2015), which makes the CCD gaps visible in the co-added images, leading to a visual aspect of a brick wall. This effect is noticeable in the scatter plot of equatorial coordinates for the Deep sample (Figure 2.22), where we compare the same small region for the Wide and Deep samples.

The coadded images of the Deep fields are approximately 3 magnitudes deeper than those from the Wide survey, resulting in a catalog with a higher density of detected sources and a higher S/N on average, as shown in the right panel of Figure 2.23. The shallow regions at the CCD gaps produce the overlap between blue and red points in the plot. The small area and the lack of homogeneity of the deep sample make it difficult to use directly to build a science sample. However, it is beneficial to understand the observational effects and calibrate the Wide sample.

Completeness

As pointed by Blanton et al. (2005b) in the context of the SDSS, and supported by Capozzi et al. (2017) in DES, the loss of faint and low surface brightness objects due to observational limitations introduces a non-negligible bias in the LF estimates. At that epoch, still, in the science verification (SV) phase of the DES, they used the SV deep field images to calibrate the wide survey sample. They reprocessed both shallow and deep co-added images in the same conditions and computed a completeness factor as a function of magnitude and surface brightness.

In this work, we take advantage of the Balrog Simulations (Suchyta et al., 2016), which was not available at the SV epoch. Balrog is a software that allows the inclusion of fake or real objects in an actual image. Then, reprocessing the image is possible to quantify the fraction of successful detection and its dependency on several properties, such as magnitude and surface brightness.

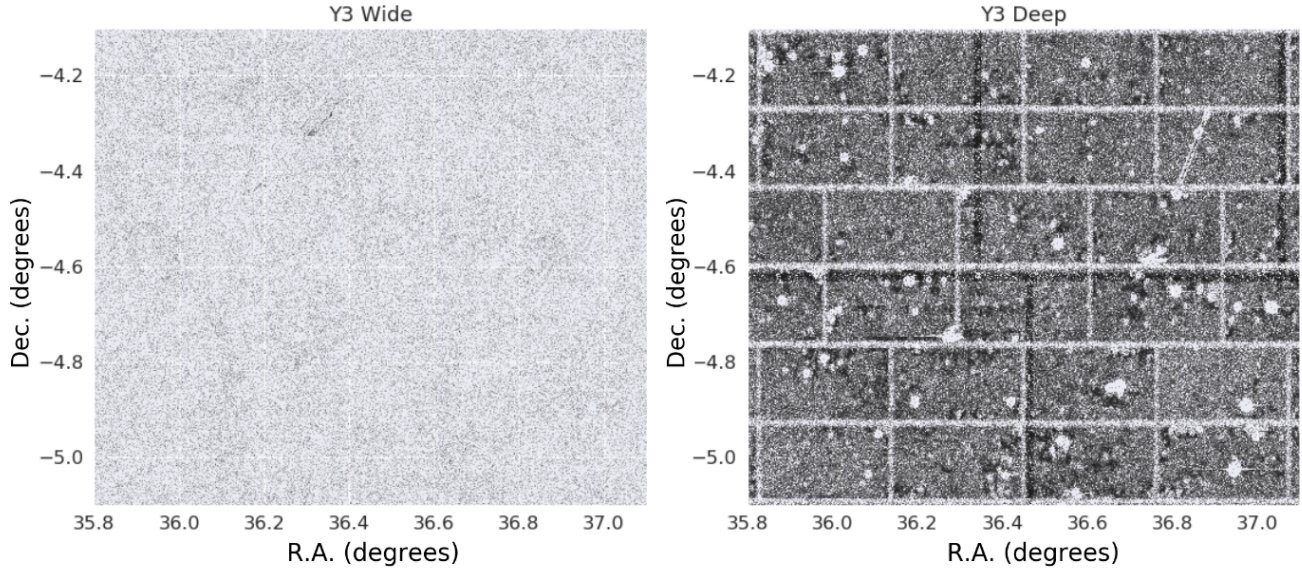


FIGURE 2.22: Comparison of spatial distribution of detected objects in Wide (left) and Deep (right) catalogs. Circles and diagonal stripes of low-density regions in the Deep sample are due to removing regions occupied by bright stars and image artifacts, such as satellite trails. The objects are plotted as small black points (pixel size), so the gray scale follows the spatial density, qualitatively. The reason for the gaps not being completely empty of objects on the right panel is that the deep catalog is also built by co-adding images with the contribution of all images available for each region, including those taken for the Wide survey.

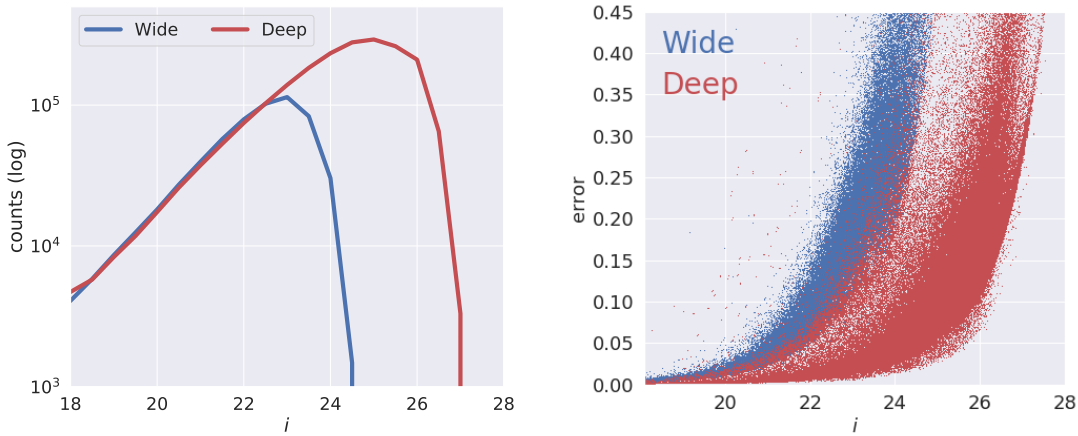


FIGURE 2.23: Comparison between DES Wide and Deep samples. Left: i -band number counts in logarithmic scale. A factor of 1.08 was applied to the deep sample to correct the loss of area between CCD gaps visible in Figure 2.22. Right panel: i -band magnitude versus error for both samples.

A Balrog catalog containing both true and detected objects is available for DES collaboration members, provided by Dr. Brian Yanny (DES internal communication). The introduced fake objects can be simulated or copied from real data. In this case, they used real galaxies from the DES Y3 Deep fields artificially “painted” into real DES Wide images. After that, the process of image reduction and source detection occurs the same way as it is for actual data, producing co-added catalogs from SExtractor products and MOF photometry.

Thus, the analysis of this simulated catalog allows us to quantify the rate of detection as a function of magnitude and surface brightness. Later it will be used to correct the LF similarly as done by Capozzi

et al. (2017) using the comparison between Deep and Wide directly. The result of this comparison is the selection function of the DES Wide sample (Figure 2.24). The advantage of using Balrog is that the comparison is based on a truth sample, where all objects are known, while if using the deep fields, one has to assume that the deep sample is complete. In Section 5.1, we describe how to use these results to correct the LF from the effects of incompleteness.

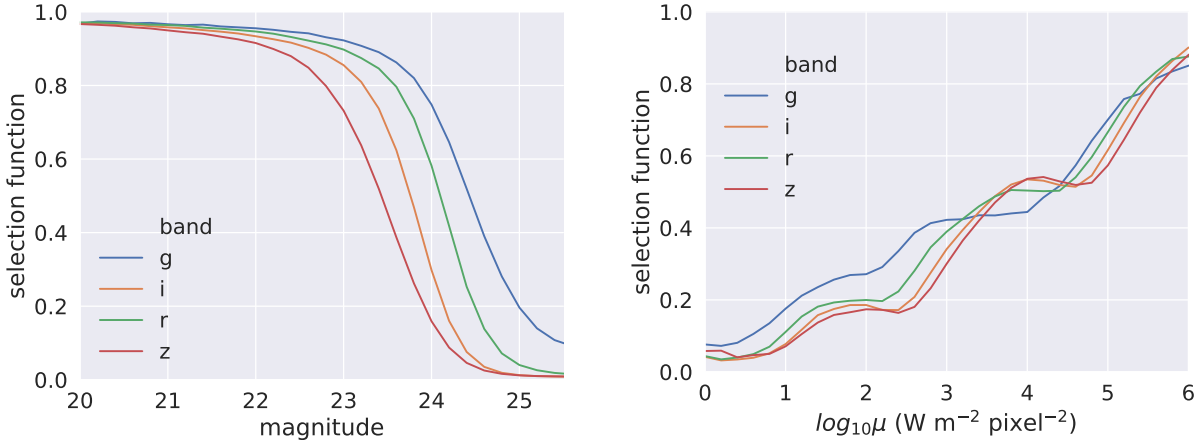


FIGURE 2.24: Selection function of DES Y3 Wide as a function of apparent magnitude MOF (left panel) and surface brightness (right panel), both computed from the detection rate in Balrog simulations. Here the surface brightness, μ is measured in logarithmic scale, in units flux/pixel² and defined as: $\log_{10}\mu = \log_{10}(CM_FLUX/CM_T)$, where CM_T is the number of pixels delimited by the edges of best fit composite model and CM_FLUX is the total flux measured in these pixels (in W m⁻²).

2.2 MICE Simulations

To validate the methodology used in this work, we rely on simulated data to answer specific questions and optimize the results with real data. The mock galaxy catalogs are free of observational effects. Therefore, one can include them gradually and evaluate their contributions to the quality of the results.

The Marenostrum Institut de Ciències de l’Espai Simulations (MICE)⁷ is a catalog of galaxies generated from a hybrid Halo Occupation Distribution (HOD) and Halo Abundance Matching (HAM) prescriptions to populate Friends-of-Friends (FOF) dark matter halos from the MICE-GC.

MICE-GC is a N-body simulation that assumes a flat Λ CDM model with input cosmological parameters as the following: $\Omega_m = 0.25$, $\sigma_8 = 0.8$, $n_s = 0.95$, $\Omega_b = 0.044$, $\Omega_{Lambda} = 0.75$, $h = 0.7$. A full description of MICE is found in Carretero et al. (2015) and in COSMOHUB⁸ platform, where the catalog is available for download.

The simulation covers one octant of the sky (~ 5000 deg²), built with no repetition of the simulation box. The angular coordinates range, in degrees, are: $0 < R.A. < 90$ and $0 < Dec. < 90$, but the transformation of coordinates from Cartesian (x, y, z) to equatorial does not follow the astronomical convention so that R.A. is actually, $90 - R.A.$ Small rotations and magnification effects are applied based on weak lensing theory. It includes mock photometry for several filters to mimic the set of magnitudes of *Illustris* past, current, and future surveys, such as COSMOS, VISTA, SDSS, DES, and EUCLID. In this work, we use the DES *ugrizY* and VISTA *JHKs* bands. Their transmission curves are presented in Figure 2.25.

⁷<http://maia.ice.cat/mice/>

⁸<https://cosmohub.pic.es/>

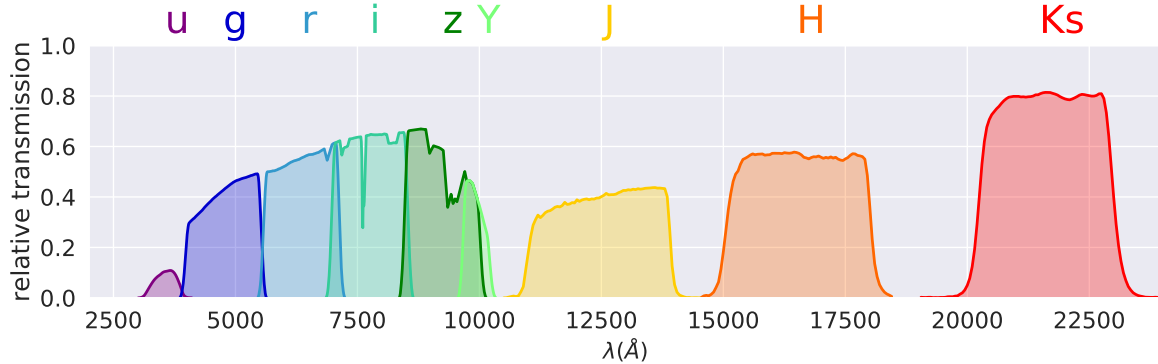


FIGURE 2.25: SDSS + DES + VHS filters transmission curves.

The catalog is complete for DES-like surveys ($i < 24$) out to $z = 1.4$, only for the following regions: $\text{Dec.} > 30$, $\text{Dec.} < 30$, and $30 < \text{R.A.} < 60$. For the local Universe, the catalog was constrained according to the SDSS the Luminosity Function measured by Blanton et al. (2003), i.e., $\phi_* = (1.49 \pm 0.04) \times 10^{-2} h^3 \text{ Mpc}^{-3}$, $M_* - 5\log_{10}h = -20.44 \pm 0.01$, $\alpha = -1.05 \pm 0.01$. It was extended for fainter luminosities according to Blanton et al. (2005b) LF, so that the minimum absolute magnitude in the r -band in MICE v2.0 is $M_r - 5\log(h) \sim -14.0$ ($L_r \sim 10^7 L_\odot$). The reference band is the SDSS $^{0.1}r$, which is the r -band SDSS filter shifted to $z = 0.1$. The mock magnitudes account for galaxy evolution based on PEGASE (Fioc et al., 1997) model libraries for spectral synthesis, but the evolutionary corrections are not applied by default. If one wishes to compare it to the observations, it is necessary to correct the magnitudes according to the Eq. 2.8.

$$m_{\text{evolved}} = m_{\text{catalog}} - 0.8 [\arctan(1.5 z) - 0.1489] , \quad (2.8)$$

According to Carretero et al. (2015), the mock galaxy colors follow the global SDSS ($^{0.1}g - ^{0.1}r$) distribution as a function of the absolute magnitude in the $^{0.1}r$ band, according to the results of Blanton et al. (2005a). The colors are the sum of three Gaussian components to represent red, green, and blue galaxy populations (see Figure 15 of Carretero et al., 2015). The galaxy clustering as a function of luminosity and color follows Zehavi et al. (2011), and the color-magnitude diagram reflects the NYU DR7 catalog (Blanton et al., 2005a).

The spectral energy distributions and dust extinctions derived from the COSMOS library (Ilbert et al., 2009), with four different extinction laws: one from Prevot et al. (1984) and 3 from Calzetti et al. (2000), varying parameters (see details in Chapter 4). The resulting redshift and magnitude distributions for $ugrizYJHKs$ photometric bands are shown in Figure 2.26.

The entire MICE catalog contains 488,609,997 ($\sim 500\text{M}$) galaxies, 329,344,245 ($\sim 330\text{M}$) halos distributed in $\sim 5,000 \text{ deg}^2$ at the redshift range $0 < z < 1.4$. The catalog is complete for DES-like survey ($i < 24$) only for the following regions: $\text{Dec.} > 30$ or $\text{Dec.} < 30$ and $30 < \text{R.A.} < 60$. From this region, similar to what was done above for DES Y3, we define a “medium” subset as an area selection of 44 HEALPix pixels $N\text{Side} = 32$, which corresponds to $\sim 147.63 \text{ deg}^2$. Its creation was motivated to serve as a test sample for the LF methodology. It is expected to have the same LF normalization as the complete simulations, with the presence of small fluctuations in LF shape, due to cosmic variance. We selected entire pixels to guarantee a contiguous area and to take advantage of the parallelization scheme available on the DES Science Portal (Gschwend et al., 2018).

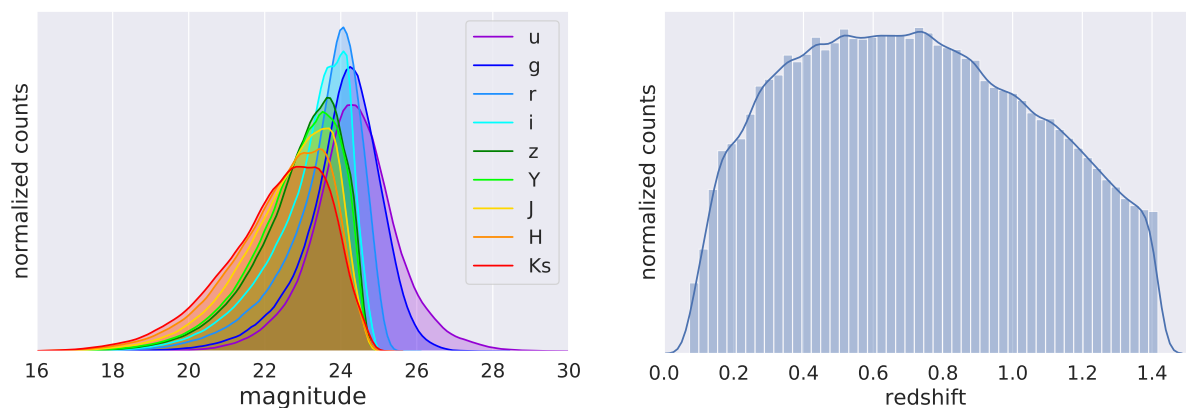


FIGURE 2.26: Apparent magnitude and redshift distributions. Both panels refer to kernel density estimations computed for MICE RANDOM data set (defined below).

Chapter 3

Photometric Redshifts



Overview

In this chapter, we present the methodology used to estimate photo-zs. We describe how to prepare training, validation, and test samples from spectroscopic and photometric data. We carry out tests with both observed and simulated data to find an optimal prescription for the algorithm configurations. We quantify and compare photo-z precision and accuracy, varying the algorithm used and the contents of the input data. We also study the usage of probability density functions to estimate the global redshift distribution, compared to the one for single photo-zs. Finally, we show the results obtained for the DES Y3 catalog, which will be used to study galaxy evolution in the next chapters.

3.1 Getting redshifts from magnitudes

The redshift (z) is one of the main ingredients in the calculation of luminosities and distances of galaxies. Since we use data from DES, our analysis naturally rely on photometric redshifts (photo- z), which require the measurement of magnitudes or colors (Baum, 1962). These photometric quantities serve as a low-resolution estimate of the underlying SED of a given object.

Both photo- z and spec- z have advantages and disadvantages. Whereas spec-zs are much more precise, the photo- z is cheaper, faster, and applicable to a much large and diverse galaxy population. In this work, we rely on the statistical power of an extensive data set where photo- z can be estimated virtually for any galaxy in the sample, even for those very faint and with low signal-to-noise detection, although their errors may be considered significant.

In the paper by Ramos et al. (2011), they shown that it is possible to obtain a remarkable agreement between the LF results based on photo- z and spec- z for $z \leq 2.0$ using photometric data from the Canada-France-Hawaii Telescope Legacy Survey (CFHTLS, Ilbert et al., 2006) and spectroscopic data from the VIMOS VLT Deep Survey (VVDS, Garilli et al., 2008; Le Fèvre et al., 2004).

3.1.1 Photo- z methods

There are two well-known types of methods to estimate photo- z : template-fitting and empirical. The first one is based on SED templates, which ideally are capable of representing all the possibilities of underlying spectra the sample. The template-fitting algorithms map the SED templates in redshift space, in small dz steps. Then they compare the theoretical fluxes from the redshifted SED templates with the observed magnitudes until finding the best correspondence using some quantitative metric (e.g., the χ^2). Some example of algorithms that use this technique are: LePhare (Arnouts et al., 1999; Ilbert et al., 2006), BPZ (Benítez, 2000), HyperZ (Bolzonella et al., 2000), and EAZY (Brammer et al., 2008).

Empirical methods rely on the use of a "true" sample to feed the training procedure and map the relationship between the desired quantity - the redshift, and the observational parameters - magnitudes, colors, and their respective errors. There is a large variety of machine learning methods used by photo- z

algorithms in the literature, such: (i) artificial neural networks: ANNz (Collister et al., 2004), ANNz2 (Sadeh et al., 2016), DESDM (Oyaizu et al., 2008a; Oyaizu et al., 2008b; Sánchez et al., 2014; Bonnett, 2015), SkyNet (Graff et al., 2014); (ii) nearest-neighbor DNF (De Vicente et al., 2016); (iii) Weights (Lima et al., 2008); (iv) Pofz (Cunha et al., 2009); (v) boosted decision trees (e.g., ArborZ, Gerdes et al., 2010); (vi) prediction trees and random forest (e.g., TPZ, Carrasco Kind et al., 2013); (vii) self organizing maps and random atlas (e.g., SOMz, Carrasco Kind et al., 2014a).

Besides these two categories, there are new methods that are growing in popularity. One of these is called *clustering redshifts*, and relies on the correlation between the clustering observed in the 2-dimensional image and the distances as a third dimension, quantified by the redshift (e.g., Bates et al., 2019; Rau et al., 2019).

Another example is the so-called *phenotypic redshifts*, which works as an empirical method, but goes a step beyond. It uses a small sample with deeper photometry in a large number of filters to break the type-redshift degeneracy. Then, it uses self-organized maps to apply the relations learned from the deep sample on wide-field surveys with a few photometric bands available, like DES (Buchs et al., 2019).

Several algorithms, including most of those listed above, also provide the redshift probability density function (PDF) estimate for each galaxy. Photo-z PDFs have mainly been used in astrophysics and cosmology as they improve the accuracy of cosmological measurements, compared to the single photo-z estimates (e.g., Mandelbaum et al., 2008; Carnero et al., 2012; Sheldon et al., 2012). One of its primary advantages is that it does not introduce biases on the calculation of the redshift distribution, $N(z)$, as discussed in Cunha et al. (2009). Nonetheless, as the photo-z PDF contains more information than a single photo-z estimate, the storage of PDFs can become a challenge as we start to deal with billions of objects, especially if computing in different scenarios, e.g., varying the photo-z algorithm, or the set of SED templates used (Carrasco Kind et al., 2014b).

There are many works in the literature comparing the performance of the most used methods (e.g., Hildebrandt et al., 2010; Abdalla et al., 2011; Sánchez et al., 2014; Bonnett et al., 2016). The classic work *PHoto-z Accuracy Testing* program (PHAT, Hildebrandt et al., 2010) reported the state of the art of photo-z performance for 12 different methods. PHAT has established a standard of photo-z quality assessment based on three quantities: photo-z bias, scatter, and outliers rate.

The PHAT tests with real data achieved $\sim 4\%$ of scattering and $\sim 7.5\%$ of outlier rates ($\sim 4.5\%$ after sample cleaning), using 18 photometric bands from the UV to IR. These outliers refer to objects with catastrophic failures in the photo-z estimate. The authors stressed the contribution of AGNs as part of the reason for the high outlier rates obtained. They recommended cleaning the sample by removing the photo-z outliers for the science applications where the sample completeness is not required. Unfortunately, this is not the case for the estimate of the Luminosity Function, so we need to pay attention to these particular objects.

Among the 12 methods compared in PHAT, in general, the empirical codes produced better results than the template-based ones. The inaccuracies result from both the templates and the photometry.

A similar conclusion was reached by Sánchez et al., 2014, using DES data from the science verification epoch. They expanded the list of metrics used in PHAT, and compared 13 different codes using SExtractor magnitudes AUTO and DETMODEL in the five standard DES bands *grizY*. They found that empirical methods generally perform better, reaching a scatter below $\sigma_{68} = 0.08$ (see definition below), although they are susceptible to the ability of the training set to represent well the data of interest. They verified that higher S/N photometry has a significant positive impact on photo-z quality, as expected. However, if the higher S/N is only for the training sample, it does not make much improvement. They also explored the incorporation of the *u*-band, which is not part of the DES strategy but is available in the DECam filter set. It resulted in a general improvement in photo-z precision for all codes, particularly for the low redshift range ($z < 0.5$), where part of the redshifted SEDs still falls into the observed UV.

We repeated these exercises by comparing four different algorithms, three training based (ANNz2, DNF, and MLZ), and one template-fitting (LePhare), also finding better results for the empirical ones, in particular, DNF (results in Section 3.2.1). Out of the eight codes available in the DES Science Portal

(Gschwend et al., 2018), we selected these four due to their best performance in previous tests using DES data, and to the possibility of producing photo-z PDFs. We briefly describe those four algorithms below.

Artificial Neural Networks 2 (ANNz2, Sadeh et al., 2016) is an update of the classical ANNz (Collister et al., 2004), which includes the generation of photo-z PDFs. This version combines different machine learning techniques, besides the standard artificial neural networks (ANN), such as boosted decision/regression trees (BDT), and k -nearest neighbors (k -NN).

The ANN uses sigmoids as activation functions in its hidden layers, and a cost function is minimized based on an independent validation set to avoid over-fitting. A k -NN weighting procedure has been embedded in the code as an optional feature if the user provides a photometric sample of reference. The main advantage of ANNz2, like any other empirical method, is that it is not sensitive to systematic errors in the observables. They are incorporated as features in the data, causing no harm to the results, as long as the photometry has precisely the same systematic errors in the training and the science samples.

We run ANNz2 using its Random Regression method with an ensemble of 10 random realizations, combining ANN and BDT. We use the same configuration as described by Sadeh et al. (2016) in the paper: ANN with two hidden layers with five and ten neurons each, and the BDT is composed of 600 trees with a minimum of 2% of the training sample in each tree node. The code generates multiple solutions with different realizations of the machine learning methods included. The single redshift estimate is the one whose method gives the best results in the validation sample. The multiple realizations are used to evaluate the uncertainties and to estimate the PDF.

Directional Neighbourhood Fitting (DNF, De Vicente et al., 2016) is an empirical algorithm based on the k -NN concept but introducing two new features: the idea of directional distance, in replacement for the Euclidean one, and a neighborhood fitting as a photo-z estimation strategy. De Vicente et al. (2016) explore three kinds of distances in the hyperspace of magnitudes: Euclidean, angular, and directional. Neighbor objects in the Euclidean distance point of view, are objects with similar magnitudes. Objects with the same colors, but with different magnitudes, are not considered neighbors. For instance, two galaxies of the same spectral type but with different sizes may have similar colors at the same redshift, so they should be neighbors for adequate training. The angular distance is defined as the normalized inner product, i.e., the cosine of the angle among the m -dimension vectors represented by the m observables. This distance groups objects with similarities in colors, but with the disadvantage of degrading quickly for larger neighborhoods, as the distance covered by an angle with fixed aperture grows more significant as the vector length increases. The directional distance is the combination of Euclidean and angular distances, providing a balance between the benefits of both approaches. It is computed directly as a product of the two other distances.

The other innovation of DNF is the neighborhood fitting. For a simple k -NN estimation, the photo-z, and its error are computed as the mean, and standard deviation of the redshifts of the k nearest objects pondered inversely to their distances. The fitting consists of determining a hyperplane that best fits the directional neighborhood in the training sample and using this plane as a prediction function for the photometric sample. The advantage of this method is that the hypersurface containing the neighbors is smoothed, avoiding abrupt changes that could lead to catastrophic errors. As the fitting is local, the fit can be a simple linear regression (in m dimensions), and the fitting residuals are considered the photo-z errors.

The photo-z PDF is computed as the following: for each one of the k nearest neighbors, a sample of z_k redshifts is generated as the neighbor's redshifts plus the residuals. The PDF is the normalized histogram of these values in redshift bin width defined by the user.

The code runs in two possible modes: ENF (Euclidean Neighbourhood Fitting, which is faster), and DNF (Directional Neighbourhood Fitting, which is more accurate). For all the DNF results we show in this chapter, we run the code in DNF mode, with $k = 80$ neighbors. De Vicente et al. (2016) recommend to seek a balance between higher statistical power (large k) and locality (small k).

Le PHotometric Analysis for Redshift Estimations (LePhare, Arnouts et al., 1999; Ilbert et al., 2006) is a classical program in FORTRAN language that performs SED fitting based on a simple χ^2 method. It computes theoretical fluxes by combining a set of SED templates, which can be observed or synthetic,

convoluted with the filters transmission curves, and one or more extinction laws. Then it creates a matrix of theoretical magnitudes in each filter in small redshift bins to scan and compare with the observed magnitudes for each galaxy in the catalog. The greatest advantages of this kind of algorithm are that it does not require a training set, and it can provide several other properties besides the redshift, especially when using synthetic SED templates. We explore this possibility in detail in the next chapter. On the other hand, there are three severe limitations in LePhare (and any other template-fitting method) that it is worth to mention. First, the strong dependency on a template library that is representative of the galaxy populations in the redshift range observed, i.e., SEDs whose evolutionary tracks cover the locus occupied by the objects from the sample in the color-magnitude space.

The second issue is degeneracy. Either by merely shifting observed SEDs to longer wavelengths or by using synthetic SEDs, which consider the evolution of stellar populations with redshift, in both cases, the SEDs of totally different spectral types at different redshifts meet each other in color-magnitude space. Thus, the probability of an object to have the best fit with one or another SED is virtually the same. This problem is aggravated when considering the reddening caused by internal extinction. In some cases, a very dusty starburst can have the same colors as a nearby early-type galaxy. Bayesian methods have been used to address this issue (e.g., Benítez, 2000), but it implies making some assumptions to define the priors. If one knows the redshift *a priori* and uses LePhare with fixed z to estimate other properties, the degeneracy problem is mitigated but not completely solved (see our results in Chapter 4).

At last, template-fitting is strongly affected by systematic errors in the observables, such as differences in zero-point calibrations, especially if they are wavelength dependent. This last issue makes it difficult to combine other photometric bands obtained from other surveys. They must be carefully calibrated in the same reference photometric system to be used together.

When running LePhare on MICE, we used the same SED templates that were used to create the simulations (the COSMOS SEDs from Ilbert et al., 2009) and apply the same extinction laws and $E(B - V)$ values to the respective ranges of templates (as detailed in Section 2.2), computing χ^2 for dz steps of 0.0125. The only difference is that we do not interpolate between SEDs, so the total number of SEDs is the same as the original set (31 SEDs), which should only slightly reduce the resolution of the results. Although LePhare does not require a training set, if available, one can use it to derive the systematic differences between the theoretical and observed magnitudes, then use this information to improve the compatibility between the inputs and the templates. Using the 30,000 galaxies of the training set described below, we find very small systematic shifts: 0.002, 0.004, 0.004, 0.001, and -0.006, for g , r , i , z , and Y , respectively, as expected since we are recovering, virtually, the same SEDs as the originals.

Trees for Photo-zs (TPZ, Carrasco Kind et al., 2013) is part of the parallel python framework named *Machine Learning and photo-Z* (MLZ). The prediction trees branches are subdivisions of the data in progressive smaller chunks. It is done by asking questions that split the data recursively until it reaches a final “leaf” containing a small number of objects. The questions are done in a way that the objects that belong to the same leaf have similar photometric properties.

A random forest is an ensemble of several prediction trees that are used in combination. The set of galaxies used to create the different trees are selected by bootstrapping the galaxies from the training sample, keeping the sample size. The different versions of the training sample are perturbed according to the errors in each variable, assuming that they follow a normal distribution. This step introduces randomness into the forest.

Once the forest is prepared, the galaxies in the test sample run through the trees until they reach their final leaves, where there are some training galaxies with known values of redshift, so the average redshift of the leaf is an approximation to the unknown object with a given probability.

Finally, all individual trees of the forest are combined to construct the PDF. We run TPZ with a forest of 100 random trees and a maximum of 5 objects in each terminal leaf.

For all the four algorithms described above, we set up the PDF minimum, maximum, and bin width as 0.0, 1.5, and 0.05, respectively.

3.1.2 Photo-z quality metrics

To quantify the photo-z accuracy and precision, we follow the trend established by PHAT and start by considering the three metrics: bias, scatter, and outliers rate. The bias gives information about systematic errors in photo-z estimates, while the scatter and the outliers rate are related to random errors. Besides these metrics, we also compute the mean squared error (*MSE*), which combines both systematic and random contributions to the errors. We establish the *MSE* as the most important metric to be considered when analyzing the results to make decisions.

The photo-z global metrics regarding the comparison between the expected value (the spec-z for real data, or the true-z for simulations) and the single estimate photo-z are computed as the following:

- **Bias ($\overline{\Delta z}$)**: the global mean of the difference $\Delta z = z^{phot} - z^{spec}$ for all the n galaxies in a sample.

$$\overline{\Delta z} = \frac{1}{n} \sum_{i=1}^n (z_i^{phot} - z_i^{spec}). \quad (3.1)$$

- **Scatter (σ_{68})**: the half of the width of the Δz distribution where 68% of the data is enclosed.
- **Outlier fraction (f_{out})**: the fraction of objects with $|z^{phot} - z^{spec}| > 0.15$ ¹.
- **Mean Squared Difference (*MSE*)**: the mean squared difference of Δz .

$$MSE = \frac{1}{n} \sum_{i=1}^n (z_i^{phot} - z_i^{spec})^2. \quad (3.2)$$

The *MSE* can also be calculated as:

$$MSE = \sigma^2 + \overline{\Delta z}^2. \quad (3.3)$$

where σ^2 is the variance of Δz . We compute errors for the metrics using a jackknife re-sampling technique of 10 samples with 90% of the data each.

We also evaluate the ability to reconstruct the redshift distribution by using the photo-z PDFs. In these cases, we adapt the concept of bias to a bias in the distribution as a whole, not considering individual objects anymore. So we define the last metric, $\overline{\Delta N(z)}$ as the following:

- **$N(z)$ bias ($\overline{\Delta N(z)}$)**: the global mean of absolute value of the difference between the counts of galaxies for the k redshift bins defined by the photo-z PDF, in comparison to the true counts, if using simulations, or the spec-z counts if using real data. We find it convenient to express this quantity in percentage:

$$\overline{\Delta N(z)} = \frac{1}{k} \sum_{j=1}^k |N(z_k)^{phot} - N(z_k)^{spec}|. \quad (3.4)$$

In the following sections, we describe in details all steps taken to compute individual photo-zs and photo-z PDFs, since the preparation of training samples, is a fundamental ingredient of the methodology.

3.1.3 Building test samples with DES data

A "training set" is a data set containing both the observable variables and the truth values of the target quantity. When the target is the redshift, traditionally, the observables are integrated flux of photons in broad-band filters, converted into magnitudes, and their errors in the different bands. Nonetheless, they

¹Following the benchmark established by PHAT

can also be any other photometric measurements, such as the morphologically related ones like size or shape parameters.

Spectroscopic redshift samples are used as truth-table due to their negligible errors in comparison to photo-z uncertainties. It is also possible to use redshifts from simulations instead of spec-zs, or both together, to artificially complete the sample in case of severe incompleteness.

In this work, we use spec-zs collected from the literature matched to DES data for two main applications: (ii) measure the photo-z quality. For the second purpose, we use two independent samples: validation and testing sets. The first is used to perform repeated tests, allowing a fine-tuning in the algorithms, leading to the choices of configuration parameters mentioned above for each code. For fair performance evaluation of the photo-z algorithms, the two sets, training, and validation should be mutually exclusive.

The testing set is also required to have no object in common with the training set, it is used just in the end of the analysis, as a final quality test. With the testing set, we compute the photo-z metrics, and these results must not have any influence in the photo-z methodology.

How to build a spec-z sample

The Australian Dark Energy Survey (OzDES, Yuan et al., 2015; Childress et al., 2017) is a five-year spectroscopic survey on the Anglo-Australian Telescope, whose primary aim is to measure redshifts of Type Ia supernovae host galaxies and derive reverberation-mapped black hole masses (Yuan et al., 2015). OzDES was designed to provide spectroscopic follow-up of targets identified from DES imaging, not only for supernova hosts but for a wide range of galaxy types and redshifts, providing a spectroscopic dataset also used to train photo-z algorithms.

Besides OzDES, we searched for available data in the literature and retrieved more than 2 million spec-z measurements from a total of 39 spectroscopic surveys data releases (listed in Table 3.1), from where 1,866,505 refer to extragalactic sources including both galaxies and quasars. The spectroscopic data collected is spread beyond the DES footprint across the whole southern hemisphere, except the region hidden behind the Milky Way disk, as shown in Figure 3.1.

The individual spec-z catalogs present a large variety of coverage and shape of redshift distributions, $N(z)$, as each has its particular purposes and scientific goals, not necessarily related to the training and calibration of photo-zs. The collection of all those spec-zs results in a two-peak distribution of redshifts, that remain evident after associating with DES galaxies (see Figures 3.2 and 3.3b).

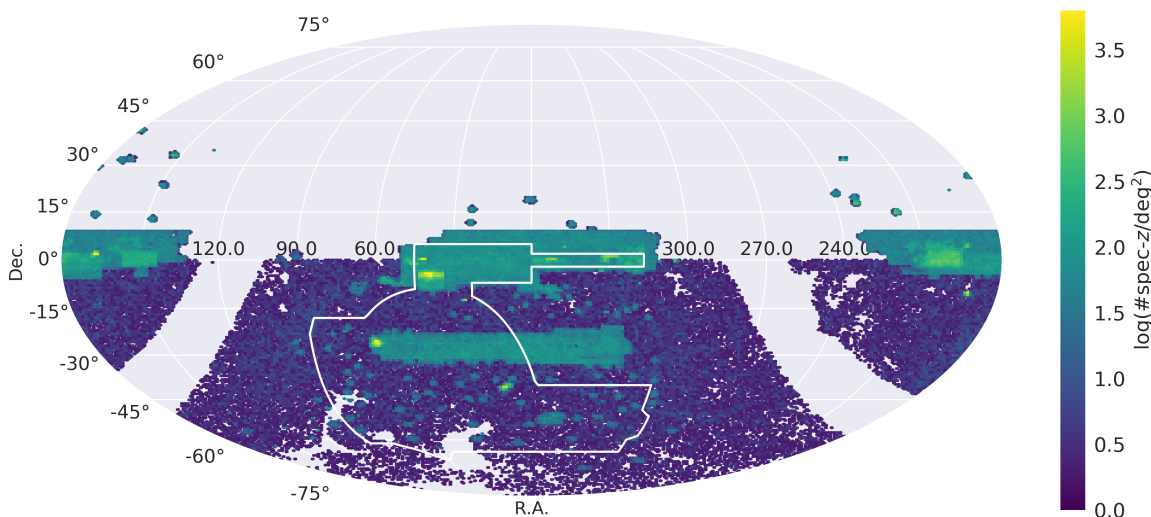


FIGURE 3.1: Projected spatial density of the complete collection of spec-z measurements by OzDES and from the literature.

#	Survey	# objects	z mean	z min	z max	Reference
1	2dF	245,591	0.12	0.00	0.35	Colless et al. (2001)
2	2dFLenS	70,079	0.40	0.09	0.69	Blake et al. (2016)
3	3D-HST	207,967	1.01	0.01	5.21	Momcheva et al. (2016)
4	6dF	109,831	0.06	0.00	0.38	Jones et al. (2009)
5	ACES	13,963	0.58	0.04	1.42	Cooper et al. (2012)
6	ATLAS	1,074	0.32	0.02	1.89	Mao et al. (2012)
7	C3R2	1,283	0.92	0.03	3.52	Masters et al. (2017)
8	CDB	541	0.58	0.25	0.91	Sullivan et al. (2011)
9	CLASH-VLT	10,183	0.50	0.02	6.15	Annunziatella et al. (2016), Balestra et al. (2016), Biviano et al. (2013), Caminha et al. (2017), Grillo et al. (2016), Karman et al. (2017), and Monna et al. (2017)
10	DEEP2	50,319	0.99	0.01	1.89	Newman et al. (2013)
11	DEIMOS 10k	10,770	1.19	0.00	6.60	Hasinger et al. (2018)
12	DES IMACS	4,654	0.60	0.00	1.37	Nord et al. (2016)
13	FMOS-COSMOS	1,153	1.55	0.75	1.74	Silverman et al. (2015)
14	GAMA	166,332	0.24	0.01	0.90	Driver et al. (2011) and Baldry et al. (2018)
15	GLASS	1,667	1.06	0.34	2.07	Treu et al. (2015)
16	LADUMA N17B331	3,794	0.39	0.0	4.18	private communication
17	LCRS	26,418	0.10	0.00	0.32	Shectman et al. (1996)
18	MOSFIRE	267	1.89	0.80	3.08	McLean et al. (2012)
19	MUSE	1,602	1.76	0.03	6.24	Urrutia et al. (2018)
20	NOAO OzDES	5,596	0.22	0.00	0.68	Yuan et al. (2015) and Childress et al. (2017)
21	OzDES	36,784	0.54	0.00	3.94	Yuan et al. (2015) and Childress et al. (2017)
22	Pan-STARRS	2,550	0.33	0.00	3.16	Rest et al. (2014), Scolnic et al. (2014), and Kaiser et al. (2010)
23	PRIMUS	213,696	0.57	0.02	4.08	Coil et al. (2011) and Cool et al. (2013)
24	SAGA	68,644	0.29	0.01	1.17	Geha et al. (2017)
25	SDSS DR14	848,046	0.59	0.00	1.95	Abolfathi et al. (2018)
26	SNLS AAOmega	417	0.60	0.07	1.17	Lidman et al. (2013), Yuan et al. (2015), and Childress et al. (2017)
27	SNLS FORS	1,496	0.51	0.03	3.75	Bazin et al. (2011), private communication
28	SNVETO	6,516	0.84	0.03	3.63	private communication
29	SpARCS	410	0.91	0.12	1.58	Muzzin et al. (2012)
30	SPT GMOS	2,243	0.56	0.07	1.24	Bayliss et al. (2016)
31	UDS	1,511	1.06	0.04	3.44	Galametz et al. (2013)
32	VIPERS	91,507	0.69	0.05	1.67	Garilli et al. (2014)
33	VUDS	698	1.78	0.19	3.75	Tasca et al. (2017)
34	VVDS	40,927	0.59	0.00	4.08	Garilli et al. (2008) and Le Fèvre et al. (2004)
35	WiggleZ	81,362	0.55	0.01	1.70	Parkinson et al. (2012)
36	XMM-LSS	383	0.42	0.19	0.65	Stalin et al. (2010)
37	XXL AAOmega	3,660	0.47	0.00	2.80	Lidman et al. (2016)
38	zCOSMOS	20,689	0.54	0.00	1.99	Lilly et al. (2009) and Knobel et al. (2012)
39	zCOSMOS Deep	920	1.87	0.06	3.44	private communication
40	ZFIRE	216	1.77	1.05	2.26	Nanayakkara et al. (2016)

TABLE 3.1: Surveys source of spectroscopic data.

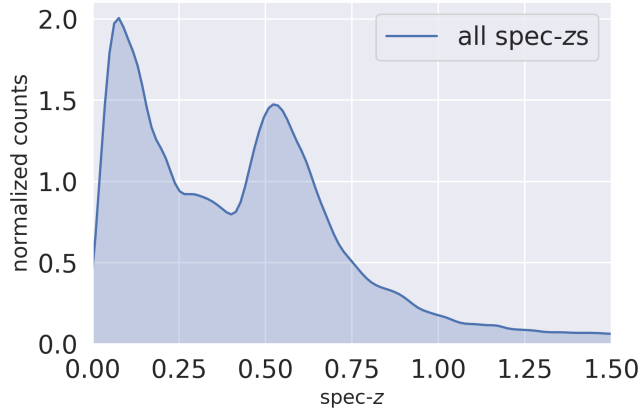


FIGURE 3.2: Redshift distribution of the entire spec-z sample.

Q_{spec}	Criteria (from Yuan et al., 2015)
6	It is a star (used to tag the supernova discoveries)
4	Redshift more than 99 percent correct. Chosen when there are multiple strong spectral line matches.
3	Redshift more than 95 percent correct. Chosen when there are multiple weak spectral line matches or a single strong spectral line match.
2	Possible redshift. It is given to targets where there are one or two very weak features (e.g., a single weak emission line that may be OII). Not recommended to use for science.
1	Unknown redshift. It is given to objects where no features can be identified.

TABLE 3.2: OzDES quality flags definitions

In OzDES, the spec-zs are measured using the software MARZ² (Hinton et al., 2016), which is a semi-automatic tool that requires the validation from a scientist based on the visual inspection of a chosen SED. The software searches for matches to the spectral emission lines. If there are no strong lines, it searches for a match with a spectrum from a template library. In the processes of validation, the “redshifter” attributes a quality flag (Q_{spec}) to each measurement following the criteria described in Table 3.2

We group all the spec-z measurements in a centralized spectroscopic database, where each survey quality flags are homogenized by translating their values to the OzDES flag schema.

Since there is a significant overlapping area among the surveys listed in Table 3.1, there exists a substantial number of multiple measurements for some objects. When creating a spectroscopic sample for photo-z purposes, we select just one measure for each galaxy available. First, we identify these multiple measurements by doing the spatial matching based on the equatorial coordinates for each object with the rest of the sample with a search radius of 1.0 arcsec. This step is done in several sub-steps using a PostgreSQL extension for spatial indexing on a sphere, called Q3C (Koposov et al., 2006) and the Starlink Tables Infrastructure Library Tool Set (STILTS, Taylor, 2006). When detecting more than one object inside the search radius, we select the measurement with the highest Q_{spec} . In the case of a tie, we choose the one obtained more recently. If there are two or more observations in the same year, we prefer the redshift with the smallest error, if available. Finally, if we still have more than one source, we prefer the one with redshift the closest as possible to the mean value of all the multiple measurements. Since we have selected a high “quality” threshold, the differences between choosing the best source or averaging between all the different matches are negligible.

After removing multiple measurements and bad data ($Q_{spec} < 3$), the spec-zs sample including all sources listed in Table 3.1 contains 1,535,560 galaxies from 40 surveys.

²<https://samreay.github.io/Marz>

Matching spectroscopic with photometric data

The next step is to join the spectroscopic and photometric data. Once again, we use Q3C to match them based on the angular separation between the objects in both data sets, with a search radius of 1.0 arcsec. To avoid multiple matches, we perform the search starting from the objects in the spectroscopic sample. If there are two or more objects from the photometric sample within the search radius around the spectroscopic object, the nearest object to the spectroscopic one is selected. The result of matching the spectroscopic sample with DES Y3 data contains 243,827 galaxies from 26 surveys.

The spatial and redshift distributions of the matched sample are shown in Figure 3.3. For clarity, we show individually only the five surveys which contribute with a more significant number of objects after the matching (SDSS, VIPERS, 2DF, GAMA, and OzDES). These five sources give a hint about the origin of the double peak feature in the $N(z)$ distribution.

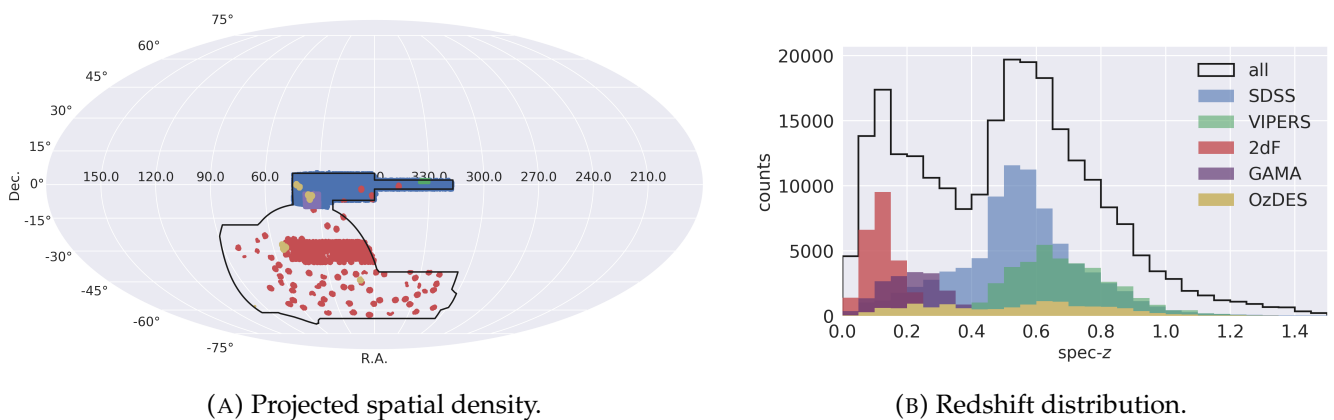


FIGURE 3.3: Spectroscopic Sample matched to DES photometric data. The colors representing each survey are the same in both panels.

Pruning the matched sample

Before sorting out galaxies to build the training, validation, and testing subsets, since we have a sizeable spectroscopic sample, we apply some data mining techniques to the matched catalog as a pre-processing step to reduce the data and also improve the quality of the results. It is essential to clean the matched spectroscopic sample from bad data that could pollute the result of training, contaminating the results of photo-z estimates when it is done for the final photometric set. On the other hand, it is also important to be careful not cleaning the sample excessively and cause severe incompleteness in color-magnitude space. The quality cuts described in the next paragraphs are applied in both the matched spec-z sample and the photometric set of reference (Y3 Gold).

The magnitude distributions of both spectroscopic (left panels) and photometric (right panels) samples are compared in Figure 3.4, represented by KDE histograms and their respective box-and-whisker diagrams. The upper panel (3.4a) refers to the samples before cleaning, and the subsequent panels show the result of each quality cut described below.

We start by removing objects that are in problematic regions identified by the systematic maps mentioned in the previous chapter (bad regions map, foreground objects map, etc., see Section 2.1.1 for details). We made this cut before the matching mentioned above, so the 240,125 resulting objects already come from “good” regions. Then, we remove from the matched sample objects with invalid values of magnitudes in any band. These values identify possible failures in the process of image reduction or object detection. For instance, in the raw catalogs available in DESDM, ± 99.0 is assigned to the magnitudes in cases that not SExtractor failures. MOF failures are marked as magnitude = 37.5 (arbitrarily), regardless of the band. The non-physical values of magnitude found in the catalog are not precisely 37.5,

because the zero-point and extinction corrections were previously applied to the entire catalog. So, what we find is a list of outliers with a magnitude close to the values mentioned above.

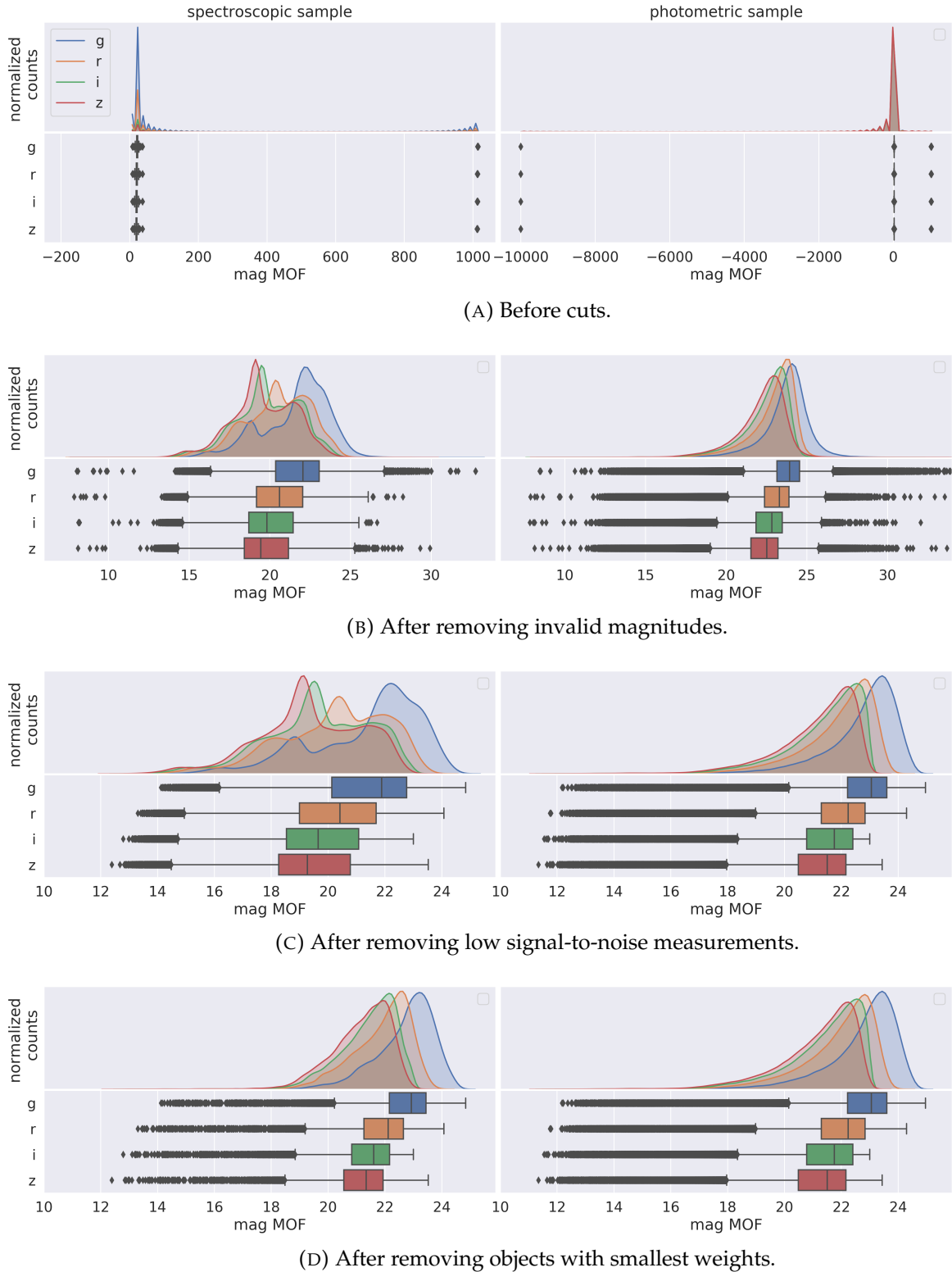


FIGURE 3.4: Spectroscopic Sample matched to DES photometric data. The colors representing each survey are the same for both panels.

Thus, the first cut removes all objects with any MOF magnitude outside the interval of $0 < \text{mag} < 35$,

which reduced the sample to 239,724. The impact of removing this tiny fraction of outliers is a better data visualization due to the appropriate scale in the x-axis in Figure 3.4b, revealing the hidden distributions.

The second cut regards the quality of data. We remove objects with $S/N < 5$. These objects might be part of the science sample, but we do not want to pollute the training with large errors. After the second cut, the spectroscopic sample size decreased to 221,852 ($\sim 92\%$ of the initial sample), while the photometric reference sample decreased from 721,780 to 255,351 ($\sim 35\%$ of the initial sample). This difference in proportions makes evident the bias present in spectroscopic samples as measurements of brighter and higher S/N objects. The magnitude distributions after the second cut are shown in Figure 3.4c.

Improving the similarity of the various sets: Use of weighting

After matching the spec-zs with DES objects and cleaning the matched sample from bad measurements, we notice, as expected, that the resulting sample's magnitude and color distributions are severely different from DES' photometric data set. Ideally, the training, validation, and testing sets should contain a mixture of galaxy populations that is representative in the colors space of the galaxies throughout the history of the Universe or, at least, throughout the part of the history which is the target of our study (regarding the wavelength covered and the expected depth of DES, we limit our analysis to $0.0 < z < 1.2$). However, the availability of spectroscopic data depends on the scientific goals of the spectroscopic surveys found on the literature and their observational limitations.

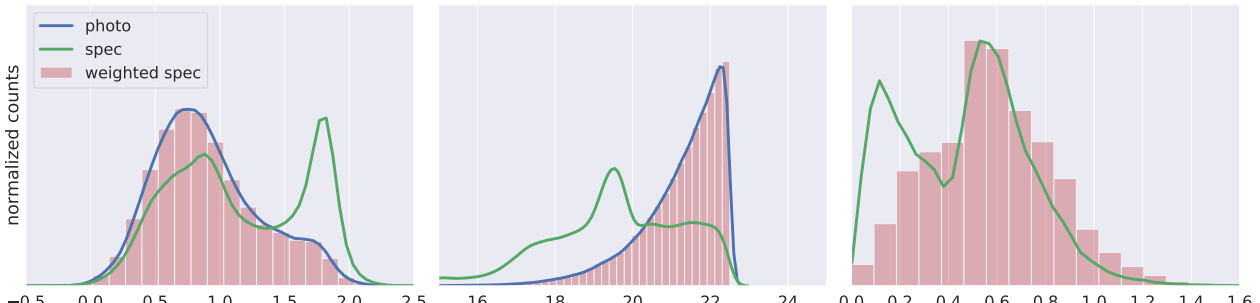
Depending on the photo-z algorithm used, the results can be very sensitive to the difference between the noise properties of both training and science samples Collister et al. (2004). Notwithstanding, for the validation and testing sets, besides the coverage in magnitude and color spaces, a realistic analysis of photo-z quality relies on the proportions of the observables, i.e., on the distributions of magnitudes, colors, and most importantly, the errors. Due to instrumental limitations, spectroscopic samples are biased to contain proportionally less faint objects, which results in a sample with a higher signal-to-noise ratio on average. This feature leads to unrealistic underestimated photo-z quality metrics.

We address this issue by weighting the clean spectroscopic sample based on the DES magnitude and color distributions. First, we compute the weights using the nearest-neighbor method described in Lima et al. (2008). They represent the supposed contribution (quantified by the relative abundance) that each object in the spectroscopic sample would have in the target photometric sample, regarding their colors and magnitudes, and the distributions of these quantities in the photometric sample. This way, the sum of all weights in the spectroscopic sample is equal to 1, and an ideal representative sample would have all weights equal to $1/N$, where N is the number of objects. Following the recommendations of the authors, we select a setup for *Weights* code to consider the five nearest neighbors in the 5-dimensional space of observables: g , r , i , z , and $g - r$, (MOF photometry).

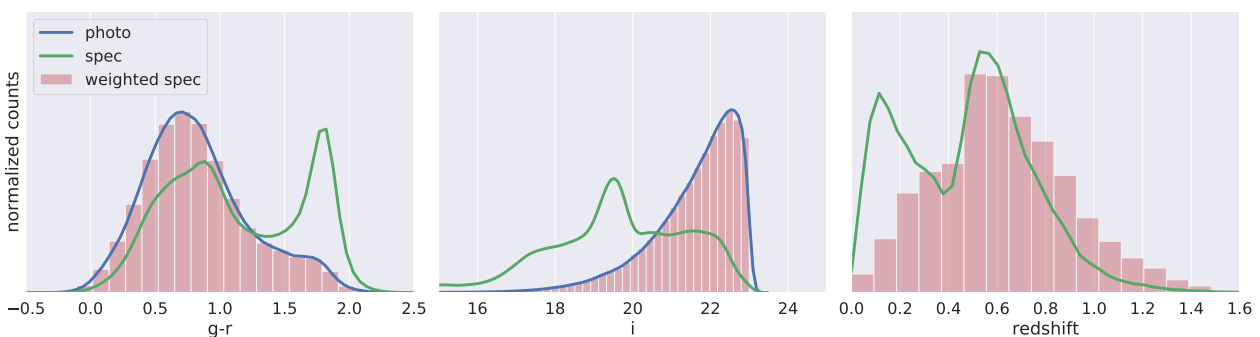
Once we have weights for each object in the spectroscopic sample, we discard those with zero or very small weights, i.e., objects that are useless to represent the properties of the photometric sample. These objects are not evenly distributed in the color-magnitude-redshift space, therefore, in order to roughly keep the shape of the weighted $N(z)$, we select the objects with the largest weights per redshift bin (of width $dz = 0.1$) so that the total number is equal to 60k, and the number per bin is proportional to a weighted histogram of the clean sample. 60k is the approximate number necessary to ensure no empty bins for the range of $0 < z < 1.5$.

The photometric sample of reference used to estimate the weights is the science sample that will be used in Chapter 5 to compute the LF, i.e., a magnitude limited sample. Hence, objects fainter than the magnitude limit have no counterpart in the photometric set. Therefore, they have zero weight. As perform tests considering different values of magnitude limit (22.5, 23.0, and 23.5) on i -band, it is necessary to repeat the weighing procedure and the sample selection for each case. Otherwise, the simple cut based on the maximum magnitude after weighting would reduce the size of the spectroscopic sample for brighter magnitude limits significantly.

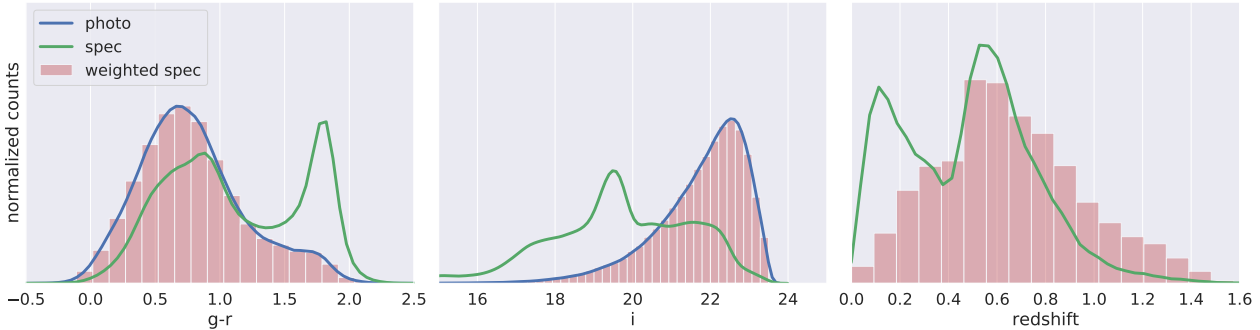
This exercise highlights the severity of the spectroscopic incompleteness at the faint magnitude regime. If merely using the weights to plot a weighted histogram, they are enough to reproduce the color $g - r$ and i -band magnitude distributions, even if pushing the magnitude limit to $i=23.5$, as shown in the Figure 3.5. Although the redshift distribution of the photometric sample is unknown, the reduction of the $N(z)$ from a double-peaked to an approximate single-peak distribution is desirable. Theoretical models predict a smooth rise of counts with increasing redshift, following proportionally the increase in the volume surveyed as a function of distance within the solid angle covered by the observations. At a certain point (in this case at ~ 0.6), the counts decrease with redshift due to the loss of faint objects. Unfortunately, the weights are not able to produce a smooth raise in the $N(z)$ for lower redshifts, and a sharp jump is observed at $z \sim 0.5$ in all the three cases shown in the right panels of Figure 3.5.



(A) Photometric sample limited to $i < 22.5$.



(B) Photometric sample limited to $i < 23.0$.



(C) Photometric sample limited to $i < 23.5$.

FIGURE 3.5: Color ($g - r$), magnitude (i) and spec-z normalized distributions of the clean spectroscopic (green curves) and photometric samples of reference (blue curves). The filled histograms refer to the weighted distributions for the clean spectroscopic sample.

After using the weights to select objects in the clean spectroscopic sample effectively, it becomes clear the lack of objects necessary to fulfill the larger bins of magnitude ($22.5 < i < 23.5$), as evident in the middle panels of Figure 3.6. The resulting pruned samples, which will be used to train photo-z

algorithms, do cover the entire range of color and magnitude, but only when limiting the magnitude to $i < 22.5$ the proportions observed in the photometric sample are recovered.

Considering the redshift distributions obtained after pruning, the scarcity of spec-z measurements in the clean spec-z sample induces an artificial valley at approximately $0.4 < z < 0.5$, regardless of the magnitude limit. If we selected a number significantly smaller than 60k, the proportions in the weighted redshift distributions would be damaged. So the choice of sample size when selecting the data based on weights is a trade-off between the independent attempts to reproduce photometric properties and the (unknown) redshift distribution simultaneously.

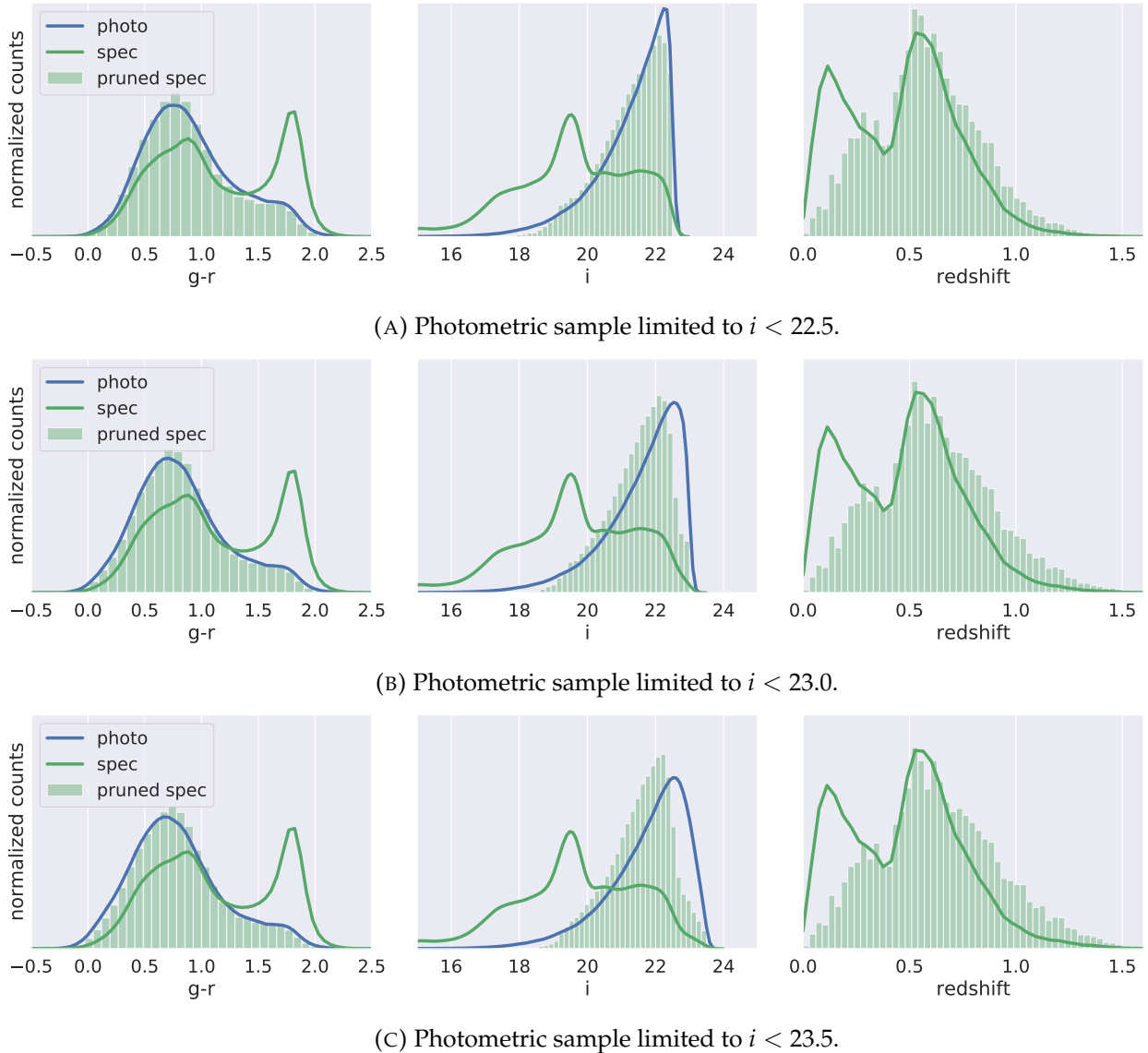


FIGURE 3.6: Color ($g - r$), magnitude (i) and spec-z normalized distributions of the clean spectroscopic (green curves) and photometric samples of reference (blue curves). The filled histograms refer to the pruned sample after selecting the 60k objects with larger weights keeping the weighted $N(z)$ proportions.

One possible approach to improve representativeness is to apply a data augmentation technique to the sample. It could be done by adding mock redshifts from simulations or by re-sampling inside the spectroscopic sample, allowing multiple entries of the same measurements, maybe adding some artificial noise to avoid identical clones. In both cases, the new data can introduce additional biases in the relative proportions of galaxy populations. We plan to investigate both possibilities in future work.

The resulting magnitude distributions in all bands are shown in Figure 3.4. There we show only the case for $i < 23.0$ as an illustration. Comparing the left and right panels, the shape of the magnitude distributions of the spectroscopic sample after the cuts are not yet identical to those from the photometric set, but they are much closer than they were for the complete spectroscopic sample before the cuts. Now, we ensure that the spectroscopic sample covers, even sparsely, the range of photometric observables spanned by the photometric sample, allowing consistent training and a realistic evaluation of the photo-z quality.

Random Sampling

To define the training, validation, and testing sets, hereafter *train*, *valid*, and *test*, we randomly split the clean spectroscopic sample (for each magnitude limited sample), in three parts, containing 30k, 10k, and 20k objects, respectively. Since the selection is random, the three subsets keep the same properties as the parent sample (see the distributions of color, magnitude, and redshift in Figure 3.7). As a basic characterization of the subsets photometric noise properties, we plot the magnitude i versus spec-z and versus the error for the *test* set ($i < 23.0$), as an example (see Figure 3.8). The *train* and *valid* sets should have similar plots.

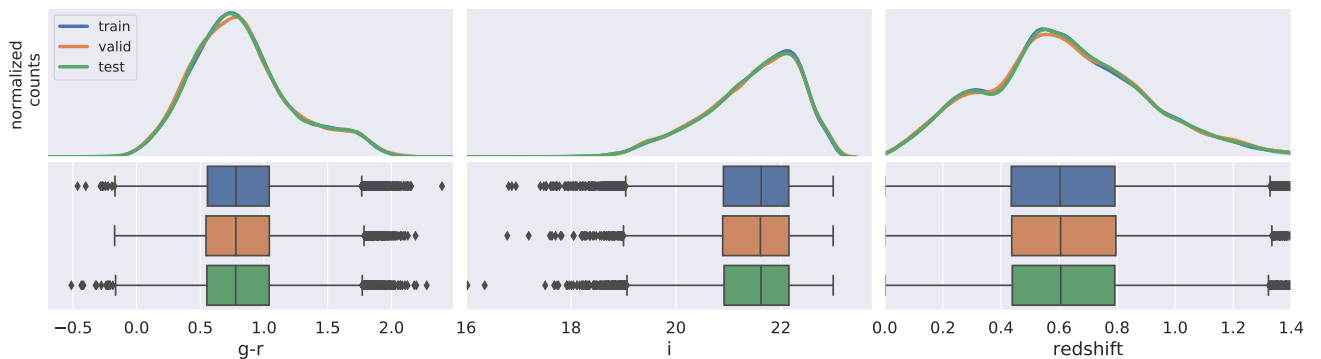


FIGURE 3.7: Properties of the three subsets: *train*, *valid*, and *test*.

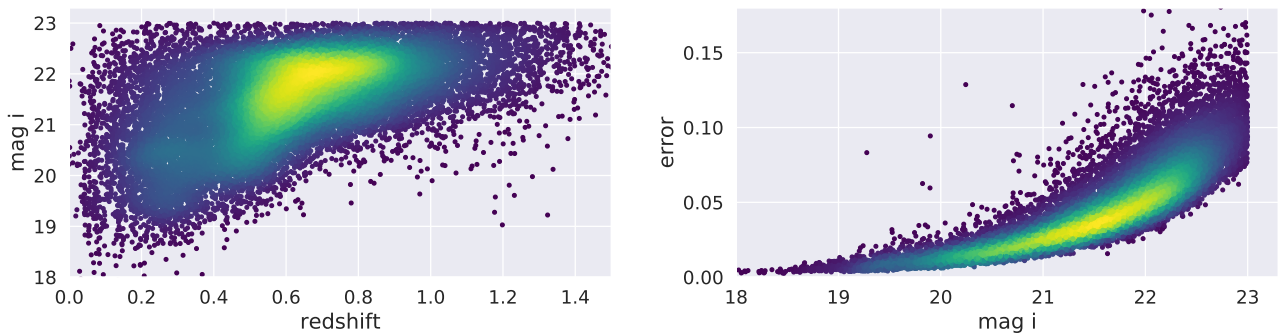


FIGURE 3.8: Characterization of the *test* subset. Left panel: i -band magnitude (MOF) versus redshift. Right panel: i -band magnitude (MOF) versus the errors. The density of points increase from dark blue towards yellow.

3.1.4 Building test samples with MICE simulations

For a fair comparison between the results obtained with a controlled sample and with real data, we define similar *train*, *valid*, and *test* subsets for MICE, with the same sizes as defined for Y3 Gold catalog above. The simulated catalog is already a “clean” sample. There are no magnitude errors and no magnitude values beyond the stringent limits for physical objects. Moreover, the catalog is already representative of the Universe up to $z = 1.4$, so the use of weights is not applicable. The only cut necessary to be kept in sync with the real data spectroscopic sample is the magnitude limit ($i < 23.0$).

Based on the sample defined in Section 2.2, we select a random sample of 60k objects that satisfy the only condition of $i < 23$. The magnitude distributions of this sample for all bands are displayed in Figure 3.9. On the right panel, we show the magnitude distributions of additional bands from external surveys of interest, other than DES, which are also available in the MICE catalog. Due to the random selection, the collection of 60k objects chosen to play the role of the “spectroscopic” sample keeps the same photometric properties as the parent sample, as shown in Figure 3.10.

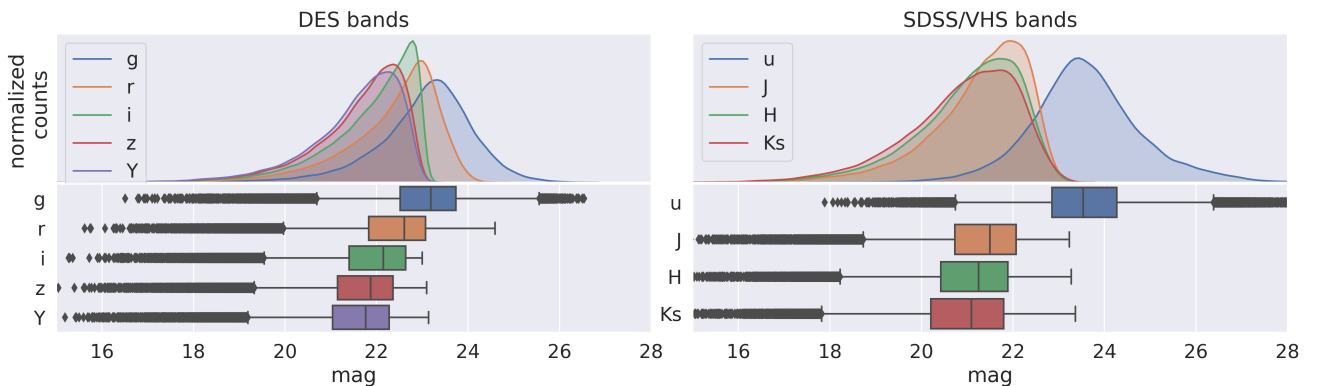


FIGURE 3.9: Photometric properties of the random selection of 60k objects built to mimic a representative “spectroscopic” sample.

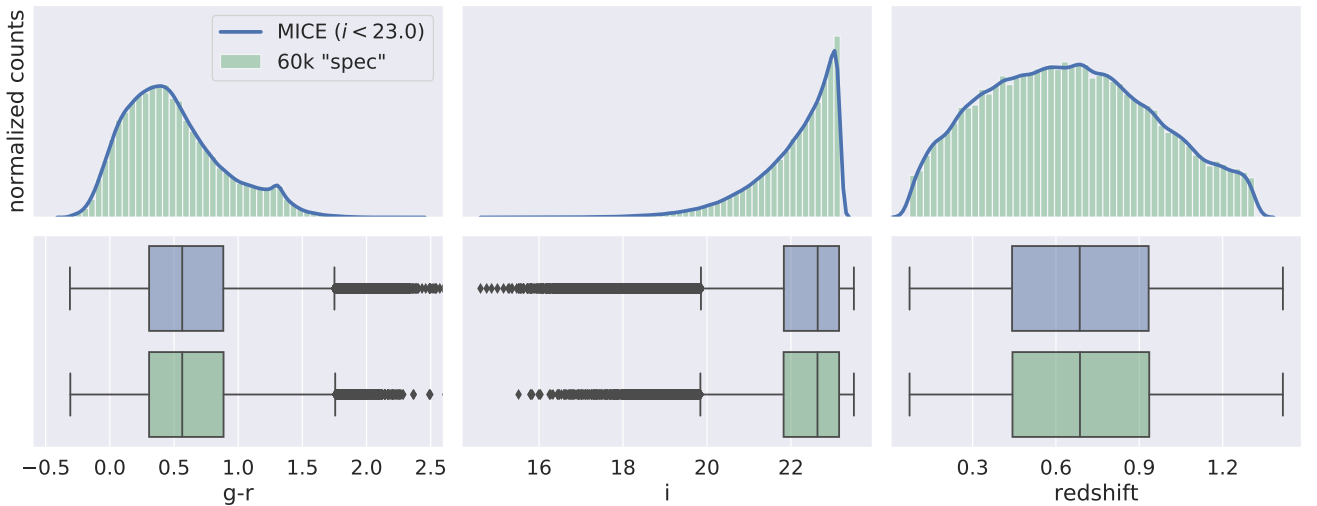


FIGURE 3.10: Comparison between the 60k selected objects and its parent sample, MICE RANDOM. From left to right: color $g - r$, magnitude i , and redshift. On the top panels, the KDE distributions, on the bottom panels, the respective box plots spanning the same observable ranges as the distributions above.

Starting from the 60k sample, we split it again, randomly, to create the *train*, *valid*, and *test* subsets containing 30k, 10k, and 20k objects, respectively, repeating the sizes of real data subsets. Once more, due to the random nature of the selection, the three sets are representative of their parent set (see Figure 3.11).

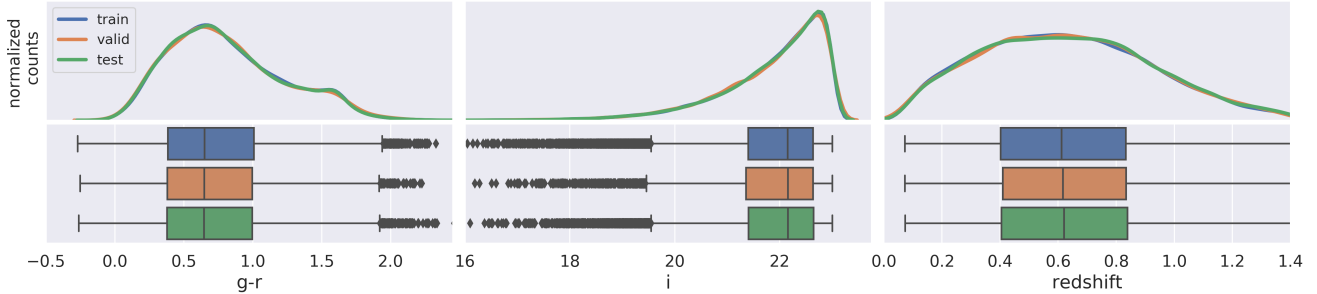


FIGURE 3.11: Properties of the three subsets: *train*, *valid*, and *test*.

Both apparent and absolute magnitudes as a function of redshift are presented in Figure 3.12 for the *test* set. Since the simulated magnitudes are perfect, there are no errors in the catalog.

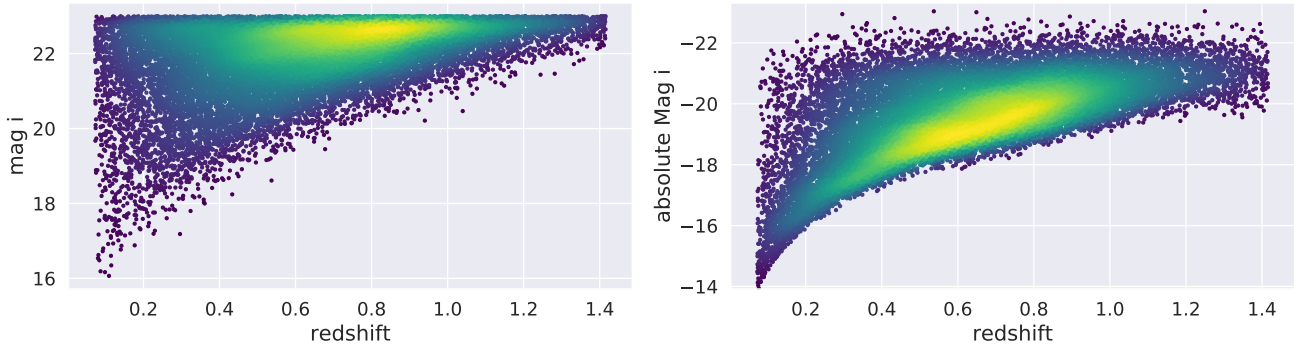


FIGURE 3.12: Characterization of the *test* subset. Redshift versus magnitude (apparent on the left, absolute on the right). The density of points increase from dark blue towards yellow.

3.2 Tests with MICE simulations

3.2.1 Evaluating the performance of photo-z methods

We start this sequence of tests by comparing the performance of the four photo-z algorithms described above: ANNz2, DNF, LePhare, and MLZ. We decided to choose a photo-z algorithm based on tests with simulations, so the results are not affected by the uncertainties present in the observations, which could disguise possible features introduced by the methods.

In the first test, we used only the magnitudes in the five standard DES bands (*grizY*) as observables input. We do not use the colors in addition to magnitudes. As a template-fitting method, LePhare does not accept colors as input, only magnitudes (or fluxes). As colors are derived from the magnitudes, they are not independent measurements. Therefore they do not bring extra information, just redundant data that would slow down the speed of the execution of the algorithm. Since all codes require the magnitude errors as input, we introduce minimal mock errors (0.01 mag) to all galaxies in the sample.

We use the *train* set with 30k galaxies to train the three empirical methods and to compute the systematic shifts to correct the observed magnitudes. Then we compute the photo-zs for the 20k galaxies in the *test* set and compared the results with the true redshift available in the catalog. The redshift distribution of the true redshifts shown in Figure 3.13 is the simple normalized histogram, while the

distributions for the results are computed as the kernel density estimates (KDE), which used a variable bin width that automatically adjusts to the amount of data in each redshift range. This choice was motivated by the improvement of clarity on displaying the results, since the KDE method tends to smooth the distribution, hiding local features in the histogram.

Just from the visual inspection of the Figure 3.13, we notice that none of the four algorithms can recover the original shape of the actual $N(z)$ just using the five DES magnitudes as input. All methods introduce artificial peaks in the distribution. Comparing the results, it is clear that DNF presents a superior performance in reconstructing the true $N(z)$ than the other methods, showing significant agreement with the expected results at $z > 0.7$.



FIGURE 3.13: Normalized redshift distribution of the *test* sample for the true values (green histogram) and the results of the four photo-z algorithms selected (blue lines).

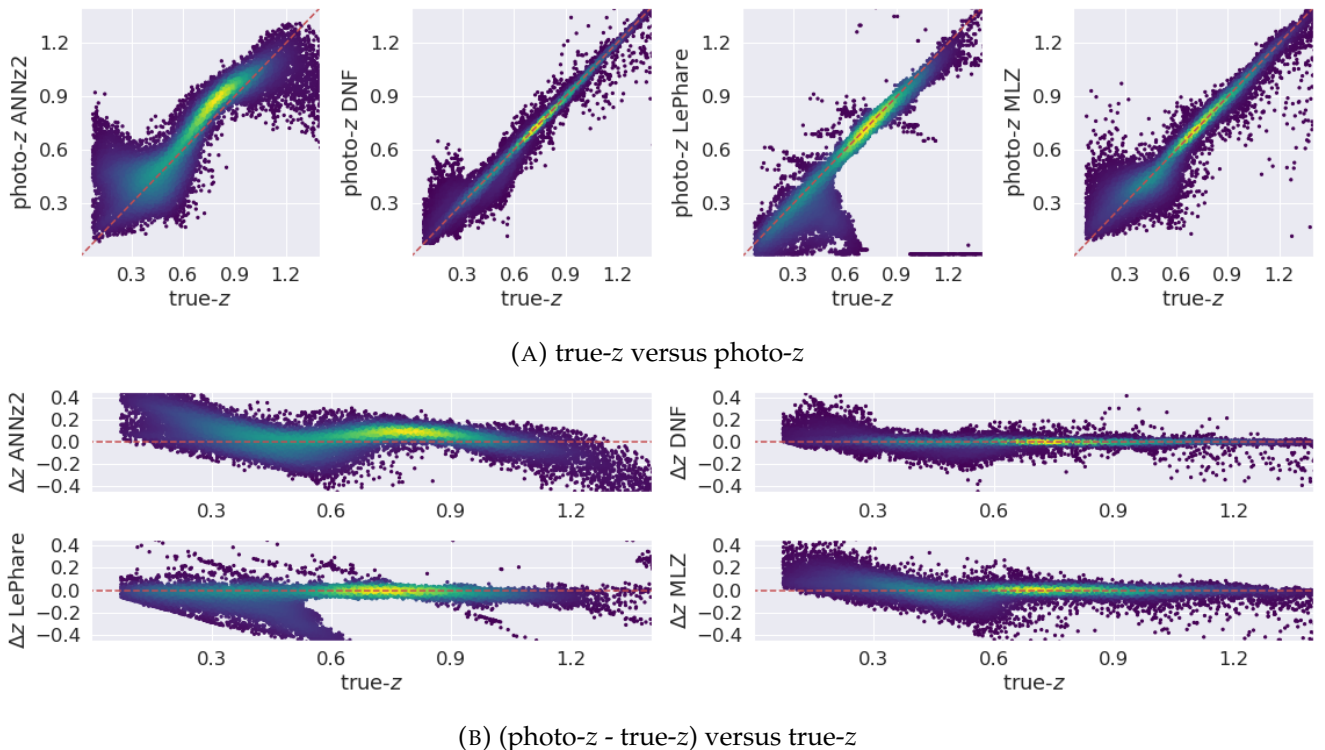


FIGURE 3.14: Direct comparison between photo-zs and true-zs object by object, color coded by density of stacked points, from dark blue to yellow in increasing order.

We have the same impression from the panels in Figure 3.14, where we plot the photo-z against the true-z for each object (panel 3.14a) and the residuals ($\Delta z = z_{phot} - z_{spec}$) as a function of the true-z (panel 3.14b). These plots are colored according to the density of stacked points, from dark blue to

yellow in increasing order. From these plots, we see that ANNz2 photo-zs are, in general, systematically overestimated, except for higher redshifts ($z > 1.0$). LePhare photo-zs are slightly underestimated as a whole, but the effect more prominent at low zs ($z < 0.6$). DNF and MLZ show no relevant systematic errors globally, although they are present in specific redshift intervals. Both lead to significant dispersion at low zs ($z < 0.6$). Comparing the results globally, DNF again shows the best performance. Interestingly, DNF is the fastest code among the four.

Another way to explore the photo-z quality is to analyze the relationship between redshift and apparent magnitude, as shown in Figure 3.15 with the same plot using the true-zs (left panel of Figure 3.12). Following the same colors to represent the density of points as in previous figures, we see the artificial peaks of $N(z)$ s in Figure 3.13 here as yellow blobs, indicating that they have most of the contribution from faint objects, which is not a surprise, since they are the majority.

Another feature visible in this figure is the absence of low photo-zs assigned to faint objects by ANNz2, which may be related to the small number of these objects in the training set, gaining a low probability in the network resulting of the training process.

Also worth to mention are the vertical stripes in LePhare's photo-zs, caused by the finite resolution in the template fitting procedure (the length of dz steps used to compute theoretical fluxes from the templates). Once more, the DNF shows the best performance among the four algorithms.

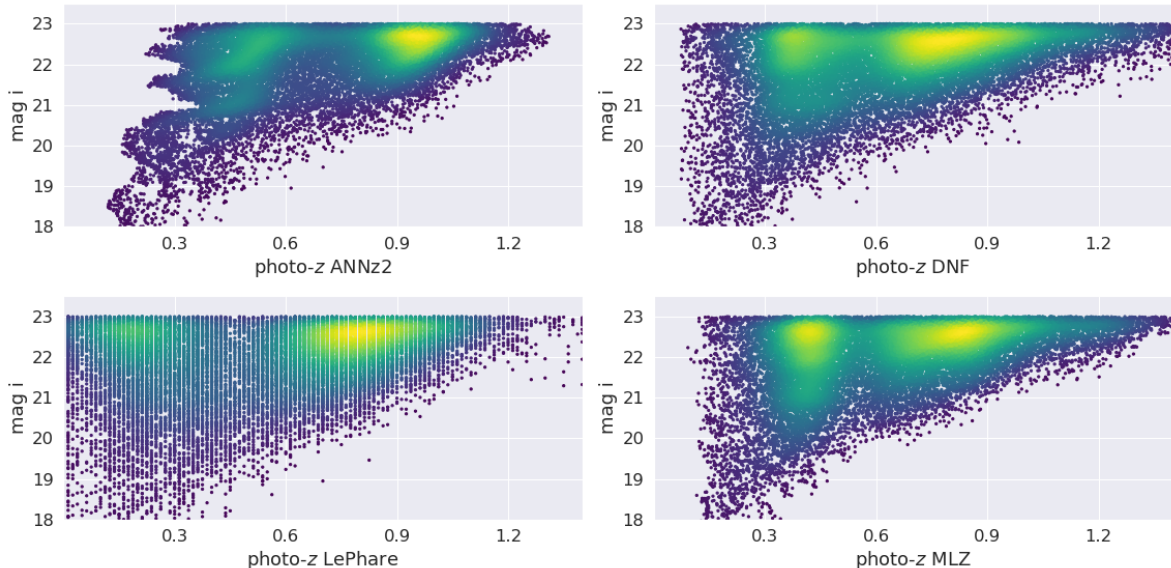


FIGURE 3.15: Apparent magnitude versus photo-z for the tested algorithms. The density of objects increases from dark blue to yellow

The visual comparison done so far would be enough to choose in favor of DNF, but we also compute the quality metrics described in Section 3.1. We show the global values in Table 3.3, Figure 3.16, and the variation as a function of redshift in Figure 3.17.

	$\overline{\Delta z}$	σ_{68}	$f_{out} (\%)$	MSE
ANNz2	0.0410 ± 0.0003	0.1103 ± 0.0003	22.37 ± 0.10	0.0231 ± 0.0001
DNF	-0.0013 ± 0.0001	0.0304 ± 0.0001	3.79 ± 0.03	0.0035 ± 0.0000
LePhare	-0.0446 ± 0.0007	0.0760 ± 0.0006	18.97 ± 0.10	0.0462 ± 0.0003
MLZ	0.0002 ± 0.0002	0.0580 ± 0.0002	9.51 ± 0.03	0.0088 ± 0.0001

TABLE 3.3: Photo-z quality metrics

In agreement with the information extracted from Figure 3.14, the overall bias ($\overline{\Delta z}$) is negligible for DNF and MLZ, positive for ANNz2, and negative for LePhare. DNF has better values for all the metrics, showing an impressive small fraction of outliers (< 4%).

We plot metrics against each other in Figure 3.16 as a graphic visualization of the same results presented in Table 3.3. On the left panel, the dashed line marks the zero level for the bias. The best results should appear close to this line and on the left side of the plot. All codes present minimal bias (the scale in the y -axis is small compared to typical photo-z errors). On the right panel, we see a possible correlation between MSE and the fraction of outliers, as expected. We compute errors for these metrics by re-sampling ten times with 9/10 of the objects each, without repetition (jackknife technique), but the error bars are too small to be visible on the plot.

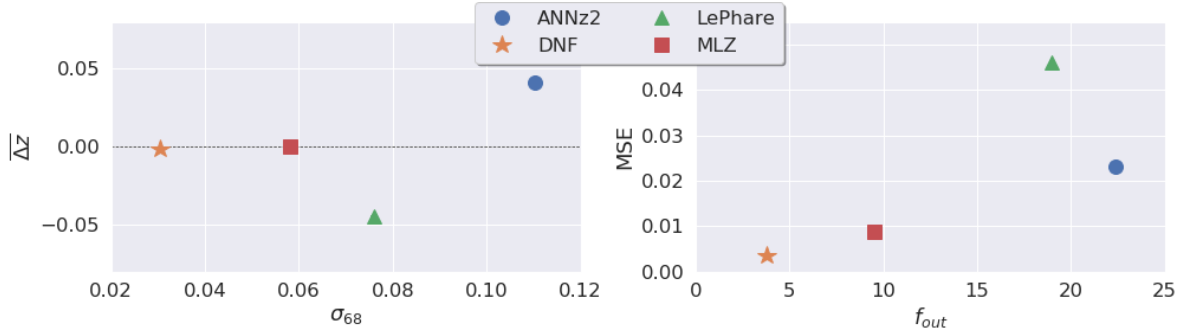


FIGURE 3.16: Global metrics for the four algorithms using DES *grizY* magnitudes (same results as Table 3.3, here as a visual representation). Left: Δz versus σ_{68} . Right: f_{out} versus MSE .

Finally, we compute the photo-z metrics and errors in redshift intervals of width $dz = 0.2$ for the four algorithms (see Figure 3.17). The trends on the bias and scatter observed in Figure 3.13 are now translated into numeric quantities. Again, the error bars are too small to be noticed. The metrics are worse in both ends of the redshift range examined, probably caused by the small number of objects in these particular bins, leading to poor statistics. There is a bump in scatter and the fraction of outliers of LePhare at $0.4 < z < 0.6$, where the $N(z)$ shows a strong disagreement with the true redshift distribution.

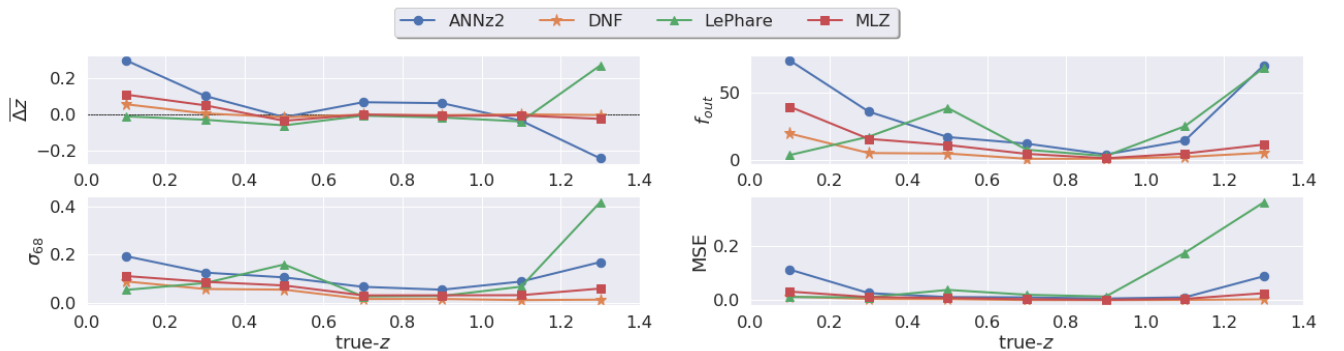


FIGURE 3.17: Photo-z metrics as a function of redshift for the four algorithms using DES *grizY* magnitudes.

Based on the results above, we conclude that, among the four methods studied, DNF is the best algorithm to compute single photo-zs estimates with DES *grizY* bands (this statement is only valid if considering the particular configurations described in Section 3.1). Therefore, from now on, all the photo-zs presented were obtained using DNF.

Although chosen as the best option, still there are issues to be improved, such as the non-negligible dispersion and fraction of outliers at the low- z regime. In the next sections, we show our efforts to mitigate these effects by adding new magnitudes from other surveys, by introducing new observables as inputs, other than magnitudes, such as shape parameters related to galaxies' morphology, or by using photo-z PDFs.

3.2.2 Using extra magnitudes

Here, we explore the impact of adding extra information to the input parameters for DNF. This is a possible approach in reality since DES has a significant fraction of its footprint that overlaps with regions covered by other surveys. However, the task of combining data from different sources is not trivial, since each survey has its depth, selection effects, calibration parameters, etc. Fortunately, empirical methods like DNF are not affected by systematic differences between sets of filters.

The addition of extra bands to extrapolate the wavelength range in the observer reference covered by DES is of particular interest to measure objects with relatively low ($z < 0.5$) and high ($z > 1.0$) redshifts. The 4000 Å break, which is a remarkable feature in early-type galaxies spectra, serves as a discriminator for photo-z determination, regardless of the method. For the two redshift ranges mentioned above, this feature falls beyond the DES bands limits, in the UV and IR, respectively.

DES was designed for dark energy studies. Although DECam has six filters available ($ugrizY$), the survey strategy prioritizes the range of the electromagnetic spectrum that is optimal for the survey purposes, which is $grizY$. For MOF magnitudes in the Y3 catalog, only $griz$ data are available for the entire catalog. The u -band measurements are restricted to specific regions such as the deep fields. Even so, we are interested to see the impact of the u -band because it will be available in the LSST.

The observation of the IR region of the spectrum is out of the DES survey plans, but there is plenty of data available that can be combined. Indeed, this combination was expected since the survey planning and has influenced the design of the survey footprint.

Banerji et al. (2015) explored the effects of adding infrared magnitudes to the DES science verification (SV) data set. They applied the “forced photometry” technique on the VISTA Hemisphere Survey (VHS) images to extract infrared fluxes in the J and K bands for the objects that were detected in DES SV images, which are deeper than those from VHS. They compared photo-z results obtained using LePhare with and without the extra bands and noticed a modest decrease on the global photo-z scatter by ~ 7 to 12%, having reached at least twice this improvement for specific redshift intervals like $0.1 < z < 0.3$ and $1.1 < z < 1.3$.

The addition of extra bands in both ends of the spectrum is expected to help in resolving the well-known problem of color-redshift degeneracy. Buchs et al. (2019) illustrate this issue showing the spectra of two different galaxies, at different redshifts, which would have similar magnitudes in the five bands $grizY$, but are distinguishable in the UV and IR ranges (Figure 3.18).

MICE data set provides observed magnitudes for some filters from surveys other than DES, such as, e.g., CFHTLS, SDSS, VHS, Euclid. In this section, we evaluate the impact of adding the SDSS u -band and three VHS bands: J , H , and K_s .

When using perfect magnitudes from simulations, it is straightforward that the more information, the better, so we do expect to see the improvements in the results. Nonetheless, we want to measure this improvement quantitatively and to determine the relative contributions from UV and IR data separately. When using real data, the addition of an extra magnitude might not necessarily lead to an improvement on the photo-z results, since the data could bring large errors that will propagate to the photo-z estimates. We will cover this subject in Section 3.3.1.

We run DNF with the same configurations as in the previous section, but varying the set of magnitudes provided as input, starting from the fundamental core of $griz$ bands, and gradually adding the u , Y , and $JHKs$ (together), so we end up with the following six magnitudes combinations (see first column of Table 3.4).

We repeat the same steps as in the previous section, starting by visually inspecting the redshift distributions (Figure 3.19), and the photo-z versus true-z (3.20) obtained for the six cases. The results shown in the upper middle panels (in both figures) are the same as those used in the comparison to the other codes above, i.e., they were obtained using the standard $grizY$ bands. This particular result is used as a reference basis for further comparison, so when we mention an improvement, it means an improvement compared to the $grizY$ case. In Figure 3.19 and in both panels of Figure 3.20, the addition

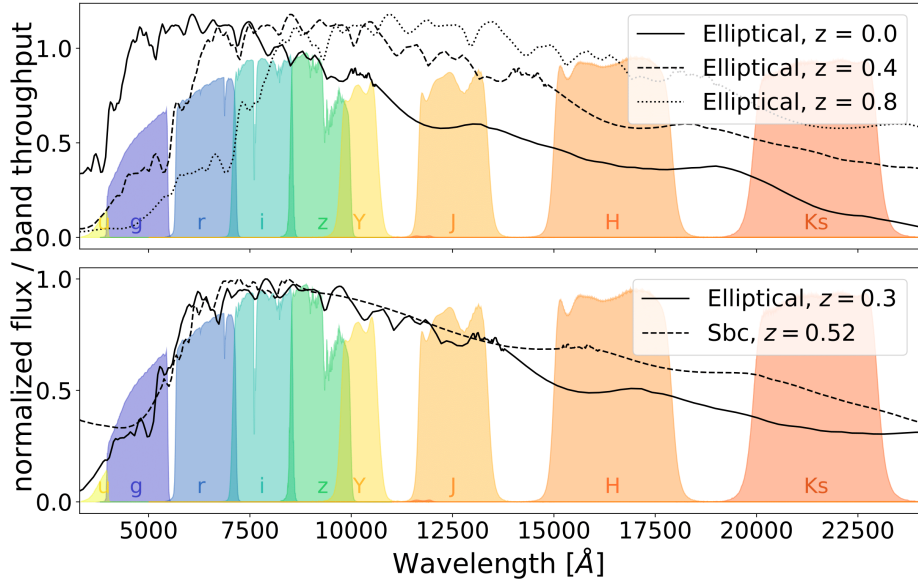


FIGURE 3.18: Examples of spectral energy distributions of galaxies in various redshifts superposed to the filter transmission curves. Upper panel: the same kind of elliptical galaxy at the three redshifts where the 4000 Å break falls in between two consecutive filters. Bottom panel: example of two galaxies with similar *grizY* photometry, but at different redshifts. The degeneracy is removed when adding UV and IR information. Image credit: Figure 1 from the article by Buchs et al. (2019).

of IR bands is done from left to right, and the *u*-band from top to bottom. So, to see the impact of adding the UV data, one should compare the first row (without *u*) to the second row (with *u*) of plots.

The first result extracted from Figure 3.19 is that the removal of the *Y* band (in simulated conditions) aggravates the artificial peak and valley introduced by wrong estimates at $z \sim 0.4$ and 0.5, respectively. Secondly, the inclusion of the *u*-band alone is not enough to remove these peaks significantly, against the expectations. Based on the results with SV data (Sánchez et al., 2014), we expected to see a significant improvement in the low- z interval with the addition of UV data. Quite the opposite, the addition of the IR bands *JHKs* is what efficiently helps to recover the true $N(z)$, even when not including the *u*-band. Indeed, Banerji et al. (2015) has anticipated that the IR extra data would also help at the low- z regime, not only at the higher redshifts where the 4000 Å break falls into the IR bands. We attribute this result to the difference in the number of extra bands available in UV (1) and IR (3). As DNF is a machine learning algorithm, the more independent variables added to the inputs, the more information is absorbed by the training that can be used to solve degeneracies in the scientific sample, improving the accuracy of the final regression.

Comparing the top to the bottom panels in Figure 3.20a (or equivalently, left to right panels in Figure 3.20b), we conclude that the effect of using the *u*-band is to reduce the scatter. For each of the three options (*griz*, *grizY*, *grizYJKHs*), the results on the +*u*-band counterpart have always a smaller dispersion than their respective pair, noticed by the narrowing of regions where points are spread. The systematic ups and downs in specific redshift intervals are preserved, but their amplitudes are reduced.

Again, an alternative way of visualizing the results is the *i*-band magnitude versus photo- z in Figure 3.21, compared to the same plot with true- z in Figure 3.12. The artificial peaks are evident by the two yellow blobs reflecting the higher density of points, while there is only one overdense region in the reference figure. Comparing the top panels with the bottom panels, the addition of the *u*-band is responsible for diminishing the intensity of the low- z peak (the yellow blob on the left), but the feature is only completely removed when including the *JHKs* bands (panels on the right). The IR data can remove the feature alone, without the necessity of using the UV (the top right panel has already only one overdense region, and is very close to the reference Figure 3.12).

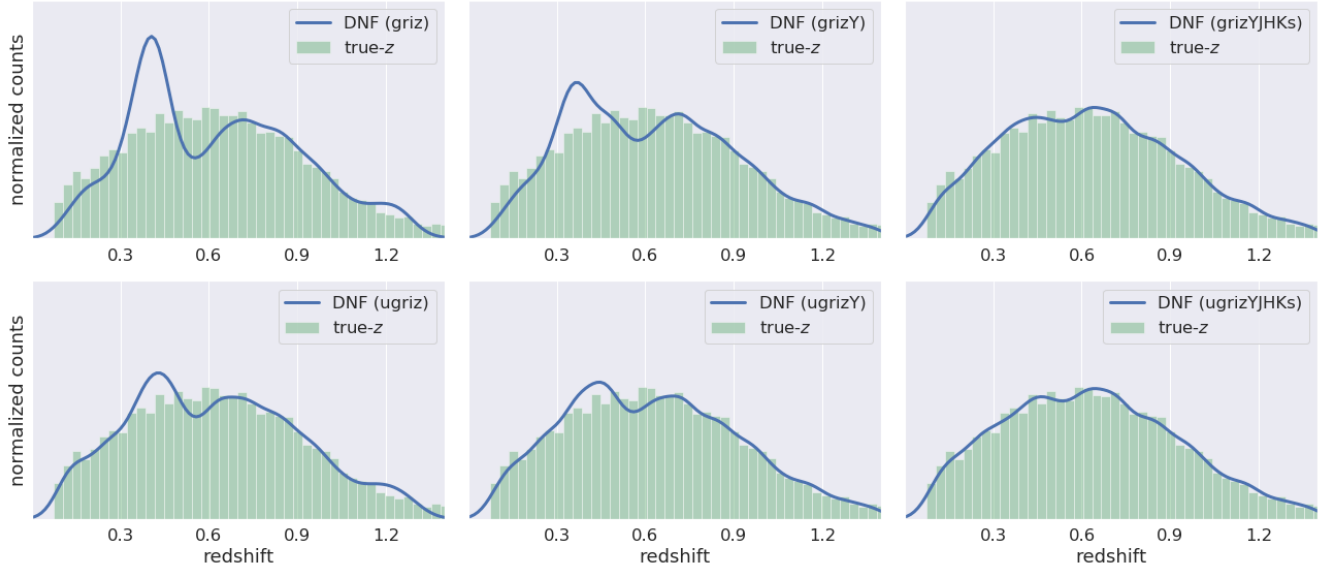


FIGURE 3.19: Normalized redshift distribution of the *test* sample for the true values (green histogram) and the recovery by photo-*z* results obtained using the six sets of magnitudes displayed in the plot legends (blue lines), showing the improvement achieved by including extra UV and IR bands.

To translate this results in numbers, we compute the same metrics as in the previous section for the six combinations of bands target of this study and present their global average results in Table 3.4 and Figure 3.22, as well as their local values at redshift bins of with $dz = 0.2$ in Figure 3.23. Once more, we compute errors using jackknife resampling, but the error bars are smaller than the marker sizes in the two figures.

Filters	Δz	σ_{68}	$f_{out} (\%)$	MSE
<i>griz</i>	-0.0036 ± 0.0002	0.0451 ± 0.0002	5.20 ± 0.04	0.0051 ± 0.0000
<i>ugriz</i>	-0.0063 ± 0.0001	0.0172 ± 0.0001	1.28 ± 0.02	0.0017 ± 0.0000
<i>grizY</i>	-0.0013 ± 0.0001	0.0304 ± 0.0001	3.79 ± 0.03	0.0035 ± 0.0000
<i>ugrizY</i>	-0.0042 ± 0.0001	0.0133 ± 0.0000	0.71 ± 0.01	0.0009 ± 0.0000
<i>grizYJHKs</i>	0.0026 ± 0.0001	0.0118 ± 0.0000	0.43 ± 0.01	0.0007 ± 0.0000
<i>ugrizYJHKs</i>	-0.0002 ± 0.0000	0.0073 ± 0.0000	0.04 ± 0.01	0.0002 ± 0.0000

TABLE 3.4: Photo-*z* quality metrics for MICE catalog using distinct set of filters.

In all cases, there are no significant values for the global bias in Table 3.4. Although systematic errors are present, their positive and negative contributions in different redshift bins end up canceling themselves, leading to global values close to zero.

The inclusion of *u*-band reduces substantially the scatter metrics in all cases, compared to the no *u*-band counterpart, but increases the bias in cases where the IR bands are not present.

The addition of the IR bands *JHKs* alone surpasses the improvements caused by the addition of *u*-band alone for all metrics, comparing to the *grizY* standard filter set. This is evident in the left panel of Figure 3.22, where the purple pentagon (*grizYJHKs*) is slightly more to the left and closer to the zero-bias dashed line than the red square (*ugrizY*).

In the right panel of Figure 3.22, the fraction of outliers is strongly correlated to *MSE*, showing a linear relationship between these two quantities. As expected, the more extra bands are added to the inputs, the better the results, so the brown diamond (*ugrizYJHKs*) is on the bottom left, and the blue circle (*griz*) is on the top right. The second point closer to the origin is the purple pentagon (*grizYJHKs*), confirming the result that the three IR bands alone improve the outcomes more than the *u*-band alone.

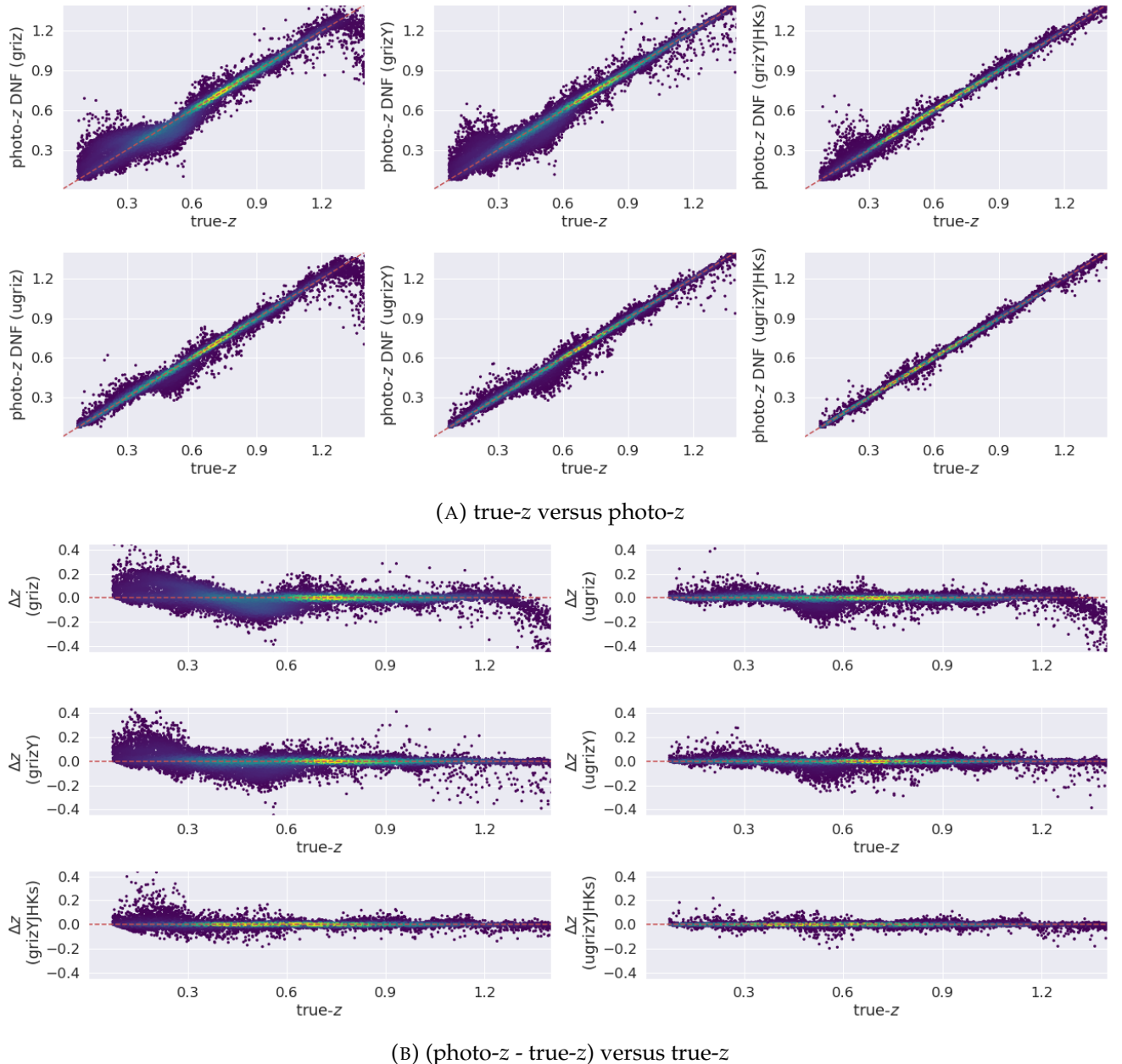


FIGURE 3.20: Direct comparison between photo-zs and true-zs object by object, color coded by density of stacked points, from dark blue to yellow in increasing order, showing the reduction of scatter caused by the addition of extra bands.

Finally, we see in Figure 3.23 that the inclusion of IR magnitudes gives a substantial help to decrease the scatter and the fraction of outliers, even at low- z . As expected, at this regime, the u -band is responsible for the more substantial improvements, as expected. The lack of Y-band has a significant negative impact at higher redshifts ($z > 1.1$) for all metrics. Interestingly, the results are pretty good at $0.7 < z < 1.1$ in all cases, showing a possible range for accurate galaxy evolution studies based only on photo-zs.

In summary, we conclude that the extra data in the UV helps to decrease the photo-z scatter, and the extra IR can remove the catastrophic errors at low- z . The combination of both is the best-case scenario, but the IR alone brings a more considerable improvement than the UV alone.

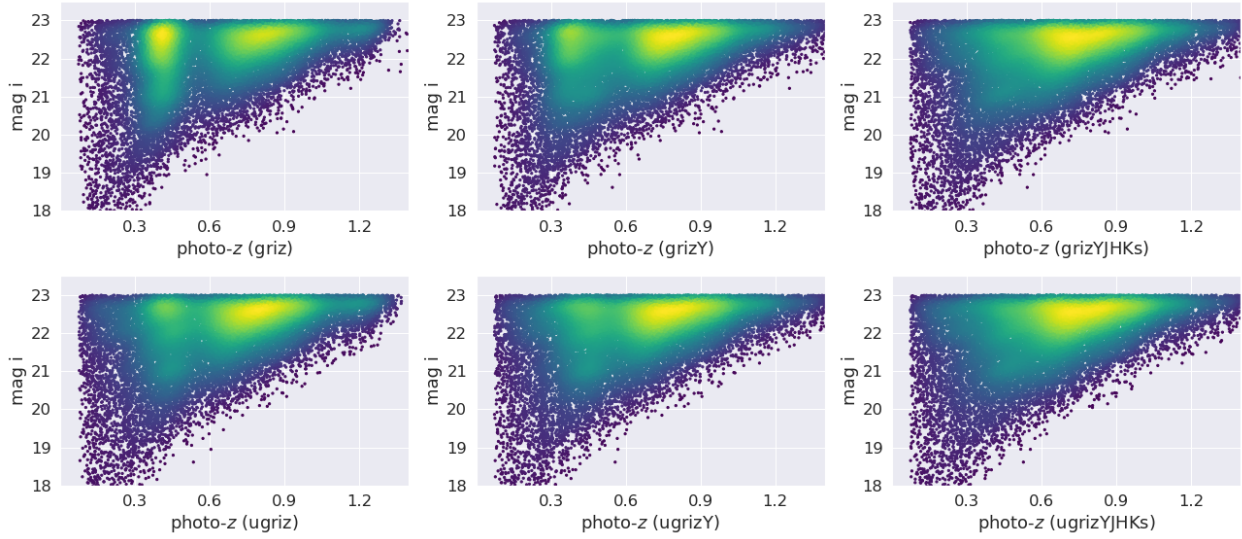


FIGURE 3.21: Apparent magnitude versus photo-z obtained with the six combinations of bands, color coded by density of stacked points, from dark blue to yellow in increasing order.

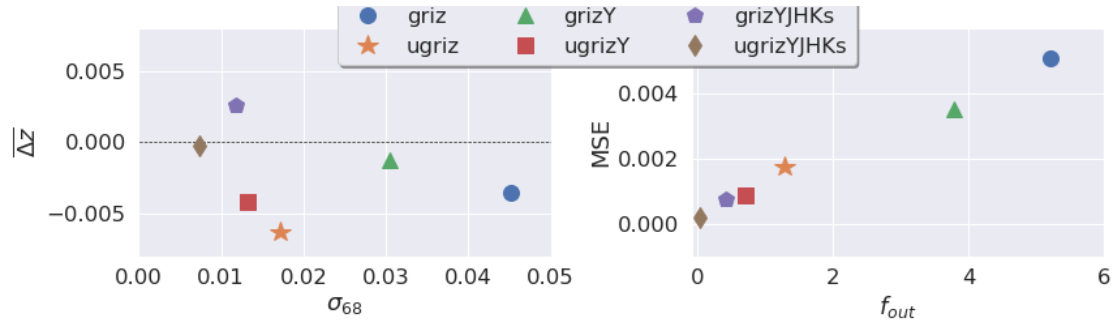


FIGURE 3.22: Global metrics comparison for the six sets of magnitudes used (same results as Table 3.4, here as a visual representation). Left: $\bar{\Delta}z$ versus σ_{68} . Right: f_{out} versus MSE.

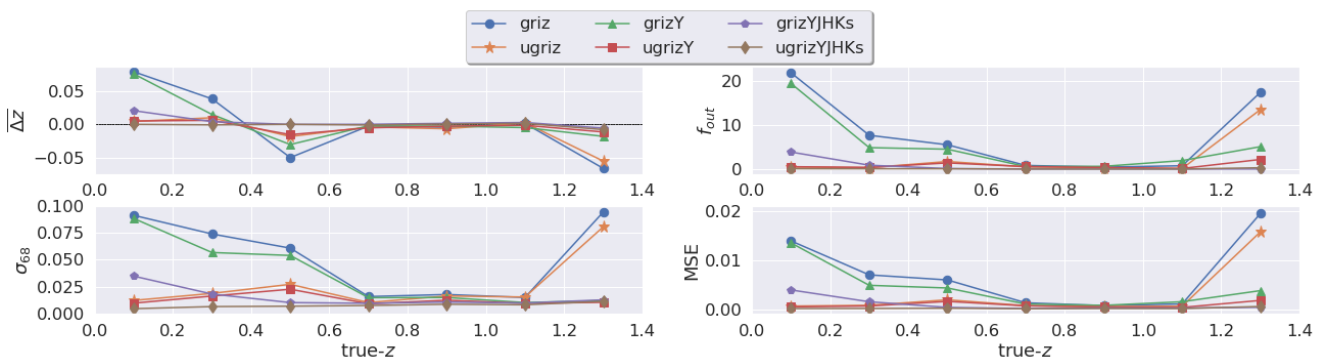


FIGURE 3.23: MICE photo-z metrics as a function of redshift, color coded by the the six sets of magnitudes tested.

3.2.3 Do shape parameters improve photo-z estimates?

One advantage of using empirical methods on the photo-z estimates is that one is not limited to use only the low-resolution measurement of the SED (represented by a sequence of magnitudes in progressive broad bands). Any other observable directly correlated with redshift is a possible input. Besides that, an

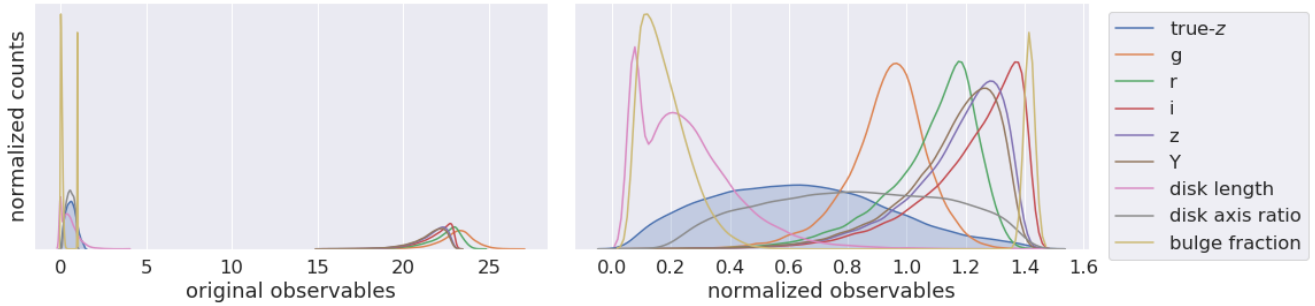


FIGURE 3.24: Distributions of MICE input parameters, before (left panel), and after (right panel) the normalization.

observable which is not directly related to redshift, but is correlated with color or morphology, possibly can be helpful to diminish the effects of degeneration in the color-magnitude-redshift space.

In this section, we start again with the magnitudes in the standard *grizY* filter set as the initial input data and study the impact of adding shape parameters to it. MICE provide measurements related to shape parameters of galaxies. We select three of them, based on their probability of being available in real observed datasets, and examine their impact on the results when used separately or together. They are:

- **Disk axis ratio (b/a):** ratio between semi-major (a) and semi-minor (b) axes of the ellipse fit to the galaxy when measuring its integrated flux.
- **Disk length (L):** object length scale (in arcsec). Despite the name, this parameter is available for all objects, not only disk galaxies.
- **Bulge fraction (B/T):** ratio of flux in the bulge component to the total flux.

This time, since we are mixing up distinct variables, the differences in scale can unbalance the machine learning process, in favor of one or another particular observable (see the distributions of the different quantities used on the left panel of Figure 3.24). Therefore, it requires an extra step before running DNF. Applying normalization to the input variables is necessary.

The procedure is to apply Eq.3.5 to convert all observables (where obs refer to the five magnitudes and three shape parameters) to the scale of the true- z , i.e., the normalized quantities are limited to the interval of $0.0 < z < 1.4$. The distributions of the normalized observables are displayed in the right panel of Figure 3.24.

$$obs_{norm} = \left[\frac{obs - min(obs)}{max(obs) - min(obs)} \times (max(z) - min(z)) \right] + min(z) . \quad (3.5)$$

Following the same steps as in the two previous sections, we start by comparing the resulting redshift distributions with that one obtained with DNF using the five DES bands (second panel from left to right in Figure 3.13, or top middle panel in Figure 3.19. To facilitate the comparison, we add this result to the distributions in Figure 3.25 as a dashed red line.

Analysing the four panels of Figure 3.25, we notice that in all cases the addition of the shape parameter, individually, improves the recovering of the correct $N(z)$ at intermediate redshifts ($z \sim 0.6$), where there is an artificial valley in the photo- z distribution when using only *grizY* magnitudes. For the lower redshifts ($z < 0.3$), surprisingly enough, the addition of the parameter b/a worsens the results by preventing the code from assigning redshifts in this range, transferring to $z \sim 0.5$ the objects that belong to $z < 0.3$. As a consequence, it leads to an underestimated count in the low- z part of the distribution. It increases the height of the artificial peak at $z \sim 0.5$ that was already present when using only magnitudes. When adding the three parameters together, the valley at $z \sim 0.6$ is replaced by a large peak, so the $N(z)$ looks worst than if using no extra parameter. We conclude that the parameter b/a is not useful as a DNF input, as it is not correlated to redshift, and its presence increases the degeneracies we are trying to remove.

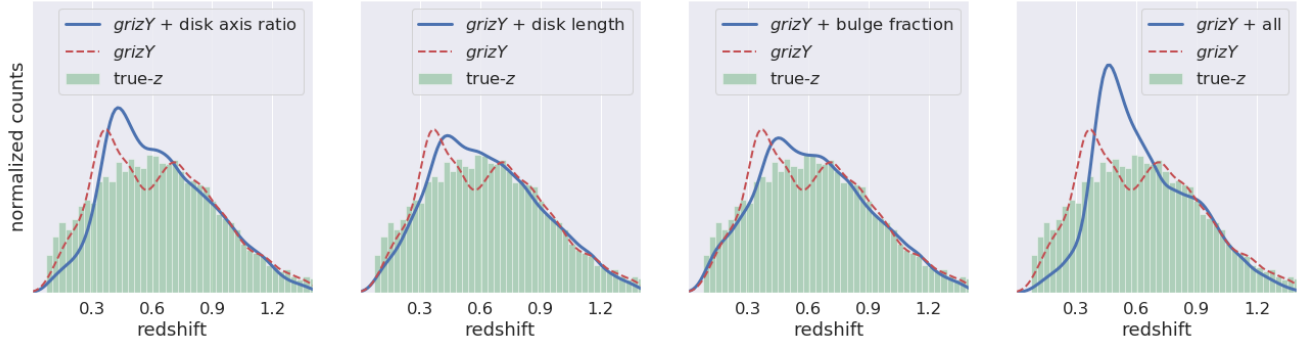


FIGURE 3.25: Normalized redshift distribution of MICE *test* sample for the true values (green histogram) and the photo-z results obtained using the five DES magnitudes *grizY* plus one or all shape parameters discussed in the text (blue lines).

Comparing the Figures 3.14 and 3.26 we notice that in all cases, the addition of shape parameters increases the scatter, even for higher redshifts where the results with DNF were “good”.

The comparison between Figures 3.15 and 3.27 also indicates that there is no substantial improvement on including shape parameters in the analysis. The two yellow blobs (that should be only one, as in Figures 3.12) are indeed spread in Figure 3.27, becoming more like the true values, but the removal of points from low- z affects the relation between magnitude and redshift drastically, making the results worst.

We do the final diagnostic now, by comparing quantitatively the photo-z metrics achieved with and without using shape parameters. Global average values are displayed in Table 3.5 and Figure 3.28, whereas the variation of these metrics with redshift is shown in Figure 3.29.

Shape parameter	$\bar{\Delta}z$	σ_{68}	f_{out} (%)	MSE
none included	-0.0013 ± 0.0001	0.0304 ± 0.0001	3.79 ± 0.03	0.0035 ± 0.0000
disk axis ratio	0.0068 ± 0.0003	0.0788 ± 0.0003	13.03 ± 0.06	0.0113 ± 0.0001
disk length	0.0033 ± 0.0002	0.0705 ± 0.0003	11.99 ± 0.04	0.0095 ± 0.0000
bulge fraction	0.0004 ± 0.0002	0.0702 ± 0.0004	12.06 ± 0.06	0.0096 ± 0.0001
all included	0.0106 ± 0.0003	0.0870 ± 0.0004	15.34 ± 0.08	0.0159 ± 0.0001

TABLE 3.5: MICE photo-z quality metrics considering shape parameters.

From Table 3.5, we notice that, except for the bias, where there is an improvement from -0.0013 to 0.0004 using bulge fraction alone, all metrics got worse by the presence of shape parameters in the input observables. This is evident in Figure 3.28, where the blue circle appears in the best position, isolated from the other points. The same result is observed in all redshift bins in Figure 3.29. Even at $z \sim 0.5$, where the $N(z)$ distributions give the impression of improvement by the using shape parameters, the metrics do not confirm this impression. Bias and dispersion increase in all cases.

Based on the bias evolution in Figure 3.29, we realize that the improvement in the global value using bulge fraction alone is a misleading result. The global metric ($\bar{\Delta}z$) is close to zero due to positive and negative contributions that, on average, cancel each other. Again, all the results are very good at $0.7 < z < 1.1$, and the presence of shape parameters makes no substantial difference for the bias and fraction of outliers, whereas they worsen the scatter significantly.

Based on the results of this test, we conclude that the pure magnitudes inputs are the best option to be used to estimate photo-zs on MICE using DNF.

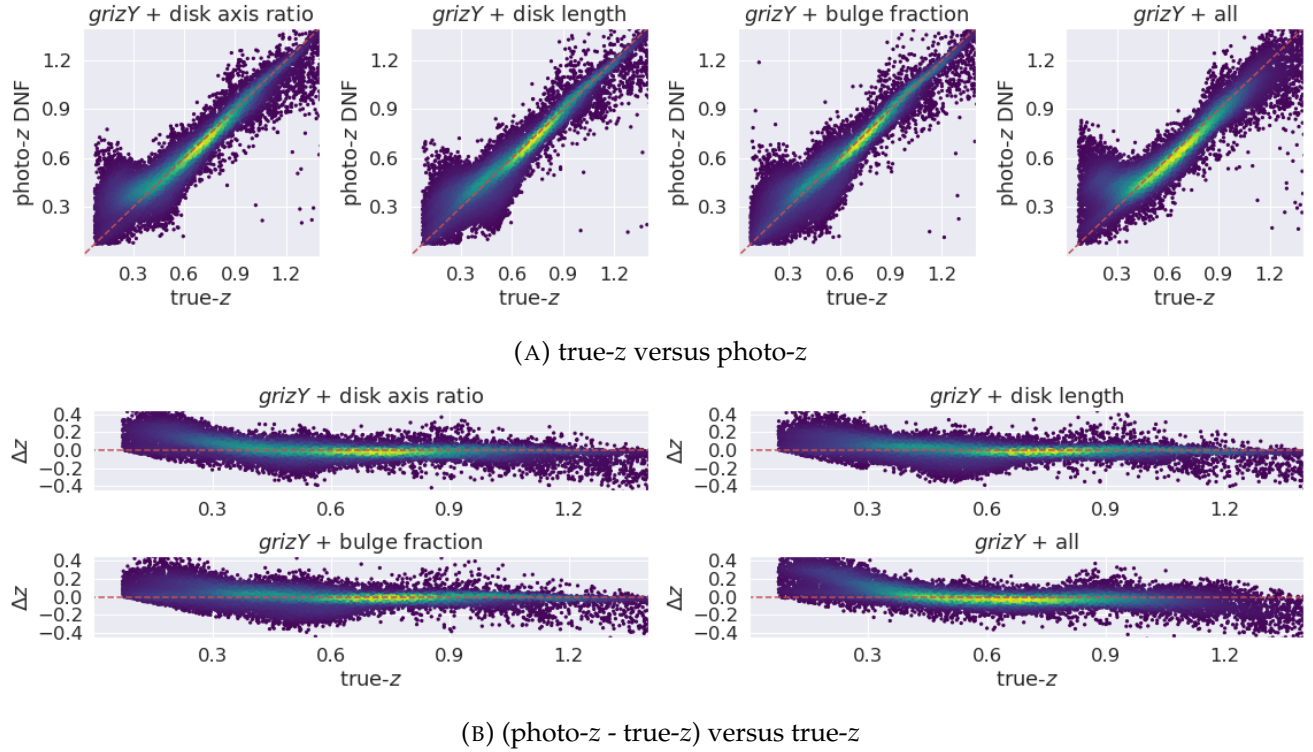


FIGURE 3.26: Direct comparison between MICE photo-zs and true-zs object by object, color coded by density of stacked points, from dark blue to yellow in increasing order.

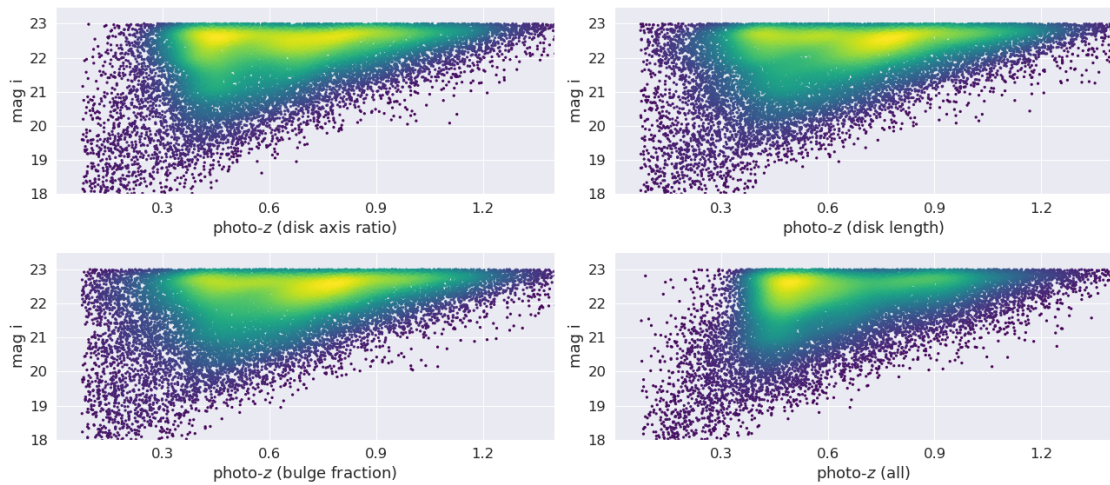


FIGURE 3.27: MICE apparent magnitude versus photo-z for several selection of shape input parameters.

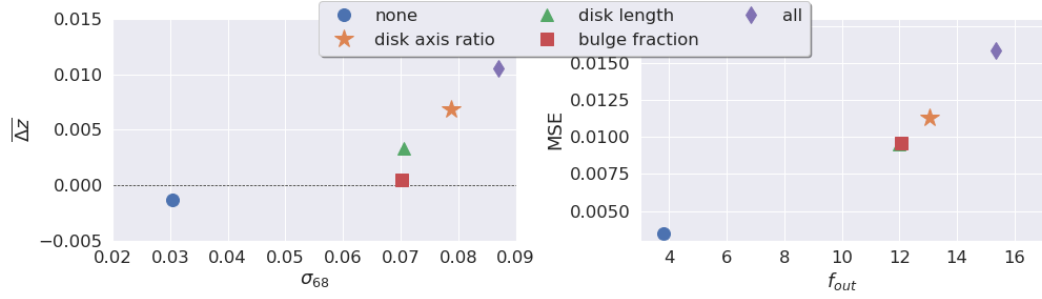


FIGURE 3.28: Global metrics comparison for the three results obtained by adding shape parameters to the input list, separately, together, and not using it. (same results as Table 3.5, here as a visual representation). Left: Δz versus σ_{68} . Right: f_{out} versus MSE .

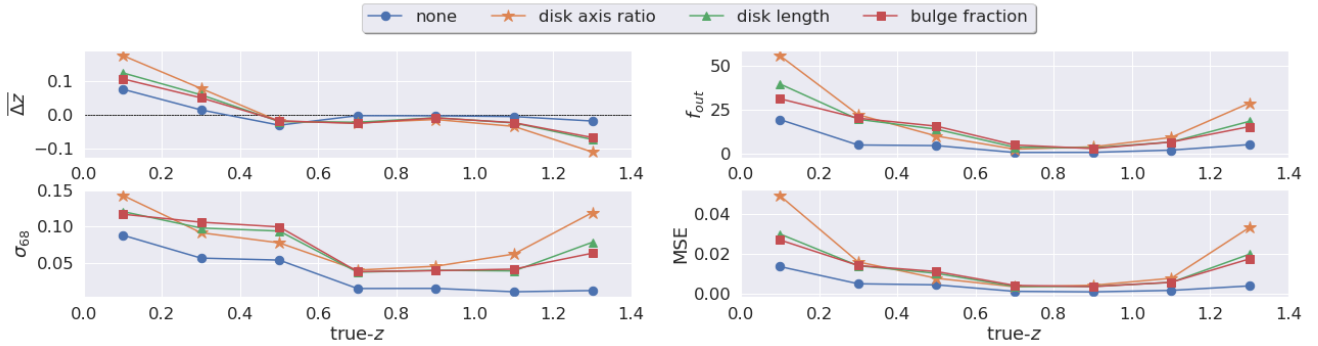


FIGURE 3.29: Photo-z metrics as a function of redshift for the three results obtained by adding shape parameters to the input list, separately, together, and not using it.

3.2.4 Using photo-z PDFs

The fourth and last test we performed with MICE aimed to quantify the impact of using the photo-z PDFs to recover the true $N(z)$ distribution. As described in Section 3.1.1, the PDFs are computed by DNF and used to estimate the photo-z. In general, when working with MICE, the PDFs have a single peak, which makes easy the photo-z determination (see Figure 3.30).

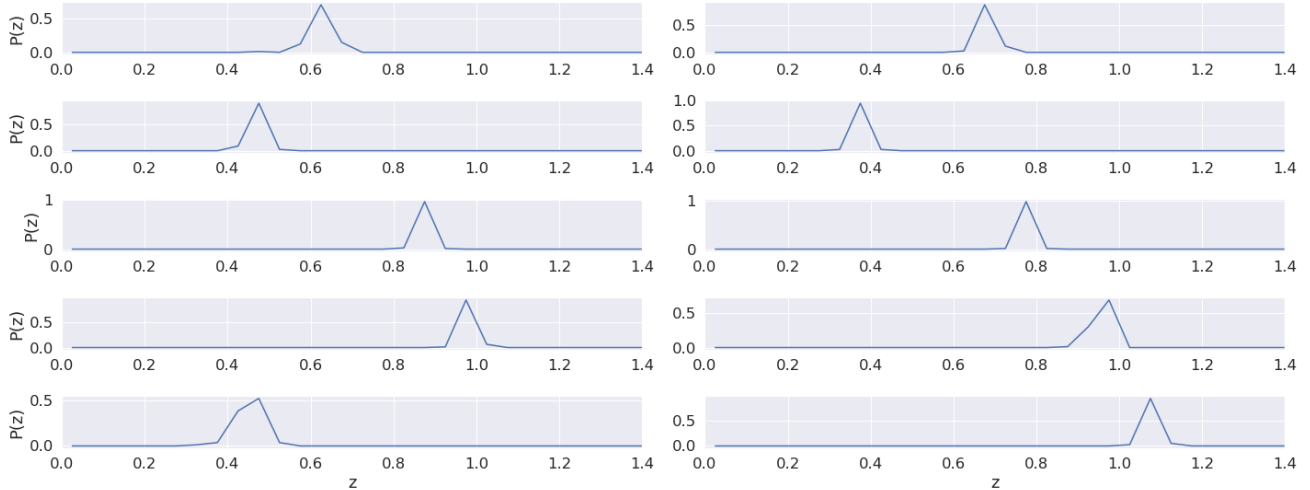


FIGURE 3.30: Example of photo-z PDFs. Probabilities of the 10 first objects of MICE catalog, arbitrarily selected as an illustration of the shape of PDF curves.

For simplicity, we do this exercise by revisiting the results of Section 3.2.2 and using the PDFs generated by DNF to reconstruct the $N(z)$ by stacking the probabilities of the n galaxies at each k -th redshift bin of width $dz = 0.05$ between $z = 0.0$ and $z = 1.4$, as:

$$N(z_k) = \sum_{j=1}^n P(z_{j,k}) . \quad (3.6)$$

This time, we do not use the KDE distribution to display the redshift distributions (see Figure 3.31) because we need to keep the same constant redshift bin width for a fair comparison to the $N(z)$ obtained from the PDFs. This explains the less smooth appearance in these redshift distributions compared to those presented in the previous sections.

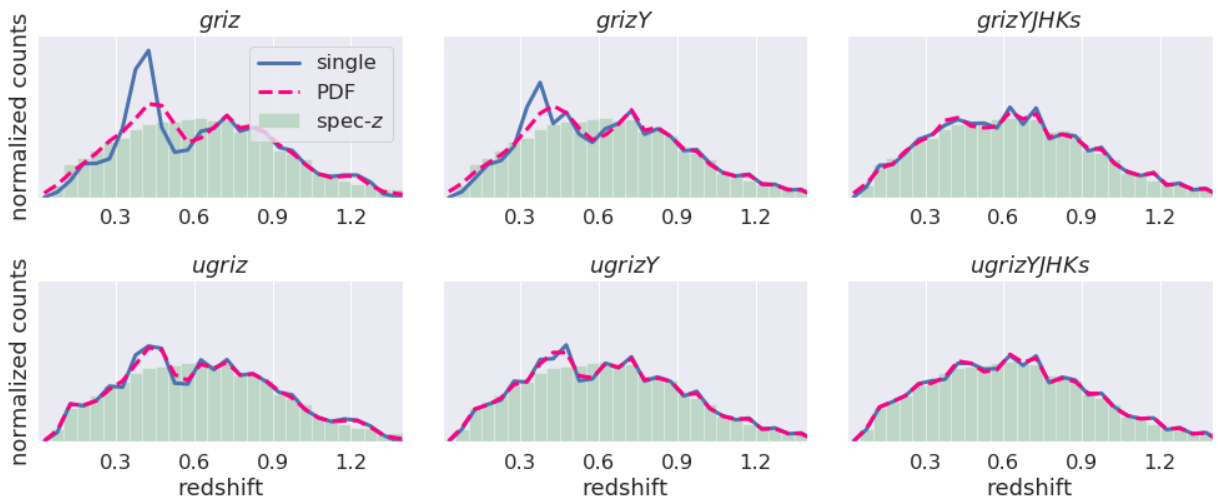


FIGURE 3.31: Normalized redshift distribution of the *test* sample for the true values (green histogram) and the photo-z results obtained using the six sets of magnitudes displayed in the plot legends (blue lines). The pink dashed lines refer to the counts obtained by stacking the probabilities of the photo-z PDF.

Comparing blue and pink lines in Figure 3.31, we notice that the usage of PDFs improves significantly the ability to reproduce the true $N(z)$, for the two cases where there are no other magnitudes from other surveys (left and middle top panels, *griz*, and *grizY*). When UV and IR data is added, there is no additional improvement coming from the PDFs apart from what the inclusion of the other magnitudes had already contributed. Comparing the top left and top middle panels with their respective bottom left and bottom middle, we concluded that the PDF has approximately the same effect on the $N(z)$ of adding the *u*-band to the inputs.

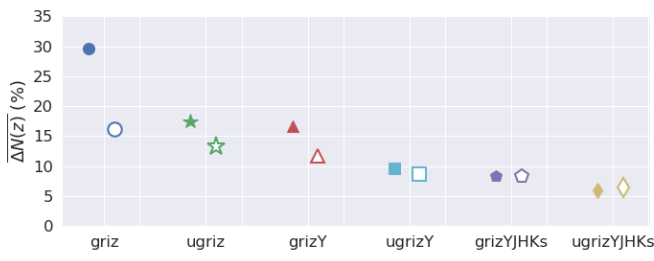


FIGURE 3.32: Global metric $\overline{\Delta N(z)}$ using photo-zs PDFs (empty markers) and single photo-zs (filled markers).

Bands	$\overline{\Delta N(z)}\ (\%)$	$\overline{\Delta N(z)}\ \text{PDF}\ (\%)$
griz	29.6	16.1
ugriz	17.5	13.3
grizY	16.7	11.7
ugrizY	9.5	8.6
grizYJHKs	8.2	8.3
ugrizYJHKs	5.9	6.4

TABLE 3.6: Global metric $\overline{\Delta N(z)}$

The numbers in Table 3.6 (see also Figure 3.32 for a graphic representation of the same results) confirm the assumptions we did based on the visual inspection of Figure 3.31. The metric $\overline{\Delta N(z)}$ only decreases significantly with the usage of PDFs when not using *JHKs*. When using only the four bands *griz*, the effect of using the PDFs is virtually the same as adding the *u*-band or the *Y*-band (decrease the percentage $\overline{\Delta N(z)}$ to approximately the half). If the IR data are available, it is preferable not to use the PDFs and compute the $N(z)$ directly counting the single photo-z estimates.

The same results are also evident in Figure 3.33. When using fewer bands, the error in the $N(z)$ determination is large, particularly at $0.3 < z < 0.6$. There is also a discrepancy at $1.1 < z < 1.3$, which is present in all cases, regardless of the set of magnitudes used. The PDF helps to reduce $\overline{\Delta N(z)}$ only in the first interval. When using more bands, especially when introducing the IR bands *JHKs*, the errors are already small, and more uniformly distributed over the redshift range studied. In this case, the PDFs are not very helpful, sometimes causing a slight worsening of the results. The bump at $1.1 < z < 1.3$ remains in all cases, even if using PDFs. This feature can be possibly explained by the small number of objects in the sample at this redshift range, making the average sensitive to outliers.

In summary, based on the results presented in this section, we conclude that the usage of PDFs can be an important tool to improve the accuracy of the photo-z estimates for the DES Y3 Wide sample, which has no UV and IR bands.

Summary of lessons learned with MICE

- The photo-z algorithm DNF presented the best performance compared with ANNz2, LePhare, and MLZ, under the same conditions. Therefore, it was chosen to be used in the remaining of this work.
- The magnitudes *JHKs* improve considerably the photo-z accuracy, including the low-*z* range ($z < 0.5$), where the 4,000 Å break of early-type galaxies falls into the UV.
- The addition of *u*-band to the standard *grizY* filter set improves the results by reducing the photo-z scatter in all the redshift range studied, but especially at low-*z*, as expected.
- The shape parameters available on MICE simulations do not seem to help on the photo-z estimates by DNF, although the method allows the usage of different observables as input, other than only magnitudes.
- Use of photo-z PDFs is helpful to improve the accuracy of the $N(z)$ estimates when using only the standard *grizY* set of magnitudes. The effect of the PDFs is similar to the addition of the *u*-band to the input parameters.
- If the IR data from *JHKs* is available, the use of PDFs slightly worsens the results; therefore, it is not recommended.

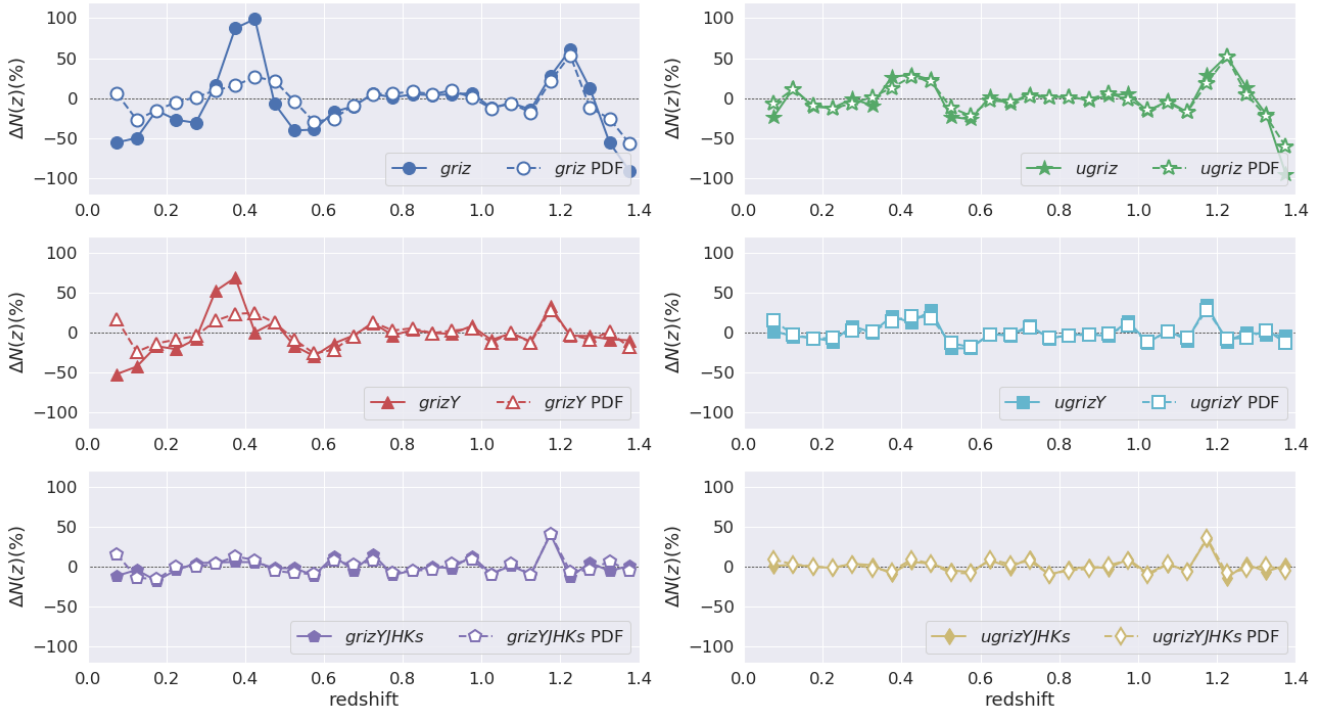


FIGURE 3.33: $\Delta N(z)$ as a function of redshift, for all the PDF bins, for the six set of magnitudes used, with and without considering the photo-z PDFs.

3.3 Tests with DES real data

3.3.1 Using different magnitude types

The Y3 Gold catalog contains different types of fluxes measurements (and magnitudes) available for the five bands *grizY*. Some magnitudes are the SExtractor’s AUTO, MODEL, DETMODEL, APER, etc (for details, see the SExtractor user guide³). Moreover, there are two other types of magnitudes computed in the post-processing phase by DESDM team, called MOF and SOF (described in Section 2.1.1). MOF is preferred within the collaboration in dark energy related working groups, but for the DES Y3 Wide catalog, the *Y*-band MOF is not available. This is because the average *S/N* ratio of magnitudes obtained with this filter, up to the third year by co-adding images, was not high enough to run the composite model fit in MOF/SOF pipelines.

According to our results obtained with MICE (Section 3.2.2), the IR photometry (including the near IR *Y*-band) is indeed relevant for the photo-z accuracy. This is evident by the remarkable difference between the $N(z)$ distributions obtained with *griz* versus *grizY* in Figure 3.19. However, this conclusion was obtained from a data set with perfect magnitudes. With real data, the large magnitude errors might propagate to the photo-z estimates, causing damage to their accuracy, instead of an improvement. Thus, in this section, we use the spectroscopic sample described in Section 3.1.3 as a truth table to explore the photo-z accuracy obtained with the traditional SExtractor AUTO magnitudes, with and without including the *Y*-band, compared side-by-side with MOF *griz*.

We used DNF, trained with the pruned *train* set containing 30,000 galaxies, and applied to the *test* set containing 20,000 galaxies, where we computed the metrics defined in Section 3.1.2. Again, the metric errors were estimated by doing jackknife resampling with 9/10 of the *test* set. The redshift distributions (Figure 3.34) obtained for the three cases mentioned above are very similar, indicating that the results are

³<https://media.readthedocs.org/pdf/sextorator/latest/sextorator.pdf>

not very sensitive to the magnitude type used, with MOF performing slightly better at higher redshifts ($z > 0.6$).

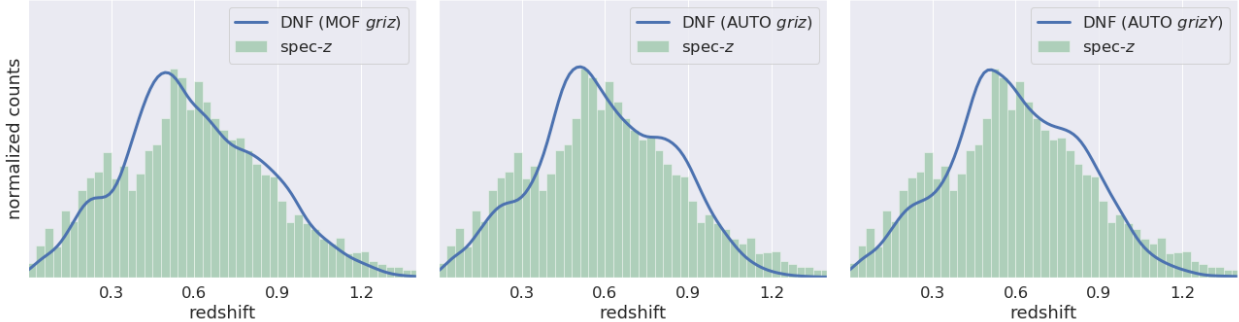


FIGURE 3.34: Normalized redshift distribution of the *test* sample for the *spec-z* values (green histogram) and the photo-z results obtained using the three sets of magnitudes displayed in the plot legends (blue lines).

Analyzing the variation of Δz with redshift (panels in Figure 3.35b), we notice a positive bias at lower redshifts ($z < 0.4$) and a negative bias at higher redshifts ($z > 0.9$) in all cases. Unlike the results using MICE, where the dispersion was large only for low redshifts, the dispersion obtained with real data is much larger and more uniformly distributed over the whole redshift range observed. This is evident from the thickness of the greenish region (slightly narrower for MOF) and a large number of outliers (dark blue points) in Figure 3.35a.

The magnitude-redshift diagram drawn with the three resulting photo-zs are also very similar among each other (Figure 3.36), and none of them can reproduce well the one with *spec-z* (Figure 3.8), at least from a visual inspection. There are notable distortions in the shape of the cloud of points, with a lack of faint objects assigned to low redshifts by DNF, not so striking but similar to what we obtained with ANNz2 on MICE (see Section 3.2.1). It is true that these objects are not very abundant in the spectroscopic sample as well, but the photo-z (for all the three cases) is moving these few objects to another redshift interval. This is probably an effect of the inadequate training on this locus in magnitude-redshift space. The machine has learned that the probability of a galaxy to occupy this position is very low, and it propagates to the results in the test sample.

The basic plots mentioned above used for photo-z results analysis are visually very similar in the three cases addressed, so the comparison can not be made by eye. We need the metrics to quantify the photo-z quality. In Table 3.7, we show the same metrics we calculated with MICE, now for DES Y3 *test* set using MOF *griz*, AUTO *griz*, and AUTO *grizY*. Based on these numbers, we confirm that the magnitude type MOF provides a better quality of photo-zs, even short in one band. The presence of the *Y*-band in magnitude AUTO increases the scatter and the fraction of outliers. It reduces the amplitude of global bias slightly, but the improvement is smaller than the error bars.

Magnitude limit	$\overline{\Delta z}$	σ_{68}	f_{out} (%)	MSE
MOF <i>griz</i>	-0.0030 ± 0.0007	0.0814 ± 0.0003	14.51 ± 0.11	0.0196 ± 0.0003
AUTO <i>griz</i>	-0.0041 ± 0.0010	0.1045 ± 0.0004	20.46 ± 0.13	0.0260 ± 0.0003
AUTO <i>grizY</i>	-0.0032 ± 0.0010	0.1070 ± 0.0004	20.79 ± 0.13	0.0268 ± 0.0003

TABLE 3.7: Photo-z quality metrics for distinct types of magnitudes in DES real data.

The adverse influence of the *Y*-band in real data can be explained by the average low *S/N* achieved with this band in DES up to the date of writing. By the way, this is the reason for the lack of *Y*-band for MOF. Besides that, the wavelength range covered by the *Y*-band is partially overlapped by the *z*-band (between $\sim 9,500$ and $\sim 10,000$ Å), so the information brought by the *Y*-band is partially redundant with the *z*-band.

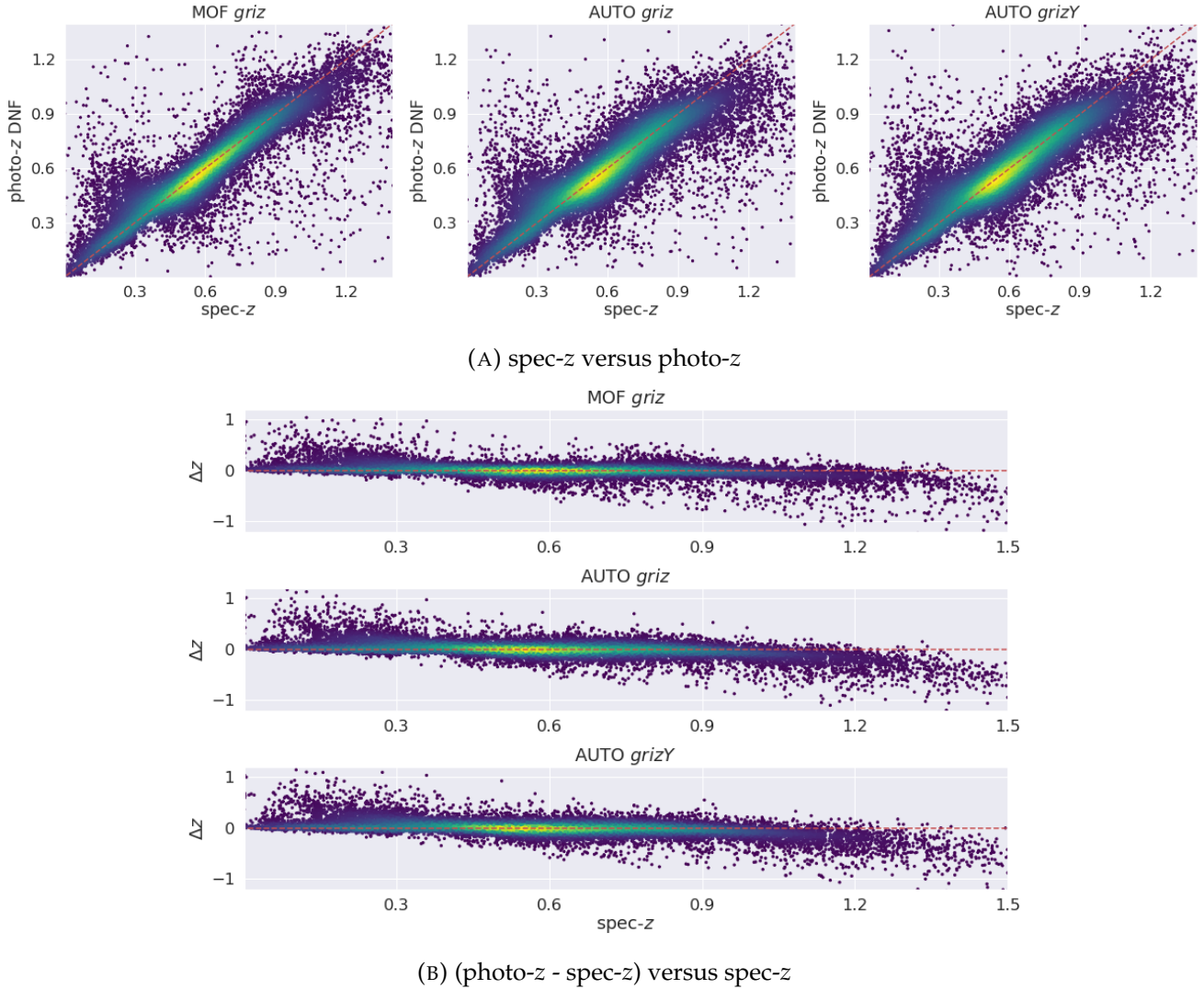


FIGURE 3.35: Comparison between photo-zs and true-zs object by object for DES real data, color coded by density of stacked points, from dark blue to yellow in increasing order. Outliers are represented by black dots.

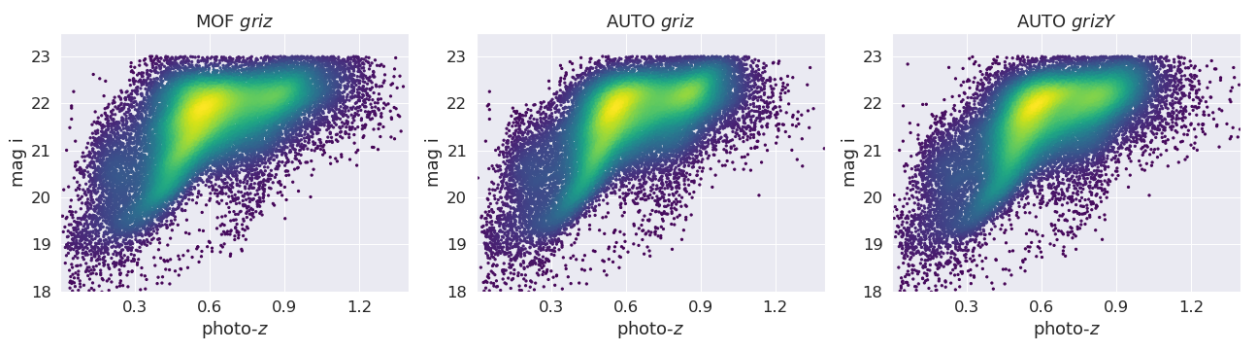


FIGURE 3.36: Apparent magnitude versus photo-zs obtained using the three different sets of magnitudes, color coded by density of stacked points, from dark blue to yellow in increasing order.

The same results of Table 3.7 are graphically exhibited in Figure 3.37. In both panels, it is clear that the presence or absence of Y-band is not very significant, in fact, with the results getting worse by the

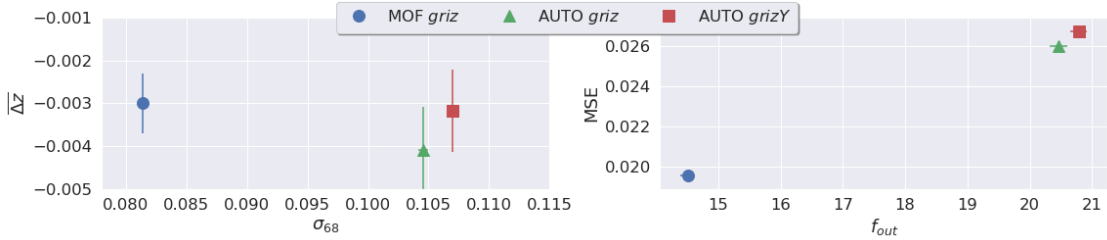


FIGURE 3.37: Global metrics comparison for the three sets of magnitudes obtained in DES real data (same results as Table 3.7), here as a visual representation). Left: Δz versus σ_{68} . Right: f_{out} versus MSE .

inclusion of the IR band. The type of magnitude is more relevant to differentiate the results, where the photo- z quality with MOF type is, by far, superior than with SExtractor’s AUTO magnitudes.

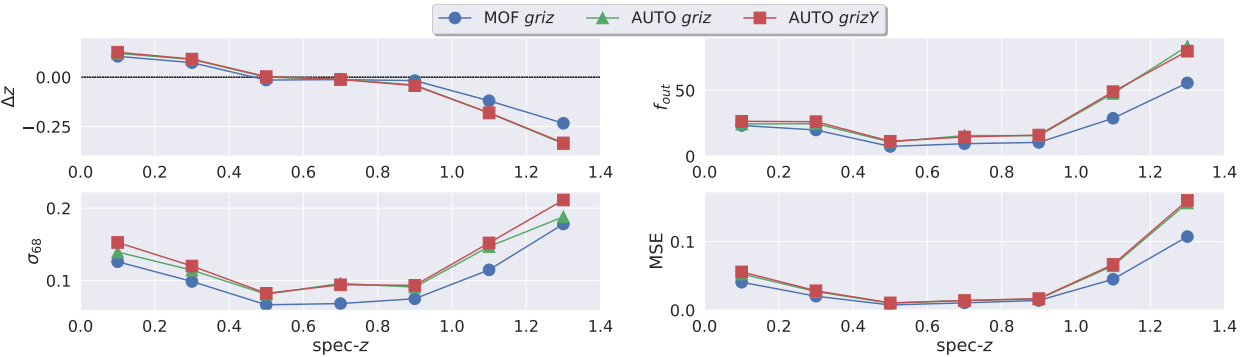


FIGURE 3.38: Photo- z metrics as a function of redshift for the three sets of magnitudes used.

The evolution of the metrics with redshift (Figure 3.38) shows similar trends for all results. In all cases, there is a positive bias at low redshifts ($z < 0.5$), and a negative bias at higher redshifts ($z > 0.9$), with a smaller amplitude for MOF griz. The dispersion is also larger at both ends of the redshift range studied. Again, with similar trends for all results, but smaller with MOF. Especially for higher redshifts, the fraction of outliers is still large, but substantially reduced by using MOF.

From the results above, we conclude that the magnitude type MOF, even with one band shorter, is better than SExtractor’s AUTO, regarding photo- z quality produced. Therefore, the results presented in the next chapters were produced using MOF magnitudes.

3.3.2 Exploring different magnitude limits

The DES is expected to reach $i \sim 24$ depth in its wide survey after the end of observations. As this work is being carried out with the survey still in progress, the data available do not reach such limit, and the depth achieved up to the date is not spatially homogeneous. In Section 2.1.1, we show the i -band depth map and discuss the spatial distribution of the approximate magnitude limit at 5σ detection. The magnitude limit threshold choice is a trade-off between including a larger area with shallower magnitude limits or selecting a smaller area with deeper magnitude limits.

In this test, we explore how the choice of maximum magnitude cut impacts on the quality of the photo- z estimates. It is expected that the larger the maximum magnitude allowed in the sample, the worse the global metrics because fainter objects have typically magnitudes measurements with lower S/N, which propagates negatively to the photo- z errors. We run DNF using MOF magnitudes for the three pruned samples described in Figure 3.6.

In contrast with the previous tests, here, the input data differ among the three results analyzed. The differences in magnitude limit propagate to the spec- z distribution. It becomes clearer if one compares

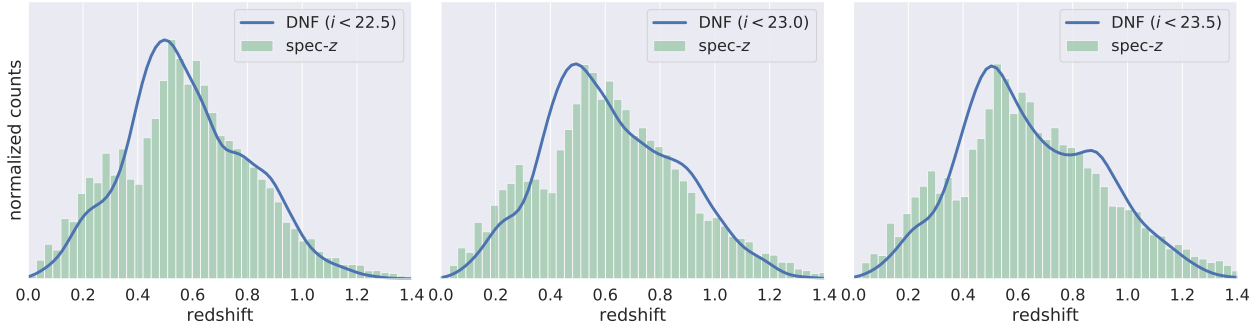


FIGURE 3.39: Normalized redshift distribution of the *test* sample for the spec-*z* values (green histogram) and the photo-*z* results obtained using the three magnitude-limited sets displayed in the plot legends (blue lines).

the counts at $z > 1.2$ on the left and right panels in Figure 3.39. From this figure, we notice that in all cases, DNF roughly compensates for the lack of objects wrongly transferring objects from $z < 0.4$ to $0.4 < z < 0.6$. The difference in the three results is most significant at $z \sim 0.9$, where the presence of fainter magnitudes ($i > 22.5$) introduces an artificial peak in the photo-*z* distribution.

The comparison between photo-*z* and spec-*z* object by object shows similar trends for all the three samples in Figure 3.40. Apart from the higher redshift range ($z > 1.2$), the differences between the results in the three cases are hardly visually noticeable. Using the metrics in Table 3.8 and Figure 3.41 to compare quantitatively, we confirm the expectations of obtaining better metrics (σ_{68} , f_{out} , and MSE) for the sample cut in a brighter magnitude ($i < 22.5$). The surprising outcome is the larger $|\bar{\Delta}z|$ for $i < 23.0$ than for $i < 22.5$. However, the difference is small and falls within the error bars.

Magnitude limit	$\bar{\Delta}z$	σ_{68}	f_{out} (%)	MSE
$i < 22.5$	0.0003 ± 0.0013	0.0757 ± 0.0011	12.3150 ± 0.4047	0.0166 ± 0.0006
$i < 23.0$	-0.0017 ± 0.0013	0.0837 ± 0.0015	14.7450 ± 0.4995	0.0186 ± 0.0008
$i < 23.5$	0.0005 ± 0.0015	0.0875 ± 0.0017	15.7550 ± 0.5191	0.0214 ± 0.0009

TABLE 3.8: Photo-*z* quality metrics for distinct magnitude-limited samples in DES real data.

The evolution of metrics with redshift is similar in the three cases, especially for intermediate redshifts ($0.2 < z < 1.2$). At lower redshifts ($z < 0.2$), the metrics are slightly better for the $i < 22.5$ sample, following the same trend as for the global metrics. This result can be explained by the increase in the average *S/N* in magnitudes when eliminating faint objects from the sample. At higher redshifts ($z < 1.2$), the results go in the opposite direction, with significant worse metrics for the $i < 22.5$ sample, likely due to the small number of objects at this redshift interval.

Based on the results discussed above, we find that the photo-*z* results are not strongly sensitive by the cut in maximum magnitude within the range of $22.5 < i < 23.5$, so the conclusions extracted from the quality tests should be the same in the three cases addressed, at least for $z < 1.0$.

3.3.3 Using photo-*z* PDFs

Now we repeat the same exercise done with MICE and compare the results with and without using photo-*z* PDFs to reconstruct the $N(z)$ distribution. As shown in Figure 3.43, the PDFs of real galaxies are not so “well-behaved” as those of simulated objects (compare to Figure 3.30). Here, the relatively large errors of observable quantities (in this case, the magnitudes) propagate as broad or multiple peaks in the PDFs.

Although we have already established MOF as the magnitude type chosen, we also compare the results using AUTO, to see how the PDFs could help in cases where MOF is not available.

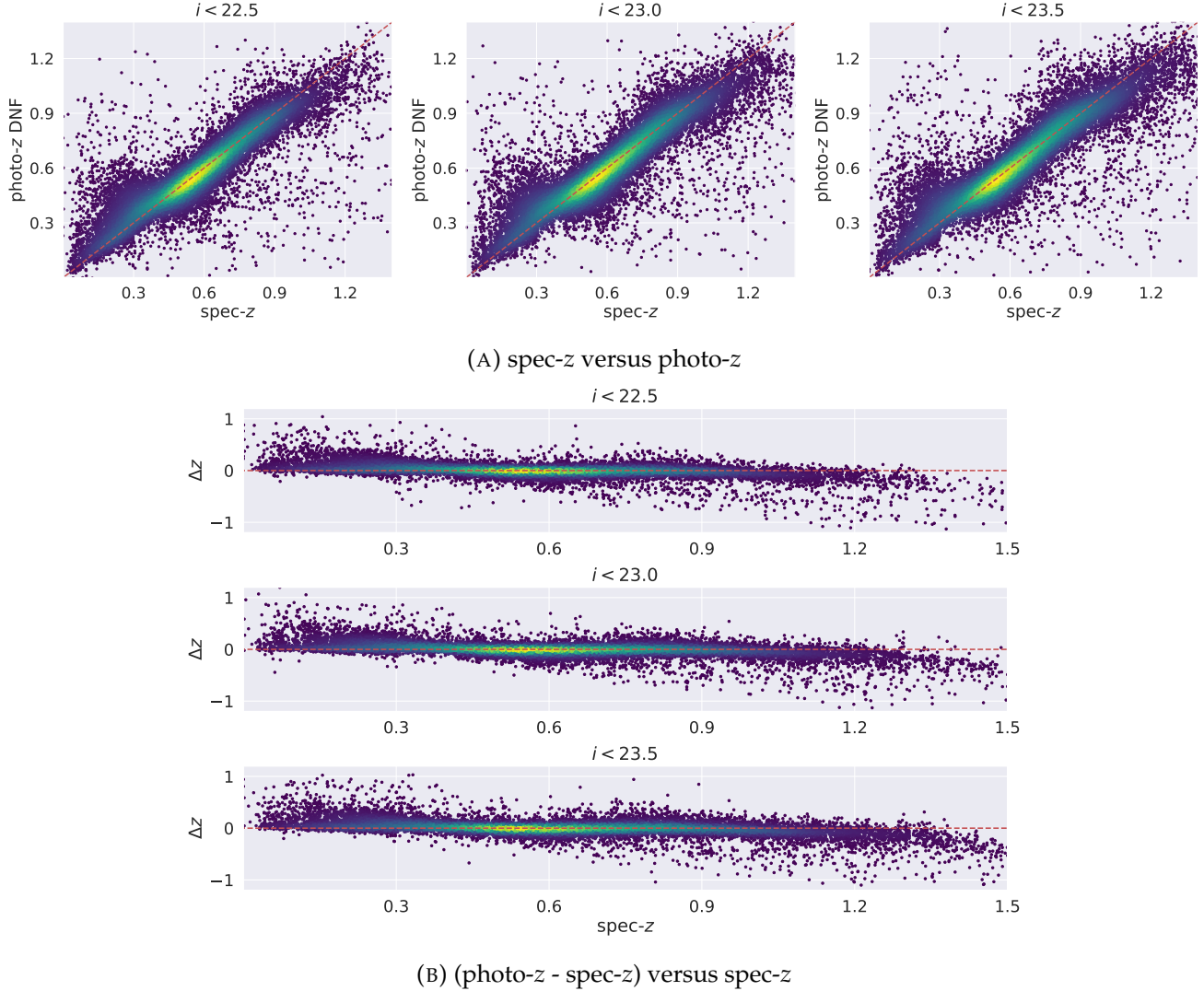


FIGURE 3.40: Comparison between photo-zs and true-zs object by object for DES real data, color coded by density of stacked points, from dark blue to yellow in increasing order. Outliers are represented by black dots.

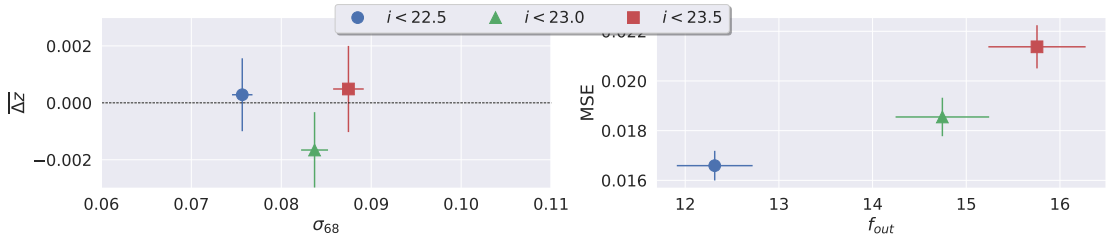


FIGURE 3.41: Global metrics comparison for the three magnitude-limited samples in DES real data (same results as Table 3.8), here as a visual representation). Left: Δz versus σ_{68} . Right: f_{out} versus MSE .

From the Figure 3.44, we notice that the usage of PDFs improves the $N(z)$ reconstruction in all cases, decreasing the differences between the true and computed counts in all the problematic ranges, i.e., it fixes the underestimated counts at $z < 0.4$ and $z > 1.0$, and the overestimated counts at $0.4 < z < 0.6$, and $0.8 < z < 1.0$.

According to the results displayed in Table 3.9 (and in Figure 3.45) the usage of PDFs reduces to less

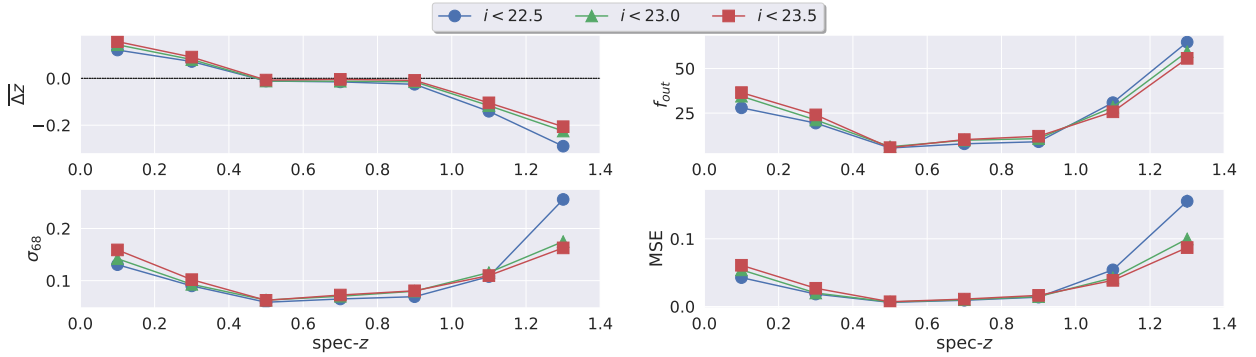


FIGURE 3.42: Photo-z metrics as a function of redshift for the three magnitude-limited samples.

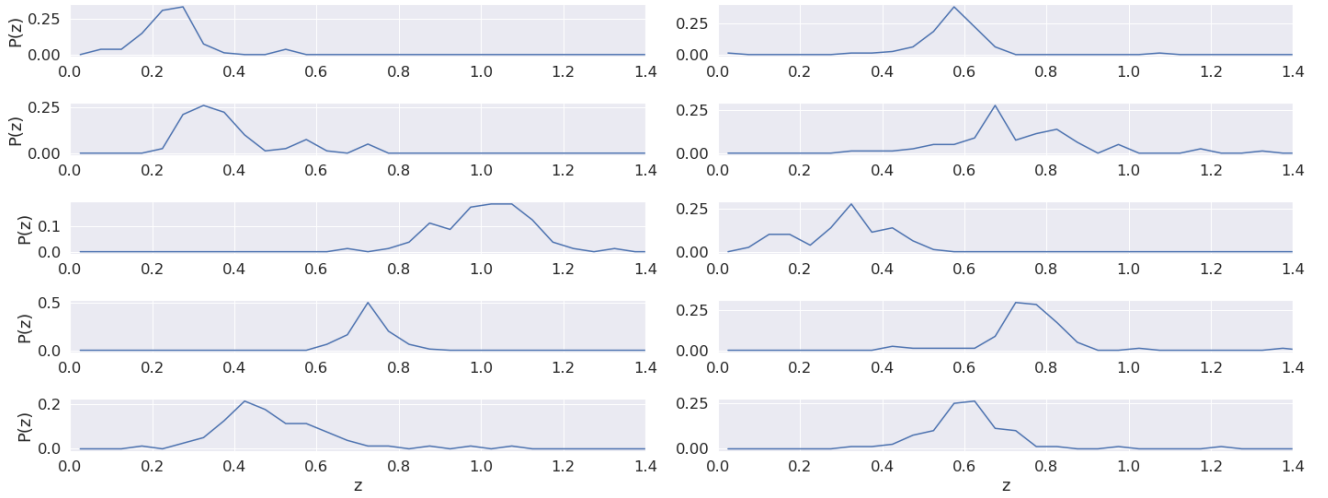


FIGURE 3.43: Example of photo-z PDFs. Probabilities of the 10 first objects of Gold catalog, arbitrarily selected as an illustration of the shape of PDF curves.

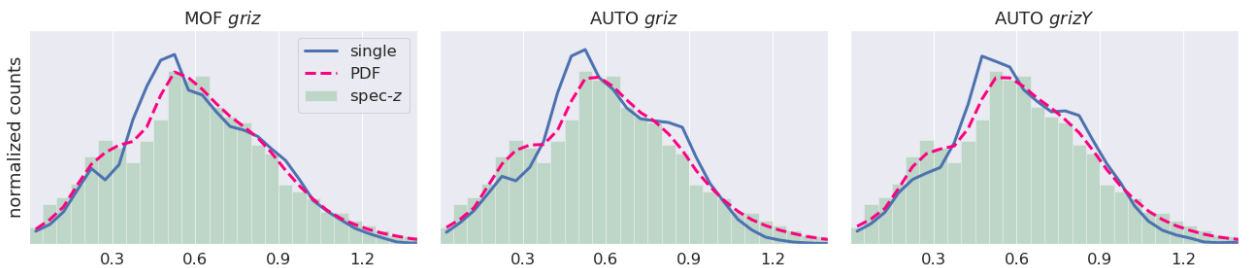


FIGURE 3.44: Normalized redshift distribution of the *test* sample for the true values (green histogram) and the photo-z results obtained using the three sets of magnitudes displayed in the plot legends (blue lines). The pink dashed lines refer to the counts obtained by stacking the probabilities of the photo-z PDF.

than half the value of $\overline{\Delta N(z)}$ in all cases. The improvement is similar for both mag types, leading to final $\overline{\Delta N(z)} \sim 12\text{--}13\%$. Again, the results without the Y-band still better than that with the IR data.

In Figure 3.46 the impressions obtained from Figure 3.44 are confirmed and quantified. The PDFs decrease the differences in counts for all the intervals with large errors, with the greatest improvement at higher redshifts. Nevertheless, the differences still large at both ends of the range studied. Based on



FIGURE 3.45: Global metric $\overline{\Delta N(z)}$ using PDF (empty markers) using single (full markers) photo-z PDFs.

TABLE 3.9: Global metric $\overline{\Delta N(z)}$

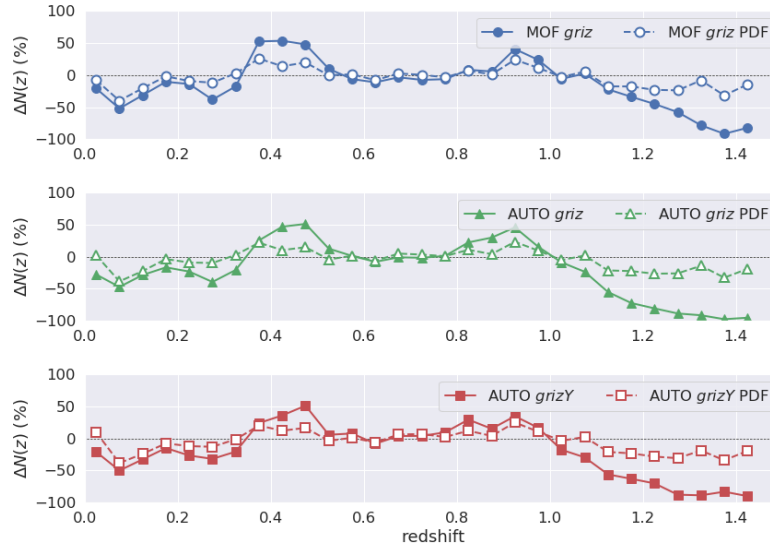


FIGURE 3.46: $\Delta N(z)$ as a function of redshift, for all the PDF bins, for the three set of magnitudes used, with and without considering the photo-z PDFs.

the results above, we conclude that the use of the PDFs is helpful to improve the $N(z)$ reconstruction, regardless of the magnitude type used and the inclusion of the Y -band.

Summary of lessons learned with spec-z sample

- The photo-z estimates obtained using the magnitude type MOF are more accurate than using SExtractor's AUTO regarding photo-z metrics studied in this chapter, even though MOF has one band less. Hence, the galaxy properties and the LF estimates presented in the chapters were produced using MOF.
- If extending the analysis to fainter magnitudes (cut in maximum magnitude $i = 23.5$), the metrics are mildly worsened in comparison to $i < 22.5$ and $i > 23.0$, without significant changes in the trends observed at $z < 1.0$.
- The usage of PDFs improves the reconstruction of the $N(z)$ in all z ranges where there are large errors when using single photo-z estimates, especially at higher redshifts. This is a strong motivation for including these probabilities in the methodology to compute the LF, as will be explained in Section 5.1

3.4 Photo-zs for DES science sample

After the extensive list of tests discussed above, we finally adopted the best configuration found so far for the DES Y3 science sample; that is, the algorithm DNF using PDFs and the input magnitudes: *griz* MOF. The expected shape of the $N(z)$ distribution is a broad and smooth one-peak asymmetric curve. Starting at $z=0$, the larger the z , the larger the number of objects observed, due to the increasing cosmic volume contained within the fixed solid angle delimited by the observed area in the sky. At some point, the distribution reaches a peak and starts to fall. At this point, the sample incompleteness caused by observational limitations start to become dominant, and the larger the z , the smaller the number of objects observed. The position of the peak is related to the magnitude limit of the survey. The deeper the survey, the peak is pushed towards larger redshifts (Lima et al., 2008).

The resulting $N(z)$ we obtain with photometric redshifts has two artificial peaks (see Figure 3.47), introduced by the limitations of the methodology. The lack of the UV and IR bands makes the method to be significantly vulnerable to the degeneracies on color-redshift relation that appear when only *griz* bands are available. This well-known effect harms the quality of the results, especially in the low redshift domain. Galaxies are wrongly transferred across redshift bins, most of them from $z < 0.3$ to $0.4 < z < 0.5$, creating the larger artificial peak at $z \sim 0.5$.

The introduction of PDFs gives a substantial help to reduce this effect, and smoothies the curve, but it is not enough to remove the artificial features completely. These uncertainties will indeed propagate to other measurements explored in the next chapters. This is a known limitation that we have to cope with, at least at the stage of writing this work. DES is ongoing, and there is one more data release upcoming soon. The Y3 catalog has already covered the total area defined in by the survey planning. The next release will include a larger number of co-added images, so the objects identified will have a better S/N on average, which naturally converts into an improvement of the photo-z quality.

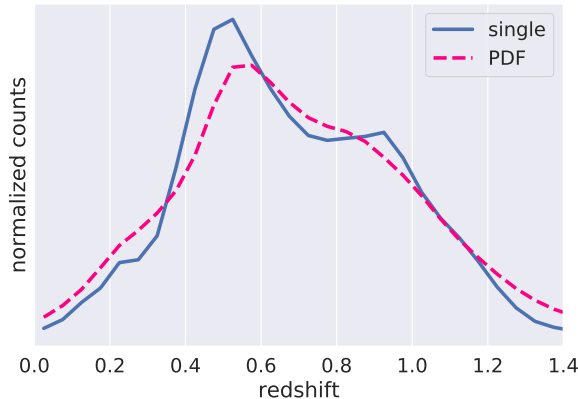


FIGURE 3.47: Redshift distribution of the DES Y3 science sample obtained with DNF, with and without using PDFs.

We obtained a reasonable homogeneous spatial distribution of $N(z)$ for the science sample, as evident in the maps of photo-z mean and standard deviation shown in Figure 3.48. These maps are partitioned in HEALPix pixels of $NSide = 4096$ and were calculated based on single photo-z estimates, which are not the information that will be effectively used to estimate the LF measurements. The LF results are based on the photo-z PDFs, as discussed next in Chapter 5, which smooths the $N(z)$ distributions. Hence, the real level of homogeneity of the data used as input for the LF should be even higher than the illustrated in the maps.

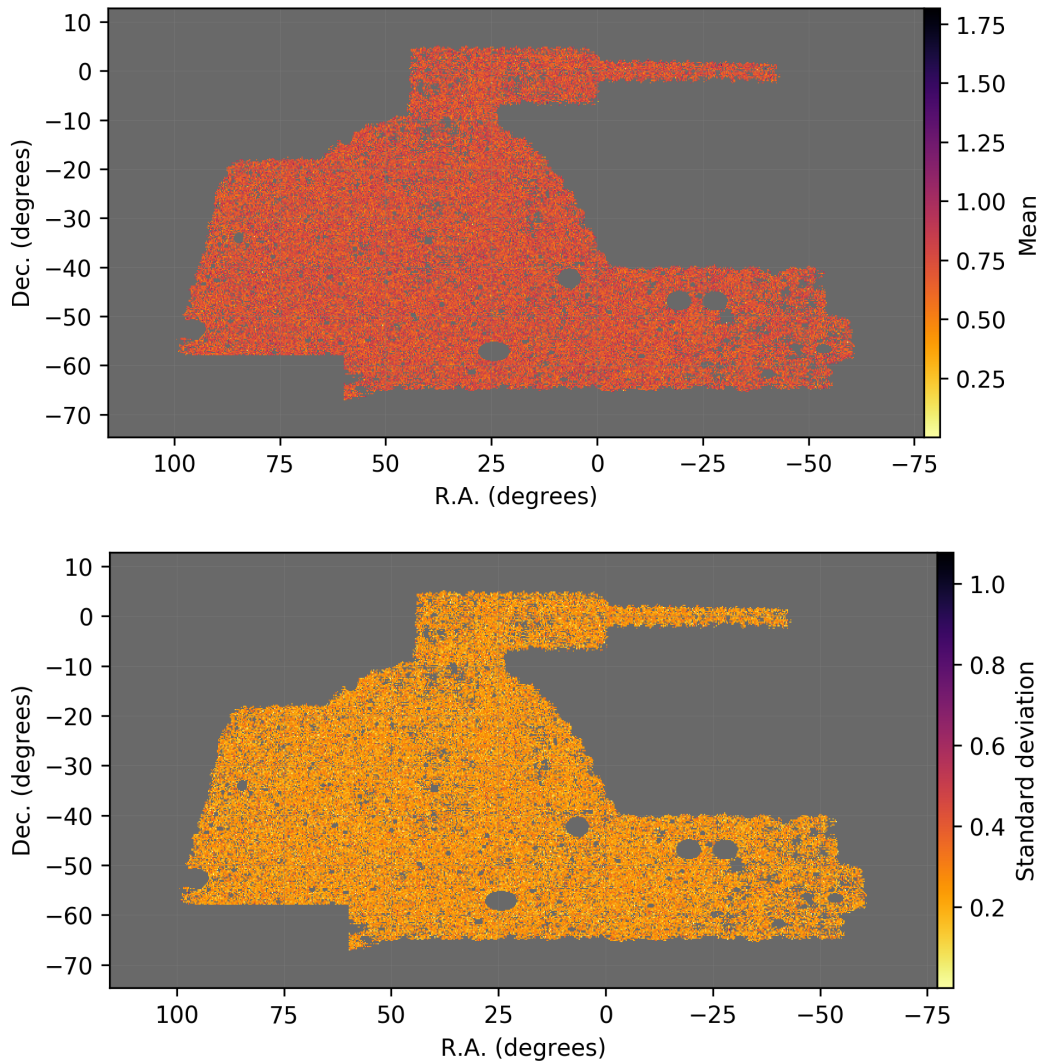


FIGURE 3.48: Spatial distribution of photo- z mean (top panel) and standard deviation (bottom panel) for the GE science sample.

Chapter 4

Galaxy Properties



Overview

In this chapter, we present the methodology used to estimate physical properties of galaxies such as absolute magnitudes, rest-frame colors, extinction, and K-correction. We use MICE simulations to test and optimize the determination of these properties. We also use a subset of DES data to find an appropriate set of spectral energy distribution templates, considering the characteristics of the data set. Finally, we apply the lessons learned to the DES Y3 Full catalog.

4.1 Basic elements to study Galaxy Evolution

In this work, we aim to study the evolution of galaxy properties, measured as a function redshift. Our analyses rely on both photometric and spectroscopic data. The former is available for all galaxies in the target sample (DES Y3 Wide). The latter is available only for a small portion of the sample, and they are used mainly for photo-z training and validation. In this section, we describe how to estimate galaxy properties, except for their redshifts, already addressed in the previous chapter.

Since we do not have the spectra for the vast majority of galaxies in our samples, we use the algorithm LePhare to assign, to each galaxy, the most representative SED from a template library. Among several template-fitting algorithms available, we chose LePhare due to its flexibility and the large variety of configuration parameters regarding galaxy physical properties.

We explained the basics of LePhare's methodology in Section 3.1. For computing photo-zs, LePhare shows to be less accurate than the empirical methods addressed in the comparison, so we use DNF for accomplishing the task of redshift determination. However, once the redshifts are estimated by any other means, LePhare can be used in its "ZFIX" mode, returning the best-fitted SED template for a given set of magnitudes and their associated errors.

We applied this method to obtain estimates of other quantities, such as K-corrections, $E(B - V)$, and absolute magnitudes. If using synthetic SED templates, the list of outcomes can be expanded to include: stellar masses, specific star formation rate, star formation history, age, and metallicity.

4.1.1 Spectral Energy Distribution templates

We start the analysis by using the 31 templates from the COSMOS library (Ilbert et al., 2009); the same set used by Carretero et al. (2015) to build MICE simulations. According to Ilbert et al. (2009), the SEDs were originally generated by Polletta et al. (2007) with the GRASIL code (Silva et al., 1998), resulting in three SEDs of elliptical galaxies and six templates of spiral galaxies (S0, Sa, Sb, Sc, Sd, and Sdm), plus 12 additional starburst (SB) templates with ages between 0.03 and 3 Gyr from Bruzual et al. (2003) models to complete the blue range of colors. Those 21 templates were then interpolated to refine the sampling in color-redshift space, resulting in the 31 templates shown in Figure 4.1.

The MICE magnitudes were derived from the templates mentioned above taking into account the dust extinction modeled by four different extinction laws: one from Prevot et al. (1984) and three

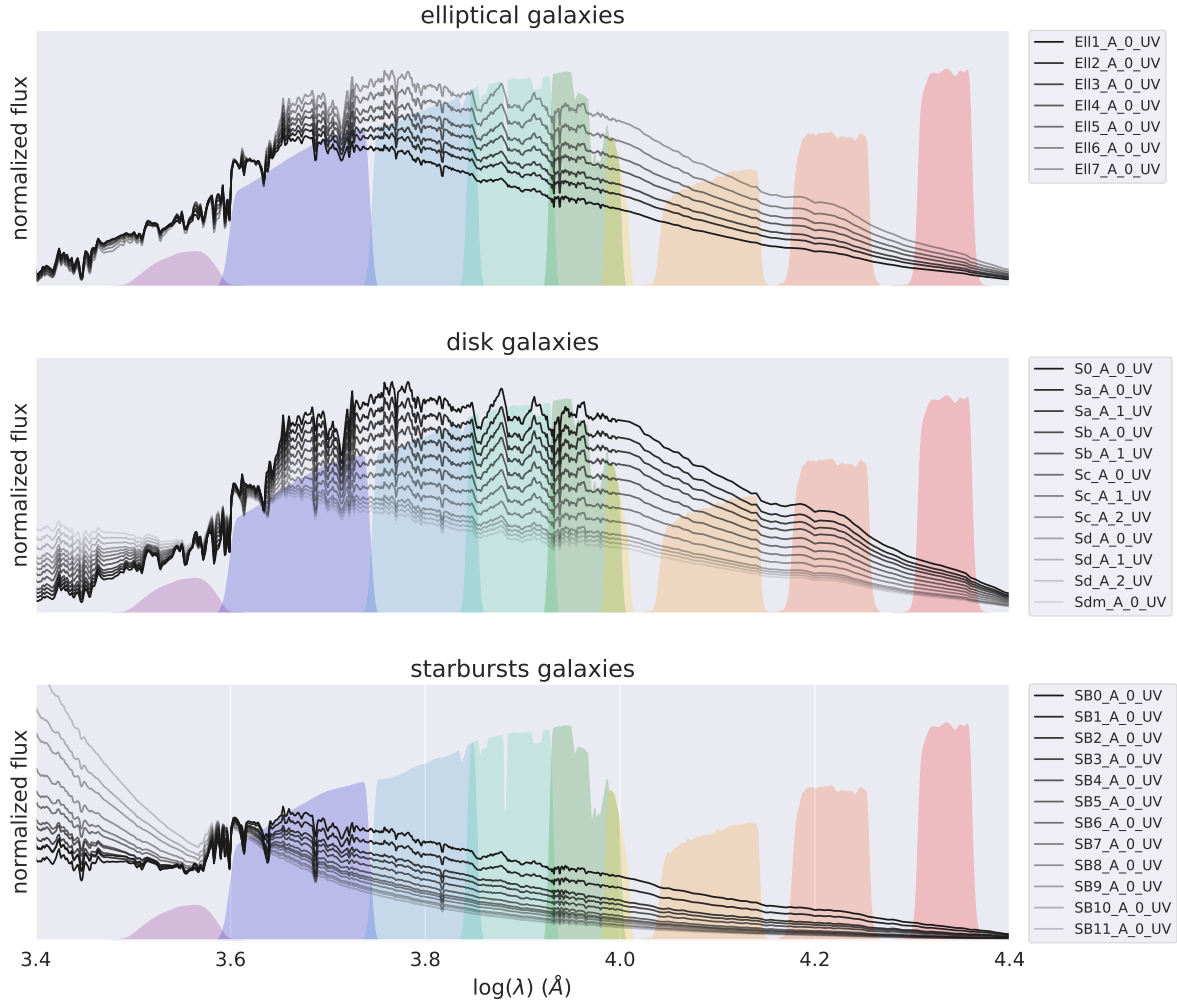


FIGURE 4.1: Restframe COSMOS library of SED templates from Ilbert et al. (2009) used to assign magnitudes to the mock galaxies in MICE catalog. The SEDs are displayed separated by morphological types. The gradient in color intensity distinguishes individual SEDs. We plotted the filter transmission curves for the $ugrizYJHKs$ bands behind the SED curves.

from Calzetti et al. (2000), depending on the templates, as shown in Table 4.1. They are combined to create interpolations between each consecutive pair templates in color space, varying the importance of contributions from each SED. For instance, the mock galaxy can be created with an artificial SED, which is 30% Ell1_A_0_UV and 70% Ell2_A_0_UV (the SED curves of Ell1_A_0_UV and Ell2_A_0_UV are in the top panel of Figure 4.1).

The AB magnitudes are derived by the Eq. 4.1, where *template* is the value of the template flux and *filter* is the value of the filter transmission curve (exhibited in the background of Figure 4.1).

$$AB = \frac{\int (\lambda \text{ template} \text{ filter}) d\lambda}{\int \frac{\text{filter}}{\lambda} d\lambda + \text{const}}. \quad (4.1)$$

When extinction is included, the value of the variable *template* is multiplied by a factor defined by the extinction laws (Eq. 4.2).

$$\text{factor} = \left(\frac{\text{ext_curve}_N}{\text{ext_curve}_0} \right)^{E(B-V)/0.2}. \quad (4.2)$$

SED Type	COSMOS SED	N	Extinction Law
Elliptical	1 - 7	0	no extinction
Disk	8 - 10	0	no extinction
Disk	11 - 19	1	Prevot $E(B-V)$ 0.2
Starburst	20 - 23	1	Prevot $E(B-V)$ 0.2
Starburst	24 - 31	2	Calzetti $E(B-V)$ 0.2
Starburst	24 - 31	3	Calzetti bump1 $E(B-V)$ 0.2
Starburst	24 - 31	4	Calzetti bump2 $E(B-V)$ 0.2

Notes to the Table - Extinction laws applied to the SED range are indicated in the second column. No extinction applied to early-type and bulge-dominant spiral SEDs. Late-type spirals and the “reddest” starbursts used the *Prevot* law. The bluest starburst SEDs were repeated three times, varying the type of *Calzetti* extinction law.

TABLE 4.1: SED templates and extinction laws used to create mock magnitudes in MICE simulations.

where ext_curve_0 means no extinction, and N defines the extinction law as in Table 4.1 (see the extinction curves in Figure 4.2).

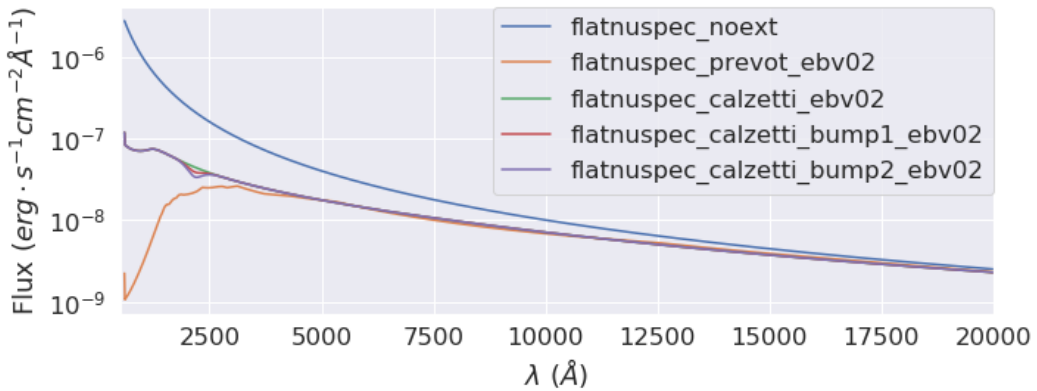


FIGURE 4.2: Extinction laws used in the creation of MICE mock galaxies, in combination with COSMOS SEDs. The blue line represents a reference curve with no extinction applied.

In our tests, we do not interpolate between templates. Therefore, we lose resolution in color-redshift space in comparison to MICE. However, the uncertainties present in DES photometric data are the dominant limitation in the color determination for DES galaxies. The excessive refined resolution would represent an increase in computational time without any gain in the precision level. Similarly, we increased the size of the $E(B-V)$ step used to create the SED grid. We consider the $0.0 < E(B-V) < 0.7$ with step of 0.1; while the simulation was created considering the interval $[0.00, 0.77]$ with step 0.01. Therefore, we used only the original 31 templates, that become 306 ($= 7 E + 3 Sp + (9 Sp \text{ Prevot} + 4 \text{ Starburst Prevot} + 8 \text{ Starburst} \times 3 \text{ Calzetti}) \times 8 E(B-V)$) when including all the combinations of extinction laws and $E(B-V)$ values.

4.1.2 K-correction

To compute the LF, one needs to consider K-corrections in the absolute magnitude estimates. Depending on the spectral type and redshift, the K-correction can be significantly large (larger than two magnitudes). It also contributes as a significant source of error to the absolute magnitude, if not correctly taken into account (Ilbert et al., 2005).

LePhare has a pre-processing step that creates a library of theoretical magnitudes used in the template-fitting process. Those magnitudes result from the combination of the SED templates and the filter transmission curves, considering the effects of internal extinction. At this stage, the user is required to

make assumptions, such as the extinction law and the $E(B - V)$ possible values, and on which SEDs to apply the extinction correction. The extinguished flux, F_λ^e is:

$$F_\lambda^e = F_\lambda^0 10^{-0.4A_\lambda} = F_\lambda^0 10^{-0.4k_\lambda E(B-V)}, \quad (4.3)$$

where F_λ^0 is the emitted flux in $\text{erg s}^{-1} \text{cm}^{-2} \text{\AA}^{-1}$ as a function of the wavelength (λ) and A_λ is the respective reddening coefficient. It is also possible to include the contribution of emission lines, artificially in the SED templates, which could be significant if working with medium width filters, according to the authors in the LePhare's manual¹. The emission lines available are: Ly α , H α , H β , OII, OIII[4959], and OIII[5007].

We tested the impact of including emission lines and found no significant improvement. For default, we do not include emission lines in our tests, unless explicitly stated.

The resulting library of theoretical fluxes (and magnitudes) contain the appropriate K_{corr} values for each SED (see equation 4.4), at each redshift bin, for each possible value of $E(B - V)$ and extinction law considered (and each age, if using synthetic templates). This by-product will be useful, not only for the template-fitting itself but also for the incompleteness corrections applied in the calculation of the LF, to be explained in Section 5.1.

The K-correction values in magnitude units are computed with the following equation, according to Oke et al. (1968):

$$K_{corr} = 2.5 \log(1 + z) + 2.5 \log \left\{ \frac{\int_0^\infty F(\lambda_0) S_i(\lambda) d\lambda}{\int_0^\infty F \left[\frac{\lambda_0}{(1+z)} \right] S_i(\lambda) d\lambda} \right\}, \quad (4.4)$$

where S_i is the non-dimensional parameter of sensitivity function in the i^{th} filter, quantified here by the filter transmission curve (Figure 2.25). The K_{corr} value obtained from Eq.4.4 is directly applied to the absolute magnitude calculation, together with the extinction correction (see Eq. 4.5). In the redshift range studied, the K-correction contribution to absolute magnitude estimates can reach 2.5 magnitudes, depending on the spectral type, as illustrated in Figure 4.3. In this figure, we use a gradient in color intensity to distinguish individual SEDs and trends according to spectral type (the same color schema used in Figure 4.1).

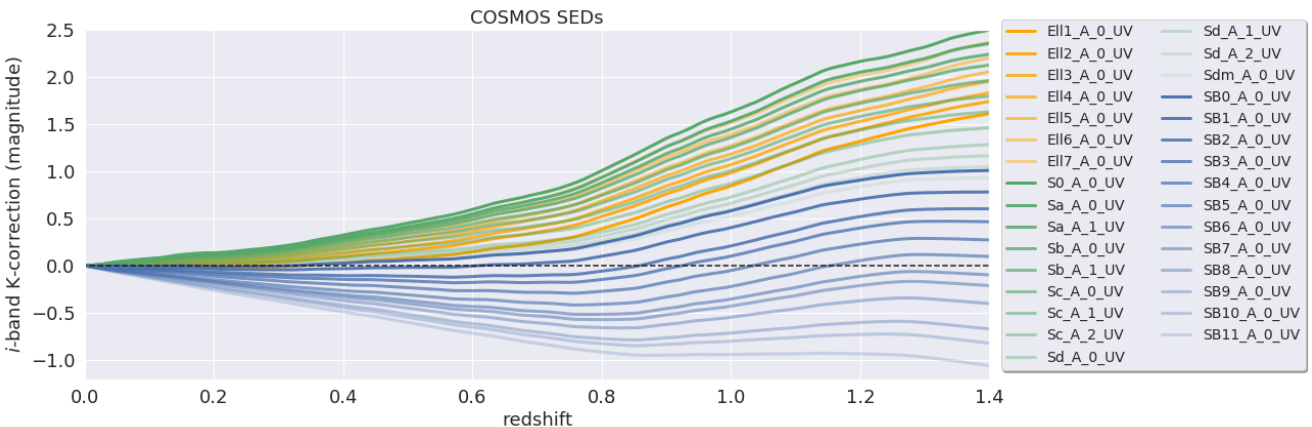


FIGURE 4.3: K-corrections as a function of redshift for the 31 SEDs that compose the COSMOS set of templates. The colors of the curves indicate morphological types: elliptical in yellow, disks in green, and starburst in blue. The dashed black line represents the zero level for reference.

¹http://www.cfht.hawaii.edu/~arnouts/LEPHARE/DOWNLOAD/lephare_doc.pdf

4.1.3 Absolute magnitudes

We compute the absolute magnitudes (M) based on the observed magnitudes (m , already corrected for galactic extinction), luminosity distance in Mpc (D_L), K-correction (K_{corr}), and extinction ($E(B - V)$), by the expression:

$$M = m - 5 \log_{10}(D_L) + 5 - K_{corr} - E(B - V), \quad (4.5)$$

where D_L is defined as:

$$D_L \equiv \sqrt{\frac{L}{4\pi F}}, \quad (4.6)$$

where L is the bolometric luminosity and F is the observed bolometric flux, two quantities we do not know. However, D_L can be determined from the redshift, by its relation to the comoving distance D_C :

$$D_L = (1 + z)D_C, \quad (4.7)$$

D_C depends on the cosmological parameters, as described by Hogg (1999):

$$D_C = \frac{c}{H_0} \int_0^z \frac{dz'}{\sqrt{\Omega_m(1+z)^3 + \Omega_k(1+z)^2 + \Omega_\Lambda}}, \quad (4.8)$$

where H_0 is the Hubble constant, the quantity that expresses the fundamental relation between distances and relative velocities due to the expansion of the Universe. Ω_m , Ω_k , and Ω_Λ represent the relative proportions of the matter (dark and baryonic), curvature, and dark energy, respectively. MICE mock catalog was created considering $H_0=70.0$ Km s⁻¹ Mpc⁻¹, $\Omega_m=0.25$, $\Omega_{Lambda}=0.75$.

When running LePhare on MICE, we set up for using the parameters accordingly. When working with DES data, we consider the cosmological parameters recently measured from the first-year data release, based on clustering and weak lensing probes (Abbott et al., 2017): $H_0=68.2$, $\Omega_m=0.301$, $\Omega_\Lambda = 0.699$. The differences in comoving distances or volumes computed using the two sets of parameters are negligible, as evident in Figure 4.4.

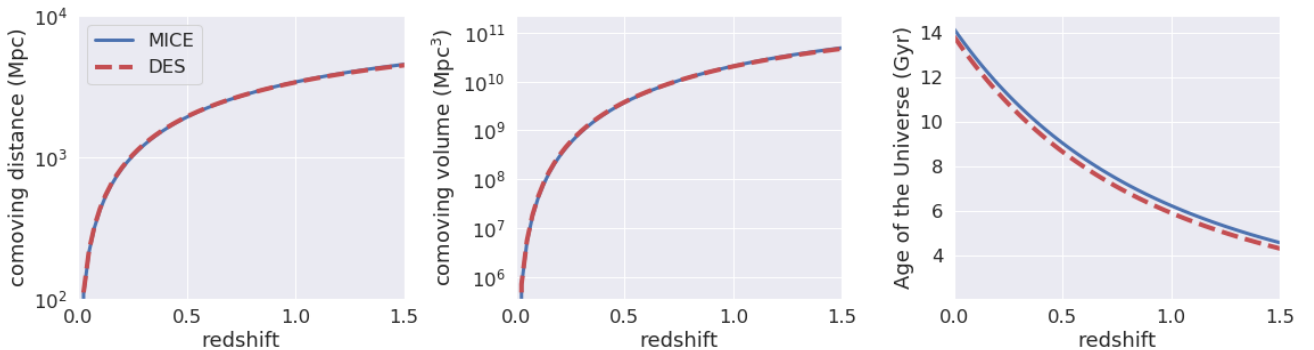


FIGURE 4.4: Comoving distance (left), comoving observed volume (middle), and age of the Universe (right) as a function of redshift considering two slightly different cosmologies, one used to create MICE simulations and the other measured by DES. The computed volumes take into account that DES only observed $\sim 1/8$ of the sky area.

To find the best fit template and then retrieve the appropriate value of K_{corr} from the theoretical library, LePhare compares the observed (F_{obs}) and templates (F_{temp}) fluxes by a standard χ^2 fitting:

$$\chi^2 = \sum_{i=1}^{N_{filters}} \left[\frac{F_{obs,i} - sF_{temp,i}}{\sigma_i} \right]^2, \quad (4.9)$$

where σ_i is the uncertainty in the F_{obs} for the i_{th} filter, and s is a normalization factor. According to Arnouts et al., 1999 "the template fluxes have been normalized to the observed ones by choosing the factor s that minimizes the χ^2 value ($\partial\chi^2/\partial s = 0$)":

$$s = \left(\sum_{j=1}^{N_{filters}} \left[\frac{F_{obs,j} F_{temp,j}}{\sigma_j^2} \right] \right) \left/ \sum_{i=j}^{N_{filters}} \left[\frac{F_{temp,j}^2}{\sigma_j^2} \right] \right. , \quad (4.10)$$

where j is the band used for the scaling, which can be different from i . This factor s is used to estimate the galaxy's stellar mass when using theoretical templates. The theoretical SEDs should provide the flux emitted per unit mass (in M_\odot), so the scale factor of the best fit solution can be interpreted as the stellar mass estimate. The other quantities, such as age, metallicity, and star formation history, are determined merely by the best fit SED. Each item in the SED grid represents a unique combination of these three parameters. Once the best fit template is determined, LePhare computes the absolute magnitude using one of the methods below:

- **Method 0:** direct measurement of m , literally as stated in Eq. 4.5. According to the authors, this method is likely to be less accurate for being very sensitive to K-correction and systematic effects in the apparent magnitudes.
- **Method 1:** similar to method 0, but using K_{corr} computed for another band. The band used is automatically chosen as the one which wavelength coverage (λ_U) the closest to the wavelength of the target band (λ_T), redshifted to the observer frame ($\lambda_U = (1+z)\lambda_T$). For instance, the absolute magnitude on the i band of a galaxy at $z = 0.2$ is computed using z -band's K_{corr} , like the following:

$$M_i = m_z - 5 \log_{10}(D_L) + 5 - K_{corr,z} - E(B-V) - (m_z^{temp} - m_i^{temp}) . \quad (4.11)$$

The term in parenthesis returns the calculation to the original i -band but using theoretical i and z magnitudes from the templates, instead of observed data. According to the authors, this method is the least template-dependent, therefore likely to be the most accurate. No wonder this is the method used by Ilbert et al., 2005.

- **Method 2:** similar to method 1, but it uses a fixed observed filter informed by the user as a reference, instead of choosing it automatically.
- **Method 3:** measured directly from the best-fit template fluxes applied in Eq. 4.5, without considering the observed magnitudes. This method is the most model-dependent among all the five methods.
- **Method 4:** similar to method 2, but it imposes the filter depending on the redshift. The filters and the valid redshift intervals should be informed in the configuration parameters.

In Section 4.2.1 we use MICE simulations to compare the results obtained from all the five methods explained above.

4.2 Tests with MICE simulations

Here we use MICE simulations to investigate various possibilities of estimating galaxy properties, to optimize the outcome when applying the same methodology to DES real data. The advantage of using MICE is to know, *a priori*, the quantities we are estimating. We adopt configuration parameters as close as possible to those used by the authors to build the simulated catalog. In the following tests we use the *valid* dataset defined in Section 3.1.4, which contains 10,000 objects randomly selected from the original catalog.

4.2.1 Absolute magnitude estimation

We run LePhare to compute the absolute magnitude using the methods listed above and compare the results with the actual values available in the simulated catalog. Regarding the method 2, where the band of reference is a choice of the user, we repeat the exercise for all filters. Nonetheless, for simplicity, we show only the results obtained with the J -band, which provides the best results among all bands. Regarding the method 4, where in addition to the bands of reference, the user is required to choose the respective redshift intervals, we adopted the $grizY$ DES bands. Hence, we adopted redshift intervals where the minimum wavelength (λ_{min}), covered by the filter transmission curve should match the 4,000 Å break

Redshift	band
0.00 - 0.35	g
0.35 - 0.69	r
0.69 - 1.06	i
1.06 - 1.32	z
1.32 - 1.40	Y

TABLE 4.2: Redshift intervals and the respective bands used in LePhare's method 4.

We start the analysis by plotting the difference between the estimated absolute magnitudes and the "true" value (ΔM), as a function of both the true value and the redshift in Figure 4.5. ΔM is analogous to the bias from photo-z analysis. In both cases, the method 1 shows the smallest dispersion. According to this figure, none of the five ways introduce significant biases in the absolute magnitude estimation. It is also evident that all methods perform slightly better for fainter absolute magnitudes.

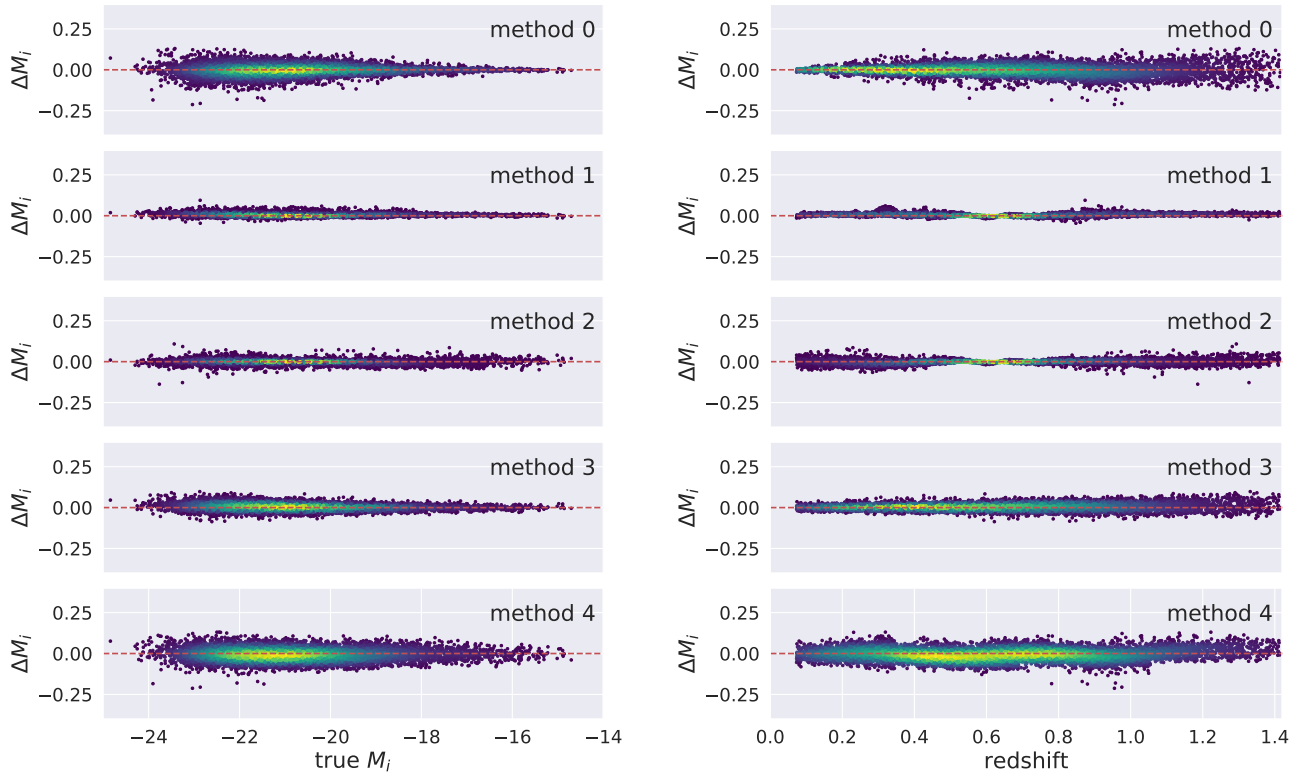


FIGURE 4.5: Absolute magnitude residuals for the five methods, in comparison to the true values of MICE simulations. On the left, ΔM as a function of true MAG. On the right, ΔM as a function of redshift.

From Figure 4.6, we realize that the dropout criteria is not the best choice. There is no overlap between our choices of redshift intervals and those from method 1, that selects the best filter automatically for reference. From this figure, we notice a small positive bias in method 1. We also observe the preference for the IR bands. This is not surprising since the method’s premise is to use a redder band, whose wavelength coverage is closer to the wavelength of the objects fluxes in their rest-frames. This procedure mitigates the uncertainties introduced by failures in K_{corr} determination.

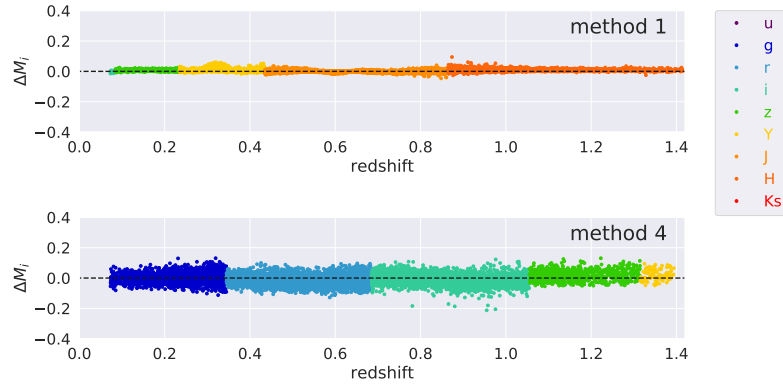


FIGURE 4.6: Absolute magnitude residuals for the methods 1 (top) and 4 (bottom), where the reference band depends on redshift. The points are colored according to the band used as reference to compute the absolute magnitude.

To quantify the results, we adapted the photo-z metrics used in the last chapter by simply exchanging Δz by ΔM . The results are displayed in Figure 4.7 and Table 4.3.

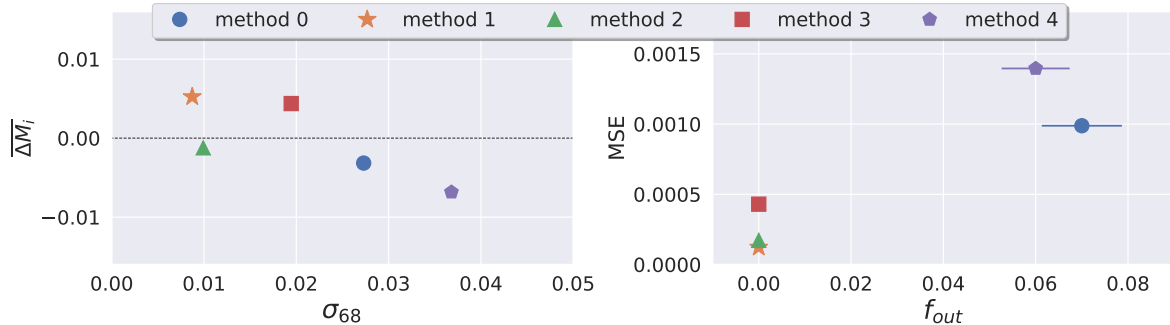


FIGURE 4.7: Quantitative comparison between the five methods to compute absolute magnitudes available in LePhare through quality metrics adapted from photo-z (same results as Table 4.3, here as a visual representation). Left: ΔM versus σ_{68} . Right: f_{out} versus MSE.

Method	ΔM	σ_{68}	f_{out} (%)	MSE
0	-0.0032 ± 0.0001	0.0273 ± 0.0001	0.07 ± 0.01	0.0010 ± 0.0000
1	0.0052 ± 0.0000	0.0087 ± 0.0000	0.00 ± 0.00	0.0001 ± 0.0000
2	-0.0012 ± 0.0000	0.0099 ± 0.0000	0.00 ± 0.00	0.0002 ± 0.0000
3	0.0044 ± 0.0001	0.0194 ± 0.0001	0.00 ± 0.00	0.0004 ± 0.0000
4	-0.0068 ± 0.0002	0.0368 ± 0.0001	0.06 ± 0.01	0.0014 ± 0.0000

TABLE 4.3: Absolute magnitude quality metrics (adapted from photo-z) for MICE *valid* set using the five methods available in LePhare.

From the metrics in Table 4.3, we confirm that method 1 is the best, except for the bias. Nevertheless, all methods introduce minimal systematic errors. We attribute the high quality of the results to the ability

to reproduce virtually the same conditions as used to create the simulations (same templates, extinction laws, and $E(B - V)$ intervals). This excellent quality of results is not expected when using real data.

Two reasons probably cause the encountered dispersion in ΔM . First, the difference in resolution of the template grid used to create the simulations is ten times larger than the one used in our test. Second and most likely, the intrinsic degeneracy in color-redshift space, which in some cases is impossible to remove, leads to almost identical values of χ^2 for different SEDs.

The variation of metrics with redshift displayed in Figure 4.8 confirms the superiority of method 1 over the others. Method 1 has the smallest scatter in all bins, especially in higher redshifts ($z > 0.9$).

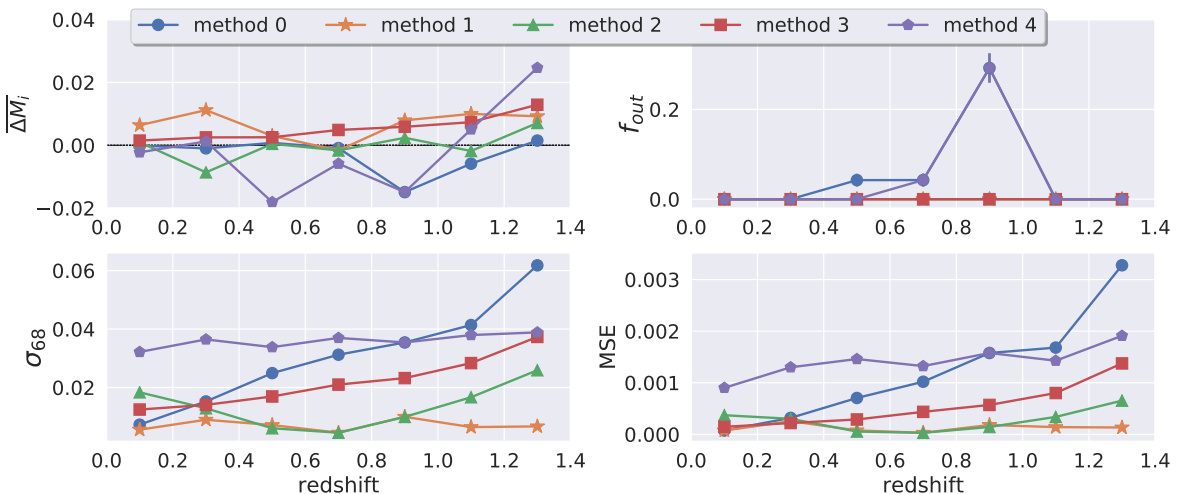


FIGURE 4.8: Absolute magnitude metrics as a function of redshift for the the five methods available in LePhare.

This first test serves as a proof of concept for the methodology of estimating absolute magnitudes using template fitting with fixed redshifts. It also helps to choose one method among the five available. Thus, we selected LePhare's method 1 to use in the next steps.

4.2.2 The impact of input data on absolute magnitude determination

In this section, we quantify the impact of possible choices for the input data on the estimation of absolute magnitudes. Using MICE *valid* subset, we run LePhare: i) with and without including other magnitudes; ii) with and without fixing the redshifts. At this stage, we have already decided not using LePhare photo-zs based on results presented in the previous chapter. Nevertheless, we repeat the exercise without fixing the redshift to confirm the strategy of setting redshifts and to measure the gain in the quality of the absolute magnitude estimation.

We start by looking at the residuals ΔM as a function of the true absolute magnitudes in Figure 4.9. The top left panel repeats the results shown in Figure 4.5 for method 1. The apparent improvement is due to the difference in the y-axis scale, here expanded to [-2,2] to allow the comparison with the results where LePhare is in charge of determining the redshifts, which are much more scattered.

Reducing the set of bands to *griz* increases the scatter, especially for the brightest objects ($MAG \lesssim -19$), but the dark color of the scattered points in top and middle right panels indicate that the number of outliers is not very large. The impact of not knowing the redshifts is very significant. The results in both bottom panels are considerably worse, especially for lower redshifts ($z < 0.5$).

The comparison between the three possible sources of redshift shows that the method of fixing a photo-z from another code is consistent with using the true-zs, and the LePhare results on calculating the absolute magnitudes can be significantly improved if the external photo-zs are more accurate than its own photo-z estimates. The middle right panel is the realistic scenario for DES Y3 Wide sample, where we use photo-z from DNF, and the filters available are only *griz*.

A similar diagnostic can be extracted from ΔM versus redshift (Figure 4.10). Comparing the top left and right panels, we see that the absence of UV and IR data causes an increase in scattering for intermediate and higher redshifts ($z \gtrsim 0.5$). The exchange of the true redshifts by the DNF photo-zs increase the scatter in all redshift range for *griz*, but the effect is mitigated, especially for $z > 0.6$, if using the extra bands. When letting the redshift free to be determined by LePhare fitting, we see the increase of catastrophic errors. LePhare fails drastically in both ends of the redshift range studied, even more, if not adding other bands.

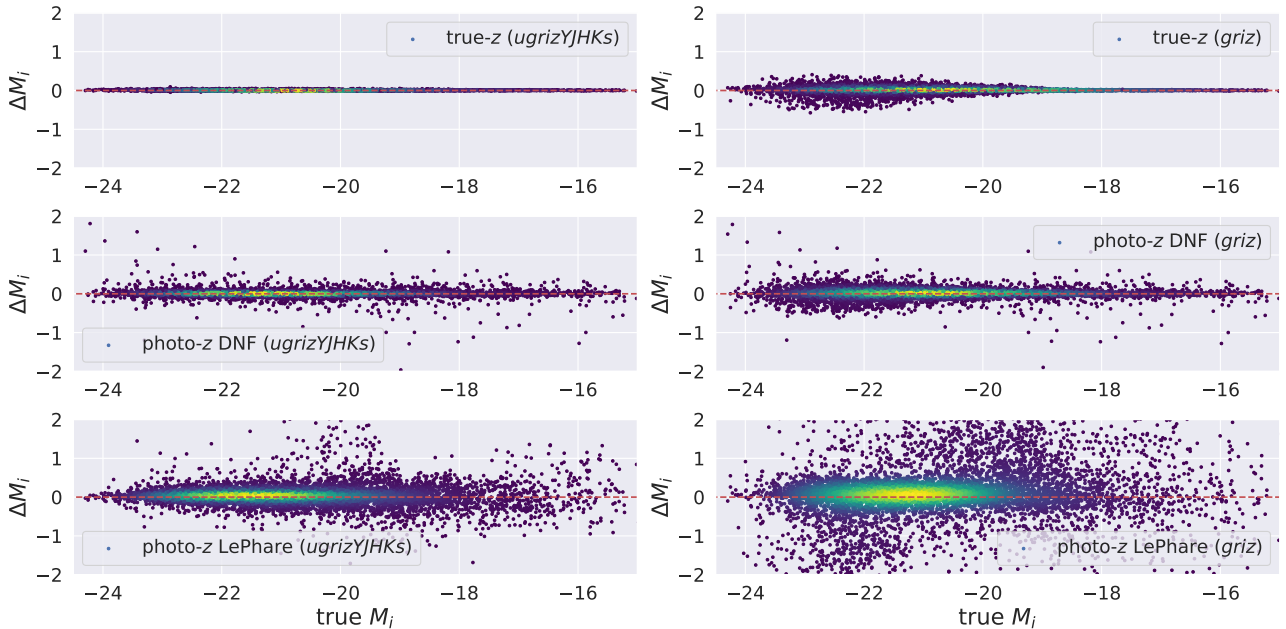


FIGURE 4.9: Absolute magnitude residuals versus true absolute magnitudes for the six variations addressed in this test. The top panels refer to results using true redshift as part of the input data. The middle panels refer to using photo-zs previously computed using DNF. The bottom panels are for letting the redshift as a free parameter to be determined by LePhare in the fitting process. The results obtained using all the bands available are on the left side; those using *griz* are on the right.

The thickness of the region occupied by points in the right middle panel of Figure 4.10 gives a rough idea of the absolute magnitude precision achieved with MICE if we simulate the complete methodology of computing photo-zs with DNF and fixing them into LePhare. This precision ($\Delta M \sim 0.01$) should limit the width of the absolute magnitude bin of the LF. As we show next, this precision is worse when dealing with real data, as expected, as a result of the propagation of the photometric errors.

The quantitative comparison is done in Table 4.4, and in Figures 4.11 and 4.12. In all cases, except for LePhare photo-zs with *griz*, the bias is minimal, indicating that the method does not introduce significant systematic errors on the absolute magnitude estimates, regardless of the origin of the redshift measurements. When LePhare is in charge of computing the photo-zs, the presence of extra bands in the input makes a big difference in increasing the quality of the absolute magnitude estimates. When the redshift is provided by another method and fixed into LePhare, these extra inputs are still helpful, but the improvement is modest.

Surprisingly enough, the results using DNF with extra bands are slightly better than those using the true redshifts, but using only *griz*. It suggests that a broader coverage of the wavelength spectrum is more important for the quality of the absolute magnitude measurements than the accuracy of the redshifts.

Regarding the results as a function of redshift (Figure 4.12), the extra bands are responsible for fixing the positive and negative biases in LePhare's results at $z \sim 0.5$ and $z \sim 1.1$ (top left panel), and

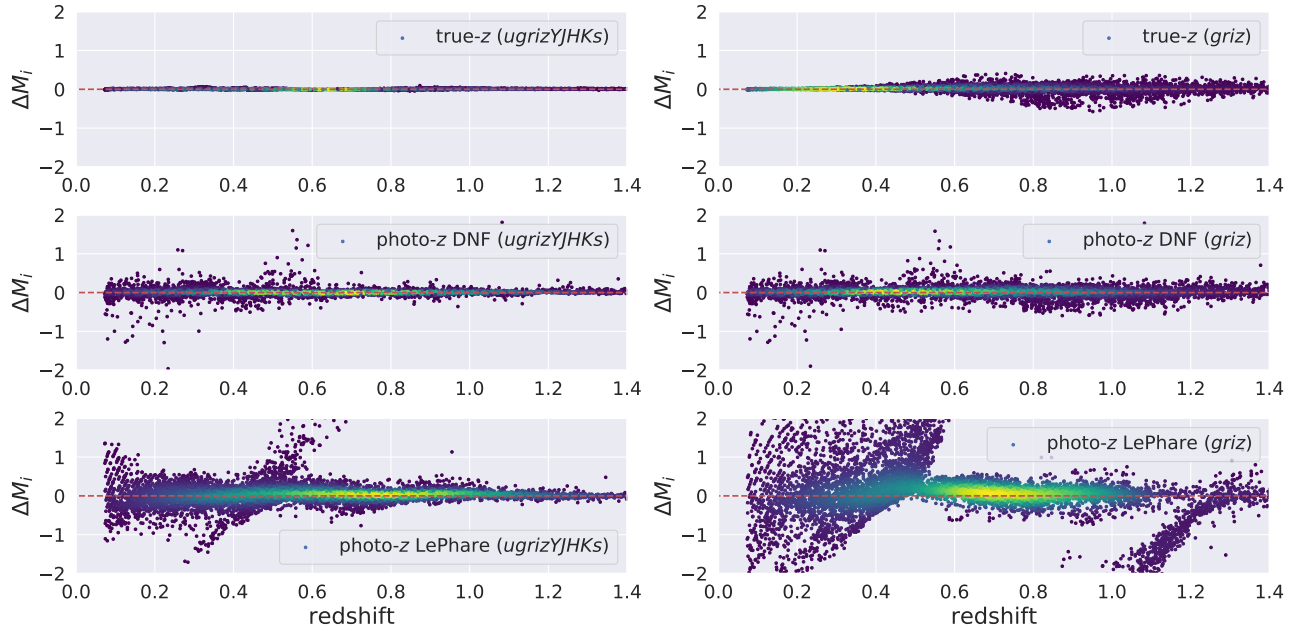


FIGURE 4.10: Absolute magnitude quality metrics (adapted from photo-z) for MICE *valid* set using different combinations of input data.

Redshift (bands used)	$\bar{\Delta M}$	σ_{68}	f_{out} (%)	MSE
true-z (ugrizYJHKs)	0.0052 ± 0.0000	0.0087 ± 0.0000	0.00 ± 0.00	0.0001 ± 0.0000
photo-z DNF (ugrizYJHKs)	0.0048 ± 0.0003	0.0369 ± 0.0002	4.17 ± 0.07	0.0087 ± 0.0005
photo-z LePhare (ugrizYJHKs)	0.0364 ± 0.0007	0.1407 ± 0.0005	30.56 ± 0.21	0.0661 ± 0.0006
true-z (griz)	0.0128 ± 0.0003	0.0430 ± 0.0001	5.43 ± 0.06	0.0060 ± 0.0001
photo-z DNF (griz)	0.0129 ± 0.0005	0.0717 ± 0.0003	11.61 ± 0.15	0.0156 ± 0.0005
photo-z LePhare (griz)	0.1768 ± 0.0028	0.3572 ± 0.0038	53.23 ± 0.17	0.7638 ± 0.0151

TABLE 4.4: Metrics for the samples tested using distinct inputs in LePhare to generate absolute magnitudes.

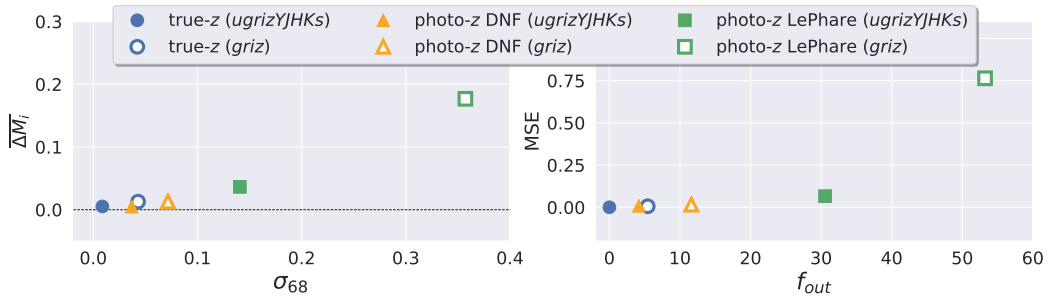


FIGURE 4.11: Quantitative comparison between the results obtained with the six combination of inputs studied (same results as Table 4.4, here as a visual representation). Left: $\bar{\Delta M}$ versus σ_{68} . Right: f_{out} versus MSE .

to reduce drastically the scatter (in both bottom panels). When the redshifts come from DNF, there is a non-negligible fraction of outliers in both ends of the redshift range studied (top right panel), which should be compensated when using photo-z PDFs.

From this section we learned that: i) using an external photo-z more accurate than LePhare's, improves the quality of absolute magnitude, as expected; ii) the methodology used above does not introduce significant systematic errors on the absolute magnitude; iii) the addition of extra bands improves the

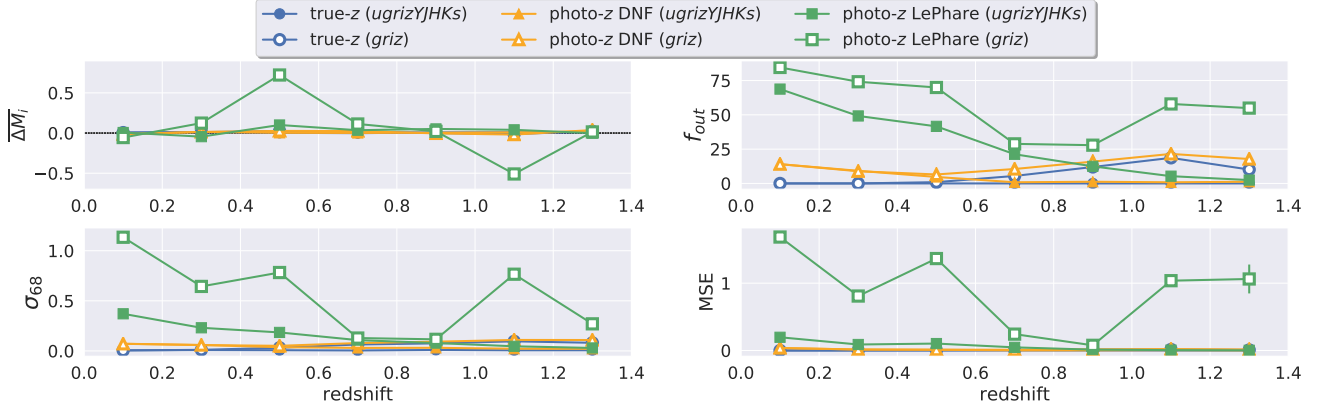


FIGURE 4.12: Absolute magnitude metrics as a function of redshift for the the six combination of inputs studied.

accuracy of absolute magnitudes, reducing the scatter of ΔM . It seems to be more important than the accuracy of the redshifts.

Summary of lessons learned with MICE

- The best method to estimate the absolute magnitude available in LePhare is the method 1. It uses the band closest to the object's SED peak in its rest frame as a reference band.
- The absolute magnitude is better determined when using a fixed external photo-z, which is more accurate than LePhare's.
- Adding extra bands improves the accuracy of absolute magnitudes. It seems to be more helpful than using true redshifts.

4.3 Exploring SED templates

In all the tests using MICE simulations, we used the COSMOS SEDs for the template fitting. These SEDs are, by definition, compatible with the simulated data set, as explained above. Even though we consider MICE being a fair representation of the real Universe at $0 < z < 1.4$, when dealing with real data the COSMOS SEDs may not be enough to describe it.

To establish benchmarks for the template-fitting results and understand their dependence on the template types, we explore their coverage in color-redshift space and the fitting performance depending on the SEDs. We start by plotting the color versus redshift for the data and the templates (Figure 4.13). The black points represent galaxies in the photometric sample. Here we use the representative *valid* sample defined in Section 3.1.4 for illustration. The colored lines show the evolution with redshift of theoretical colors given by the templates. Each line is a unique combination of a template, extinction law, and $E(B-V)$ value. As expected, all regions occupied by points are covered by at least one template, since the points were artificially derived from the curves in the simulations.

A similar diagnostic is done in the color-color diagrams in Figure 4.14. These figures show the tracks drawn by redshifting the template. No evolutionary changes in stellar populations are taken into account here. The left panel covers all the redshift range present in the data set ($0 < z < 1.4$) at once. From these figures, we notice a few outliers at the edges of the zone covered by the templates. These minimal differences come from: i) small fluctuations in magnitudes intentionally added in the simulation process to avoid identical clones in the sample; ii) these objects were originated based on one of the templates we choose to skip the interpolations and $E(B-V)$ extra values; or iii) both factors combined. Anyway, these

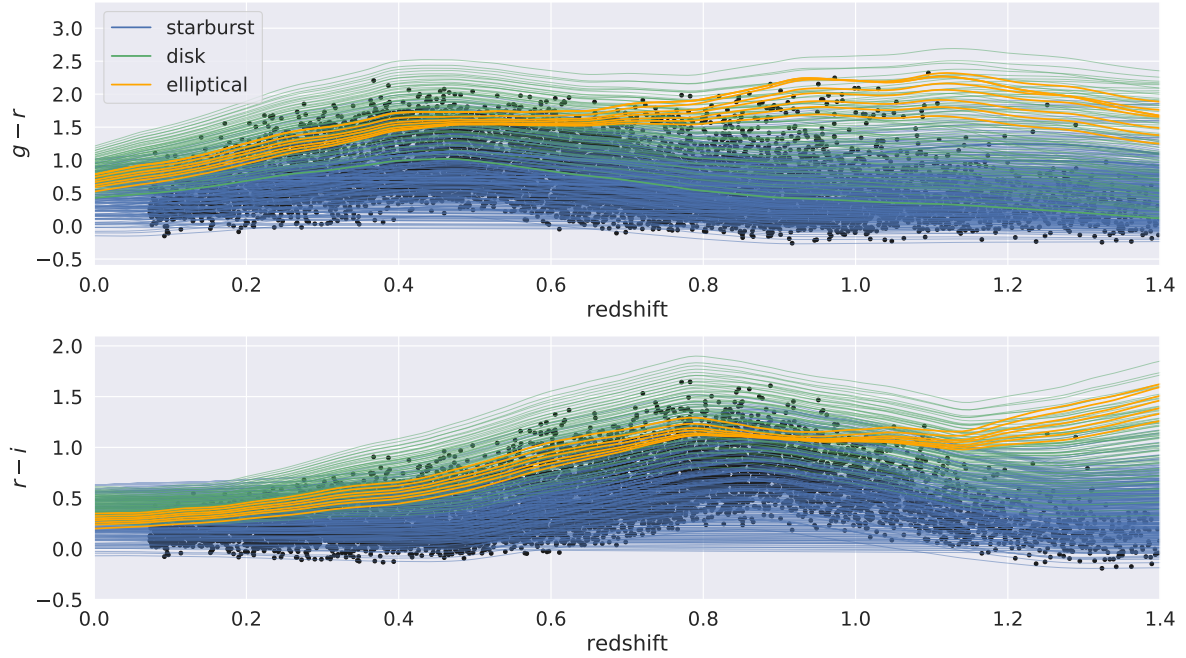


FIGURE 4.13: Template coverage of color-redshift space. Black points: apparent colors from MICE catalog. Coloured lines: theoretical colors obtained from the COSMOS SED templates. In blue: starburst galaxies; in green: disk galaxies; in yellow: elliptical galaxies.

diagrams serve as a validation of the compatibility between the downloaded templates and the data we selected to perform tests.

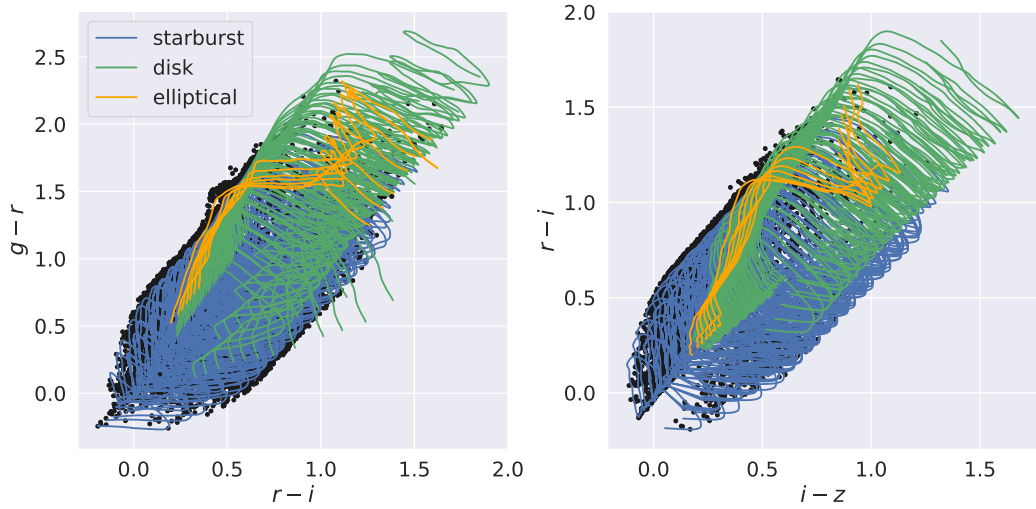


FIGURE 4.14: Template coverage of color-color space. Black points: apparent colors from MICE catalog. Coloured lines: theoretical colors obtained from the COSMOS SED templates. In blue: starburst galaxies; in green: disk galaxies; in yellow: elliptical galaxies.

The large predominance of blue lines in Figures 4.13 and 4.14 are the result of combinations of templates and extinction or $E(B - V)$ values for starburst templates. This unbalance in SED types in the final list of templates was a choice of the authors of the simulation, and we follow the prescriptions present in the article (Carretero et al., 2015) that describes the simulated data set.

Although elliptical galaxies are rarer in nature than disks and starbursts (Mo et al., 2010), we draw attention to the fact that the proportions of templates available for the fitting can introduce biases in

galaxy properties measurements, especially in regions of the color-redshift space where there is a large degeneracy between distinct templates. SEDs from different galaxy types might provide a similar χ^2 . Thus, the best fit template is probably one for the type with the largest number of SEDs available, and the sample is biased to have more galaxies classified as starburst galaxies than it has in reality. Later in the text, we discuss to what extent this template set is appropriate for real data and present viable alternatives.

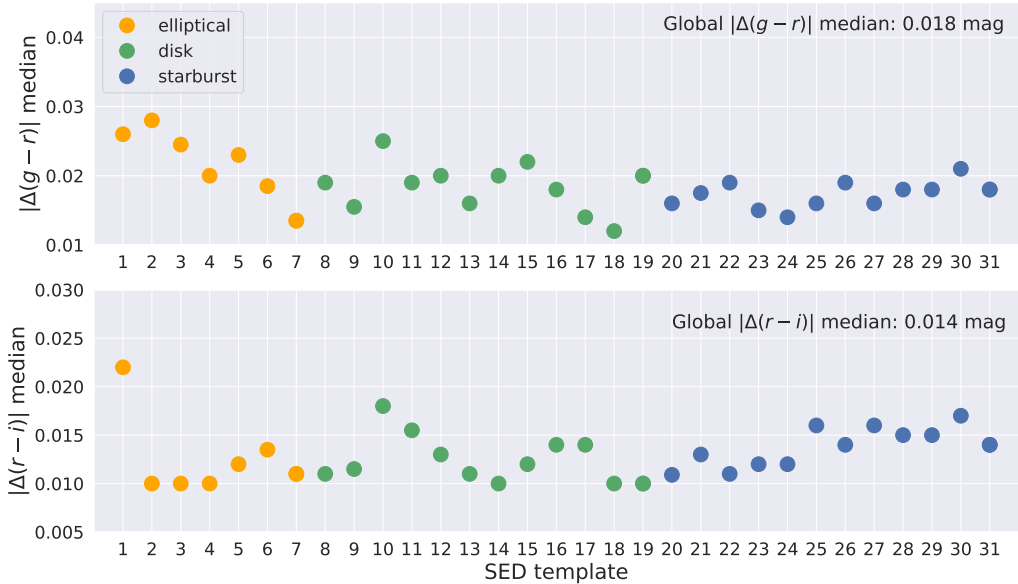


FIGURE 4.15: Median of the residuals for colors $g - r$ and $r - i$ by comparing the apparent colors from the catalog and the theoretical colors from the templates assigned to each individual galaxy.

Based on the results of Section 4.2.2, we analyze the success of the template fitting for each SED. We explore the realistic case for DES Wide data, i.e., the inputs are the $griz$ magnitudes, and the redshifts are estimated by DNF. Nevertheless, the results shown below are still optimistic due to the lack of magnitude errors. We compare the “observed” (mock) colors $g - r$ and $r - i$ with the theoretical counterparts obtained from the template of the best fit for each galaxy. Then, we compute the median for each group of galaxies assigned to the same SEDs (see Figure 4.15). The overall discrepancy in magnitudes is minimal (<0.02), with small fluctuations. All results are similar. There is no particular SED or morphological type to highlight for providing better or worse results.

Taking advantage of the simulated sample, we compare the absolute magnitude estimated by LePhare with the correct value available in the catalog (see Figure 4.16). The empty circles represent the results obtained using all the nine bands available and the true redshift from the simulations, for reference. This time, we notice a trend that is morphology-dependent: the elliptical galaxies tend to have their absolute magnitudes better estimated and the starburst worse, although the differences are not substantial. The most significant median of ΔM is for the starburst template 29 (SB9_A_0_UV.sed), which is below 0.06. For real data, we expect these values to be larger due to the propagation of the photometric errors.

Finally, we explore the effect of adding extinction to the templates for the creation of the library of theoretical magnitudes. As mentioned above, MICE apparent magnitudes were generated from the absolute ones, using the COSMOS templates applying extinction in the $E(B - V)$ interval of [0.00, 0.77], with step 0.01. We do the reverse exercise of recovering the absolute magnitudes starting from the apparent ones, but with a lower resolution in the set of templates ($E(B - V)$ ([0.0, 0.7], with step 0.1). The use of high values of $E(B - V)$ makes the blue templates to invade the locus of the red ones in the color-redshift and color-color diagrams, as seen in Figures 4.13 and 4.14. Note that the green lines go above the yellow ones. This behavior happens because there is no extinction applied to the elliptical

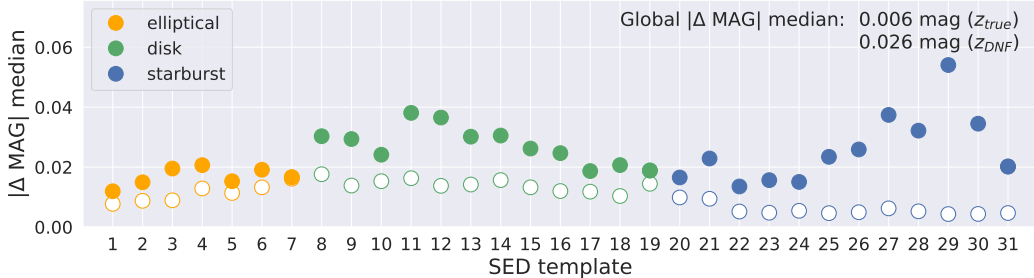


FIGURE 4.16: Median of the residuals for absolute magnitude by comparing the true value from the simulation and the LePhare’s estimates, binned by the best-fit templates assigned to each galaxy. The empty circles represent the results using all the nine bands available and the true redshift from the simulations.

templates. This effect is harmful to the template fitting accuracy because it increases the degeneration in the color-redshift space.

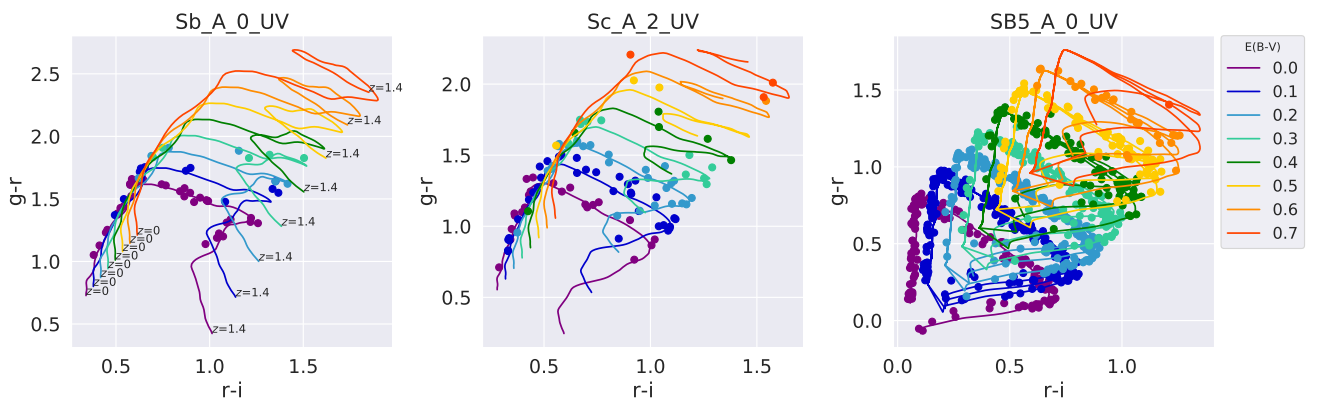


FIGURE 4.17: Three examples of SED tracks as a function of redshift and the respective galaxies assigned by the best fit, for the seven values of $E(B - V)$.

To illustrate the effect mentioned above, in Figure 4.17, we show the color-color diagram $g - r$ vs. $g - i$ for the objects assigned to the three templates: spiral Sb, spiral Sc, and a starburst SB5 (chosen randomly for illustration). The SED tracks as a function of redshift are plotted in colors, depending on the $E(B - V)$ value. The points assigned to each one of these combinations of templates and extinctions are colored accordingly. From the comparison among the three panels, we conclude that the “more late-type” the template, the larger the number of objects assigned to large values of $E(B - V)$.

In summary, using DES magnitudes and DNF photo-zs fixed into LePhare template fitting with COSMOS SEDs, we are able to reproduce MICE synthetic magnitudes within a median error of ~ 0.02 magnitudes for elliptical, ~ 0.04 for disk and ~ 0.05 for starbursts galaxies (spectral types).

The results shown above are obtained with LePhare, using the “perfect” mock magnitudes as input and using the same set of SED templates used to create them. Next, we study how the observational uncertainties affect the template fitting results and try to define an optimal template set to represent the real data. For this purpose, we use the DES Deep sample as a reference, due to its larger completeness in comparison to DES Wide. Differently from MICE, when using real data we consider flat Λ CDM with $\Omega_m = 0.301$, $\Omega_\Lambda = 0.699$ (Abbott et al., 2017), and $H_0 = 69.3 \text{ km s}^{-1}\text{Mpc}^{-1}$ (Abbott et al., 2018a), based on recent results on cosmology obtained by DES collaboration.

We start by attempting to reuse the same template set used on MICE: the COSMOS SEDs. Firstly, we repeat the check whether the templates are compatible to the data points by plotting the colors versus redshift (Figure 4.18) and color-color diagrams (Figure 4.19), as done for MICE in Figures 4.13 and 4.14.

The black points are a random selection of 10,000 objects from the pruned Deep sample. In color versus redshift plot, the data seems to be well covered by the templates, except for a few outliers in the reddest values of $g - r$.

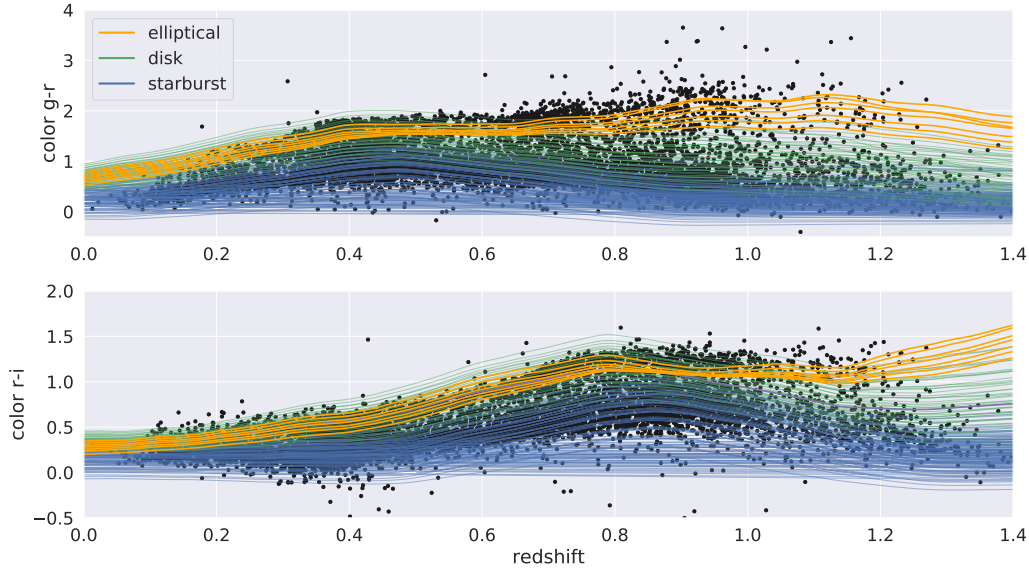


FIGURE 4.18: Template coverage of color-redshift space. Black points: apparent colors from DES Deep catalog. Coloured lines: theoretical colors obtained from the COSMOS SED templates. In blue: starburst galaxies; in green: disk galaxies; in yellow: elliptical galaxies.

The color-color diagram reveals a significant population of points at the margins of the region covered by the templates and a cloud of red outliers. We eyeballed these objects and confirmed they are real galaxies, mostly faint objects with large magnitude errors. The main reason for the scattering observed beyond the locus occupied by the templates is probably the large uncertainties in observed magnitudes. We show three examples in Figure 4.20. Images are retrieved using the *Target Viewer*² tool available on the DES Science Portal.

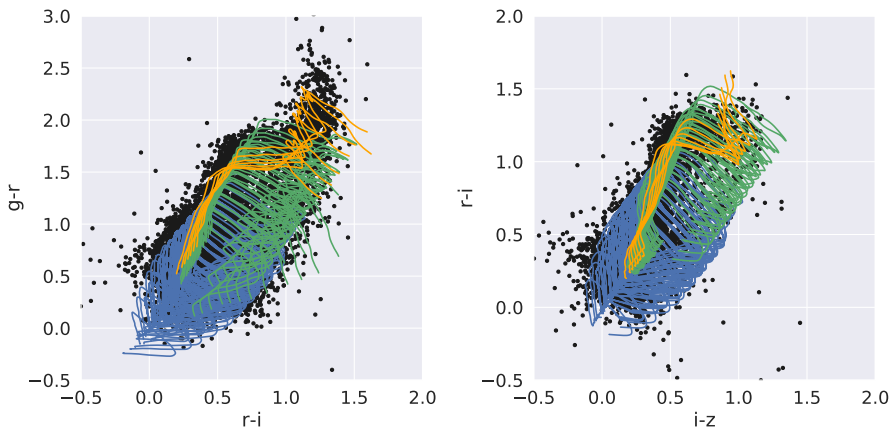


FIGURE 4.19: Template coverage of color-color space. Black points: apparent colors from DES Deep catalog. Coloured lines: theoretical colors obtained from the COSMOS SED templates. In blue: starburst galaxies; in green: disk galaxies; in yellow: elliptical galaxies.

²<https://desportal.cosmology.illinois.edu/target/>

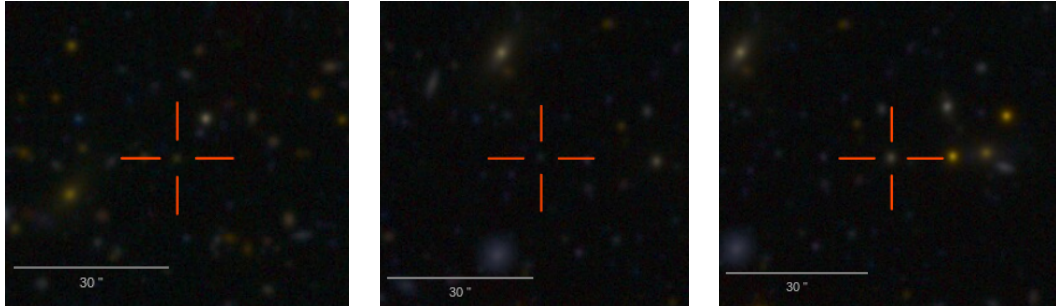


FIGURE 4.20: Visual inspection of typical outliers in color-redshift diagram. The five filters $griZY$ were used to compose the colored image. the individual contributions are represented by the colors: dark blue (g), light blue (r), green (i), yellow (z), and red (Y).

On an *ad hoc* basis, we added several theoretical templates to the main set, aiming to fill these gaps where there are objects without a correspondent template in color-color space. This choice is the result of a trial and error exercise selecting the new templates from libraries such as the BC03 models (Bruzual et al., 2003), M05 models (Maraston, 2005), the M09 models (Maraston et al., 2009), and the PEGASE2 models (Fioc et al., 1997).

To help with the decision, besides the visual inspection of the color-color diagrams, we also compare the global median of χ^2 value of the best fit for each galaxy and the median of the difference between observed and theoretical colors. These quantities are not a guarantee of the accuracy of the absolute magnitude estimations but are indicators of compatibility between the data and the template used to describe it. Unlike the simulated sample, here we do not have access to the true value of absolute magnitude to compare results. Therefore, these metrics were used just comparatively to help on the choice for the “best” template set. Nevertheless, none of the options explored was able to cover all the points on the diagram.

The final template list contains two additional groups. The first one has ten models of luminous red galaxies (LRG) from M09 to cover the reddest objects in $g - r$, varying ages from 1 to 12 Gyr, with no extinction applied. These templates were built based on composite stellar population models used to describe the massive red galaxies that can be the product of a history of one or more mergers, with several bursts of star formation during their lives. The models were improved based on the comparison to observations, leading to a recipe of including 3% of the stellar mass in old, metal-poor stars (see details in Maraston et al., 2009).

The second group is made up of five models of young simple stellar populations with Salpeter IMF, low metallicity ($[Z/H] = -1.35$), and “red morphology” from M05 models, varying ages from 0.025 to 0.2 Gyr. In this case, we apply the same extinction law as used for the bluest SEDs for MICE, based on their proximity in color-color space (see the final list of templates and extinction laws in Table 4.5).

The result of adding the new template is a modest improvement on the coverage of data points in color-redshift and color-color diagrams, although there are a few outliers remaining, as shown in Figures 4.21 and 4.22.

The updates of Figures 4.1 (SED templates flux versus wavelength) and 4.3 (K-correction as a function of redshift) including the new templates are shown in Figures 4.24 and 4.23. In Figure 4.24 one can notice the similarity between the LRG and elliptical templates, as well as the SSPs and starbursts. Based on the position of lines in Figure 4.21, after all, we interpret the addition of the new templates as an extrapolation in both directions, red and blue.

In Figure 4.25 we compare the observed colors with theoretical colors ($\Delta(g - r)$ and $\Delta(r - i)$) obtained from the best fit SED in both cases: using the original COSMOS SEDs and using our augmented set COSMOS + MARASTON SEDs. The introduction of the new SEDs and the subsequent redistribution of galaxies among the templates causes a mild decrease in the $\Delta(g - r)$, with no impact on $\Delta(r - i)$. This comparative analysis gives an impression of how well the set of templates is able to represent the

Hubble Type	COSMOS SED	N	Extinction Law
LRG	1 - 10	0	no extinction
Elliptical	11 - 7	0	no extinction
Disk	18 - 20	0	no extinction
Disk	21 - 29	1	Prevot $E(B - V) 0.2$
Starburst	30 - 33	1	Prevot $E(B - V) 0.2$
Starburst	34 - 41	2	Calzetti $E(B - V) 0.2$
Starburst	34 - 41	3	Calzetti bump1 $E(B - V) 0.2$
Starburst	34 - 41	4	Calzetti bump2 $E(B - V) 0.2$
SSP	42 - 46	4	Calzetti bump2 $E(B - V) 0.2$

Notes to the Table - No extinction was applied to LRGs, early-type, and bulge-dominant spiral SEDs. Late-type spirals and the “reddest” starbursts were given the *Prevot* law. The bluest starburst SEDs were repeated three times, varying the type of *Calzetti* extinction law. The SSP models are added only to the Calzetti bump2 law.

TABLE 4.5: COSMOS templates plus ancillary templates from LRG and SSP models.

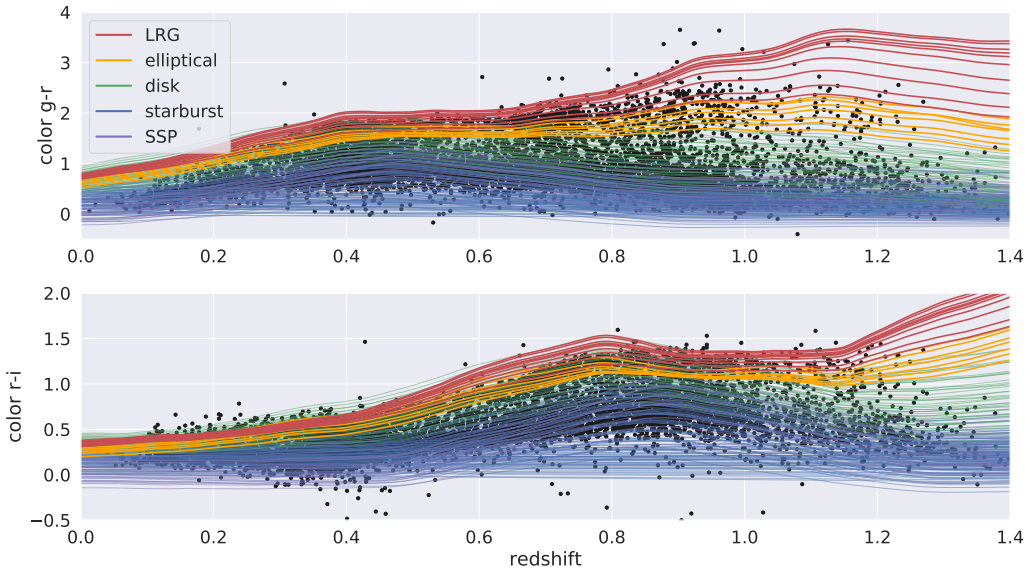


FIGURE 4.21: Template coverage of color-redshift space. Black points: apparent colors from DES Deep catalog. Colored lines: theoretical colors obtained from the COSMOS SED templates. In blue: starburst galaxies; in green: disk galaxies; in yellow: elliptical galaxies.

observed colors. Notwithstanding, a good agreement between observed and theoretical colors so not guarantee accuracy on the template fitting since distinct SED templates can derive similar colors, both fitting very well the same hypothetical object.

Comparing Figures 4.25 and 4.15, we observe the impact of the uncertainties in observed magnitudes on the ability to represent galaxy colors with theoretical colors from SED templates. The median $\Delta(g - r)$ and $\Delta(r - i)$ becomes ~ 6 times larger when using DES real data, compared with MICE objects.

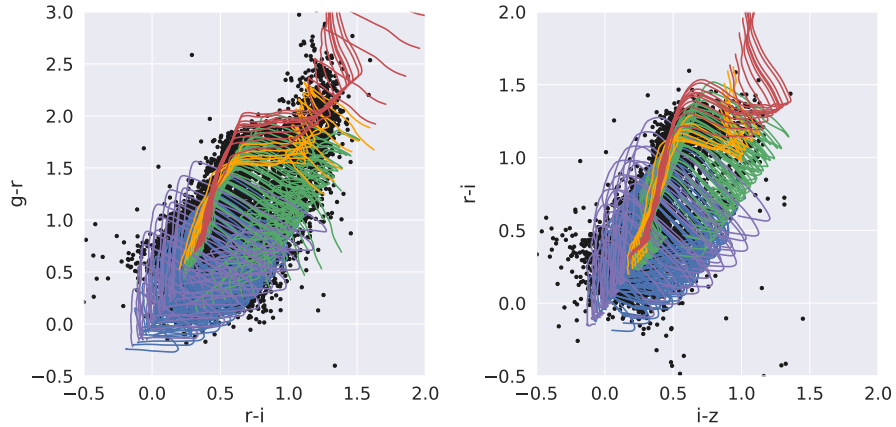


FIGURE 4.22: Template coverage of color-color space. Black points: apparent colors from DES Deep catalog. Colored lines: theoretical colors obtained from the COSMOS SED templates. In blue: starburst galaxies; in green: disk galaxies; in yellow: elliptical galaxies.

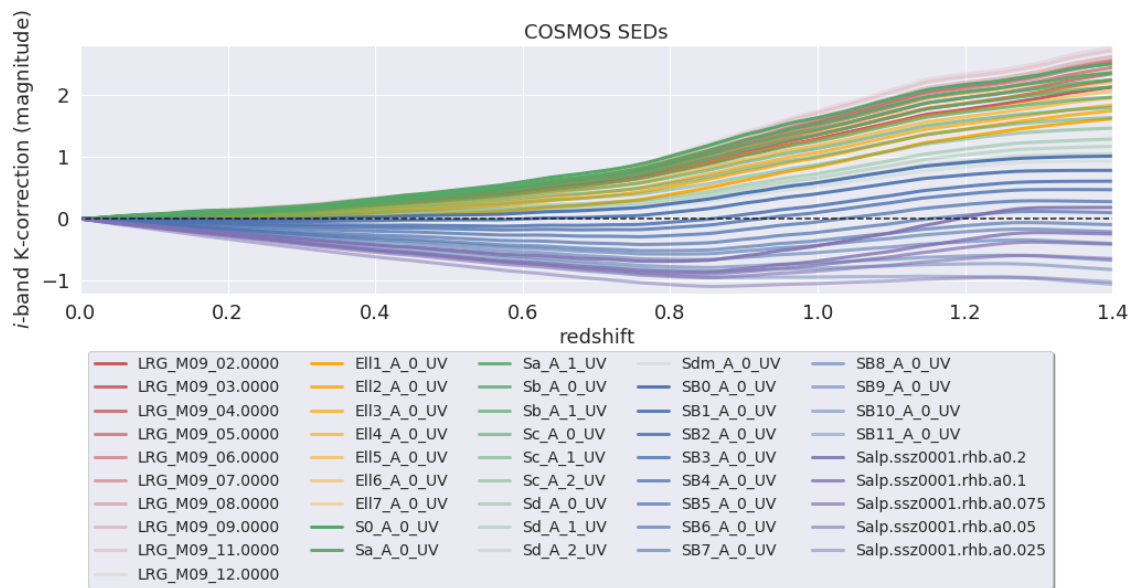


FIGURE 4.23: *K*-corrections as a function of redshift for the 46 SEDs that compose the COSMOS set of templates plus 15 ancillary synthetic templates from M05 and M09 models. The morphological or model type colors the curves: LRG in red, elliptical in yellow, disks in green, starburst in blue, and SSP in violet. The dashed black line represents the zero level for reference.

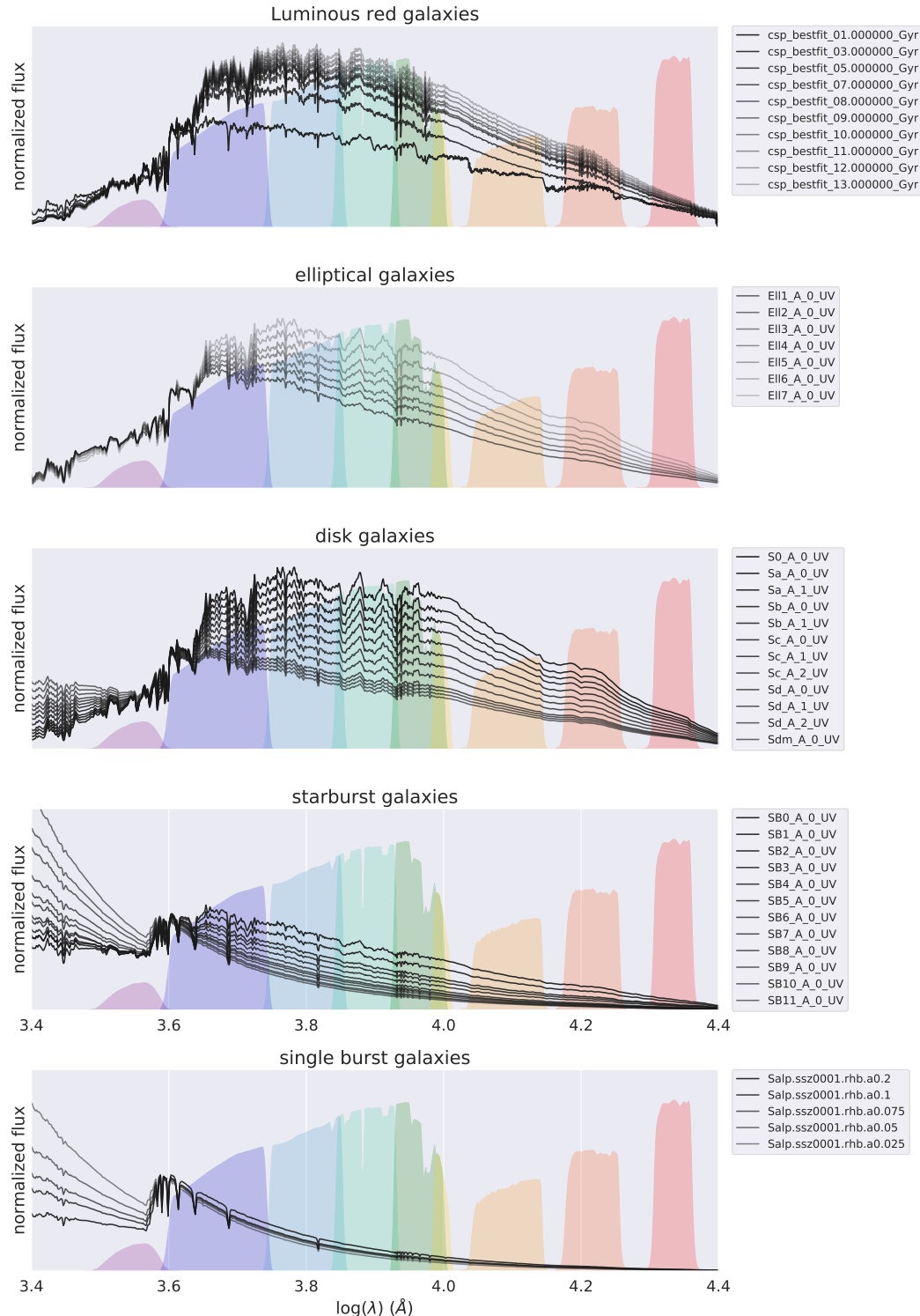


FIGURE 4.24: Top and bottom panels: new templates added to the COSMOS SEDs (three middle panels). The gradient in color intensity distinguishes individual SEDs. The filter transmission curves for the $ugrizYJKHs$ bands are plotted behind the SED curves.

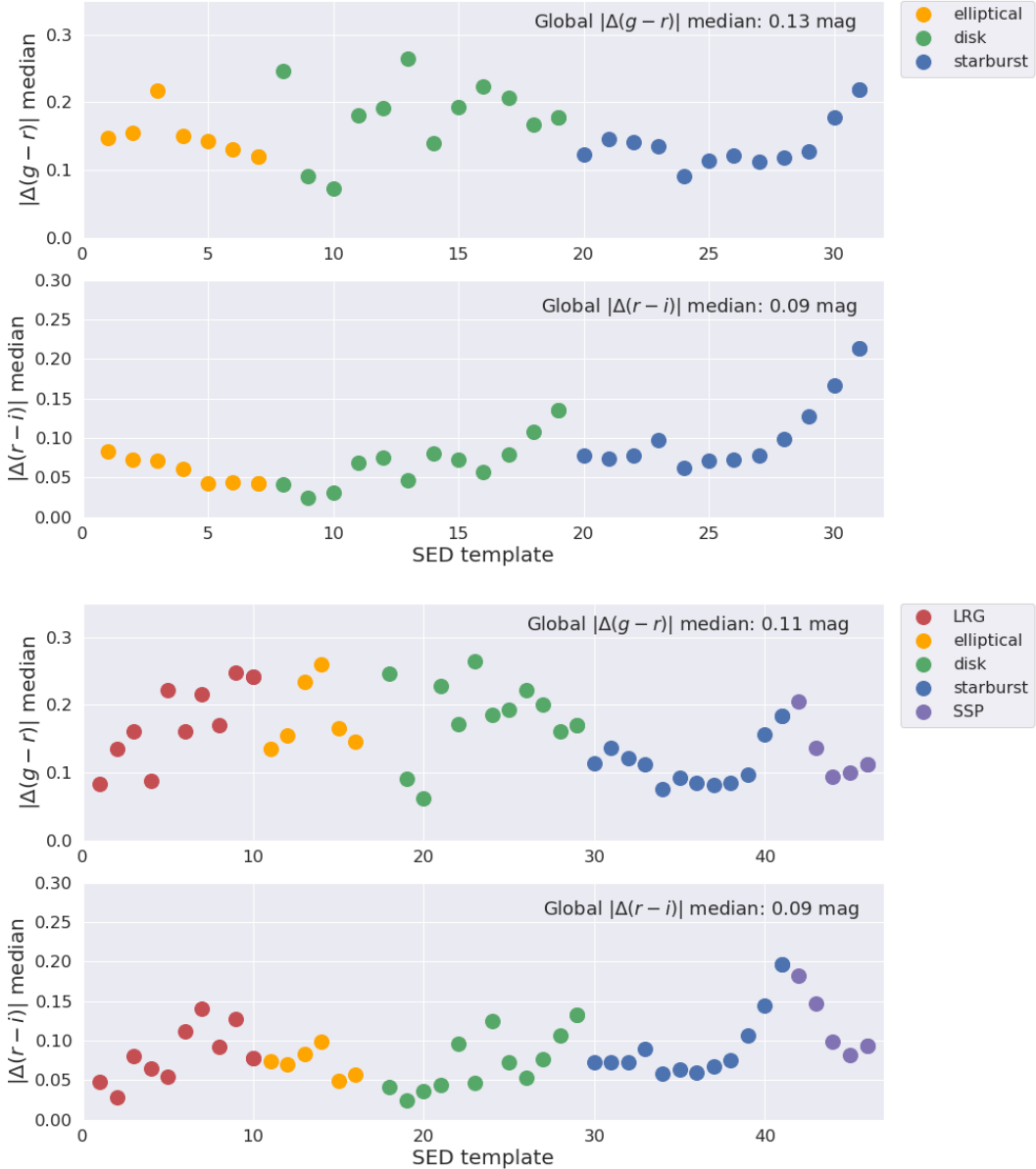


FIGURE 4.25: Median of the residuals for colors $g - r$ and $r - i$ by comparing the apparent observed colors from the catalog and the theoretical colors from the templates assigned to each individual galaxy. The two top panels refer to the case when using only COSMOS SEDs, and the two bottom panels the case when using all the 46 templates.

4.4 Absolute magnitudes of DES science sample

Finally, we run LePhare for the DES science sample using DNF photo-z fixed and applying the set of SED templates discussed above to obtain absolute magnitudes and K-corrections that will be used to estimate the LF in the next chapter. The resulting distributions of absolute magnitudes in $griz$ bands are presented in Figure 4.26. These magnitudes represent the estimates considering the single photo-z provided by DNF. As we discuss in the next chapter, the actual values of M that contributes to the LF estimates are derived several times for each galaxy, for each redshift bin of the photo-z PDF using the appropriate K-corrections provided by LePhare template library.

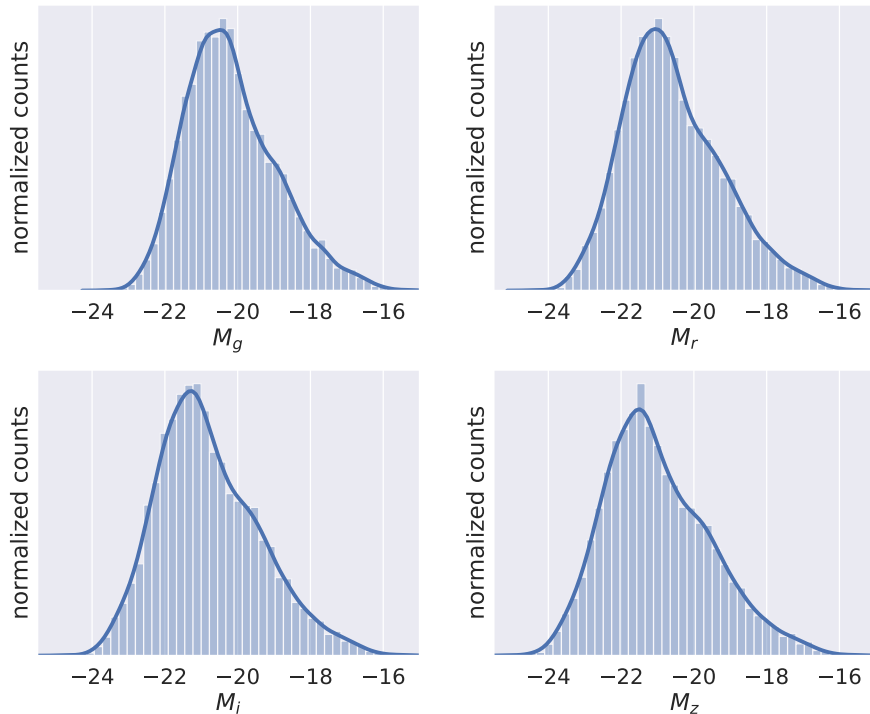


FIGURE 4.26: Absolute magnitude distributions for the $griz$ bands obtained with LePhare using the augmented SED template set (COSMOS + MARASTON SEDs).

Chapter 5

Galaxy luminosity function



Overview

In this chapter, we address the Luminosity Function, the primary statistical tool used to probe galaxy evolution in this work. We describe the methodology to adapt the $1/V_{max}$ method to include photo-z probability density functions. We perform tests with MICE simulations, using the lessons learned to get the best results with DES Y3 data. Also, we explore several sources of errors and define procedures to mitigate them. Finally, we present the analysis of DES Y3 LF for early and late-type galaxies classified based on morphology and its implications for galaxy evolution. We compare our results with recent findings from the literature and discuss possibilities of improvements for future work.

5.1 Luminosity Function

The Galaxy Luminosity Function, LF or $\Phi(L)$, measures the comoving number density of galaxies per interval of luminosity (or absolute magnitude) for a given sample of the observable Universe, and may be described by:

$$dN = \Phi(L) dL dV. \quad (5.1)$$

We are interested in quantifying the evolution of the LF over the cosmic time (represented by redshift), to trace the possible changes in number density and brightness of the galaxies since $z \sim 1.0$.

The LF is commonly parameterised by the Schechter function (Eq. 5.2, Schechter, 1976), a combination of two curves: an exponential with a rapid decrease at the bright-end, and a power-law at the faint-end, that meet in a central pair (ϕ^* , L^*). As a function of luminosity, LF can be expressed by:

$$\Phi(L)dL = \phi^* \left(\frac{L}{L^*} \right)^\alpha e^{-(L/L^*)} \frac{dL}{L^*}. \quad (5.2)$$

ϕ^* and L^* can be interpreted as characteristic values of normalization and luminosity that characterize a galaxy sample. The exponent α defines the slope of $\Phi(L)$ at the faint-end. The LF can be rewritten in terms of absolute magnitudes by assuming:

$$\Phi(M)dM = -\Phi(L)dL, \quad (5.3)$$

where the negative sign accounts for the increasing magnitude when decreasing in luminosity due to the logarithmic definition of magnitudes, which makes the relationship between L^* and the characteristic absolute magnitude M^* such that:

$$M - M^* = -2.5 \log \left(\frac{L}{L^*} \right). \quad (5.4)$$

Substituting Eqs. 5.3 and 5.4 into the Eq. 5.2 yields:

$$\Phi(M)dM = 0.4 \ln 10 \phi^* 10^{0.4(\alpha+1)(M-M^*)} e^{-10^{0.4(M-M^*)}} dM. \quad (5.5)$$

Some studies of the LF in the local Universe (e.g., Blanton et al., 2005b) show the evidence of a double function as a result of the presence of two underlying distinct galaxy populations. Thus, it would be necessary two pairs of constants $(\phi_1^*, \alpha_1), (\phi_2^*, \alpha_2)$, besides L^* or M^* to describe the LF, such that:

$$\Phi(L)dL = \left[\phi_1^* \left(\frac{L}{L^*} \right)^{\alpha_1} + \phi_2^* \left(\frac{L}{L^*} \right)^{\alpha_2} \right] e^{-(L/L^*)} \frac{dL}{L^*}, \quad (5.6)$$

or, analogously:

$$\Phi(M)dM = 0.4 \ln 10 \left[\left(\phi_1^* 10^{0.4(\alpha_1+1)(M-M^*)} \right) + \left(\phi_2^* 10^{0.4(\alpha_2+1)(M-M^*)} \right) \right] e^{-10^{0.4(M-M^*)}} dM. \quad (5.7)$$

The number density of galaxies, (ρ) , brighter than L can be estimated as:

$$\rho = \int_L^\infty \Phi(L)dL = \phi^* \int_{L/L^*}^\infty \left(\frac{L}{L^*} \right)^\alpha e^{-L/L^*} d \left(\frac{L}{L^*} \right) = \phi^* \Gamma(\alpha + 1, L/L^*), \quad (5.8)$$

where $\Gamma(\alpha + 1, L/L^*)$ is the incomplete Gamma¹ function, which diverges for $\alpha < -1$ as $L/L^* \rightarrow 0$. However, the luminosity density, (j) , of galaxies brighter than L is obtained by the expression:

$$j = \int_L^\infty L \Phi(L)dL = \phi^* \int_{L/L^*}^\infty \left(\frac{L}{L^*} \right)^{\alpha+1} e^{-L/L^*} d \left(\frac{L}{L^*} \right) = \phi^* L^* \Gamma(\alpha + 2, L/L^*), \quad (5.9)$$

converges for $\alpha > -2$. The total luminosity density is a useful quantity that represents the total amount of light emitted per unit volume, which can be related to contribution from luminous matter to the mass density of the Universe given a mass-to-light ratio. We compute j within the luminosity interval $[L_{low}, L_{up}]$, which varies according to the redshift bin and magnitude limit, as:

$$j = \phi^* L^* [\Gamma(\alpha + 2, L_{up}/L^*) - \Gamma(\alpha + 2, L_{low}/L^*)]. \quad (5.10)$$

j can be calculated in unit solar luminosity (L_\odot) by rewriting the Eq. 5.4 as:

$$\frac{L}{L_\odot} = 10^{0.4(M_\odot - M)}, \quad (5.11)$$

where $M_\odot = 4.52$ is the i -band absolute magnitude of the Sun² (to be substituted in Eq. 5.10).

LFs have been quantified over decades, almost for every existent extensive extragalactic survey. This relatively simple and handy tool remains popular in the astronomical community, although it still imposes challenges to its measure due to biases introduced by observational limitations (e.g., Johnston, 2011). Instead of merely counting galaxies in magnitude bins, to take the observational uncertainties into account, there are many LF estimators available in the literature. They may be: parametric (e.g., the maximum likelihood estimator (Sandage et al., 1979), and the step-wise maximum likelihood estimator (STY) (Efstathiou et al., 1988)); or non-parametric methods (e.g., the $1/V_{max}$ method (Schmidt, 1968), the ϕ/Φ method Turner (1979), and the C^- method (Lynden-Bell, 1971)). All methods present advantages and disadvantages.

For this work, we choose to use the traditional non-parametric method $1/V_{max}$. One weakness of the $1/V_{max}$ method is that it assumes spatial homogeneity of the sample, so it is sensitive to the cosmic variance fluctuations due to large scale structures. This issue should not invalidate our results because

¹ $\Gamma(a, b) = \int_{L_{lim}}^\infty t^{(a-1)} e^{-b} dt$

²<http://mips.as.arizona.edu/~cnaw/sun.html>

we are estimating the LF in large volumes. On the other hand, Blanton et al. (2003) discussed the artificial number density evolution caused by galaxies changing their magnitude bins due to a small luminosity evolution inside the same redshift bin. This effect can be significant at the bright end, where there are fewer objects, so the magnitude bin change of a few objects would produce a significant error. The method $1/V_{max}$ has the advantage of having a relatively simple implementation. Besides, as a non-parametric method, it does not require any assumption of the LF shape *a priori*, and its result provides the normalization without the necessity of an extra calculation.

Willmer et al. (2006) demonstrated that the $1/V_{max}$ method provides a more robust estimate of Schechter parameters than STY using a sample of galaxies from DEEP2. They showed that the Schechter parameters are less sensitive to changes in the fainter magnitude limit when using the $1/V_{max}$ method than if using the STY method. Moreover, Faber et al. (2007) obtained virtually the same results using both ways.

The $1/V_{max}$ estimator revisited

The $1/V_{max}$ method derives from the V/V_{max} completeness estimator, a simple way to detect the presence of Malmquist Bias or number density evolution in a galaxy sample. This estimator relies on the assumption of spatial homogeneity. V is the volume of the sphere delimited by the distance to a given galaxy, and V_{max} is the volume at the maximum distance the same galaxy would be observable, given its intrinsic luminosity and the instrumental limitations.

As we compute V/V_{max} for the galaxies, some will be close to their V_{max} limit ($V/V_{max} \rightarrow 1$), others will be far from it ($V/V_{max} \rightarrow 0$). If there is spatial homogeneity, the V/V_{max} ratio is expected to be uniformly distributed between 0 and 1, so the overall average is 1/2. An observed deviation from this value can be interpreted as evidence of sample incompleteness, or else, as an indication of number density evolution. If $V/V_{max} > 1/2$, the probability to find a galaxy closer to its V_{max} limit is larger than the chance to find a galaxy far from its limit. It means that comparing densities along the line of sight, galaxies were more numerous in the past than in the present. In the LF estimator, the factor $1/V_{max}$ works like a weight applied to the number counts to compensate for the galaxies that are missed by the observations because they are beyond the V_{max} limit determined by their apparent magnitude and the magnitude limit of the survey.

The number density in a given absolute magnitude bin centered at M is given by:

$$\Phi(M) = \sum_{j=1}^N \frac{1}{V_{max,j}}, \quad (5.12)$$

and the Poisson fluctuations are computed as the RMS on each absolute magnitude bin as:

$$\sigma(M) = \left[\sum_{j=1}^N \frac{1}{V_{max,j}}^2 \right]^{1/2}, \quad (5.13)$$

where V_{max} is the spherical comoving volume delimited by the comoving distance, $D_{c,max}$ (Hogg, 1999), in which the galaxy would be detected by the survey, given the galaxy's intrinsic luminosity and the survey's magnitude limit. $D_{c,max}$ is given by:

$$D_{c,max} = \frac{c}{H_0} \int_0^{z_{max}} \frac{dz'}{\Omega_m(1+z)^3 + \Omega_k(1+z)^2 + \Omega_\Lambda}, \quad (5.14)$$

where Ω_m , Ω_k , and Ω_Λ are the cosmological density parameters for matter, curvature and dark energy, respectively. As we assume a flat Λ CDM model, the comoving volume is:

$$V_{max} = \frac{4\pi}{3} (D_{c,min}^3 - D_{c,max}^3) area_{frac}, \quad (5.15)$$

where $area_{frac}$ is the fraction of the sky area effectively observed. We estimate this factor based on the detection fraction HEALPix map (see Section 2.1.1 for details).

To solve the integral in Eq. 5.14, one needs to determine the limits z_{min} , the lower limit of the redshift bin where estimate the LF, and z_{max} , specified for each galaxy at the redshift where distance d is d_{max} . If a galaxy is bright enough to be detectable at any distance within a redshift bin, z_{max} assumes the value of the bin's redshift upper limit. Otherwise, the algorithm scans the redshift bin of width Δz (in most cases we use $\Delta z=0.2$), in small steps of dz (usually $dz=0.02$), and compare the supposed apparent magnitude of the galaxy at each step with the magnitude limit of the survey (Eq. 5.16), until reaching the point at which the galaxy becomes faint enough not to be detected anymore.

$$m_{step} = M + 25 + 5 \log_{10}(D_L) + K_{corr}, \quad (5.16)$$

where D_L is the luminosity distance and K_{corr} is the K-correction. As K_{corr} varies with galaxy's SED and z , for each step, we get K_{corr} value from LePhare's library of theoretical magnitudes. Hence, we set $dz=0.02$ for compatibility with the results presented in the last chapter.

As stressed by Blanton et al. (2005b) about SDSS, our DES sample also suffer from surface brightness (μ) selection effects. As with any photometric catalog, the DES Y3 data set has intrinsic incompleteness related to instrumental and observational limitations. DES collaboration created a solution to correct this problem. The Balrog simulation (Suchyta et al., 2016, see details in Section 2.1.2) consists of artificially injecting objects from more in-depth images in real standard DES images, then repeat the source detection and quantify the rate of successful detection of inserted objects in the augmented image. As described in Section 2.1.1, when defining the science sample, we removed regions where the average magnitude limit is brighter than 23.5. Consequently, the correction factor is, on average, small because areas drastically affected by incompleteness were excluded from the analysis.

We include the completeness correction in the $1/V_{max}$ formula as proposed by Fried et al. (2001), and followed by other authors (e.g., Wolf et al., 2003; Baldry et al., 2012; Capozzi et al., 2017) as an additional weight in combination with V_{max} (Eq. 5.17). The correction factor $C(m, \mu)$ is calculated simultaneously as a function of magnitude and surface brightness, as a 2-dimensional selection function estimated from the fraction of successful detection in Balrog (see Figure 5.1). The number density in a given absolute magnitude bin centered at M , and corrected by the completeness factor $C(m, \mu)$, is given by:

$$\Phi(M) = \sum_{j=1}^N \frac{1}{C_j(m, \mu) V_{max,j}}. \quad (5.17)$$

Finally, our last adaptation of the traditional $1/V_{max}$ method is the introduction of the photo-z PDF. As the photo-z uncertainties are substantial when using only *griz* bands to estimate them, as shown in Figure 3.43, one galaxy can have a non-zero probability to be assigned to several dz bins, including dz bins that belong to different large Δz redshifts bins. Hence, the same galaxy may contribute to different bins of LF, as we compute them separately for each Δz interval. We include this uncertainty in the LF estimation by adding the same galaxy in the $1/V_{max}$ sum several times, weighted by its $P(z)$ value at each dz bin. Therefore, operationally, we also must ensure that DNF provides PDFs compatible with the same dz width as LePhare does for the K_{corr} library.

The final expression for the LF estimator computed for every center of absolute magnitude bin, with edges M_1 and M_2 becomes:

$$\Phi\left(\frac{M_1 + M_2}{2}\right) = \int_{M_1}^{M_2} \Phi(M) dM = \sum_{j=1}^N \frac{1}{P_j(z) C_j(m, \mu) V_{max,j}}. \quad (5.18)$$

One crucial aspect to take into account is the absolute magnitude domain where the LF is valid for a given flux-limited sample. It is well established that the faint-end is populated by numerous and faint dwarf galaxies and suffers from selection effects related to the depth of the observations (e.g., Blanton et al., 2005b; Loveday et al., 2012). On the other hand, the bright-end populated by rare luminous galaxies,

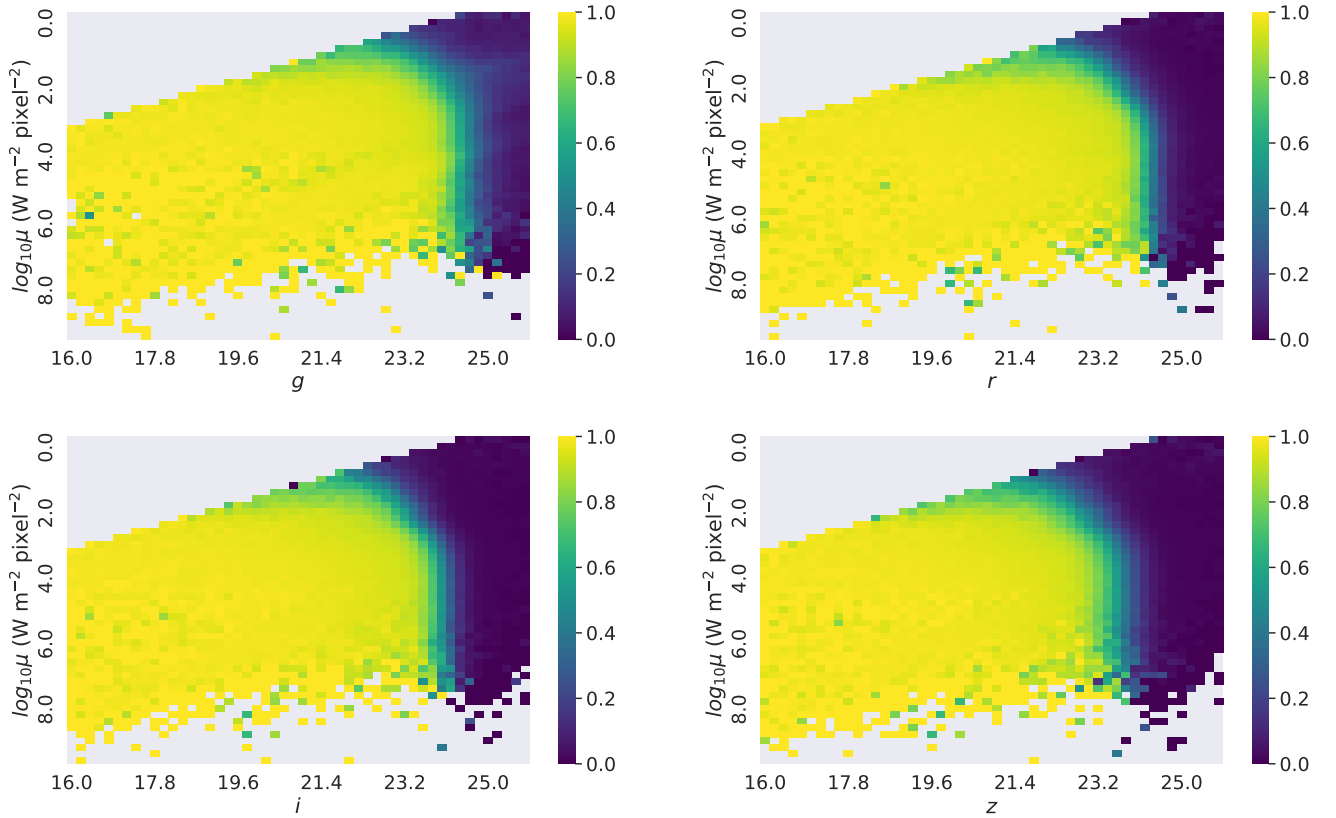


FIGURE 5.1: Completeness factor $C(m, \mu)$ represented by the color map as a function of $griz$ apparent magnitude and surface brightness. The surface brightness is computed in logarithmic scale in unit $\text{W m}^{-2} \text{pixel}^{-2}$, as detailed in Chapter 2.

suffer from selection effects related to cosmic variance and contamination by quasars and AGNs. Apart from these two obvious considerations, to define the absolute limits proper for the analysis of our sample at each redshift interval, it is necessary to consider the intrinsic bias present in the global LF. This happens because not all galaxy types are visible in the same absolute magnitude intervals due to their different K-corrections. Ilbert et al. (2004) demonstrated that this effect is more significant when the filter used to compute the LF is far from the rest-frame filter in which galaxies are selected. Positive K_{corr} push red galaxies outside the volume boundaries defined by the magnitude limit, while negative K_{corr} pull the blue galaxies inside the observable volume, making the number counts to be overestimated for blue and underestimated for red galaxies.

A way to bypass this problem is to define a valid absolute magnitude range where all galaxy types are visible for a given redshift, paying the price of throwing away a considerable part of the data. When plotting the LF in the following figures, we let explicit this limit with a vertical dashed line. It marks the maximum value of absolute magnitude where the results are trustworthy, and the points can be used to fit a Schechter function.

We estimate the absolute magnitude limits as a function of redshift based on the i -band apparent magnitude limit ($i < 23.5$). The maximum possible value of K_{corr} is given by the SED templates as a function of redshift (see Figures 4.3 and 4.23 in Chapter 4), considering the upper value of redshift bins studied. The results are displayed in Figure 5.2.

Dealing with cosmic variance

Due to the existence of large scale structures, observational estimates of number density, and related quantities (as the LF) are affected by cosmic variance, the position-dependent variation in number density

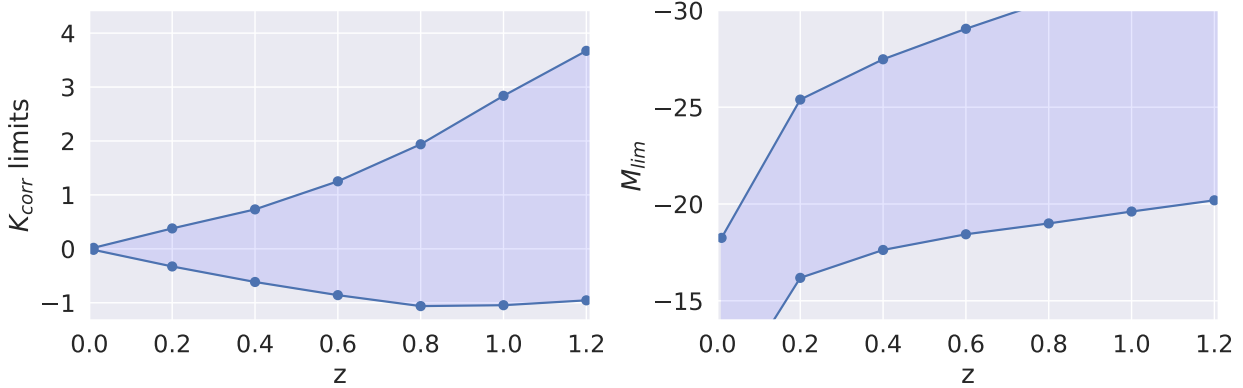


FIGURE 5.2: Left: upper and lower limits of K-corrections. Right: upper and lower limits of absolute magnitude for LF analysis. Both plots are in function of redshift (z).

beyond Poisson fluctuations (Somerville et al., 2004). As pointed by Faber et al. (2007), the cosmic variance impact on the LF is more important for red galaxies, due to their higher degree of clustering compared to the blue population. A common strategy adopted by pencil-beam surveys to minimize the cosmic variance effects is to point the telescope to multiple sightlines (Somerville et al., 2004).

Since DES observes a large cosmic volume, in comparison to the observed clustering scale of galaxies, the cosmic variance should not be a dominant source of uncertainties. Considering the total volume in our science sample, the relative cosmic variance σ_v^2 is virtually zero. However, as we split the sample in redshift bins to study the LF evolution, σ_v^2 can be small, but non-negligible especially at the first redshift bin, where the comoving volume observed is smaller. Therefore, we incorporate the contribution of cosmic variance to the LF error budget by estimating the LF for several small areas and calculating the variance of the collective LF results. This strategy was also motivated by parallel computing using the *embarrassingly parallel workload* approach (Foster, 1995), which was not only useful but also necessary to handle DES data.

We adopted patches of the sky delimited by HEALPix pixels of $NSide = 32$, which is equivalent to $\sim 3.4 \text{ deg}^2$. For this area, the cosmic volume probed in the first redshift bin ($0 < z < 0.2$) is about $2 \times 10^5 \text{ Mpc}^3$, which leads to a cosmic variance of $\approx 30\%$ for each pixel. As an example, we show in Figure 5.3 the results of the LF in the first redshift bin for one single pixel of $NSide = 32$, for MICE on the left, and for DES on the right. For DES, it is also plotted the LF of early and late-type galaxy populations in red and blue colors, respectively. The error bars refer to Poisson errors, and the vertical dashed line refers to a rough estimation of the average absolute magnitude limit considering the faintest apparent magnitude of the sample and the upper limit of the redshift bin. A fit to a double Schechter function is displayed for visual check and comparison among other bins.

The final Schechter parameters are obtained after the combination of the partial results from all pixels. On the top panel of Figure 5.4, we show the result for all individual pixels plotted together as thin lines. The consolidated LF is the mean of $\Phi(M)$ for each M bin, and the error attributed to cosmic variance is the standard deviation of Φ mean. Although the median is often a more robust measurement than the mean, in this case, the median is problematic for the bright-end, where galaxies are rare. The presence of many pixels empty of very bright galaxies sets the median to zero. In the middle panel of Figure 5.4, we inform the number of pixels that contributed to the mean. For the faint end, we apply a 3σ clipping before computing the Φ mean, to avoid the contribution of pixels severely affected by incompleteness. For the bright-end, we do not apply any cut. Otherwise, the empty pixels would not contribute to the effective area, artificially pushing the Φ mean to higher values, as the volume would be underestimated. For MICE SMALL sample, the total number of pixels (regions) is 44, and the sample does not suffer from incompleteness. The same is not necessarily true for DES real data.

Once calculated, the mean values of $\Phi(M)$, the Poisson, and cosmic variance contributions to the

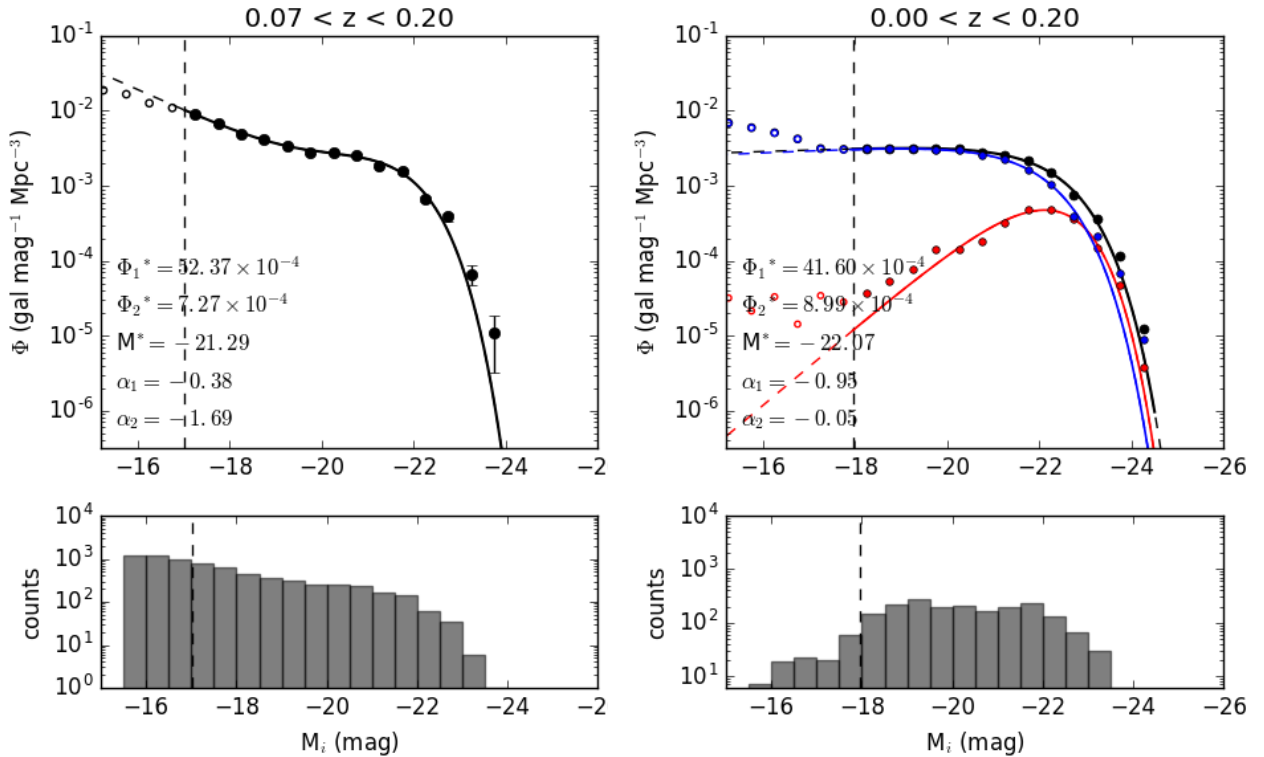


FIGURE 5.3: Top: LF of one HEALPix pixel $NSide = 32$ randomly selected from MICE sample (left panel) and from DES sample (right panel, where the red color refers to early-types, blue to late-types, and black to all galaxies). The solid lines refer to the best fit to the double Schechter function. Parameters displayed on the plot refer to the total sample. The empty circles represent points beyond the valid range of absolute magnitude, therefore not included in the fit. Bottom: the unweighted number counts for the same absolute magnitude bins as the LF.

error bars are added in quadrature. We use a non-linear least squares method available in Scipy³ Python library to fit the Schechter function, in its single or double form depending on the redshift bin considered.

In the next two sections, we explore the results of a battery of tests involving aspects of the methodology and potential sources of systematic errors.

³https://docs.scipy.org/doc/scipy/reference/generated/scipy.optimize.curve_fit.html

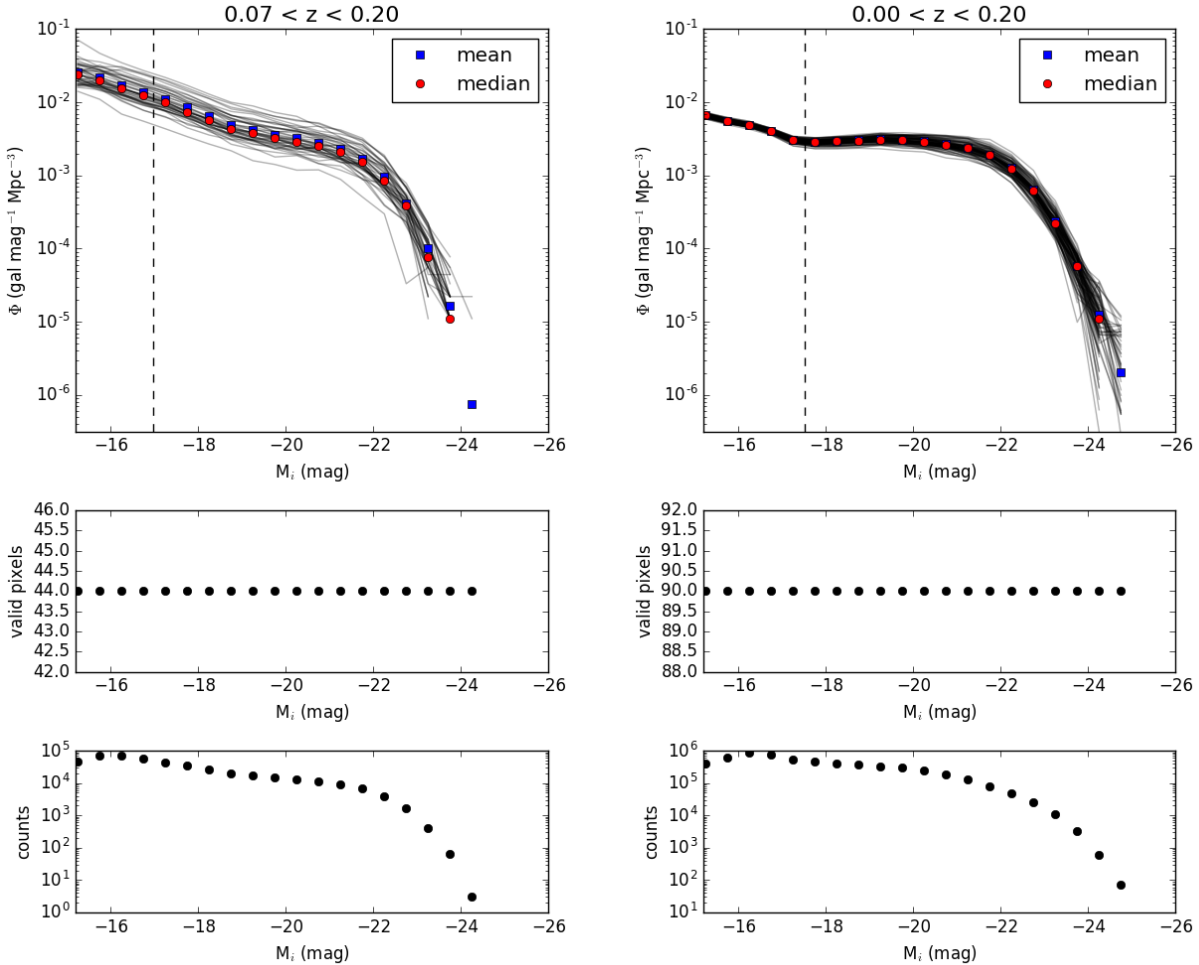


FIGURE 5.4: The combination of the LF results from individual pixels present in the MICE sample (left panels) and DES sample (right panels). Middle panels show the number of valid pixels that contributed to the mean (after 3σ clipping to remove outliers at the fain-end). On the bottom, the total counts in valid pixels.

5.2 Tests with MICE simulations

5.2.1 LF algorithm validation

So far, we have computed photo-zs using DNF, absolute magnitudes, and K-corrections using LePhare, both well-tested tools available to the public. Since we are introducing the photo-z PDFs, the completeness factor, and K-corrections in the core of LF calculation, it was necessary to write a new algorithm from scratch. Thus, the first step is to test and validate this new tool against a truth table. For this purpose, again, we use MICE simulations. Although the publications about MICE do not provide the same values we seek (i -band LF in z intervals), we have a hint of the actual values from those of the SDSS (Blanton et al., 2005b), the observational measurements based on which the MICE catalog was designed.

Before anything else, we mention two important caveats. First, we draw attention to the fact that it is not possible to reproduce the same redshift range studied in SDSS. Blanton et al. (2005b) surveyed local Universe (up to $z = 0.05$). MICE catalog contains objects at $0.07 < z < 1.4$. So we compute the LF at $0.07 < z < 0.1$ as a best-effort to reproduce SDSS' measurements.

Second, the i -band used in MICE catalog refers to DES set of filters. Since SDSS and DES i -band filters are not identical, and it is possible to find small discrepancies in the magnitudes which propagated to the LF. We also allude to the fact that Blanton et al. (2005b) published the results of Schechter parameters in

terms of the dimensionless Hubble parameter, h . Therefore, it was necessary to convert their numbers for a direct comparison to our results (we adopt $h=0.7$).

The first test is to validate the $1/V_{max}$ algorithm. To avoid biases and to evaluate only the method, we compute MICE LF using the true values of redshift and absolute magnitudes available in the catalog. Therefore, the LF estimator is simplified to Eq. 5.12.

We compute the LF and fit the results to the double Schechter function. We compare the results with the Schechter parameters informed by Blanton et al. (2005b) converted to incorporate $h=0.7$ in Table 5.1 and Figure 5.5.

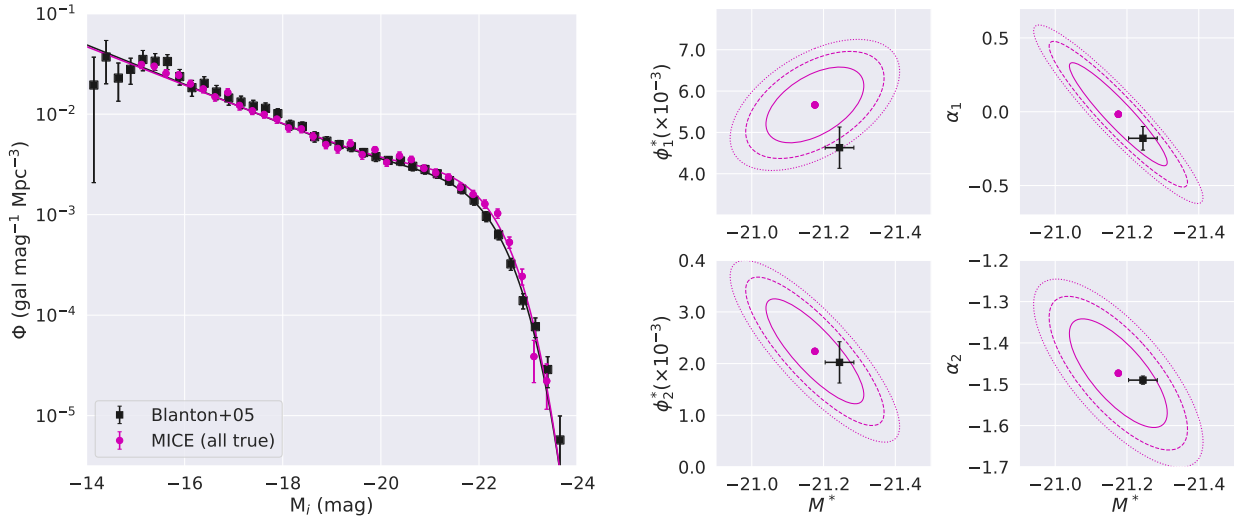


FIGURE 5.5: Left: i -band luminosity function of SDSS ($z < 0.05$, points from Blanton et al. (2005b), converted to $h=0.7$) in black, and MICE in pink. The black line represents the double Schechter function built using the original parameters published by the authors. Right: Schechter parameters corresponding 68% (solid lines), 95% (dashed lines), and 99.7% (dotted lines) error contours obtained from the fitting.

We observe in the left panel of Figure 5.5 a good agreement, overall the interval examined, between the LFs for MICE and Blanton et al. (2005b). On the right side, we observe a proper agreement in all parameters, except for ϕ_1^* .

From our experience, the result of curve fitting using the non-linear least-squares method is susceptible to the magnitude domain included in the fitting. The dashed vertical line in Figure 5.6 refer to the estimate of the absolute magnitude limit ($M_{lim} = m_{lim} - 25 - 5 \log_{10}(D_L)$), a faint threshold for “trustworthy” measurements. We removed the points with magnitudes fainter than M_{lim} , and repeated the curve fitting, for both samples. We do not consider the SDSS’ proper M_{lim} . Instead, we do the exercise of selecting the same magnitude range for both samples as a way to make a fair comparison.

Parameter	SDSS (original)	SDSS (new fit)	MICE
$\phi_1^* \times 10^{-3}$	4.63 ± 0.50	5.73 ± 0.54	6.02 ± 0.41
$\phi_2^* \times 10^{-3}$	2.02 ± 0.40	1.49 ± 0.95	1.81 ± 0.33
M^*	-21.25 ± 0.04	-21.22 ± 0.06	-21.22 ± 0.01
α_1	-0.18 ± 0.08	-0.31 ± 0.14	-0.15 ± 0.03
α_2	-1.49 ± 0.01	-1.61 ± 0.02	-1.54 ± 0.01

TABLE 5.1: Double Schechter fit parameters for the validation of $1/V_{max}$ algorithm using MICE simulations.

In summary, the disagreement observed in Figure 5.5 may reflect the differences in the fitting methodology. Our procedure tends to result in a slightly steeper faint-end, although this outcome is strongly sensitive to the domain of magnitudes considered in the fit.

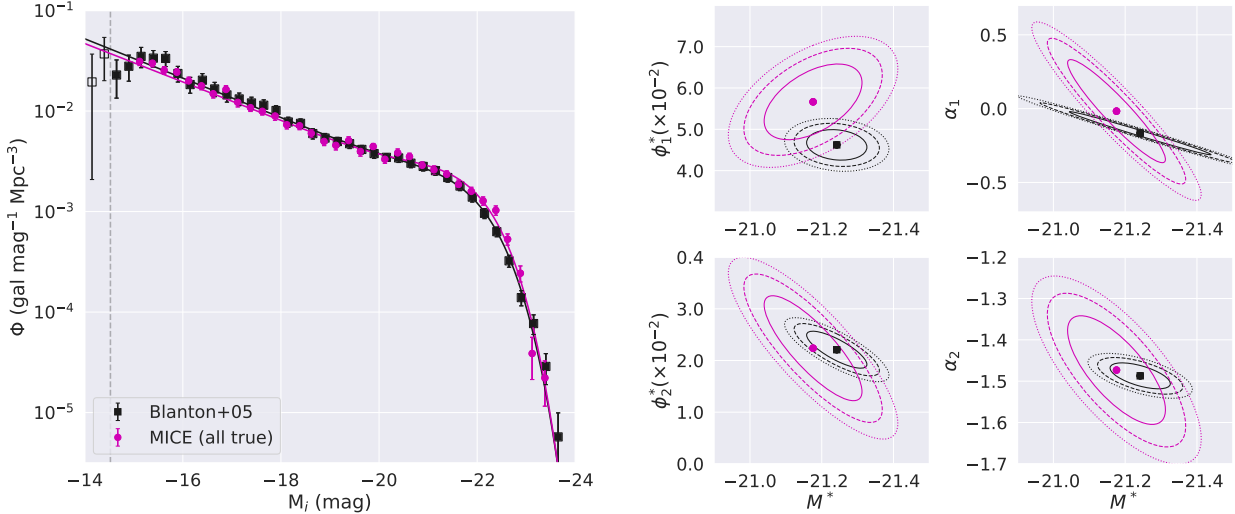


FIGURE 5.6: Left: i -band luminosity function of SDSS ($z < 0.05$, points from Blanton et al. (2005b), converted to consider $h=0.7$) in black, and MICE in pink. The vertical dashed line refers to the absolute magnitude limit M_{lim} discussed above. Right: Schechter parameters corresponding 68% (solid lines), 95% (dashed lines), and 99.7% (dotted lines) error contours obtained from the fitting after removing magnitude bins fainter than M_{lim} .

Considering the reasonable agreement between SDSS and MICE results, and all the potential sources of biases regarding the intrinsic differences of these two samples, we consider validated the LF algorithm using true redshifts and magnitudes. Thus, we can move forward and study the sources of errors in the next section.

5.2.2 Evaluating sources of errors in the LF determination

In this section, we use the MICE SMALL sample to study the errors in the LF estimate introduced by limitations of the methodology or the observations. We gradually add each contribution that may have an impact on the results.

In Section 5.2.1, we computed the MICE i -band LF using the true values of redshift and magnitudes for the low redshift interval $0.07 < z < 0.1$. Now we compute MICE LF, also using the true values of redshift and absolute magnitude, but for the redshift interval covered by DES data. We refer to these tests as “MICE *all true*”, and are considered as a fiducial reference sample, represented as blue squares in Figures 5.7 to 5.13. We do not include $z > 0.1$ bins in the LF validation above because we do not know the evolutionary model used to create MICE. Therefore, we do not have enough information to compare the results, as we did with the SDSS LF for the low- z regime. Nonetheless, we try to reproduce the LF results of the “*all true*” case, using different inputs and methods.

In the previous chapters, we studied how different sets of magnitudes impacted on photo-zs and template fitting determinations. Here, we inspect the propagation of these uncertainties into the LF.

One of the primary sources of errors is the degeneration of templates in the color-redshift space, which leads to a wrong estimate of the K_{corr} , placing such galaxy in an incorrect magnitude bin. Besides, as we consider the K-corrections in the calculation of V_{max} , an inadequate representation for the galaxy by the fitted template can also change the weight that such galaxy contributes to the number density.

The template set used is the COSMOS SEDs with increased UV fluxes, described in Section 4.2. We tried to reproduce the same configurations used by the authors to build the simulated catalog, except by the lower resolution in the grid of $E(B-V)$ values allowed for the fitting. Another concern when using data from a photometric survey is the quality of photometric redshifts, especially if using a small number of broad photometric bands to compute photo-zs. In Sections 3.2.4 and 3.3.3 we demonstrate

how the use of photo-z PDFs can improve the accuracy on the $N(z)$ determination, but a small margin of uncertainties introduced by the photo-z method remains.

In the following sections, we compare the LF fits and the Schechter parameters and the luminosity density obtained with true simulated redshifts and magnitudes with those obtained after varying input parameters and methodology. At the end of the section, we present a table summarizing the parameters obtained in the tests. However, in most cases, the analyses are done qualitatively, based on the visual inspection plots.

Impact of the photo-z method to the LF

We use the absolute magnitudes computed by LePhare with fixed photo-zs from DNF, still using the true apparent magnitudes from the simulations as input. The goal is to evaluate the errors introduced by the method itself, i.e., using photo-zs from DNF and absolute magnitudes from LePhare instead of the true values for z and M , including or not the photo-z PDFs in the LF estimator, without taking into account the contamination from observational biases. For this test, we use the set of magnitudes available in DES Y3 data (*griz*).

First, we inspect the low redshift regime. Unlike we did in the previous section, here we push the limit towards $z = 0.2$. Nevertheless, the upturn in the LF points is still present, so we fit the points to the double Schechter function (top panel in Figure 5.7). The use of calculated photo-zs and absolute magnitudes causes a substantial decrease in the values of Φ at the faint-end (yellow circles). Introducing the PDFs in the method mitigates this effect. At the bright-end, the results obtained using photo-zs are overestimated. Surprisingly, this effect seems to be more significant when using PDFs, but still within the error bars for the single z and the “all true” cases. A possible explanation is that the bright end is composed of fewer objects, so its results are more sensitive to small differences. A few galaxies with non-negligible probabilities in the PDF bins that fall into that redshift range of $\Delta z=0.2$ would translate into some contribution in the bright end that makes a great difference, even if their PDF peak is located at another redshift bin of $\Delta z=0.2$. Visually, this effect is amplified due to the logarithmic scale of the plots.

For redshifts higher than 0.2, we fit the LF to the single Schechter function (middle and bottom panels in Figure 5.7). For the two bins with the largest z , the determination of α is challenging because the faint magnitude limit is very close to M^* . Thus, we fix the α value to be the same as that from the previous bin; a common approach observed in the literature (e.g., Zucca et al., 2009; Ramos et al., 2011).

Differently from the first z bin, for $z > 0.2$ there is a trend to overestimate the faint-end and underestimate the bright-end densities when using single photo-zs. This effect has a strong dependence on redshift – the larger the z , the more significant the difference from the “all true” results. It looks like that the more critical photo-z errors systematically underestimate the absolute magnitudes. So, galaxies in a given z bin possibly move from the bright to the faint part of the LF. However, we can not claim such an effect because photo-z errors can be large enough to transfer galaxies between redshift bins of width 0.2. Therefore, galaxies with wrong photo-z measurements may provoke incompleteness in a given z bin and contaminates another one.

On the other hand, when using photo-z PDFs, the effect is the opposite of that with single values. The PDFs cause an overestimation of the bright-end and underestimation of the faint-end. The latter can be easily misinterpreted as a problem of limiting magnitude since the values of Φ become smaller as magnitude goes faint, but we highlight that Φ starts to fall, even at magnitudes brighter than the magnitude limit.

The parameters corresponding to the best fit for the four bins using single Schechter function are displayed in Figure 5.8. Surprisingly enough, although there is a large discrepancy between $\Phi(M)$ for single-zs and the “all true” LFs at both ends of the function, the characteristic density ϕ^* is hardly affected. However, when using PDFs, we observe a systematic shift to higher densities for $z = 0.4$ but preserving the overall trends of “all true” ϕ^* .

Regarding the characteristic magnitude M^* , the LF with PDFs reproduce reasonably well the “all true” LF up to $z = 0.8$. For the interval of $0.8 < z < 1.0$, M^* is ~ 0.4 magnitudes brighter than the “all

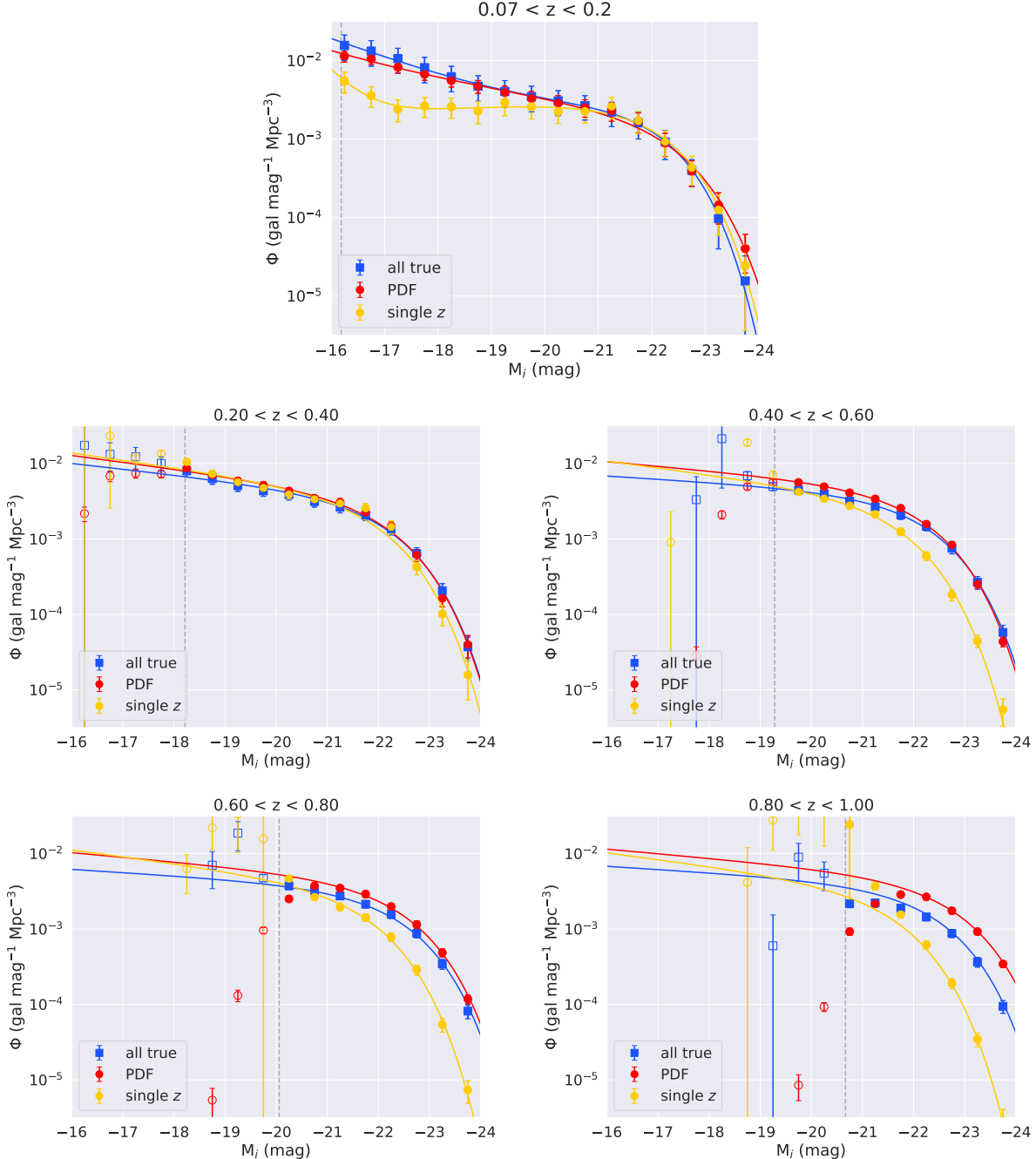


FIGURE 5.7: Global LF of MICE test sample. Comparison using different photo-z methodologies: single photo-zs (yellow circles), and photo-z PDFs in (red circles). “all true” (blue squares) means the LF computed with true redshifts and magnitudes provided by MICE simulation. Empty markers refer to points that are not included in the fit to the Schechter function for being fainter than the absolute magnitude limit (dashed vertical line).

“true” LF. The single photo-z LF provides fainter M^* in all z bins, where the difference to the “all true” case is more substantial with larger redshifts. The luminosity density shows a similar behavior as M^* , with a small discrepancy, observed at $z > 0.8$, including for the LF using PDFs. The faint-end slope α is underestimated in both cases using photo-z, with smaller biases for the LFs with PDFs. We see no evolution in α for $z > 0.3$ because α is fixed *ad hoc*. In summary, from the analysis of the LFs using photometric redshifts, we conclude that the photo-z PDFs are useful to mitigate the effects of photo-z

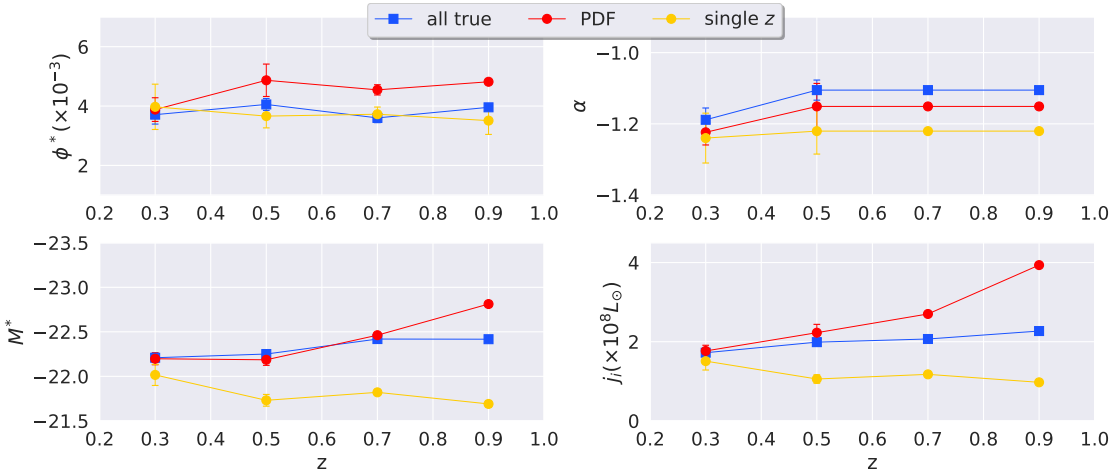


FIGURE 5.8: Evolution of Schechter parameters ϕ^* ($\text{gal mag}^{-1} \text{Mpc}^{-3}$), M^* , α , and the luminosity density, j_i , for the same redshift intervals of Figure 5.7 with fits to a single Schechter function.

errors in the LF. Therefore it is worth to include this methodology when estimating LF for DES.

Impact of adding u -band in the LF

The next test aims to evaluate the impact of adding the u -band and forecast possible sources of improvements in the near future with LSST. We recall that the potential improvements we expect to achieve with LSST go far beyond the effects of adding the u -band. LSST will provide larger area and depth, therefore a better representation and statistical significance.

We continue to analyze the i -band LF, so the presence of the u -band would only contribute indirectly, by affecting the results of photo-z and absolute magnitude measurements. Hence, we repeat the LF estimates using photo-z PDFs, now using both the PDFs and absolute magnitudes computed with $ugriz$ bands, still perfect theoretical apparent magnitudes from the simulation.

From Figure 5.9, we notice that the addition of the u -band only impacts the first redshift bin significantly, and such impact is by far less important than the observed in the previous test when adding photo-z PDFs. It is not a surprise, because this band covers the ultraviolet range of the electromagnetic spectrum. As we observe larger redshifts, galaxies SEDs become u -dropout. The impact of the u -band in MICE LF in the lowest z bin is an improvement in both ends of the function, in comparison to the “all true” case. The new band reduces the overestimated values of Φ at the bright-end and increases the underestimated values at the faint-end. For the other z bins, the effect of adding the u -band is negligible. The same conclusion comes from the evolution of Schechter parameters in Figure 5.10. There is a small positive shift in ϕ^* for $z < 0.5$ when adding the u -band, worsening the recovery of the “all true” LF, but this difference is within the error bars.

Impact of magnitude errors in the LF

After understanding the systematic errors introduced by aspects inherent of the methodology, now we introduce the apparent magnitude errors to evaluate the contribution of observational limitations to the LF error budget. MICE catalog does not provide errors for the magnitudes. Therefore, we simulated them based on the characteristic noise present in DES Y3 data.

We explored DES data and modeled the relationship between magnitudes and errors (see Figure 2.12 in Chapter 2), finding an exponential curve that better adjusts to the data on each filter. Then, we applied a random perturbation to each magnitude measurement as the characteristic error at that magnitude multiplied by a factor from a Gaussian probability distribution. The resulting mock error distributions

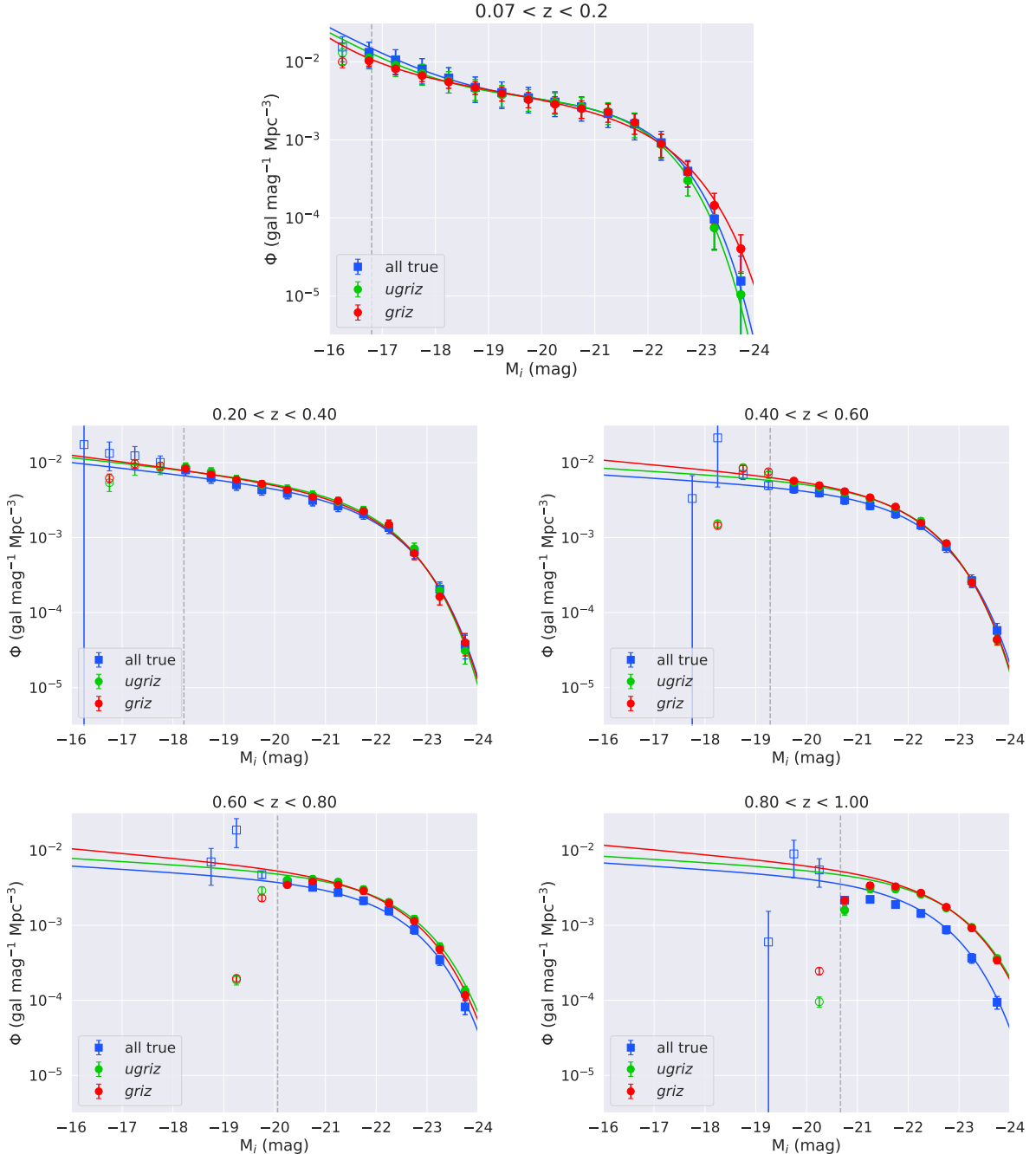


FIGURE 5.9: Global LF of MICE test sample. Comparison of LF obtained using the u -band to compute photo-z PDFs (green circles), without u -band (red circles), and absolute magnitudes, compared to “all true” (blue squares). Empty markers refer to points that are not included in the fit to the Schechter function for being fainter than the absolute magnitude limit (dashed vertical line).

are displayed in Figure 5.11. The maximum values of errors depend on the band because they were added to the magnitude-limited sample, i.e., after removing galaxies with $i < 23.5$.

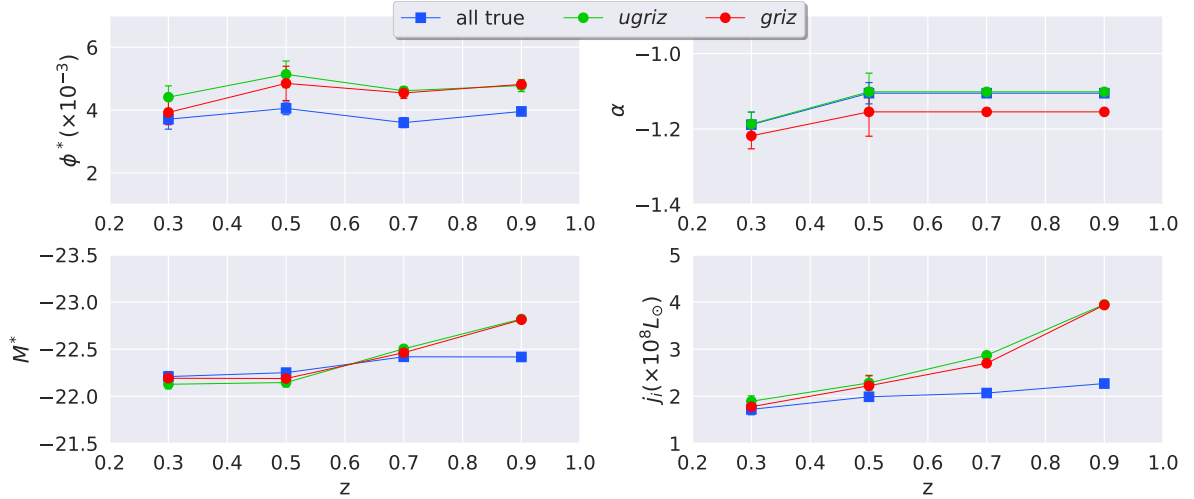


FIGURE 5.10: Evolution of Schechter parameters ϕ^* (gal mag $^{-1}$ Mpc $^{-3}$), M^* , α , and the luminosity density, j_i , for the same redshift intervals of Figure 5.10 where the LF fits to a single Schechter function.

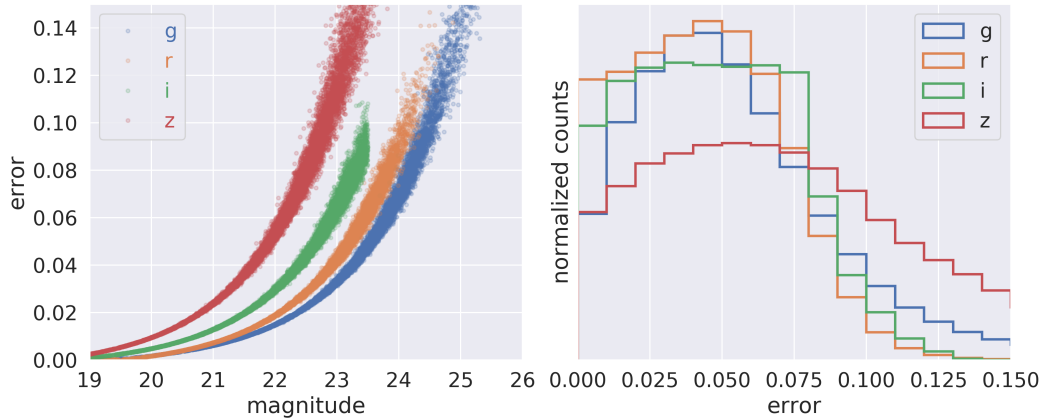


FIGURE 5.11: Mock griz magnitude errors applied to MICE catalog (respectively in blue, orange, green, and red). Left panel: magnitude versus errors. Right panel: Normalized distribution of errors.

As expected, the addition of magnitude errors causes a considerable impact on the faint-end of the LF, where objects are supposed to have a lower signal-to-noise ratio. This effect is inversely proportional to the redshift, mostly because the extreme faint-end is absent in the LF of higher redshifts due to limiting magnitudes. Cyan circles in Figure 5.12 (LF measurements after including magnitude errors) are on top of the red circles (LF from perfect magnitudes) at the bright-end of all the redshift bins. On the other hand, at the faint-end, they diverge depending on the bin. In the first bin, the magnitude errors cause a small decrease in Φ , accentuating the effect already created by the photo-z, whilst at the second redshift bin ($0.2 < z < 0.4$), the cyan points at the faint-end go in the opposite trend of the red circles. The overall effect is a negative bias at $z < 0.6$, and a positive bias at $z > 0.6$, both with small amplitudes.

From Figure 5.13, we learn that the predominant source of systematic errors in ϕ^* depends on redshift. The errors introduced by the methodology used to estimate redshifts and absolute magnitudes contribute most significantly at higher redshifts ($z > 0.6$). On the other hand, the propagation of photometry uncertainties dominates the shift in ϕ^* at lower redshifts ($z < 0.6$).

M^* and j_i keep the same evolutionary trend as those obtained without adding magnitude errors. The effects observed at the faint-end in Figure 5.12 propagates more substantially to α , which is underestimated

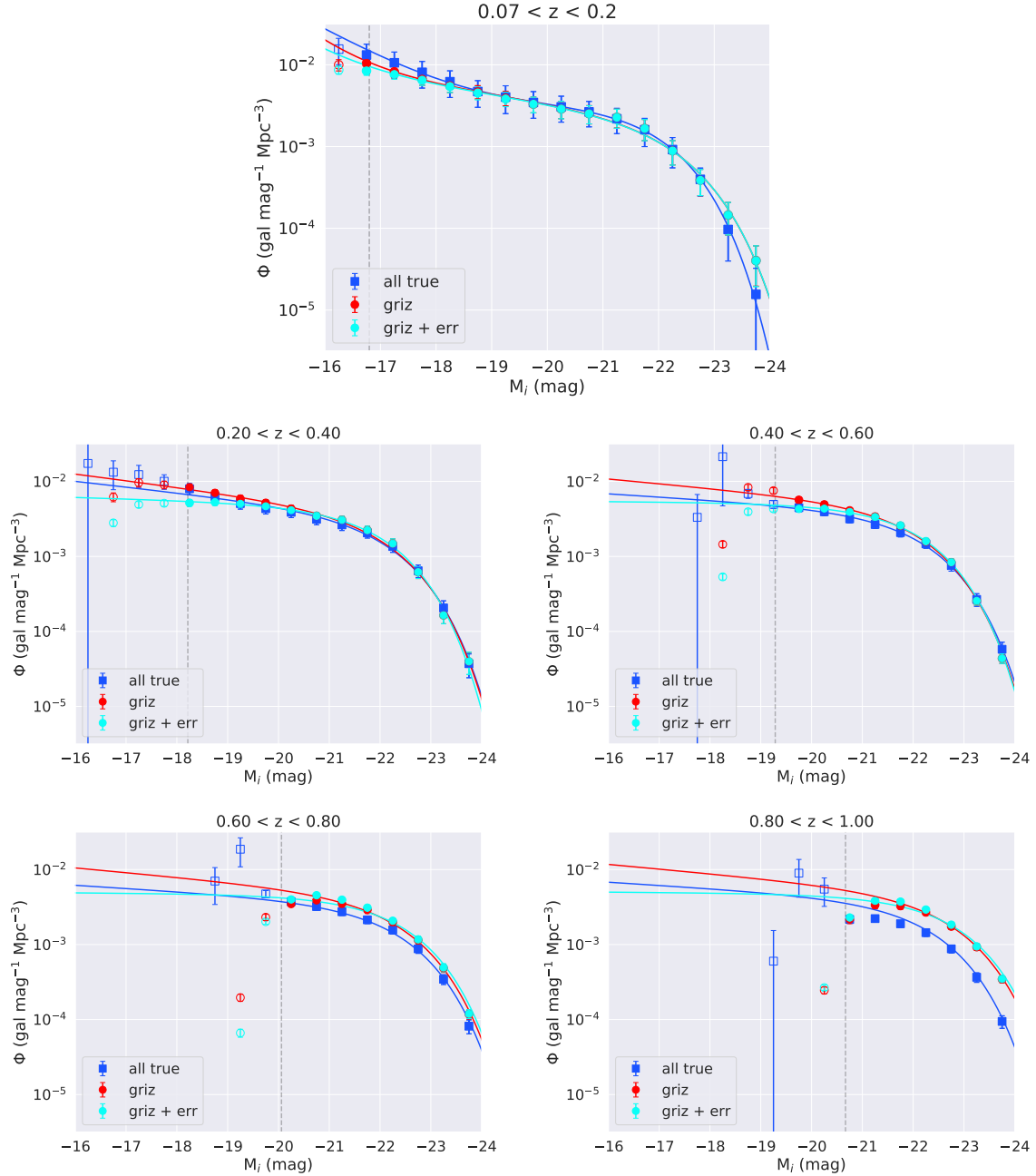


FIGURE 5.12: Global LF of MICE test sample. Comparison of results obtained with (cyan circles) and without (red circles) introducing mock magnitude errors, compared to “all true” case (blue squares). Empty markers refer to points that are not included in the fit to the Schechter function for being fainter than the absolute magnitude limit (dashed vertical line).

(in absolute value) in the lower redshifts, and this trend continues to higher redshifts because we adopted a fixed slope when the faint-end is difficult to be defined.

In Table 5.2 we compare the results obtained for the “all true” case and the realistic conditions (*griz* + magnitude errors), side-by-side. The last columns show the amplitude of the discrepancies obtained in absolute values and percentages. These systematic errors will not necessarily be the same when dealing with real data. Since we do not know the true LF for higher z bins, we are not sure if our results using true redshifts and true absolute magnitudes are a perfect representation of the original MICE LF. Otherwise, we could apply this bias corrections directly to the results with observed data. Nevertheless, they can

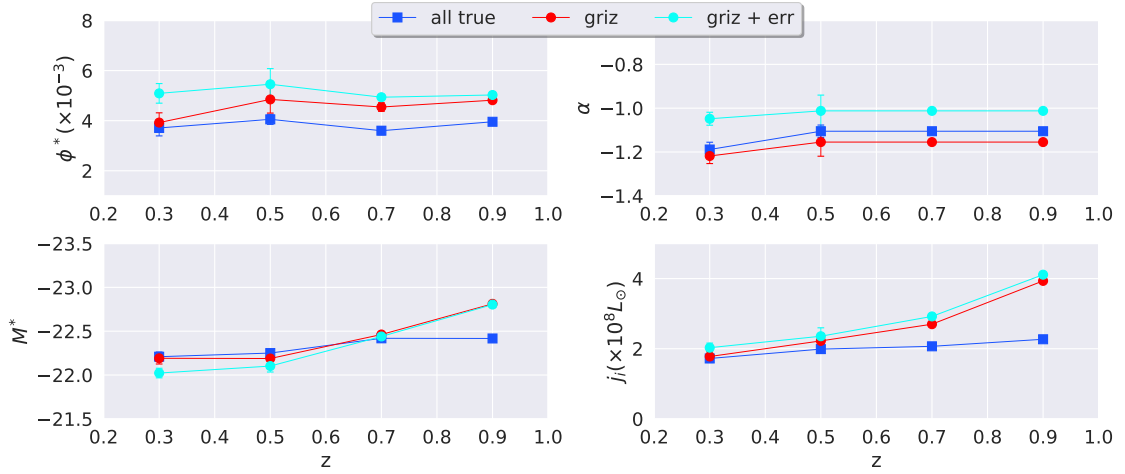


FIGURE 5.13: Evolution of Schechter parameters ϕ^* (gal mag $^{-1}$ Mpc $^{-3}$), M^* , α , and the luminosity density, j_i , for the same redshift intervals of Figure 5.12 where the LF fits to a single Schechter function.

shed light on the interpretation of the results in the next section, possibly helping to understand the DES LF results.

From the three tests presented in this section, we conclude that we can obtain reasonably accurate estimates of M^* for $z < 0.8$ domain, even though using photometric redshifts with just four broad bands.

z interval	Parameter	all true	$griz + err$	Δ	%
$0.2 < z < 0.4$	$\phi^* \times 10^{-3}$	3.71 ± 0.32	5.09 ± 0.39	1.38	37.23
	M^*	-22.21 ± 0.05	-22.02 ± 0.05	0.19	0.84
	α	-1.19 ± 0.03	-1.05 ± 0.03	0.14	11.80
	$j_i \times 10^8 L_\odot$	1.72 ± 0.11	2.03 ± 0.13	0.31	17.86
$0.4 < z < 0.6$	$\phi^* \times 10^{-3}$	4.05 ± 0.20	5.46 ± 0.63	1.40	34.56
	M^*	-22.25 ± 0.03	-22.10 ± 0.07	0.15	0.67
	α	-1.11 ± 0.03	-1.01 ± 0.07	0.09	8.41
	$j_i \times 10^8 L_\odot$	1.99 ± 0.09	2.36 ± 0.24	0.37	18.47
$0.6 < z < 0.8$	$\phi^* \times 10^{-3}$	3.60 ± 0.16	4.94 ± 0.10	1.34	37.13
	M^*	-22.42 ± 0.03	-22.44 ± 0.01	-0.02	-0.09
	α	-1.11 ± 0.00	-1.01 ± 0.00	0.09	8.41
	$j_i \times 10^8 L_\odot$	2.07 ± 0.06	2.92 ± 0.04	0.85	41.23
$0.8 < z < 1.0$	$\phi^* \times 10^{-3}$	3.96 ± 0.05	5.03 ± 0.13	1.07	27.03
	M^*	-22.42 ± 0.00	-22.80 ± 0.01	-0.39	-1.73
	α	-1.11 ± 0.00	-1.01 ± 0.00	0.09	8.41
	$j_i \times 10^8 L_\odot$	2.27 ± 0.01	4.11 ± 0.05	1.84	81.16

Notes to the Table - the fifth column (Δ) is the difference between the results in the third (all true) and fourth ($griz+err$) columns. The last column refers to the percentage difference in comparison to the all true case.

TABLE 5.2: Schechter fit parameters.

Summary of lessons learned using MICE

In this section, we have learned that:

- The use of photo-z PDF has a positive impact on the attempt to recover the LF of MICE simulation, in comparison with the LF computed with the true values of z and M provided by the simulated catalog. At the faint end, this technique helps to mitigate the underestimation in galaxy counts at

lower redshifts ($z < 0.2$) and the overestimation at intermediate and higher redshifts ($0.2 < z < 1.0$). It also helps to correct the underestimation produced by single photo-zs at the bright-end at $0.2 < z < 1.0$. For higher redshifts ($0.8 < z < 1.0$), the use of photo-z PDF provokes an excessive correction at the bright-end, causing an overestimation of the results.

- The addition of the u -band to the set of observables used to compute z and M has a mild impact on the LF results. There is a modest improvement in the recovering of the MICE “all true” LF, noticeable only at the lower z interval studied ($z < 0.2$).
- The uncertainties of magnitude measurements have a slight impact on the faint-end of the LF. The small bias can be positive or negative, depending on the redshift interval studied.
- ϕ^* s are systematically overestimated, and the relative contributions of different sources of errors depend on the redshift range. The uncertainties in the magnitude measurements dominate at lower redshifts ($z < 0.4$). In contrast, the intrinsic limitations of the methodology (the usage of photo-z PDFs and M estimates from template fitting) dominate at intermediate and higher redshifts ($z > 0.4$).

5.3 Tests with real data

In this section, we report tests performed with the GE science samples defined in Section 2.1.1 but do not discuss the implications of the results in the context of galaxy evolution yet. The final results and discussion will be found in Section 5.4 and Chapter 6. For now, we address aspects of the methodology that might affect the results. To recap: we computed photo-z PDFs with DNF and absolute magnitudes with LePhare, using *griz* MOF apparent magnitudes, considering Λ CDM model with cosmological parameters from DES Y1 dark energy measurements published by Abbott et al. (2017) and Abbott et al. (2018a) ($\Omega_m = 0.301$, $\Omega_\Lambda = 0.699$, $H_0 = 69.3 \text{ km s}^{-1} \text{ Mpc}^{-1}$).

5.3.1 Correcting for sample incompleteness

As mentioned above, we included incompleteness correction as additional weight in the LF estimator. As it can be seen in Figure 2.24, the completeness factor is equal or very close to 1.0 for all magnitudes below 23.5, except for the very low surface-brightness regime. Hence, the effects of Balrog corrections on the LF results are quite small. In Figure 5.14 we show the corrected (in blue) and uncorrected (in pink) results for the five redshift bins studied, this time starting at $z = 0$. The difference in the results caused by the correction is only noticeable for the absolute magnitude bins of the LF that are fainter than the absolute magnitude limit, i.e., in the domain where the measurements do not account for the fitting to the Schechter function.

In Figure 5.14, the LF of the first redshift bin ($0 < z < 0.2$) exhibits an upturn at $M \sim -18$, suggesting a better representation given by the double Schechter function. Comparing to Blanton et al. (2005b) results in Figure 5.5, the values of Φ at the faint-end are considerably smaller than the expected for the local Universe, and the completeness factor defined by Balrog is not properly correcting this effect. This is because the underestimated faint-end is not a consequence of the loss of faint dwarf galaxies in the observations. Instead, it is because these objects have poor photo-z measurements, and consequently, bad absolute magnitude determination. So, they are transferred to other bins. This is a consequence of the distorted $N(z)$ distribution obtained for the science sample, even using the PDFs.

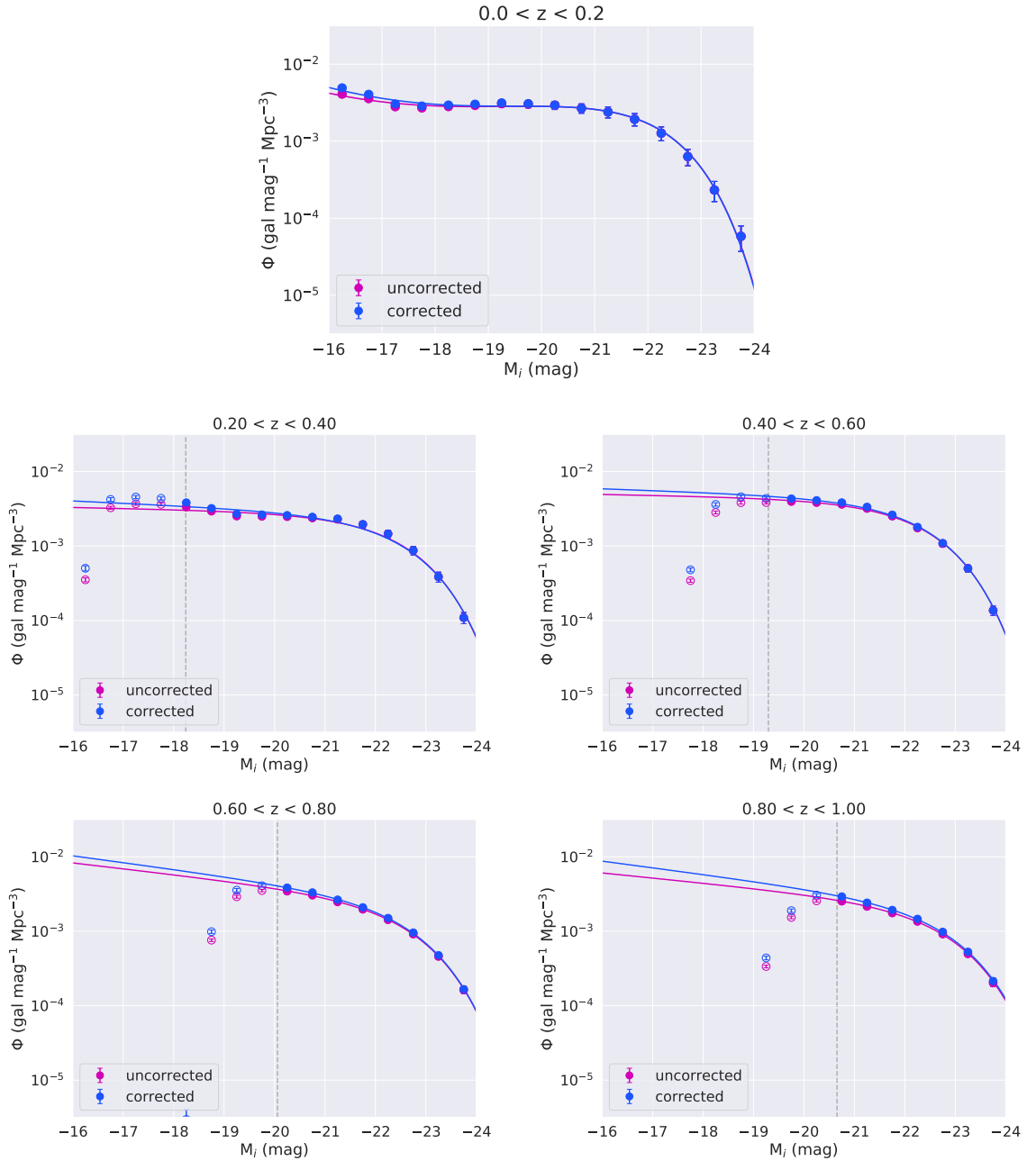


FIGURE 5.14: Global LF of DES Y3 medium sample. Comparison between results obtained with (blue) and without (pink) the correction factor from Balrog. Vertical dashed lines refer to the absolute magnitude limit.

In Section 4.3 we discussed how the magnitude-redshift diagram is affected by this problem, causing severe incompleteness observed as empty spaces in the lowest z bins of the diagram. This issue raises a red flag for the further interpretation of LF evolution. This first test on the topic of incompleteness reveals that the lowest z bins LF are strongly biased. The reason is well known, but the solution is not yet.

The second redshift bin ($0.2 < z < 0.4$) also suggests a double Schechter shape, with a small decrease in Φ levels at $M \sim -19.5$. We are not sure if this is a real effect or an artificial feature. Anyway, we forced an adjustment to a single Schechter function to obtain the same parameters as in the remaining bins, to be able to compare their evolution in Figure 5.15. There, we find that the completeness correction hardly affects the Schechter parameters of the global LF, except for the faint-end slope α . The LFs with

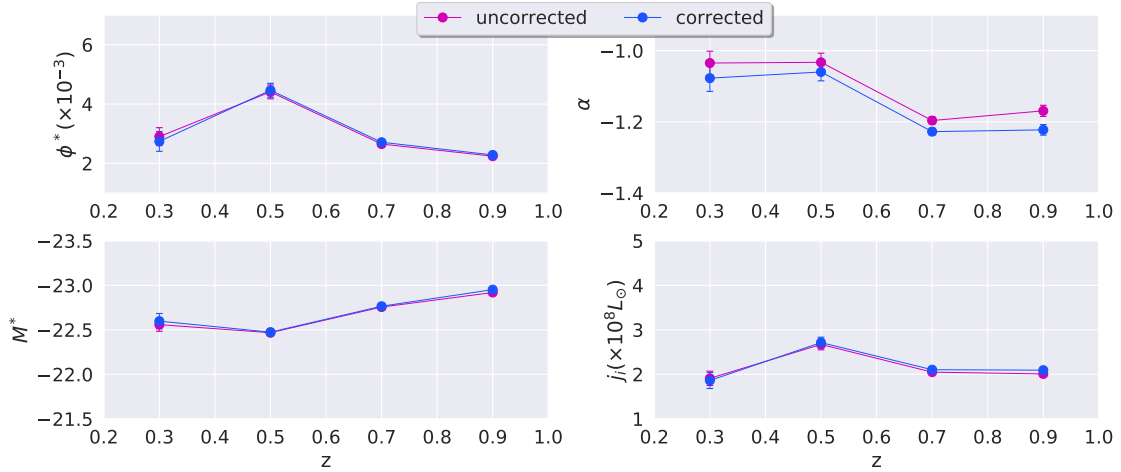


FIGURE 5.15: Evolution of Schechter parameters ϕ^* (gal mag $^{-1}$ Mpc $^{-3}$), M^* , α , and the luminosity density, j_i , for the same redshift intervals of Figure 5.14 where the LF fits to a single Schechter function. Results obtained with (blue) and without (pink) the correction factor from Balrog.

Balrog corrections show a slightly steeper faint-end (a more negative value of α) in all z bins studied, approximately by the same factor, keeping the same trends as the uncorrected LF.

5.3.2 Exploring dependence on area

The objective of the second test with real data is to evaluate the dependence of the Schechter parameters on the area covered by the sample. We compared samples of three sizes: $\sim 7 \text{ deg}^2$ (so-called small), $\sim 260 \text{ deg}^2$ (named medium), and $\sim 5000 \text{ deg}^2$ (large). The largest set is the total science sample.

The definition of the smallest dataset is related to technical aspects of the DES Science Portal, the infrastructure framework where the data is processed (see Appendix A for more details). The set is a standard sample used for quick tests in all the chain of pipelines. Of particular interest to photo-z tests, it was chosen to overlap a region that is very rich in public spectroscopic redshifts from previous surveys. The sample has originally 9 HEALPix pixels of $NSide = 32$, but only two pixels satisfy the science requirements established in Section 2.1.1. The medium data set is an intermediate area, defined as a circular selection close to the center of the footprint. We repeated the same set of plots presented in the tests above, i.e., the LF in z bins of width=0.2 in Figure 5.16 and the evolution of Schechter parameters in Figure 5.17.

From the visual inspection of Figure 5.16, we notice that the small sample provides results quite close to the medium and large samples, with modest deviations in both, the bright-end (underestimated Φ) and the faint-end (overestimates Φ). These small discrepancies turn out into non-negligible differences in the Schechter parameters in Figure 5.17, pushing their values beyond the error bars of the medium and large results in several cases. For all the parameters, the differences are larger at the lower redshifts, which is expected since, for evenly spaced redshift bins, the larger the z , the larger the comoving volume observed. α is the only parameter that shows a large deviation at $0.8 < z < 1.0$, which is also expected because, at this redshift range, the absolute magnitude limit is close to M^* making difficult the definition of the faint-end.

Still in Figure 5.16, we highlight that the medium and large areas provide virtually the same parameters so that, in most cases, the blue circles are hidden behind the green ones. This impacts the Schechter parameters in Figure 5.17, where the settings for the medium sample are also almost identical to those for the large sample. It indicates that the medium sample is large enough to be considered as a good representation of the large sample in terms of the impact of cosmic variance. Since we explored three sizes of areas, we do not have enough information to state what would be the minimum area where the

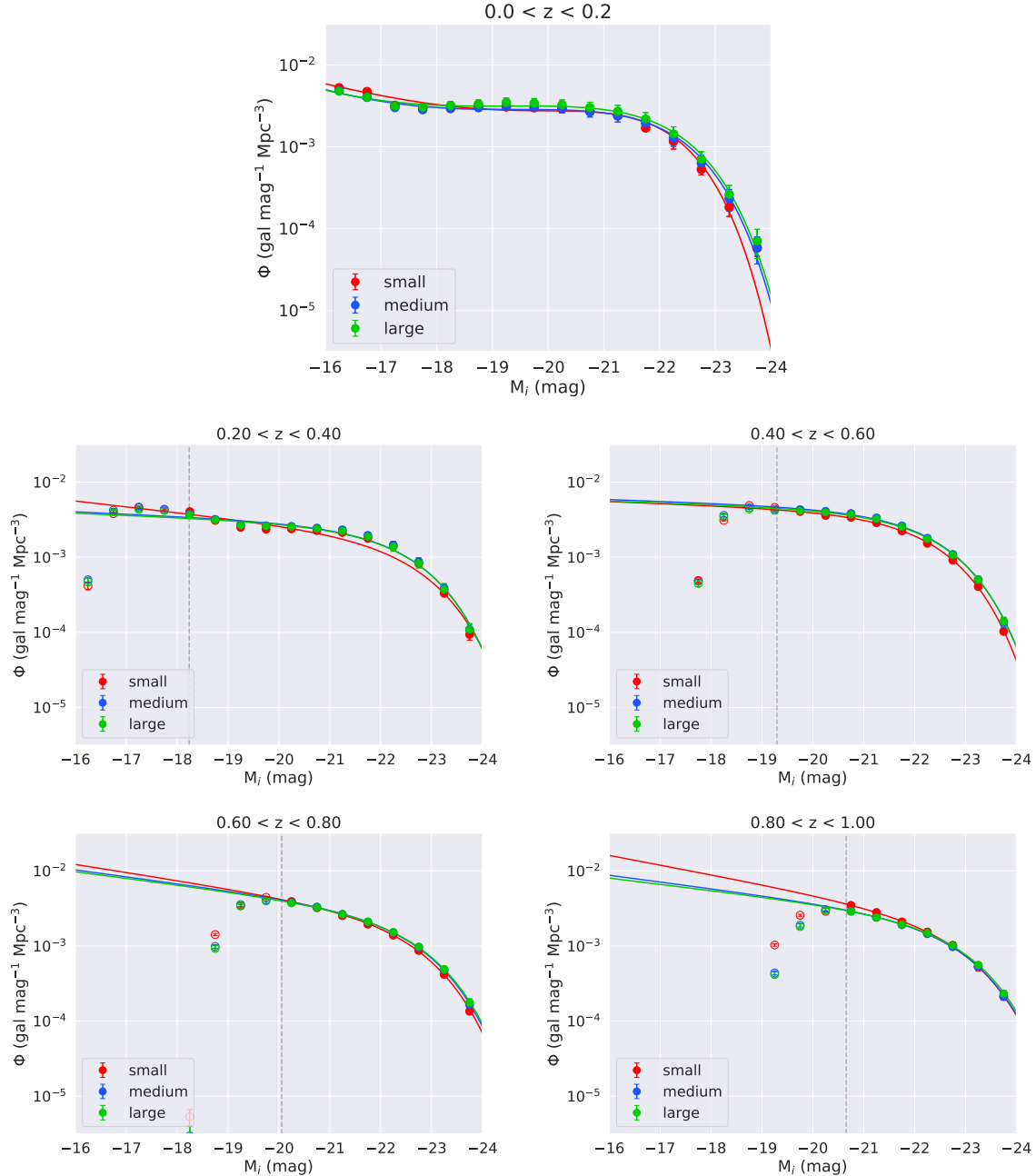


FIGURE 5.16: Global LF of DES Y3 samples in three different sizes: small (red), medium (blue), and large (green). Vertical dashed lines refer to the absolute magnitude limit.

sample becomes spatially homogeneous. However, these results give us two limits to keep in mind when comparing our findings to the literature. LF computed on samples that cover an area $\leqslant 7\text{deg}^2$ might be severely affected by cosmic variance effects, whereas those that include 260 deg^2 or more are probably not.

Lessons learned using DES data

In this section, we learned that:

- The completeness correction based on Balrog simulations do not contribute significantly to the LF results.

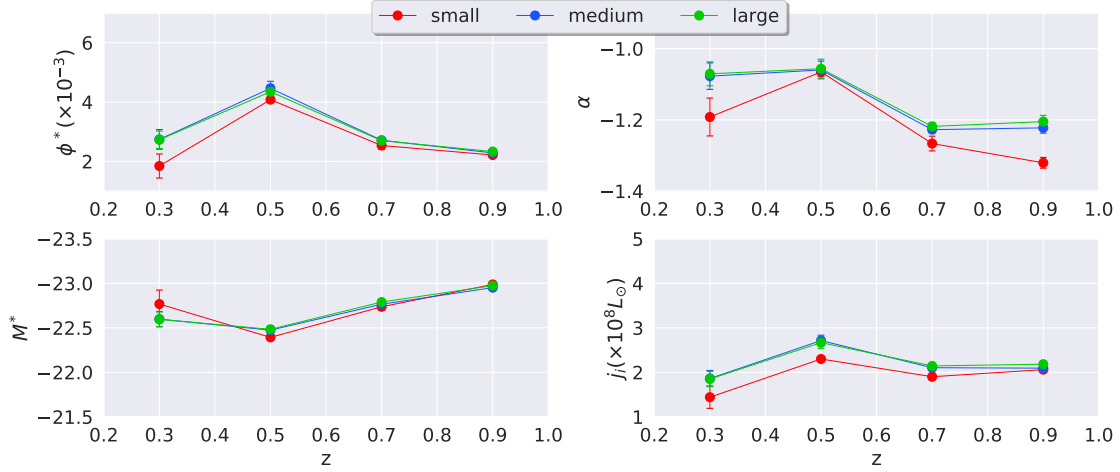


FIGURE 5.17: Evolution of Schechter parameters ϕ^* (gal mag $^{-1}$ Mpc $^{-3}$), M^* , α , and the luminosity density, j_i , for the same redshift intervals of Figure 5.16 where the LF fits to a single Schechter function.

- ~ 7 deg 2 of coverage is not enough to compute the LF without an important influence of cosmic variance effects.
- Although less precise, the LF computed on ~ 260 deg 2 should provide similar results as using the total sample of $\sim 3,400$ deg 2 .

5.4 DES Y3 global and galaxy populations LF

In this section, we present the luminosity function estimated at five redshift bins for the DES Y3 science sample, analyzing the global and the specific LF for distinct galaxy populations separately.

5.4.1 Global LF

Here, we show the determination of global LF and compare our findings against results from the literature. These external results were extracted from five publications using data from four surveys (SDSS, VVDS, CFHTLS, GAMA). We selected, preferably, authors who used the same photometric band or at least covered approximately the same wavelength range. We also included in the comparison the preliminary results from the science verification (SV) phase of DES, when the survey released the first data set internally, still with ongoing calibrations and fine-tuning of data acquisition and reduction. Hence, one should be careful when drawing conclusions based on these data. It is important to mention that the methodology adopted and the characteristics of the SV data are not the same as we have for DES Y3. At the SV epoch, the MOF photometry was not available yet, the photo-z algorithm (TPZ) was another from what we used (DNF), and they used Monte-Carlo simulations to account for the PDF.

It is usual to find authors providing results in terms of the Hubble parameter h . For a proper comparison, we convert the results that were published as a function of h to incorporate values we adopt in our measurements ($H_0 = 68.2$, and $h = H_0/100$). In most cases, the authors parameterized their LF results using the traditional Schechter function and provided the Schechter parameters. If so, we plot the curves correspondent to their set of parameters. One exception is Bates et al. (2019) who provided only the measurements of $\Phi(M)$, so the results presented in Table 5.5 are based on the curve fitting done by ourselves. Loveday et al. (2012) provided parameters for a double power-law Schechter function, so the direct comparison with our results is not possible. Therefore, we only compare with their results for the luminosity density, which is shown separately at the bottom of 5.5 due to the very different binning.

To make a fair comparison, we put together some of the most relevant characteristics of each previous work we mention, such as the magnitude limit, m_{lim} , the faintest absolute magnitude, M_{max} , with Φ measurements at the lowest z bin, and the number of galaxies, N_{gal} , included in the sample, in the Table 5.3.

Survey	z method	z range	area (deg 2)	m_{lim}	M_{max}	N_{gal}
SDSS (Blanton et al., 2005b)	spec-z	0.00 – 0.05	2,221	$r < 17.5$	$M_i < -14.2$	2.8×10^4
VVDS (Ilbert et al., 2005)	spec-z	0.05 – 2.00	1.2	$I_{AB} \leq 24.0$	$M_{I_{AB}} \lesssim -14.8$	1.1×10^4
CFHTLS (Ramos et al., 2011)	photo-z	0.05 – 2.00	4	$i'_{AB} < 24.0$	$M_{i'} \lesssim -15.8$	3.9×10^5
GAMA (Loveday et al., 2012)	spec-z	0.002 – 0.50	48	$i < 18.7$	$M_i \lesssim -12.5$	1.0×10^4
DES SV (Capozzi et al., 2017)	photo-z	0.00 – 1.00	155	$i < 23.0$	$M_i \lesssim -15.0$	4.0×10^6
SDSS (Bates et al., 2019)	spec-z	0.20 – 0.80	1,214	$i < 21.0$	$M_i \lesssim -20.4$	1.1×10^6
DES Y3 (this work)	photo-z	0.00 – 1.00	3,438	$i < 23.5$	$M_i \lesssim -15.0$	1.7×10^8

TABLE 5.3: Characteristics of previous works (approximated values).

We split our sample in redshift bins of width $\Delta z = 0.2$, following the same approach as the majority of the authors addressed. Bates et al. (2019) provided results in redshift bins of width $\Delta z = 0.1$. The points shown in Figure 5.18 are the average $\Phi(M)$ on the respective pair of z bins to match the correspondent bins of width $\Delta z = 0.2$. As shown in Chapter 3, we have data for galaxies beyond $z \sim 1.5$. However, we narrow down the analysis to $z < 1.0$ because the absolute magnitude limit of the DES Y3 sample at $z > 1.0$ is too close or brighter than M^* at that z , making it impossible to obtain an acceptable fit to the Schechter function. We expect to push this limit to $z \sim 1.4$ when the final data release becomes available.

As Blanton et al. (2005b) found for SDSS, in DES, we also observe an upturn in the LF at a low redshift regime, which fits better to a double Schechter function. As a little caveat, although SDSS results covered only the range of $z < 0.05$, and VVDS only covers $0.05 < z < 0.2$, we plotted the curve for SDSS and VVDS results among our and other authors' results for $0.0 < z < 0.2$ in Figure 5.18. We also notice a hint of double Schechter at the second bin ($0.2 < z < 0.4$). The parameters obtained for the best fit to double Schechter functions are shown in Table 5.4. Likewise, we perform fitting to single Schechter function at all z bins to compare with previous results. The parameters are presented in Table 5.5.

At the bright-end of the first redshift bin ($0.0 < z < 0.2$, the top panel of Figure 5.18), our results agree within the errorbars with Ilbert et al. (2005) and Ramos et al. (2011) on higher values of Φ than Blanton et al. (2005b) found for SDSS. As DES Y3 sample covers a larger volume, we are in a good position to detect very bright objects that are rare, but not difficult to be measured once they are found. Although SDSS' LF was estimated on a reasonably large area, they limited the measurements to $z < 0.05$. Therefore some rare objects could be detected at $0.05 < z < 0.2$ and contribute to the bright-end. It could explain the higher values of $\Phi(M)$ from VVDS and CFHTLS. Even so, besides the larger errorbars, we recognize that our estimates have a none-negligible positive bias at the bright-end, as already revealed by the tests using MICE simulations. Although bright objects are accurately measured with a high signal-to-noise ratio, they are susceptible to color-magnitude degeneracies when they are classified, which can artificially move them to a wrong redshift or absolute magnitude bin. This is the typical case where data in the u -band could help significantly, bringing more information on the UV range to break degeneracies at low redshifts. In Section 5.2 we demonstrated that the u -band would help to mitigate the overestimation of Φ at the bright-end (see Figure 5.9). Ilbert et al. (2006) and Ramos et al. (2011) have already anticipated that the lack of u -band would make the LF estimation a challenge for DES at $z < 0.4$.

Still on the first redshift bin, we notice that Ramos et al. (2011) and Blanton et al. (2005b) agree reasonably on the faint-end slope in spite of using different Schechter functions to fit the data. They obtained a faint-end significantly steeper than Ilbert et al. (2005). At this magnitude regime, we observe an unsettling disagreement between the DES results and other works. Interestingly, we obtained virtually the same results as Capozzi et al. (2017). Blanton et al. (2005b) argued that the estimate of the luminosity function is strongly affected by the surface brightness selection effects, and diffuse blue disks dominate the faint-end at low- z . Apparently, the partial data releases of DES (both SV and Y3) are still strongly affected by incompleteness, and the correction applied based on Balrog simulations is not enough to

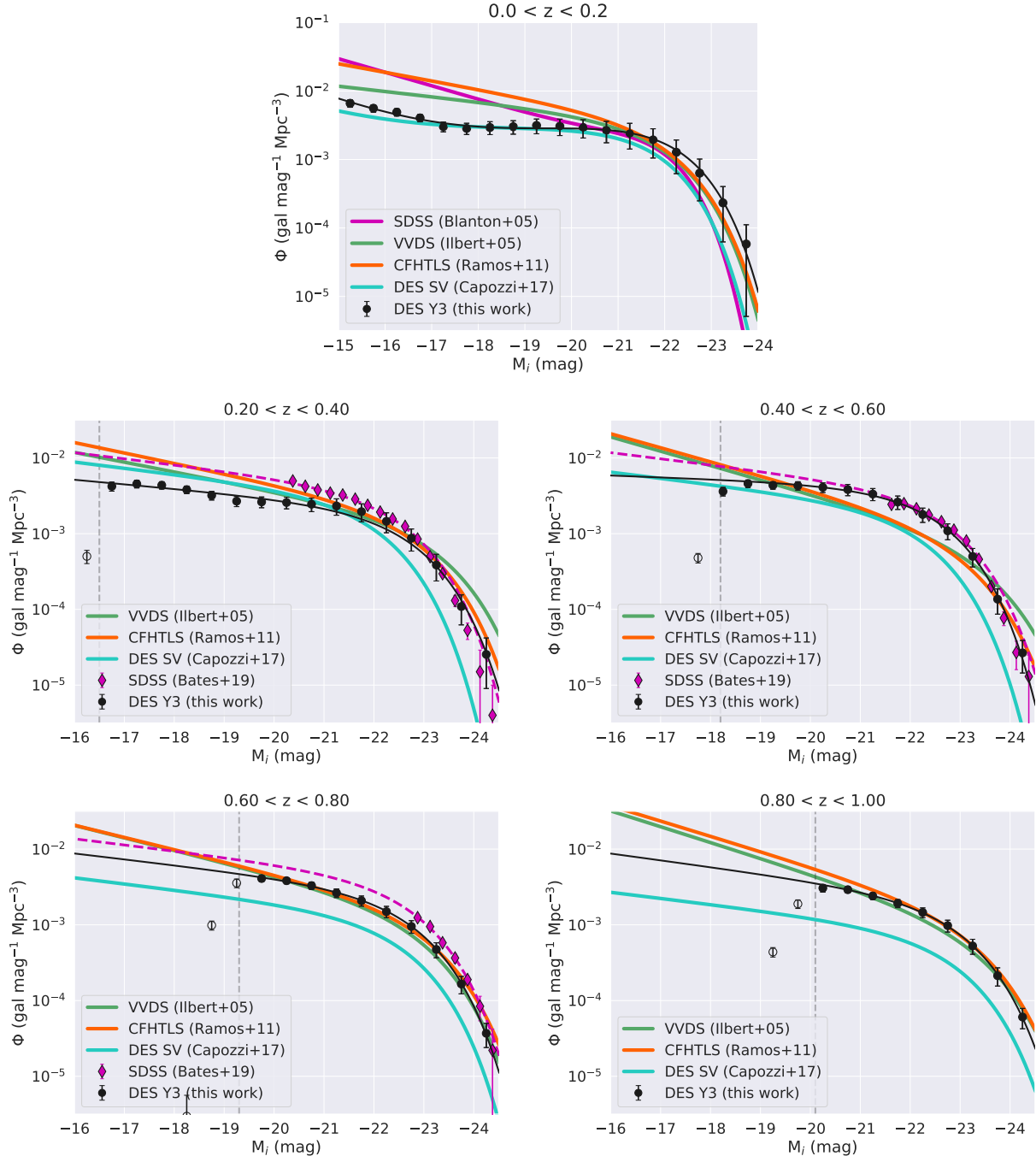


FIGURE 5.18: Global LF comparison with previous results from the literature: SDSS (pink), VVDS (green), CFHTLS (orange), DES SV (cyan), DES Y3 (this work)(black). Results from the literature are plotted as solid lines. The curve fit done by ourselves for SDSS LF at $z > 0.2$ is plotted as dashed lines (there we adopted α fixed = -1.2 due to the lack of data at the faint-end). Vertical dashed lines refer to the absolute magnitude limit.

compensate for the loss of low surface-brightness galaxies. Indeed, Capozzi et al. (2017) discussed the impact of severe incompleteness in the lowest z bin, and they excluded the results for $z < 0.2$ from the analysis of evolution. Moreover, the tests with MICE also showed that the faint-end estimates are underestimated when using photo-zs, which is mitigated by the usage of PDFs, but not entirely solved. Therefore, we attribute the low counts at the faint-end as a combination of observational and methodological factors, which includes systematic errors on photo-z and M estimates.

At the other redshift bins, there is also some degree of disagreement among the authors. We notice that our estimates at the faint-end are systematically below the average, resulting in α less negative than those found by other authors. At intermediate redshifts ($0.2 < z < 0.4$), our results for the bright-end agree well with most of the previous results, except by the DES SV. At $0.4 < z < 0.6$, our estimates for the bright-end match with SDSS', which are significantly higher than DES SV, VVDS, and CFHTLS. Finally, at the higher z bin, our results for the bright-end agree with VVDS and CFHTLS and reveals that our sample starts suffering by incompleteness effects at least two magnitude bins brighter than the vertical line suggesting that we overestimate the absolute magnitude limit.

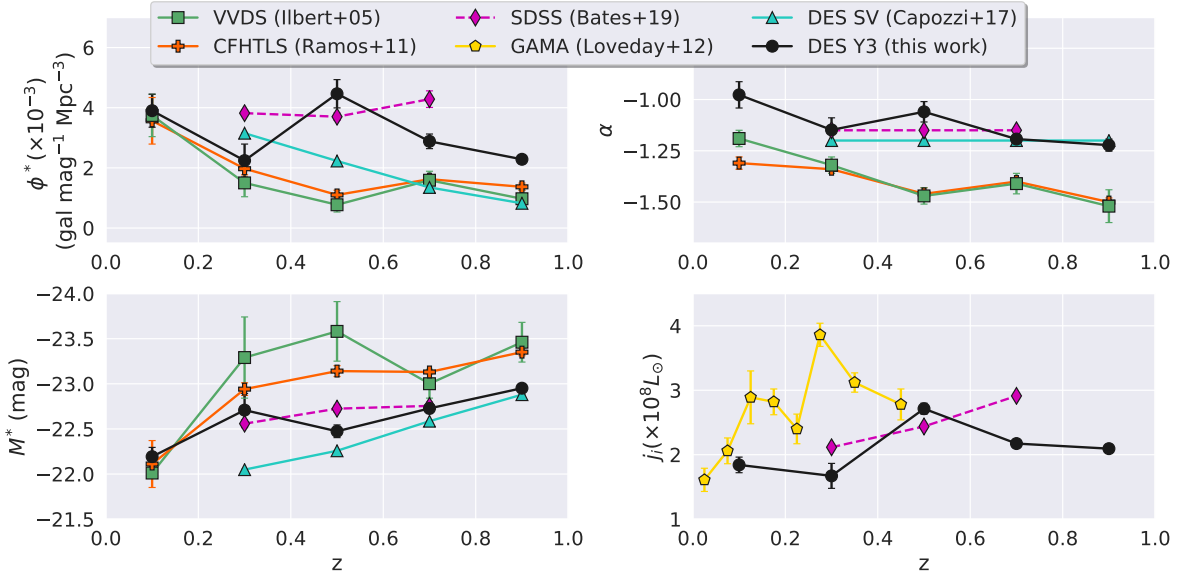


FIGURE 5.19: Evolution of Schechter parameters and luminosity density for the redshift intervals in Figure 5.18, adjusted to a single Schechter function (parameters in Table 5.5). Results from the literature are plotted as solid lines. SDSS LF fit done by ourselves is plotted as dashed line. Luminosity density results from GAMA are plotted in yellow. The colors are the same as in Figure 5.18.

The overall disagreement observed in the LF curves in Figure 5.18 translates into different evolution of Schechter parameters in Figure 5.19, which reinforces the idea that the evolution of the luminosity function is a subject in astrophysics still far for being completely understood. Nevertheless, we can extract some evolutionary trends in common, such an overall increase of M^* and a decrease of ϕ^* with redshift, besides differences in normalization and the oscillation of points. In Figure 5.20 we show the linear fit of the points in Figure 5.19 to facilitate the visualization of trends.

We found that the characteristic density ϕ^* increased by a factor of ~ 1.7 between $z \sim 0.9$ and $z \sim 0.1$, an intermediate value between 1.5 and 2.6, found by Ilbert et al. (2005) and Ramos et al. (2011) respectively for the same redshift interval. Capozzi et al. (2017) found the same trend, but with a much more significant factor (~ 4) for a shorter redshift interval (between $z \sim 0.9$ and $z \sim 0.3$).

We encountered that the characteristic luminosity is fading since $z \sim 1.0$, but we obtained a modest increase of 0.76 magnitudes between $z \sim 0.9$ and $z \sim 0.1$, which would be equivalent to an average dimming of 0.15 magnitudes per redshift bin of $\Delta z = 0.2$. Ilbert et al. (2005), Ramos et al. (2011) and Capozzi et al. (2017) found most significant evolution for the same interval. They measured an average dimming of ~ 0.30 , ~ 0.25 , and ~ 0.23 magnitudes per redshift bin, respectively. Bates et al. (2019) found no evidence of substantial evolution between $0.2 < z < 0.8$, just analyzing the LF curves, without any parametrization, suggesting passive evolution at this epoch. However, given the oscillation observed in the other results, likely the redshift interval they covered is not large enough to observe a significant evolution. The overall dimming of the characteristic magnitude is consistent with other indicators found in the literature, such as the star formation rate. At this epoch ($z < 1$), most of the ordinary galaxies

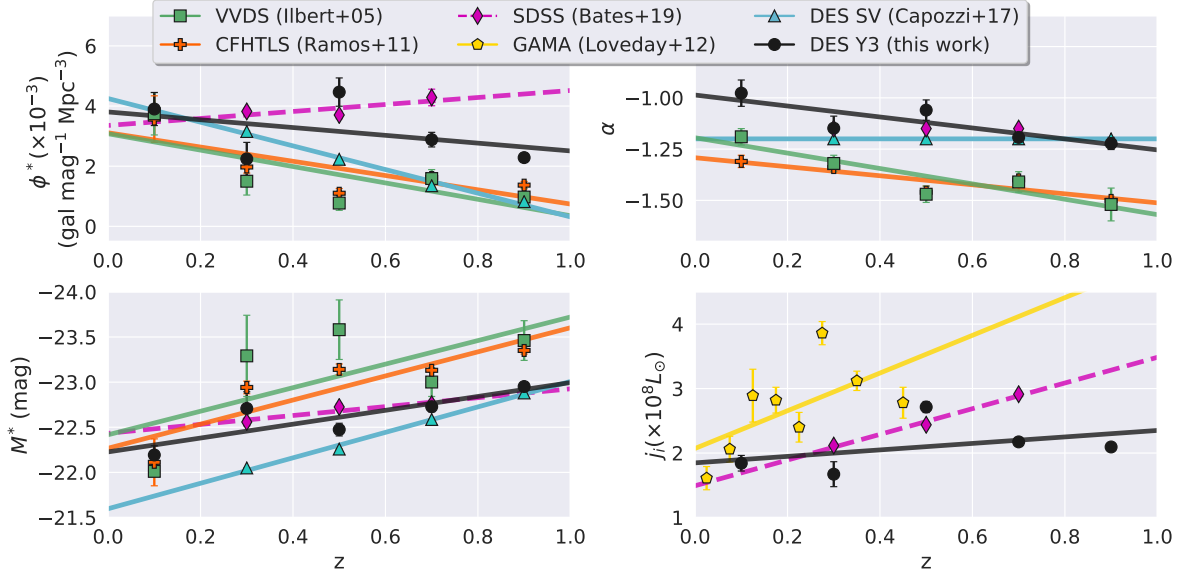


FIGURE 5.20: Same points as in Figure 5.19. Here the lines represent the linear fit to the results. The angular and linear coefficients obtained for DES Y3 for ϕ^* , M^* , α , and j are, respectively: (-1.30, 3.80), (-0.77, -22.23), (-0.27, -0.99), and (0.50, 1.85).

($M \approx M^*$) are just evolving passively. The peak in overall star formation activity occurred at $z \sim 2$. Since then, the average SFR has been steadily declining over time (Madau et al., 2014).

It is not trivial to interpret the evolution in luminosity and number density because they are strongly degenerate. A change in ϕ^* could be motivated by either a real difference in the overall number density as a consequence of mergers by the migration of M^* galaxies to other magnitude bins or the combination of both factors. The observed increase of ϕ^* with cosmic time can be associated with the overall fading of galaxies, so the LF knee moves gradually to fainter magnitudes, where galaxy populations are most abundant.

Therefore, the general evolutionary trend is better constrained by the luminosity density, j (Loveday et al., 2012), since it refers to the total amount of light emitted per unit volume at a given epoch of the Universe. Our estimates of j are close to those published by GAMA at $z \sim 0.1$ and $z \sim 0.5$ but disagree significantly at $z \sim 0.3$. This difference may be explained by the fact that GAMA is much shallower than DES, and it is strongly affected by spectroscopic targeting selection effects. Besides, GAMA observed a much smaller area than DES, not as small as VVDS, but possibly small enough to suffer from cosmic variance at some level. In our results, we do not observe significant evolution in the global luminosity density. The bump at $z \sim 0.5$ is likely an artificial effect introduced by photo-z significant uncertainties.

The general trend of underestimating the galaxy counts at faint-end is evident in the top right panel of Figure 5.19, where for DES Y3 are shifted to less negative values of α concerning the other results. Nevertheless, we also observe a steepening of $\Delta\alpha \approx -0.3$ with increasing redshift between $z \sim 0.1$ and $z \sim 0.9$, in agreement with Ilbert et al. (2005), who found $\Delta\alpha \approx -0.3$ and close to Ramos et al. (2011), who found $\Delta\alpha \approx -0.2$. The evolution of the faint-end slope is attributed to the changes in the relative contribution of different galaxy populations, subject of the next section.

Survey	z range	$\phi_1^* \times 10^{-3}$	$\phi_2^* \times 10^{-3}$	M^*	α_1	α_2
SDSS (Blanton et al., 2005b)	$z < 0.05$	4.28 ± 0.50	1.87 ± 0.40	-21.30 ± 0.04	-0.18 ± 0.08	-1.49 ± 0.01
DES SV (Capozzi et al., 2017)	$z < 0.20$	3.94 ± 0.05	0.10 ± 0.05	-21.63 ± 0.02	-0.88 ± 0.02	-1.59 ± 0.08
DES Y3 (this work)	$z < 0.20$	4.92 ± 0.68	0.11 ± 0.12	-21.99 ± 0.13	-0.77 ± 0.11	-1.65 ± 0.15

TABLE 5.4: Double Schechter fit parameters at low z .

Parameter	z	VVDS	CFHTLS	SDSS	GAMA	DES SV	DES Y3 (this work)
$\phi^* \times 10^{-3}$ (gal mag $^{-1}$ Mpc $^{-3}$)	0.0—0.2	$3.74^{+0.70}_{-0.61}$	3.57 ± 0.77	—	—	—	3.90 ± 0.55
	0.2—0.4	$1.50^{+0.46}_{-0.49}$	1.97 ± 0.20	4.22 ± 0.09	—	—	2.24 ± 0.55
	0.4—0.6	$0.77^{+0.24}_{-0.23}$	1.10 ± 0.16	3.96 ± 0.12	—	—	4.46 ± 0.47
	0.6—0.8	$1.59^{+0.30}_{-0.27}$	1.62 ± 0.07	4.42 ± 0.27	—	—	2.88 ± 0.24
	0.8—1.0	$0.97^{+0.50}_{-0.26}$	1.37 ± 0.12	—	—	0.823 ± 0.003	2.29 ± 0.14
	0.0—0.2	$-22.01^{+0.00}_{-0.00}$	-22.11 ± 0.26	—	—	—	-22.19 ± 0.10
	0.2—0.4	$-23.29^{+0.45}_{-0.75}$	-22.94 ± 0.07	-22.47 ± 0.03	—	-22.049 ± 0.005	-22.71 ± 0.18
	0.4—0.6	$-23.58^{+0.33}_{-0.45}$	-23.14 ± 0.06	-22.67 ± 0.03	—	-22.258 ± 0.004	-22.47 ± 0.07
	0.6—0.8	$-23.00^{+0.16}_{-0.18}$	-23.13 ± 0.02	-22.72 ± 0.04	—	-22.586 ± 0.003	-22.73 ± 0.06
	0.8—1.0	$-23.46^{+0.22}_{-0.26}$	-23.35 ± 0.04	—	—	-22.880 ± 0.003	-22.95 ± 0.04
α	0.0—0.2	$-1.19^{+0.04}_{-0.04}$	-1.31 ± 0.03	—	—	$-1.2(\text{fixed})$	-0.98 ± 0.06
	0.2—0.4	$-1.32^{+0.04}_{-0.04}$	-1.34 ± 0.02	-1.15	—	$-1.2(\text{fixed})$	-1.15 ± 0.06
	0.4—0.6	$-1.47^{+0.04}_{-0.04}$	-1.46 ± 0.03	-1.15	—	$-1.2(\text{fixed})$	-1.06 ± 0.05
	0.6—0.8	$-1.41^{+0.05}_{-0.05}$	-1.40 ± 0.01	-1.15	—	$-1.2(\text{fixed})$	-1.19 ± 0.03
	0.8—1.0	$-1.52^{+0.08}_{-0.08}$	-1.50 ± 0.02	—	—	$-1.2(\text{fixed})$	-1.22 ± 0.03
	0.0—0.2	—	—	—	2.35 (average)	—	1.84 ± 0.00
	0.2—0.4	—	—	2.12 ± 0.03	3.13 (average)	—	1.67 ± 0.00
	0.4—0.6	—	—	2.46 ± 0.03	—	—	2.71 ± 0.00
$j_i \times 10^8$ (L_\odot)	0.6—0.8	—	—	2.91 ± 0.04	—	—	2.17 ± 0.00
	0.8—1.0	—	—	—	—	—	2.09 ± 0.00
	0.00—0.05	—	—	—	1.61 ± 0.18	—	—
	0.05—0.10	—	—	—	2.06 ± 0.20	—	—
	0.10—0.15	—	—	—	2.89 ± 0.41	—	—
$j_i \times 10^8$ (L_\odot)	0.15—0.20	—	—	—	2.82 ± 0.20	—	—
	0.20—0.25	—	—	—	2.40 ± 0.23	—	—
	0.25—0.30	—	—	—	3.86 ± 0.18	—	—
	0.30—0.40	—	—	—	3.12 ± 0.15	—	—
	0.40—0.50	—	—	—	2.78 ± 0.24	—	—

TABLE 5.5: Single Schechter fit parameters and luminosity density.

5.4.2 LF of galaxy populations

The group of astronomical objects classified as “galaxies” is composed of a diverse population of individual objects that can be split into subgroups sharing characteristics in common. The definition of subcategories is a useful tool to map demographic properties and their evolution, trying to associate the resulting characteristics that are observable with their origin in physical processes. Classifications can be arbitrary, but they are really useful when the features used as criteria bring extra information. Analogously as in Biology, where living beings are categorized considering their evolutionary kinship, galaxy populations are separated in groups that share similarities in their evolution.

One of the main goals of this work is to study the evolution of the LF for different galaxy populations, and we adopted the morphological criteria to separate populations and measure them separately. During the research, we explored other systems of classification, for instance, based purely on colors or spectral types. The choice for the morphological classification is motivated by the better definition of the two populations in color-magnitude space, in comparison to other systems. As we are using preliminary data from an ongoing survey, the overall signal-to-noise ratio obtained up to the date is relatively low. The large errors in magnitude measurements spread the points in the CMD, making it difficult to define a trustworthy separation. It is worth to mention that morphological classification also requires high signal-to-noise and high-resolution images, so the confidence level of the classification depends on redshift considering that distant objects appear like point sources on the images.

The classification adopted is based on the light profile of objects in the coadded images. As mentioned in Chapter 2, the MOF photometry is based on the image fitting to a composite model that combines contributions from two light profiles: *de Vaucouleurs* and exponential. The morphological parameter *fracdev* (defined in Section 2.1.1) is the fraction of *de Vaucouleurs* model that contributes to the composite model fit to the image in MOF photometry, i.e., *fracdev*=1 is characteristic value for pure elliptical galaxies, and *fracdev*=0 for pure disk galaxies (100% exponential model).

We consider early-type galaxies those whose images were best fit to a model, which is more than 80% *de Vaucouleurs* profile. They can be interpreted as elliptical, spheroidal, or bulge-dominated systems, allowing the presence of a minor disk component, roughly equivalent to Ell, S0, and Sa Hubble types. The remaining objects are classified as late-type, so it comprehends disk-dominated objects, allowing some contribution of a bulge. The choice of *fracdev*=0.8 is arbitrary and tries to compensate for the difference in surface brightness of the different morphological components. We allow a substantial amount of *de Vaucouleur* fraction in late-types because, in bulge+disk systems, the light emitted by the disk component is commonly diffuse, contributing less to the final profile, so a 50% – 50% division would misplace many disk-dominated systems into the bulge-dominated category.

The resulting color-magnitude ($g - r$ versus g) and color-color ($g - r$ versus $r - i$) are presented in Figures 5.21 and 5.22 for the populations individually and for the total sample, showing that the classification adopted correlates strongly with the color-magnitude separation that defines the red sequence and the blue cloud.

We observe variations on the proportions of *fracdev* (Figure 5.23), and consequently on the fraction of early and late-types (5.24) in the redshift range studied in this work. There is a decreasing in the relative number of late-type galaxies, joined by an increasing of early-type galaxies. This trend is in agreement with the most accepted evolutionary scenario, where a small fraction of the late-type galaxies would experience major merges followed by quenching of star formation and dissolution of the disk structure, becoming early-type galaxies. The change in relative proportions propagates to the early/late specific luminosity functions, as we see in Figure 5.25.

We found three publications addressing the LF for early and late-types based on the *i*-band: Ramos et al. (2011), Loveday et al. (2012), and Bates et al. (2019), from which only the first one provided values for the single Schechter parameters estimates. Therefore, we extend the comparison with the literature and include comments on some works based on other photometric bands. We are aware that in some cases, the results are not comparable because different wavelength ranges bring distinct information. Nevertheless, we compare overall evolutionary trends keeping this caveat in mind.

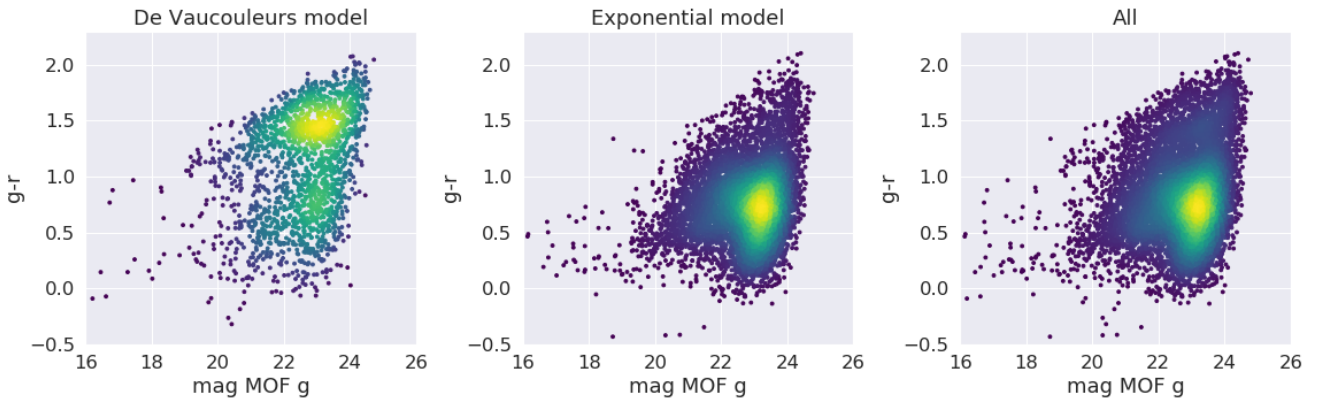


FIGURE 5.21: Color-magnitude diagram $g - r$ versus g for the two populations separately, early-type (predominantly adjusted to de Vaucouleurs model) on the left panel, late-type (predominantly adjusted to exponential model) on the middle panel, and the whole sample on the right panel. The density of points increase from dark blue to yellow.

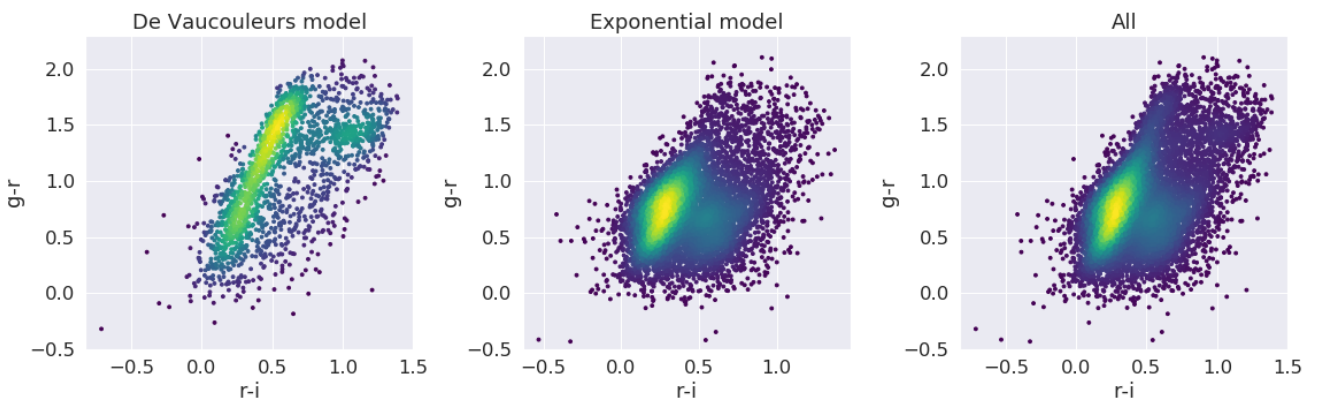


FIGURE 5.22: Color-color diagram $g - r$ versus $r - i$ for the two populations separately, early-type (predominantly adjusted to de Vaucouleurs model) on the left panel, late-type (predominantly adjusted to exponential model) on the middle panel, and the whole sample on the right panel. The density of points increase from dark blue to yellow.

Starting by the lowest redshift bin ($z < 0.2$, top panel of Figure 5.25), although the results of the global LF have already indicated a severe impact of incompleteness at the faint-end, the results for individual populations also show a clear upturn in the curve shape, making it better adjusted to a double Schechter function (parameters in Table 5.6). A similar upturn was previously observed by Loveday et al. (2012) in GAMA early-type LFs for the five bands analyzed ($ugriz$), which they attributed to the presence of dust-reddened disk galaxies. Nonetheless, as with the global LF, they found a better fit using double power-law, instead of double Schechter function.

The faint-end slope is strongly dependent on the galaxy type (steep for late-type and descending for early-type, a clear feature in Figure 5.25), but not much dependent on redshift, as evident by the almost flat lines on the top right panel of Figure 5.26. The faint-end is strongly dominated by late-type galaxies, in agreement with all results found in the literature (e.g., Ilbert et al., 2006; Zucca et al., 2006; Faber et al., 2007; Ramos et al., 2011), confirming that the faint regime is populated by low surface brightness exponential disks and predominantly blue, as stated by Blanton et al. (2005b). This feature is observed at all z bins we investigate, also evident by the similarity between the blue and black lines in α evolution, apart from the red line.

At the bright-end of the first bin ($z < 0.2$), the dominance of morphological type invert in comparison to the faint-end. According to our results, the brightest galaxies are predominantly spheroidal, and

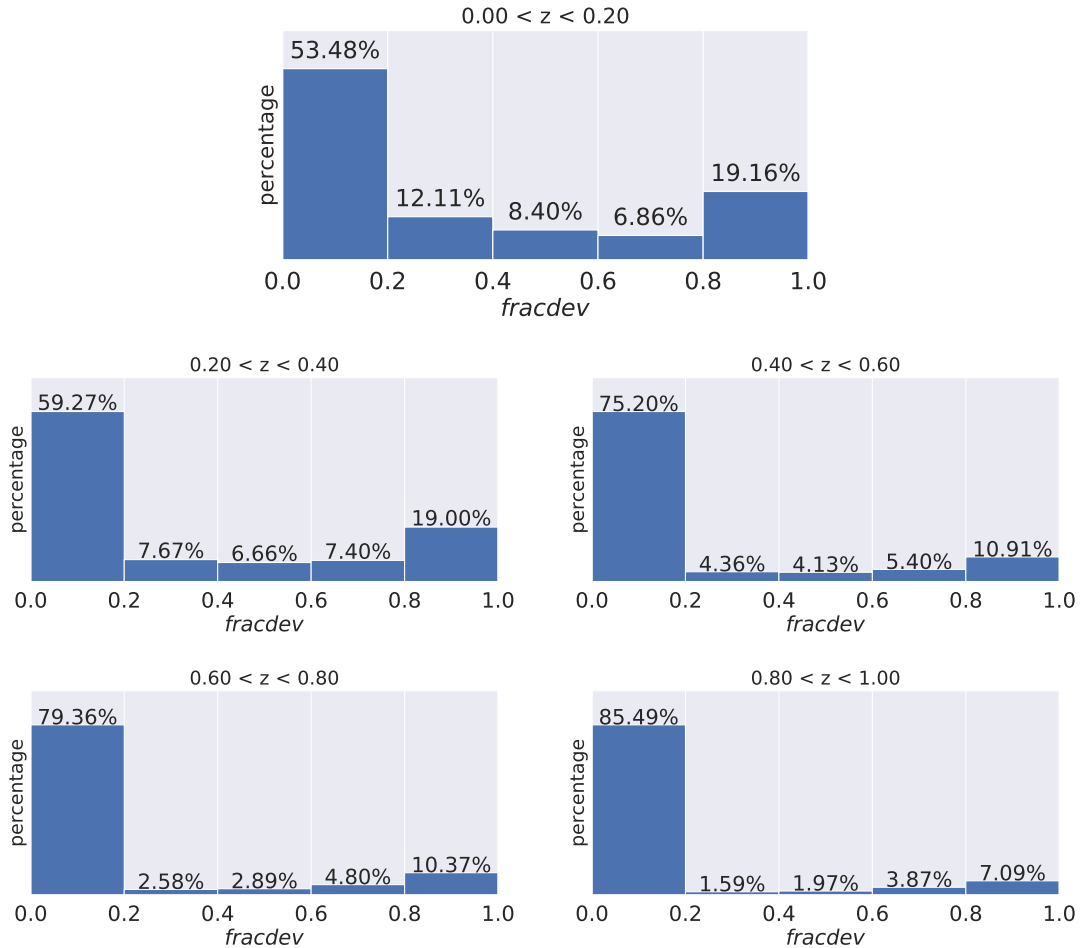


FIGURE 5.23: Distribution of $fracdev$ parameter in the GE science sample in redshift intervals.

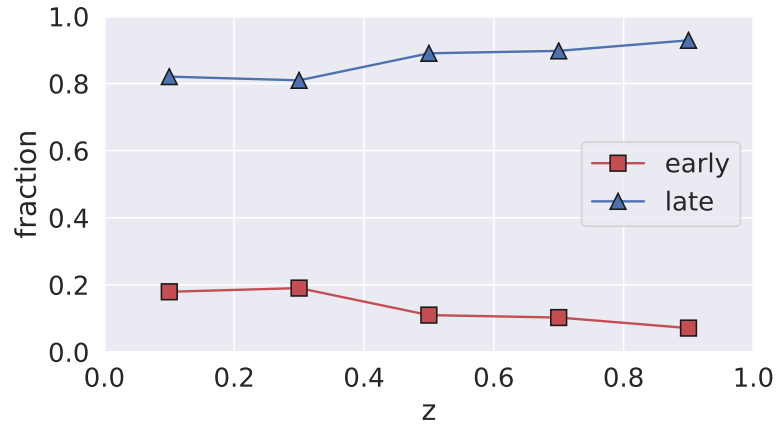


FIGURE 5.24: Fraction of early (in red) and late (in blue) type galaxies as a function of redshift.

very bright disks are rare. This result is in agreement with observations in the local Universe (Mo et al., 2010), and could be interpreted as an outcome of a hierarchical scenario, where the brightest galaxies would form by a history of mergers, resulting in very large objects gravitationally supported by velocity dispersion, therefore exhibiting a de Vaucouleurs light profile. The dominance of early-type galaxies

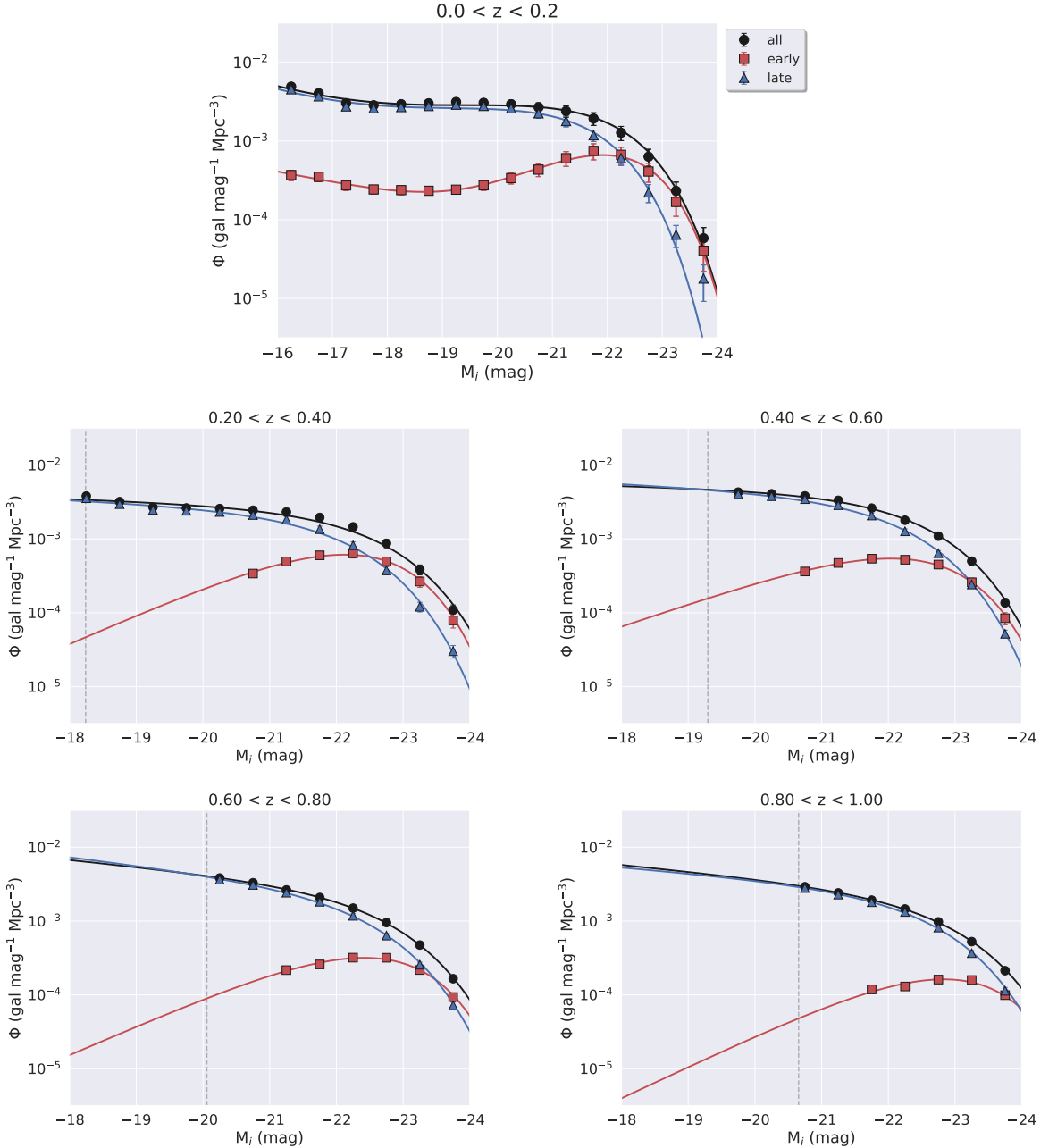


FIGURE 5.25: LF of early (red squares) and late-type (blue triangles) galaxies separately. Global LF in black circles for comparison. The results of fitting to the Schechter function are shown in Tables 5.6 and 5.7. Vertical dashed lines refer to the absolute magnitude limit.

at the bright-end increases with time. At $z \sim 0.7$ the contributions from early and late types to the two brightest magnitude bins are comparable. Before that, late-type dominated at all magnitude ranges. At higher redshifts ($z > 0.2$), there is no strong evidence of double Schechter shape in LF curves, possibly due to the fact that the fain-end is substantially incomplete, even for intervals of magnitude brighter than the absolute magnitude limit we estimate. Looking towards increasing redshifts, we notice that Φ at the brightest magnitude bin is approximately constant for early-type galaxies, suggesting that these objects were already in place before $z=1$, and most of the evolution occurred for magnitudes around M^* , or fainter. An exception is the first redshift bin ($z < 0.2$), where Φ at the brightest magnitude bin is significantly lower, but it could be a consequence of smaller comoving volume included in this redshift bin in comparison to the others, so the rarest objects are undersampled.

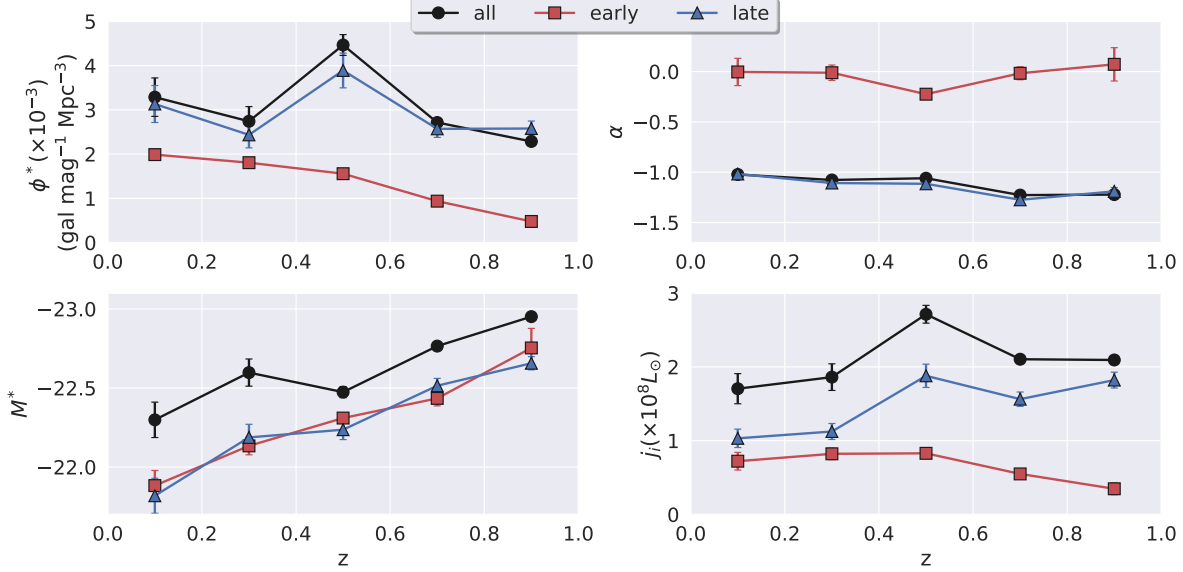


FIGURE 5.26: Evolution of Schechter parameters for the redshift intervals in Figure 5.25, adjusted to a single Schechter function (parameters in Table 5.7).

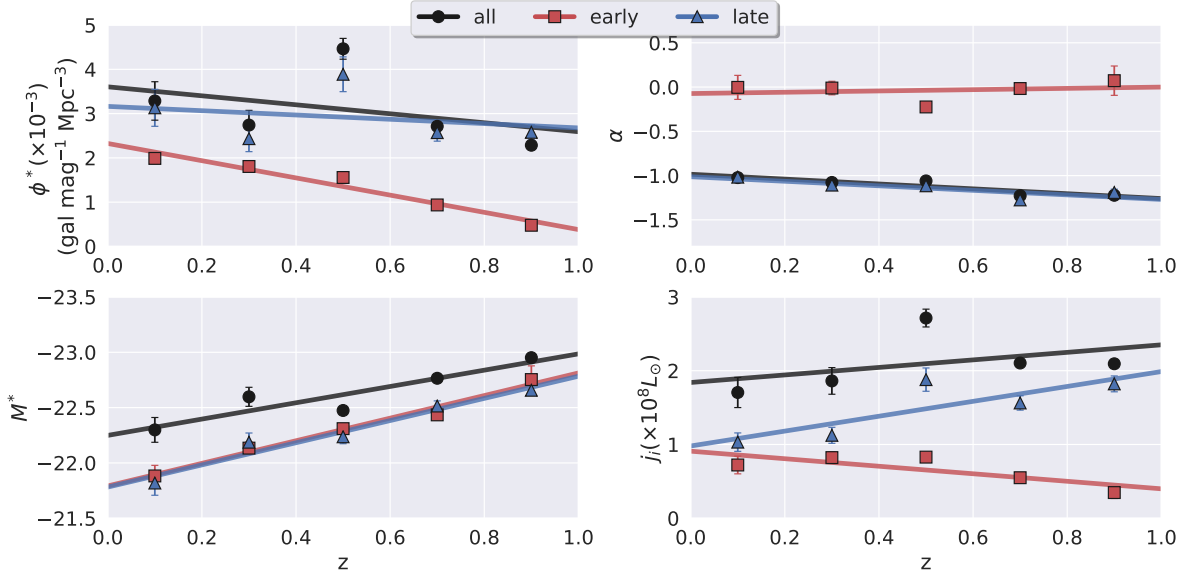


FIGURE 5.27: Same points as in Figure 5.26. Here the lines represent the linear fit to the results. The angular and linear coefficients obtained for ϕ^* , M^* , α and j are, respectively: (-1.94, 2.33), (-1.02, -21.79), (0.07, -0.07), and (-0.51, 0.91) for early-types, and (-0.49, 3.16), (-1.00, -21.78), (-0.26, -1.01), and (1.01, 0.98) for late-types.

Just like with the global LF, we also explore the evolution of best fit Schechter parameters through two ways of visualization, with and without adjusting the points to a linear function (Figures 5.26, and 5.27). On the four panels of Figure 5.26, it is easy to notice a bump around $z=0.5$ in the evolution of all parameters (positive or negative, depending on the parameter), escaping from the global trend of the other points. When visualizing the linear fit in Figure 5.27, it becomes clearer that the results for $z=0.5$ are outliers. This feature is artificially introduced by systematic errors, predominantly caused by the photo-z method. As we discuss at the end of Chapter 3, the redshift distribution of the science sample has an artificial peak introduced by systematic errors which are mitigated by the usage of PDFs, but not completely removed. The study to better understand and correct these systematic effects are subject to

ongoing work.

Analyzing the number density evolution, we notice a significant rise in early-type ϕ^* with decreasing redshift (a factor of ~ 4 between $z \sim 0.9$ and $z \sim 0.1$), while late-type ϕ^* present a mild rise ($\sim 21\%$). As M^* becomes faint with time, the number of galaxies with $\Phi \approx \phi^*$ increases. The difference between the ϕ^* evolution of the two types corroborates the hypothesis of transformation from late to early-type is still ongoing for ordinary galaxies ($M \sim M^*$). Previous works based on bluer bands also observed a rise in number density for early-types⁴, but found late-type ϕ^* constant (Faber et al., 2007) or declining in with cosmic time (Wolf et al., 2003; Ilbert et al., 2006; Zucca et al., 2006; Zucca et al., 2009). That outcome can be understood by the fact that bluer bands are more sensitive to changes in the star-formation activity, so the evolution is more detectable than in the i -band.

The luminosity evolution of individual types follows the same pattern as the global LF: an overall dimming of M^* with cosmic time. We found similar evolution for both types in the i -band LF, while Ramos et al. (2011) found that late-types M^* are fading much more quickly than early-types. One possible explanation is that their classification is based on the result of SED fitting, instead of morphology. Although the SED names follow the names of Hubble's morphological types, they represent the light from the mix of stellar populations typically present in these kinds of galaxies. Since the primary observables that led to SED fitting are fluxes (or magnitudes), the spectral classification must be interpreted more as a color indicator revealing predominant stellar populations than as an assumption of galaxies' morphologies. As pointed by Nakamura et al. (2003), the classification based on spectral indicators is more sensitive to small-scale changes in star-formation activity than morphological classification, so the strong evolution in Ramos et al. (2011) results shall be related to star formation history.

The results for the faint-end slope shows no significant evolution. While α is virtually constant for early-types, it barely increases for late-types, following the same path as the global LF. This parameter is commonly set as a fixed value by many authors, some fix it for all z intervals studied (e.g., Faber et al., 2007), and another fit is just for the highest z bins, where the determination of the LF faint-end is most difficult (e.g., Zucca et al., 2009; Ramos et al., 2011). Ilbert et al. (2006), for instance, determined α only for the interval $0.4 < z < 0.8$, and fixed the encountered value for the remaining bins in both directions, higher and lower valued of redshift. Our results show significantly lower values of $|\alpha|$ in comparison to the average found in the literature. We understand this outcome as a piece of evidence that the sample is still affected by incompleteness, despite the efforts to correct such effect using Balrog simulations. We had already reached that conclusion with the global LF, and a better solution to this problem is a subject of ongoing work. However, Capozzi et al. (2017) have argued that the evolutionary trends of ϕ^* and M^* are not very sensitive to the freedom of the parameter α on the fitting procedure, so the conclusions extracted from the other parameters should not change drastically when we manage to improve the LF faint-end estimates.

Finally, we find a stronger evolution of the luminosity density j for individual types than for the whole population. Early and late-types evolve in opposite directions with, increasing j for early, and decreasing j for late-type objects with cosmic time. Late-type galaxies are typically fainter than early-type, especially in i -band, which is not very sensitive to star formation activity. But, they are much more numerous, so the balance is that total j is decreasing with time, evident by the descending line with decreasing z on the bottom right panel of Figure 5.27. An alternative way to visualize the transferring of the relative importance of early and late-types on the total j is to follow the percent contribution of individual types as a function of z (Figure 5.28). We find that early-types approximately doubled their contribution since $z \sim 0.9$. This rise indicates that the total amount of stellar mass present in early-type galaxies with $M \approx M^*$ is increasing with time.

⁴Disclaimer: here we are generalizing the concept of early-type. The authors used different criteria to separate a bimodal population in two groups, e.g., red vs. blue, spectral early vs. spectral late, bulge-dominated vs. disk-dominated, etc. The classifications are not equivalent, but they preserve more characteristics in common than differences.

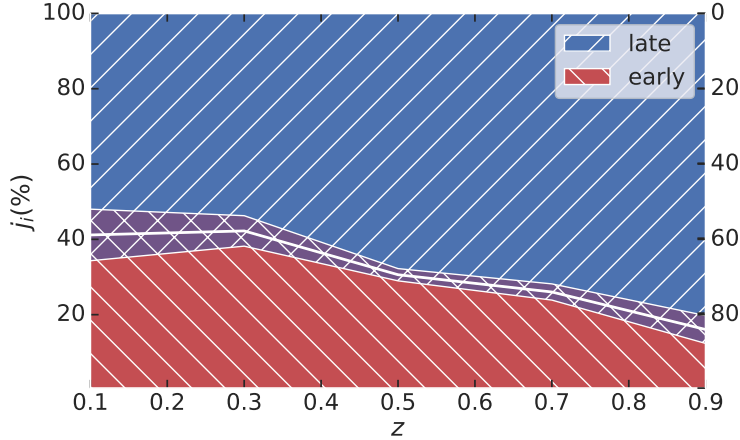


FIGURE 5.28: Percentage contribution of galaxy populations to the total luminosity density j as a function of redshift. The violet region corresponds to an uncertain range due to errors in j estimates of individual types.

Type	$\phi_1^* \times 10^{-3}$	$\phi_2^* \times 10^{-3}$	M^*	α_1	α_2
all	4.92 ± 0.68	0.11 ± 0.12	-21.99 ± 0.13	-0.77 ± 0.11	-1.65 ± 0.15
early	1.88 ± 0.67	0.07 ± 0.17	-21.84 ± 0.15	0.12 ± 0.15	-1.35 ± 0.19
late	4.44 ± 0.67	0.14 ± 0.17	-21.52 ± 0.15	-0.76 ± 0.15	-1.65 ± 0.19

TABLE 5.6: Double Schechter fit parameters.

Parameter	z	All	Early-types	Late-types
$\phi^* \times 10^{-3}$	$0.0 < z < 0.2$	3.29 ± 0.43	1.99 ± 0.12	3.13 ± 0.42
	$0.2 < z < 0.4$	2.74 ± 0.33	1.81 ± 0.07	2.43 ± 0.29
	$0.4 < z < 0.6$	4.46 ± 0.24	1.56 ± 0.04	3.89 ± 0.39
	$0.6 < z < 0.8$	2.71 ± 0.06	0.94 ± 0.03	2.57 ± 0.19
	$0.8 < z < 1.0$	2.29 ± 0.07	0.48 ± 0.02	2.58 ± 0.17
M^*	$0.0 < z < 0.2$	-22.30 ± 0.11	-21.88 ± 0.10	-21.82 ± 0.11
	$0.2 < z < 0.4$	-22.60 ± 0.09	-22.13 ± 0.06	-22.19 ± 0.08
	$0.4 < z < 0.6$	-22.47 ± 0.04	-22.31 ± 0.03	-22.24 ± 0.06
	$0.6 < z < 0.8$	-22.76 ± 0.01	-22.43 ± 0.05	-22.51 ± 0.05
	$0.8 < z < 1.0$	-22.95 ± 0.02	-22.75 ± 0.12	-22.66 ± 0.04
α	$0.0 < z < 0.2$	-1.02 ± 0.03	-0.00 ± 0.14	-1.02 ± 0.04
	$0.2 < z < 0.4$	-1.08 ± 0.04	-0.01 ± 0.08	-1.11 ± 0.04
	$0.4 < z < 0.6$	-1.06 ± 0.02	-0.22 ± 0.04	-1.12 ± 0.05
	$0.6 < z < 0.8$	-1.23 ± 0.01	-0.02 ± 0.06	-1.27 ± 0.03
	$0.8 < z < 1.0$	-1.22 ± 0.01	0.07 ± 0.17	-1.19 ± 0.04
$j_i \times 10^8 L_\odot$	$0.0 < z < 0.2$	1.70 ± 0.20	0.72 ± 0.12	1.03 ± 0.12
	$0.2 < z < 0.4$	1.86 ± 0.18	0.82 ± 0.08	1.12 ± 0.11
	$0.4 < z < 0.6$	2.71 ± 0.12	0.83 ± 0.04	1.88 ± 0.16
	$0.6 < z < 0.8$	2.10 ± 0.04	0.55 ± 0.05	1.56 ± 0.10
	$0.8 < z < 1.0$	2.09 ± 0.06	0.35 ± 0.08	1.82 ± 0.11

TABLE 5.7: Schechter fit parameters and luminosity density.

Chapter 6

Summary and conclusions

We explored galaxy evolution analysing the galaxy luminosity function for several populations.

The Samples

We used photometric data from the three first years of observations of the Dark Energy Survey and ancillary data from spectroscopic surveys available in the literature. We also used data from simulations (MICE) to test and validate several aspects of the methodology.

The sample selection was performed in two steps. First, we used ancillary maps and masks to remove entire regions which do not satisfy quality requirements. Second, we removed point sources, spurious objects, and galaxies fainter than magnitude 23.5 (*i*-band). The cleaning procedure removes approximately one-third of the original data set. We also defined an analogous data set with MICE and used it to evaluate the quality of both photo-z and absolute magnitude estimates, besides to understand the impact of some decisions made along the process.

Photo-zs

We built training, validation, and test samples from the combination of DES data with spectroscopic data obtained from public releases of surveys. We applied data mining and weighting techniques to the spectroscopic sample, aiming to select a pruned sub-sample that has photometric properties similar to those of the photometric data (regarding color and magnitude distributions). We adopted photo-z metrics similar to those used by Hildebrandt et al. (2010) and Sánchez et al. (2014) to analyze the results of the various tests quantitatively. With this weighted test set, we demonstrated that *griz* MOF magnitudes provide more accurate photo-zs than *grizY* SExtractor's AUTO. The results seem not being very sensitive to magnitude limit cuts within the range of $22.5 < i < 23.5$.

For the simulated catalog, we selected a random subset and split it into three parts to play the role of training, validation, and test samples. We compared results obtained using different photo-z algorithms and found DNF as the best choice for providing smaller bias and less scatter than ANNz2, LePhare, and MLZ when using DES-like magnitudes. We also quantified the impact of using extra magnitudes from external surveys and other input quantities, such as shape parameters. The latter seemed to worsen the photo-z results provided by DNF. We also evaluated the impact of using photo-z PDFs to recover the redshift distribution from magnitudes, instead of using single photo-z.

We verified that extra bands helped significantly to improve photo-z quality. The addition of UV data decreased the photo-z scatter at lower redshifts. The extra IR data removed the catastrophic errors at low-z and decreased the photo-z scatter in both ends of the redshift range studied. The combination of both is optimal, expanding the wavelength range in both ends of the spectrum. Comparing the two contributions separately, the IR brings larger improvements than the UV.

We demonstrated that if using only *griz*, the photo-z failures introduce artificial peaks on the $N(z)$ distribution, even if the training set is representative regarding the photometric properties of the test sample and has accurate magnitudes. This outcome can be explained by the high degree of degeneracy in the color-redshift relation, which is not possible to disentangle only using the four optical bands.

The usage of photo-z PDFs are quite helpful to improve the accuracy of the $N(z)$ estimates, but the improvement is substantial precisely when using the DES standard set of magnitudes. The effect of the PDFs is quantitatively similar to the addition of the u -band to the input parameters. If the IR data from $JHKs$ are available, the use of PDFs does not bring any extra improvement on recovering the $N(z)$.

Galaxy properties

The absolute magnitudes were estimated using the template-fitting algorithm LePhare, with fixed redshift previously computed using DNF. Tests with MICE demonstrated that the best method to recover the absolute magnitudes from the apparent magnitudes and redshift is to use the band closest to the object SED in its rest frame as a reference and use theoretical magnitudes to return to the desired band (in our case, the i -band). Thus, the higher the redshift, the redder the band used to estimate the absolute magnitudes, reinforcing the importance of adding data from IR surveys to the DES default data set. Moreover, when comparing different combinations of input data, the presence of IR bands revels to me more helpful than the true redshifts, i.e., absolute magnitudes are better estimated with DNF photo-zs, DES bands plus IR bands than with true redshifts and only DES bands.

We explored the coverage of the color-redshift and color-color diagrams by the COSMOS SED template set for MICE and DES samples. As MICE magnitudes were derived from COSMOS SEDs, the template set naturally provided a good representation of the galaxy colors in this sample. For DES data, the standard template set COSMOS was not enough to cover the scattering of points in color-color and color-redshift diagrams. To tackle this issue, on an *ad hoc* basis, we extrapolated the template set by adding synthetic templates from MARASTON models on both color extremes. On the red side, we added ten SED models of LRGs. On the blue side, we added five SEDs derived from simple stellar population models.

Luminosity function

To estimate the LF, we adapted the classical $1/V_{max}$ method to take into account incompleteness correction and photo-z PDFs. The former was computed based on the selection function of Balrog simulations, and the latter was provided by DNF photo-z algorithm. Again, we used MICE simulations to validate the method and to explore the dependence of the results on the input and methodology variations. With MICE, we demonstrated how the incorporation of photo-z PDFs in the LF estimator is a powerful trick to minimize the impact of photo-z uncertainties propagated to the LF results. At lower redshifts ($z < 0.2$), the inclusion of the u -band in the photo-z calculation helped to mitigate the overestimation of $\Phi(M)$ at the bright-end. At higher redshifts ($z > 0.4$), the systematic errors are dominated by contributions from limitations of the methodology (e.g., photo-z low accuracy, the degeneracy of SED templates, etc.), whereas at lower redshifts ($z < 0.4$), uncertainties in the magnitude measurements are most significant.

Comparing results obtained with different sample sizes (varying the area), we noticed that the total area of DES is much larger than the necessary to produce LF results without a significant impact of cosmic variance. This is a lesson learned to be applied in future work. As the total area is not necessary, we can prioritize depth and raise the threshold of magnitude limit in the region selection based on the depth map. For the final DES data release, we plan to use the 10σ detection map, allowing only the pixels that are at least one magnitude deeper than the limiting magnitude adopted in the object selection.

Galaxy evolution

We studied the evolution of the i -band galaxy LF at $z < 1$ in bins of $\Delta z = 0.2$ by tracing the variations of Schechter parameters ϕ^* , M^* , and α , and the luminosity density (j) in that z interval. We compared our results with recent findings from the literature that used the same photometric band, or that covered a similar wavelength range. There is not a perfect agreement among the several results, which is probably

a consequence of differences in the surveys' characteristics, calibrations, and methodologies. Therefore, we carried out the analyses paying attention to the evolutionary trends observed in each result, instead of comparing the parameter values. In general, for the global LF, we found similar trends, but with lower rates of change than those from the literature. We found a slight dimming of global M^* and j , with a modest increase in ϕ^* with cosmic time. This overall dimming of characteristic luminosity is compatible with a general decreasing of average SFR, which would have peaked at $z \sim < 2$ (the Lilly-Madau's plot).

We split the DES Y3 dataset into two galaxy populations called early-type (bulge-dominated) and late-type (disk-dominated) based on a morphological indicator extracted from the process of image reduction. We studied the evolution of the LF parameters for these two populations separately, and their relative contributions to the total luminosity density observed at $z < 1$. Late-type galaxies dominate the LF faint-end in all redshift bins. In contrast, the dominance at the bright-end depends on the redshift. At higher redshifts, the number density of very bright objects (≤ -22.5) is larger for late-types than for early-types. With decreasing redshift, these quantities decrease and become smaller than the values of $\phi(M)$ for the early-type population.

We observed that the characteristic luminosities are dimming with cosmic time for both types. The characteristic number density evolution is positive with time, with a larger rate for the early-type population. The combination of luminosity and number density evolution yields a mild decrease in the global luminosity density that is the result of a significant decrease in j for late-types accompanied by an increase in j for early-types. In the redshift range studied the early-type contribution to the total luminosity density boosted from $\sim 20\%$ to $\sim 40\%$.

We are able to extract evidences that favors a hierarchical scenario of galaxy evolution, accompanied by two sorts of downsizing. The first is the classical meaning of the term downsizing conceived by Cowie et al. (1996), where the star formation activity peaked at larger and more massive galaxies in the past, then in smaller and less massive in the present. We do not measure star formation indicators directly in this work to be able to make this statement as a strong conclusion, but the overall dimming of M^* and the decreasing of j point to that direction.

We observe a number density evolution compatible with the transformation of part of the late-type population into early-type galaxies since $z \sim 1.0$, combined with a decrease in the contribution of the faintest galaxies to the LF with time. This evidence could be interpreted as a transformation of smaller galaxies forming larger systems, as predicted in the hierarchical scenario.

However, when looking to the LF bright-end, we do not notice significant evolution since $z \sim 1.0$, so these brightest objects should have been already formed before this epoch, while ordinary galaxies continue building up mass in recent times. This could be an extrapolation of the concept of downsizing, in this case, regarding galaxy formation. Thus, the brightest galaxies would form first, still hierarchically by the assembling of smaller dark matter halos and merging galaxies. This effect could be explained by the influence of the environment, which we did not explore in this work. Higher density environments would serve as a catalyst for building-up massive and bright galaxies, so the first massive objects would form in the central regions of clusters. The same process of mergers would still occurring in lower density regions but in slower cadence. We plan to investigate the LF in different environments in the near future, taking advantage of the Wavelet Z Photometric (WAZP, Aguena et al. 2019, in prep.) cluster finder available in the DES Science Portal.

Perspectives

The discussion above represents preliminary conclusions drawn from a partial data release of DES. During the survey, we had the opportunity to build a whole infrastructure to allow the study of galaxy evolution, since the treatment of the data, passing through photometric redshifts and absolute magnitude estimates, reaching the implementation of a new method of estimating the LF, adapted from the classical $1/V_{max}$, accounting for a large number of corrections and improvements along all the steps of the process. The results presented in this thesis are proof of the concept that the “machinery” is ready to produce results as soon as the final data release is available, which is expected to happen next year. Therefore we

foresee a promising future of studies, both in the short term with the final DES data release and medium and long term with LSST. Until then, we plan to tackle a number of improvements, as discussed below.

The most relevant and direct improvement should come from the data itself. The DES Y3 contains data from the three first years of observations with the DECam. The final data release will include data from six years of observations. The number of coadded images that will be used to compose the Y6 catalog is larger than twice the number that was for Y3 because the third season of observations suffered a harsh impact from bad weather. The average number of images used at each pixel is ~ 3.8 , as shown in Section 2.1.1. For Y6, this number is expected to be ~ 10 , reaching the nominal depth predicted on the survey planning. Moreover, the DES collaboration is preparing a science sample from the deep fields described in Section 2.1.2, adding u -band photometry obtained with the DECam in the last seasons plus infrared data in $JHKs$ bands from UltraVISTA (McCracken et al., 2012) and VIDEO (Jarvis, 2012) surveys. The deep field coadded images are built with up to 200 exposures of 90 seconds, allowing a significantly higher signal to noise and better sampling of low surface brightness galaxies.

Regarding the data handling, we plan to:

- Review the foreground mask to eliminate the residual contamination by the light from bright stars that were not completely masked in the current version;
- Investigate and remove the contamination by QSOs and AGNs.
- Investigate alternative methods for star/galaxy classification to improve the completeness and purity of the galaxy sample.
- Review the signal-to-noise threshold to apply on the depth map — as we demonstrated in tests with MICE, a couple of hundreds of square degrees are enough to avoid effects of cosmic variance on the LF, so in the next tests we will prioritize pixels with deeper magnitude limit to guarantee a high signal-to-noise ratio, paying the price of removing a substantial fraction of the total area.
- Use the DES deep fields to investigate the reasons behind the lack of objects at the faint-end, especially at lower redshifts.

Regarding the methodology, we plan to:

- Extend the analysis to other photometric bands.
- Include the estimation of stellar masses in the pipeline to include the stellar mass function (MF) in the study.
- Explore different LF/MF estimators, e.g., step-wise maximum likelihood method (Efstathiou et al., 1988).
- Compute LF and MF for cluster and field galaxies separately.
- Continue the investigation to better understand the sources of systematic errors.
- Deepen in the studies on SED template set definition, investigating methods to deal with color-magnitude degeneracies.
- Explore different synthetic templates (e.g., Bruzual et al., 2003), using them to extract more information from galaxies besides absolute magnitudes and K-corrections.
- Use the LSST simulations to fine-tune all the steps and optimize the infrastructure to handle an even larger amount of data.

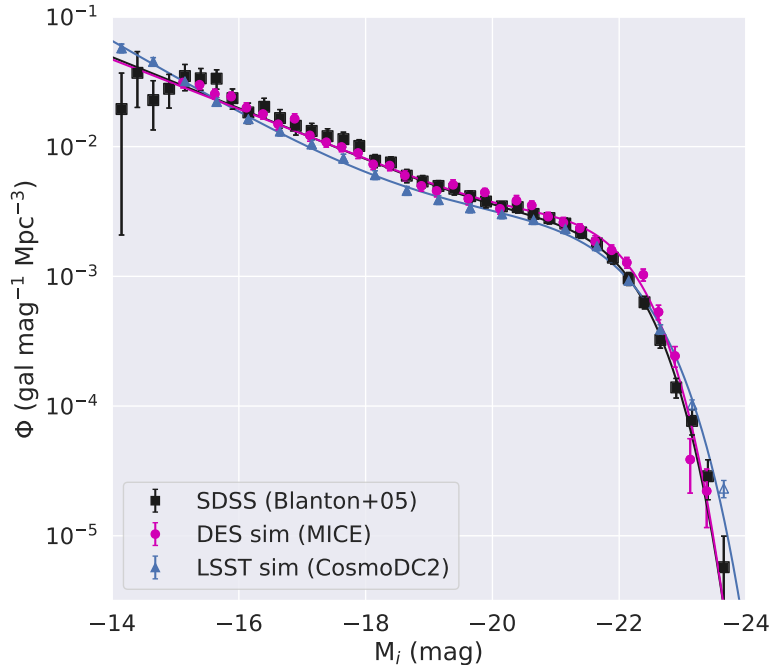


FIGURE 6.1: Luminosity function of galaxies at $z < 0.05$ from SDSS (Blanton et al., 2005b) in black, and at $z < 0.2$ for DES and LSST simulations, in pink and blue respectively.

In fact, we have already started the preparation for LSST. In Figure 6.1, we show the first measurement of the LF based on the CosmoDC2 simulation (Korytov et al., 2019) in preparation for the LSST, showing a clear double Schechter behavior, similar to what we obtained for DES simulations (MICE), which was based on SDSS LF. This preliminary result makes it clear that the deep LSST photometry will make it possible to measure the faint-end without loss beyond $M = -15$.

The survey strategy will two approaches: a huge volume associated to a *wide-fast-deep* survey ($18,000 \text{ deg}^2$, single epoch, $m_r < 24.5$), and the deep drilling fields, a narrow deep survey through the stacking of several longer exposures ($200\text{--}400 \text{ deg}^2$, stacked, $m_r < 27, 10\sigma$). All this covered by six optical filters ($ugrizY$). The data from this unprecedented volume of the sky will provide conditions for astronomers to explore how galaxies, especially the faintest, behave in different environments and epochs. One of the major challenges of LSST will be how to handle blending in crowded fields as the projected density of galaxies will rapidly increase.

We are especially interested in the deep drilling fields, which will be optimal for galaxy evolution studies owe to the very deep photometry containing the u -band, covering a large enough area. These characteristics will improve significantly the photometric redshift quality, which will propagate to galaxy properties measurements, LF, and MF estimates.

It should be mentioned that even before this, some progress will be possible with DES final dataset (Y6), and data that will be produced during the initial commissioning phase of LSST. The DES Y6 also includes a deep sample built from the supernova fields, which will contain u -band DECam photometry and IR data obtained from UltraVISTA and VIDEO, covering an area of $\sim 10 \text{ deg}^2$. The LF pipeline has been adapted to allow the usage of data from LSST, which has a different format and requires specific tools to be accessed. Now that the whole infrastructure is available, we are in a good position to carry out this work in the near future.

Bibliography

- Abazajian, K. N. et al. (2009). "The Seventh Data Release of the Sloan Digital Sky Survey". In: ApJS 182, pp. 543–558. DOI: [10.1088/0067-0049/182/2/543](https://doi.org/10.1088/0067-0049/182/2/543). arXiv: [0812.0649](https://arxiv.org/abs/0812.0649).
- Abbott, T. M. C. et al. (2006). "Cerro Tololo Inter-American Observatory, Victor M. Blanco 4-m Telescope, and the Dark Energy Survey". In: *Society of Photo-Optical Instrumentation Engineers (SPIE) Conference Series*. Vol. 6267. Proc. SPIE, p. 62673M. DOI: [10.1117/12.672527](https://doi.org/10.1117/12.672527).
- (2016). "The Dark Energy Survey: more than dark energy - an overview". In: MNRAS 460, pp. 1270–1299. DOI: [10.1093/mnras/stw641](https://doi.org/10.1093/mnras/stw641). arXiv: [1601.00329](https://arxiv.org/abs/1601.00329).
- (2017). "Dark Energy Survey Year 1 Results: Cosmological Constraints from Galaxy Clustering and Weak Lensing". In: *ArXiv e-prints*. arXiv: [1708.01530](https://arxiv.org/abs/1708.01530).
- (2018a). "Dark Energy Survey Year 1 Results: A Precise H_0 Estimate from DES Y1, BAO, and D/H Data". In: MNRAS 480, pp. 3879–3888. DOI: [10.1093/mnras/sty1939](https://doi.org/10.1093/mnras/sty1939). arXiv: [1711.00403](https://arxiv.org/abs/1711.00403).
- (2018b). "The Dark Energy Survey Data Release 1". In: *ArXiv e-prints*. arXiv: [1801.03181 \[astro-ph.IM\]](https://arxiv.org/abs/1801.03181).
- Abdalla, F. B. et al. (2011). "A comparison of six photometric redshift methods applied to 1.5 million luminous red galaxies". In: MNRAS 417, pp. 1891–1903. DOI: [10.1111/j.1365-2966.2011.19375.x](https://doi.org/10.1111/j.1365-2966.2011.19375.x). arXiv: [0812.3831](https://arxiv.org/abs/0812.3831).
- Abolfathi, B. et al. (2018). "The Fourteenth Data Release of the Sloan Digital Sky Survey: First Spectroscopic Data from the Extended Baryon Oscillation Spectroscopic Survey and from the Second Phase of the Apache Point Observatory Galactic Evolution Experiment". In: ApJS 235, 42, p. 42. DOI: [10.3847/1538-4365/aa9e8a](https://doi.org/10.3847/1538-4365/aa9e8a). arXiv: [1707.09322](https://arxiv.org/abs/1707.09322).
- Aihara, Hiroaki et al. (2018). "The Hyper Suprime-Cam SSP Survey: Overview and survey design". In: PASJ 70, S4, S4. DOI: [10.1093/pasj/psx066](https://doi.org/10.1093/pasj/psx066). arXiv: [1704.05858 \[astro-ph.IM\]](https://arxiv.org/abs/1704.05858).
- Annis, J., S. Bridle, F. J. Castander, et al. (2005). "Constraining Dark Energy with the Dark Energy Survey: Theoretical Challenges". In: *ArXiv Astrophysics e-prints*. eprint: [astro-ph/0510195](https://arxiv.org/abs/astro-ph/0510195).
- Annunziatella, M. et al. (2016). "CLASH-VLT: Environment-driven evolution of galaxies in the $z = 0.209$ cluster Abell 209". In: A&A 585, A160, A160. DOI: [10.1051/0004-6361/201527399](https://doi.org/10.1051/0004-6361/201527399). arXiv: [1510.05659](https://arxiv.org/abs/1510.05659).
- Arnouts, S. et al. (1999). "Measuring and modelling the redshift evolution of clustering: the Hubble Deep Field North". In: MNRAS 310, pp. 540–556. DOI: [10.1046/j.1365-8711.1999.02978.x](https://doi.org/10.1046/j.1365-8711.1999.02978.x). eprint: [astro-ph/9902290](https://arxiv.org/abs/astro-ph/9902290).
- Arnouts, S. et al. (2001). "ESO imaging survey. Deep public survey: Multi-color optical data for the Chandra Deep Field South". In: A&A 379, pp. 740–754. DOI: [10.1051/0004-6361:20011341](https://doi.org/10.1051/0004-6361:20011341). arXiv: [astro-ph/0103071 \[astro-ph\]](https://arxiv.org/abs/astro-ph/0103071).
- Baldry, I. K. et al. (2012). "Galaxy And Mass Assembly (GAMA): the galaxy stellar mass function at $z < 0.06$ ". In: MNRAS 421, pp. 621–634. DOI: [10.1111/j.1365-2966.2012.20340.x](https://doi.org/10.1111/j.1365-2966.2012.20340.x). arXiv: [1111.5707](https://arxiv.org/abs/1111.5707).
- (2018). "Galaxy And Mass Assembly: the G02 field, Herschel-ATLAS target selection and data release 3". In: MNRAS 474, pp. 3875–3888. DOI: [10.1093/mnras/stx3042](https://doi.org/10.1093/mnras/stx3042). arXiv: [1711.09139](https://arxiv.org/abs/1711.09139).
- Balestra, I. et al. (2016). "CLASH-VLT: Dissecting the Frontier Fields Galaxy Cluster MACS J0416.1-2403 with approx. 800 Spectra of Member Galaxies". In: ApJS 224, 33, p. 33. DOI: [10.3847/0067-0049/224/2/33](https://doi.org/10.3847/0067-0049/224/2/33). arXiv: [1511.02522](https://arxiv.org/abs/1511.02522).
- Banerji, M. et al. (2015). "Combining Dark Energy Survey Science Verification data with near-infrared data from the ESO VISTA Hemisphere Survey". In: MNRAS 446, pp. 2523–2539. DOI: [10.1093/mnras/stu2261](https://doi.org/10.1093/mnras/stu2261). arXiv: [1407.3801](https://arxiv.org/abs/1407.3801).

- Bates, Dominic J. et al. (2019). "Mass functions, luminosity functions, and completeness measurements from clustering redshifts". In: MNRAS 486.3, pp. 3059–3077. DOI: [10.1093/mnras/stz997](https://doi.org/10.1093/mnras/stz997). arXiv: [1810.01767 \[astro-ph.GA\]](https://arxiv.org/abs/1810.01767).
- Baum, W. A. (1962). "Photoelectric Magnitudes and Red-Shifts". In: *Problems of Extra-Galactic Research*. Ed. by G. C. McVittie. Vol. 15. IAU Symposium, p. 390.
- Bayliss, M. B. et al. (2016). "SPT-GMOS: A Gemini/GMOS-South Spectroscopic Survey of Galaxy Clusters in the SPT-SZ Survey". In: ApJS 227, 3, p. 3. DOI: [10.3847/0067-0049/227/1/3](https://doi.org/10.3847/0067-0049/227/1/3). arXiv: [1609.05211](https://arxiv.org/abs/1609.05211).
- Bazin, G. et al. (2011). "Photometric selection of Type Ia supernovae in the Supernova Legacy Survey". In: A&A 534, A43, A43. DOI: [10.1051/0004-6361/201116898](https://doi.org/10.1051/0004-6361/201116898). arXiv: [1109.0948](https://arxiv.org/abs/1109.0948).
- Beckwith, S. V. W., M. Stiavelli, A. M. Koekemoer, et al. (2006). "The Hubble Ultra Deep Field". In: AJ 132, pp. 1729–1755. DOI: [10.1086/507302](https://doi.org/10.1086/507302). eprint: [astro-ph/0607632](https://arxiv.org/abs/astro-ph/0607632).
- Benítez, N. (2000). "Bayesian Photometric Redshift Estimation". In: ApJ 536, pp. 571–583. DOI: [10.1086/308947](https://doi.org/10.1086/308947). eprint: [astro-ph/9811189](https://arxiv.org/abs/astro-ph/9811189).
- Bertin, E. (2011). "Automated Morphometry with SExtractor and PSFEx". In: *Astronomical Data Analysis Software and Systems XX*. Ed. by I. N. Evans et al. Astronomical Society of the Pacific Conference Series, p. 435.
- Bertin, E. and S. Arnouts (1996). "SExtractor: Software for source extraction." In: A&AS 117, pp. 393–404. DOI: [10.1051/aas:1996164](https://doi.org/10.1051/aas:1996164).
- Binney, J. and S. Tremaine (1987). *Galactic dynamics*.
- Biviano, A. et al. (2013). "CLASH-VLT: The mass, velocity-anisotropy, and pseudo-phase-space density profiles of the $z = 0.44$ galaxy cluster MACS J1206.2-0847". In: A&A 558, A1, A1. DOI: [10.1051/0004-6361/201321955](https://doi.org/10.1051/0004-6361/201321955). arXiv: [1307.5867](https://arxiv.org/abs/1307.5867).
- Blake, C. et al. (2016). "The 2-degree Field Lensing Survey: design and clustering measurements". In: MNRAS 462, pp. 4240–4265. DOI: [10.1093/mnras/stw1990](https://doi.org/10.1093/mnras/stw1990). arXiv: [1608.02668](https://arxiv.org/abs/1608.02668).
- Blanton, M. R. et al. (2003). "The Galaxy Luminosity Function and Luminosity Density at Redshift $z = 0.1$ ". In: ApJ 592, pp. 819–838. DOI: [10.1086/375776](https://doi.org/10.1086/375776). eprint: [astro-ph/0210215](https://arxiv.org/abs/astro-ph/0210215).
- (2005a). "New York University Value-Added Galaxy Catalog: A Galaxy Catalog Based on New Public Surveys". In: AJ 129, pp. 2562–2578. DOI: [10.1086/429803](https://doi.org/10.1086/429803). eprint: [astro-ph/0410166](https://arxiv.org/abs/astro-ph/0410166).
- (2005b). "The Properties and Luminosity Function of Extremely Low Luminosity Galaxies". In: ApJ 631, pp. 208–230. DOI: [10.1086/431416](https://doi.org/10.1086/431416). eprint: [astro-ph/0410164](https://arxiv.org/abs/astro-ph/0410164).
- Bolzonella, M., J.-M. Miralles, and R. Pelló (2000). "Photometric redshifts based on standard SED fitting procedures". In: A&A 363, pp. 476–492. eprint: [astro-ph/0003380](https://arxiv.org/abs/astro-ph/0003380).
- Bonnett, C. (2015). "Using neural networks to estimate redshift distributions. An application to CFHTLenS". In: MNRAS 449, pp. 1043–1056. DOI: [10.1093/mnras/stv230](https://doi.org/10.1093/mnras/stv230). arXiv: [1312.1287](https://arxiv.org/abs/1312.1287).
- Bonnett, C. et al. (2016). "Redshift distributions of galaxies in the Dark Energy Survey Science Verification shear catalogue and implications for weak lensing". In: Phys. Rev. D 94.4, 042005, p. 042005. DOI: [10.1103/PhysRevD.94.042005](https://doi.org/10.1103/PhysRevD.94.042005). arXiv: [1507.05909](https://arxiv.org/abs/1507.05909).
- Brammer, G. B., P. G. van Dokkum, and P. Coppi (2008). "EAZY: A Fast, Public Photometric Redshift Code". In: ApJ 686, pp. 1503–1513. DOI: [10.1086/591786](https://doi.org/10.1086/591786). arXiv: [0807.1533](https://arxiv.org/abs/0807.1533).
- Bray, Tim et al. (2008). *Extensible markup language (XML) 1.0*.
- Bruzual, G. and S. Charlot (2003). "Stellar population synthesis at the resolution of 2003". In: MNRAS 344, pp. 1000–1028. DOI: [10.1046/j.1365-8711.2003.06897.x](https://doi.org/10.1046/j.1365-8711.2003.06897.x). eprint: [astro-ph/0309134](https://arxiv.org/abs/astro-ph/0309134).
- Buchs, R. et al. (2019). "Phenotypic redshifts with self-organizing maps: A novel method to characterize redshift distributions of source galaxies for weak lensing". In: *arXiv e-prints*, arXiv:1901.05005, arXiv:1901.05005. arXiv: [1901.05005 \[astro-ph.CO\]](https://arxiv.org/abs/1901.05005).
- Burke, D. L. et al. (2018). "Forward Global Photometric Calibration of the Dark Energy Survey". In: AJ 155, 41, p. 41. DOI: [10.3847/1538-3881/aa9f22](https://doi.org/10.3847/1538-3881/aa9f22). arXiv: [1706.01542 \[astro-ph.IM\]](https://arxiv.org/abs/1706.01542).
- Calzetti, D. et al. (2000). "The Dust Content and Opacity of Actively Star-forming Galaxies". In: ApJ 533, pp. 682–695. DOI: [10.1086/308692](https://doi.org/10.1086/308692). eprint: [astro-ph/9911459](https://arxiv.org/abs/astro-ph/9911459).

- Caminha, G. B. et al. (2017). "A refined mass distribution of the cluster MACS J0416.1-2403 from a new large set of spectroscopic multiply lensed sources". In: A&A 600, A90, A90. DOI: [10.1051/0004-6361/201629297](https://doi.org/10.1051/0004-6361/201629297). arXiv: [1607.03462](https://arxiv.org/abs/1607.03462).
- Capak, P. et al. (2004). "A Deep Wide-Field, Optical, and Near-Infrared Catalog of a Large Area around the Hubble Deep Field North". In: AJ 127.1, pp. 180–198. DOI: [10.1086/380611](https://doi.org/10.1086/380611). arXiv: [astro-ph/0312635 \[astro-ph\]](https://arxiv.org/abs/astro-ph/0312635).
- Capak, P. et al. (2007). "The First Release COSMOS Optical and Near-IR Data and Catalog". In: ApJS 172.1, pp. 99–116. DOI: [10.1086/519081](https://doi.org/10.1086/519081). arXiv: [0704.2430 \[astro-ph\]](https://arxiv.org/abs/0704.2430).
- Capozzi, D. et al. (2017). "Evolution of Galaxy Luminosity and Stellar-Mass Functions since $z = 1$ with the Dark Energy Survey Science Verification Data". In: arXiv e-prints. arXiv: [1707.09066](https://arxiv.org/abs/1707.09066).
- Carlstrom, J. E. et al. (2011). "The 10 Meter South Pole Telescope". In: PASP 123, p. 568. DOI: [10.1086/659879](https://doi.org/10.1086/659879). arXiv: [0907.4445 \[astro-ph.IM\]](https://arxiv.org/abs/0907.4445).
- Carnero, A. et al. (2012). "Clustering of photometric luminous red galaxies - II. Cosmological implications from the baryon acoustic scale". In: MNRAS 419, pp. 1689–1694. DOI: [10.1111/j.1365-2966.2011.19832.x](https://doi.org/10.1111/j.1365-2966.2011.19832.x). arXiv: [1104.5426](https://arxiv.org/abs/1104.5426).
- Carrasco Kind, M. and R. J. Brunner (2013). "TPZ: photometric redshift PDFs and ancillary information by using prediction trees and random forests". In: MNRAS 432, pp. 1483–1501. DOI: [10.1093/mnras/stt574](https://doi.org/10.1093/mnras/stt574). arXiv: [1303.7269](https://arxiv.org/abs/1303.7269).
- (2014a). "SOMz: photometric redshift PDFs with self-organizing maps and random atlas". In: MNRAS 438, pp. 3409–3421. DOI: [10.1093/mnras/stt2456](https://doi.org/10.1093/mnras/stt2456). arXiv: [1312.5753 \[astro-ph.IM\]](https://arxiv.org/abs/1312.5753).
 - (2014b). "Sparse representation of photometric redshift probability density functions: preparing for petascale astronomy". In: MNRAS 441, pp. 3550–3561. DOI: [10.1093/mnras/stu827](https://doi.org/10.1093/mnras/stu827). arXiv: [1404.6442 \[astro-ph.IM\]](https://arxiv.org/abs/1404.6442).
- Carretero, J. et al. (2015). "An algorithm to build mock galaxy catalogues using MICE simulations". In: MNRAS 447, pp. 646–670. DOI: [10.1093/mnras/stu2402](https://doi.org/10.1093/mnras/stu2402). arXiv: [1411.3286 \[astro-ph.GA\]](https://arxiv.org/abs/1411.3286).
- Chang, C. et al. (2018). "Dark Energy Survey Year 1 results: curved-sky weak lensing mass map". In: MNRAS 475, pp. 3165–3190. DOI: [10.1093/mnras/stx3363](https://doi.org/10.1093/mnras/stx3363). arXiv: [1708.01535](https://arxiv.org/abs/1708.01535).
- Childress, M. J. et al. (2017). "OzDES multifibre spectroscopy for the Dark Energy Survey: 3-yr results and first data release". In: MNRAS 472, pp. 273–288. DOI: [10.1093/mnras/stx1872](https://doi.org/10.1093/mnras/stx1872). arXiv: [1708.04526](https://arxiv.org/abs/1708.04526).
- Coil, A. L. et al. (2011). "The PRISM Multi-object Survey (PRIMUS). I. Survey Overview and Characteristics". In: ApJ 741, 8, p. 8. DOI: [10.1088/0004-637X/741/1/8](https://doi.org/10.1088/0004-637X/741/1/8). arXiv: [1011.4307](https://arxiv.org/abs/1011.4307).
- Colless, M. et al. (2001). "The 2dF Galaxy Redshift Survey: spectra and redshifts". In: MNRAS 328, pp. 1039–1063. DOI: [10.1046/j.1365-8711.2001.04902.x](https://doi.org/10.1046/j.1365-8711.2001.04902.x). eprint: [astro-ph/0106498](https://arxiv.org/abs/astro-ph/0106498).
- Collister, A. A. and O. Lahav (2004). "ANNz: Estimating Photometric Redshifts Using Artificial Neural Networks". In: PASP 116, pp. 345–351. DOI: [10.1086/383254](https://doi.org/10.1086/383254). eprint: [astro-ph/0311058](https://arxiv.org/abs/astro-ph/0311058).
- Conselice, C. J. et al. (2016). "The Evolution of Galaxy Number Density at $z < 8$ and Its Implications". In: ApJ 830, 83, p. 83. DOI: [10.3847/0004-637X/830/2/83](https://doi.org/10.3847/0004-637X/830/2/83). arXiv: [1607.03909](https://arxiv.org/abs/1607.03909).
- Content, R., A. Cimatti, M. Robberto, et al. (2008). "Offspring of SPACE: the spectrograph channel of the ESA Dark Energy Mission EUCLID". In: Space Telescopes and Instrumentation 2008: Optical, Infrared, and Millimeter. Vol. 7010. procspie, 70104S. DOI: [10.1117/12.805409](https://doi.org/10.1117/12.805409).
- Cool, R. J. et al. (2013). "The PRISM Multi-object Survey (PRIMUS). II. Data Reduction and Redshift Fitting". In: ApJ 767, 118, p. 118. DOI: [10.1088/0004-637X/767/2/118](https://doi.org/10.1088/0004-637X/767/2/118). arXiv: [1303.2672](https://arxiv.org/abs/1303.2672).
- Cooper, M. C. et al. (2012). "The Arizona CDFS Environment Survey (ACES): A Magellan/IMACS Spectroscopic Survey of the Chandra Deep Field-South". In: MNRAS 425, pp. 2116–2127. DOI: [10.1111/j.1365-2966.2012.21524.x](https://doi.org/10.1111/j.1365-2966.2012.21524.x). arXiv: [1112.0312](https://arxiv.org/abs/1112.0312).
- Cowie, Lennox L. et al. (1996). "New Insight on Galaxy Formation and Evolution From Keck Spectroscopy of the Hawaii Deep Fields". In: AJ 112, p. 839. DOI: [10.1086/118058](https://doi.org/10.1086/118058). arXiv: [astro-ph/9606079 \[astro-ph\]](https://arxiv.org/abs/astro-ph/9606079).
- Cunha, C. E. et al. (2009). "Estimating the redshift distribution of photometric galaxy samples - II. Applications and tests of a new method". In: MNRAS 396, pp. 2379–2398. DOI: [10.1111/j.1365-2966.2009.14908.x](https://doi.org/10.1111/j.1365-2966.2009.14908.x). arXiv: [0810.2991](https://arxiv.org/abs/0810.2991).

- Dawson, Kyle S. et al. (2016). "The SDSS-IV Extended Baryon Oscillation Spectroscopic Survey: Overview and Early Data". In: AJ 151.2, 44, p. 44. DOI: [10.3847/0004-6256/151/2/44](https://doi.org/10.3847/0004-6256/151/2/44). arXiv: [1508.04473 \[astro-ph.CO\]](https://arxiv.org/abs/1508.04473).
- De Vicente, J., E. Sánchez, and I. Sevilla-Noarbe (2016). "DNF - Galaxy photometric redshift by Directional Neighbourhood Fitting". In: MNRAS 459, pp. 3078–3088. DOI: [10.1093/mnras/stw857](https://doi.org/10.1093/mnras/stw857). arXiv: [1511.07623](https://arxiv.org/abs/1511.07623).
- Desai, S. et al. (2012). "The Blanco Cosmology Survey: Data Acquisition, Processing, Calibration, Quality Diagnostics, and Data Release". In: ApJ 757, 83, p. 83. DOI: [10.1088/0004-637X/757/1/83](https://doi.org/10.1088/0004-637X/757/1/83). arXiv: [1204.1210 \[astro-ph.CO\]](https://arxiv.org/abs/1204.1210).
- DESI Collaboration et al. (2016). "The DESI Experiment Part I: Science, Targeting, and Survey Design". In: *arXiv e-prints*, arXiv:1611.00036, arXiv:1611.00036. arXiv: [1611.00036 \[astro-ph.IM\]](https://arxiv.org/abs/1611.00036).
- Dressler, A. (1980). "Galaxy morphology in rich clusters: implications for the formation and evolution of galaxies." In: ApJ 236, pp. 351–365. DOI: [10.1086/157753](https://doi.org/10.1086/157753).
- Driver, S. P. et al. (2011). "Galaxy and Mass Assembly (GAMA): survey diagnostics and core data release". In: MNRAS 413, pp. 971–995. DOI: [10.1111/j.1365-2966.2010.18188.x](https://doi.org/10.1111/j.1365-2966.2010.18188.x). arXiv: [1009.0614](https://arxiv.org/abs/1009.0614).
- Drlica-Wagner, A. et al. (2018). "Dark Energy Survey Year 1 Results: The Photometric Data Set for Cosmology". In: ApJS 235, 33, p. 33. DOI: [10.3847/1538-4365/aab4f5](https://doi.org/10.3847/1538-4365/aab4f5). arXiv: [1708.01531](https://arxiv.org/abs/1708.01531).
- Efstathiou, G., Richard S. Ellis, and Bruce A. Peterson (1988). "Analysis of a complete galaxy redshift survey. II. The field-galaxy luminosity function." In: MNRAS 232, pp. 431–461. DOI: [10.1093/mnras/232.2.431](https://doi.org/10.1093/mnras/232.2.431).
- Elvin-Poole, J. et al. (2018). "Dark Energy Survey year 1 results: Galaxy clustering for combined probes". In: Phys. Rev. D 98.4, 042006, p. 042006. DOI: [10.1103/PhysRevD.98.042006](https://doi.org/10.1103/PhysRevD.98.042006). arXiv: [1708.01536](https://arxiv.org/abs/1708.01536).
- Faber, S. M. et al. (2007). "Galaxy Luminosity Functions to $z \sim 1$ from DEEP2 and COMBO-17: Implications for Red Galaxy Formation". In: ApJ 665, pp. 265–294. DOI: [10.1086/519294](https://doi.org/10.1086/519294). eprint: [astro-ph/0506044](https://arxiv.org/abs/astro-ph/0506044).
- Fausti Neto, A. et al. (2018). "DES science portal: Creating science-ready catalogs". In: *Astronomy and Computing* 24, 52, p. 52. DOI: [10.1016/j.ascom.2018.01.002](https://doi.org/10.1016/j.ascom.2018.01.002). arXiv: [1708.05642 \[astro-ph.IM\]](https://arxiv.org/abs/1708.05642).
- Fioc, M. and B. Rocca-Volmerange (1997). "PEGASE: a UV to NIR spectral evolution model of galaxies. Application to the calibration of bright galaxy counts." In: A&A 326, pp. 950–962. eprint: [astro-ph/9707017](https://arxiv.org/abs/astro-ph/9707017).
- Fitzpatrick, E. L. (1999). "Correcting for the Effects of Interstellar Extinction". In: PASP 111, pp. 63–75. DOI: [10.1086/316293](https://doi.org/10.1086/316293). eprint: [astro-ph/9809387](https://arxiv.org/abs/astro-ph/9809387).
- Flaugh, B. (2005). "The Dark Energy Survey". In: *International Journal of Modern Physics A* 20, pp. 3121–3123. DOI: [10.1142/S0217751X05025917](https://doi.org/10.1142/S0217751X05025917).
- Flaugh, B. et al. (2015). "The Dark Energy Camera". In: AJ 150, 150, p. 150. DOI: [10.1088/0004-6256/150/5/150](https://doi.org/10.1088/0004-6256/150/5/150). arXiv: [1504.02900 \[astro-ph.IM\]](https://arxiv.org/abs/1504.02900).
- Foster, Ian (1995). *Designing and building parallel programs : concepts and tools for parallel software engineering*. Reading, Mass: Addison-Wesley. ISBN: 9780201575941.
- Franceschini, A. et al. (2006). "Cosmic evolution of the galaxy's mass and luminosity functions by morphological type from multi-wavelength data in the CDF-South". In: *Astronomy and Astrophysics* 453.2, pp. 397–421. DOI: [10.1051/0004-6361:20054360](https://doi.org/10.1051/0004-6361:20054360). arXiv: [astro-ph/0601003 \[astro-ph\]](https://arxiv.org/abs/astro-ph/0601003).
- Fried, J. W. et al. (2001). "The luminosity function of field galaxies and its evolution since $z=1$ ". In: A&A 367, pp. 788–800. DOI: [10.1051/0004-6361:20000466](https://doi.org/10.1051/0004-6361:20000466). arXiv: [astro-ph/0012343 \[astro-ph\]](https://arxiv.org/abs/astro-ph/0012343).
- Galametz, A., the CANDELS Team, et al. (2013). "CANDELS Multiwavelength Catalogs: Source Identification and Photometry in the CANDELS UKIDSS Ultra-deep Survey Field". In: ApJS 206, 10, p. 10. DOI: [10.1088/0067-0049/206/2/10](https://doi.org/10.1088/0067-0049/206/2/10). arXiv: [1305.1823 \[astro-ph.CO\]](https://arxiv.org/abs/1305.1823).
- Gallagher III, J. S. and J. P. Ostriker (1972). "A Note on Mass Loss during Collisions between Galaxies and the Formation of Giant Systems". In: AJ 77, p. 288. DOI: [10.1086/111280](https://doi.org/10.1086/111280).
- Garilli, B. et al. (2008). "The Vimos VLT deep survey. Global properties of 20,000 galaxies in the $I_{AB} < 22.5$ WIDE survey". In: A&A 486, pp. 683–695. DOI: [10.1051/0004-6361:20078878](https://doi.org/10.1051/0004-6361:20078878). arXiv: [0804.4568](https://arxiv.org/abs/0804.4568).

- (2014). "The VIMOS Public Extragalactic Survey (VIPERS). First Data Release of 57 204 spectroscopic measurements". In: A&A 562, A23, A23. DOI: [10.1051/0004-6361/201322790](https://doi.org/10.1051/0004-6361/201322790). arXiv: [1310.1008](https://arxiv.org/abs/1310.1008).
- Geha, M. et al. (2017). "The SAGA Survey. I. Satellite Galaxy Populations around Eight Milky Way Analogs". In: ApJ 847, 4, p. 4. DOI: [10.3847/1538-4357/aa8626](https://doi.org/10.3847/1538-4357/aa8626). arXiv: [1705.06743](https://arxiv.org/abs/1705.06743).
- Gerdes, D. W. et al. (2010). "ArborZ: Photometric Redshifts Using Boosted Decision Trees". In: ApJ 715, pp. 823–832. DOI: [10.1088/0004-637X/715/2/823](https://doi.org/10.1088/0004-637X/715/2/823). arXiv: [0908.4085 \[astro-ph.CO\]](https://arxiv.org/abs/0908.4085).
- Gonçalves, T. S. et al. (2012). "Quenching Star Formation at Intermediate Redshifts: Downsizing of the Mass Flux Density in the Green Valley". In: ApJ 759, 67, p. 67. DOI: [10.1088/0004-637X/759/1/67](https://doi.org/10.1088/0004-637X/759/1/67). arXiv: [1209.4084](https://arxiv.org/abs/1209.4084).
- Górski, K. M. et al. (2005). "HEALPix: A Framework for High-Resolution Discretization and Fast Analysis of Data Distributed on the Sphere". In: ApJ 622, pp. 759–771. DOI: [10.1086/427976](https://doi.org/10.1086/427976). eprint: [astro-ph/0409513](https://arxiv.org/abs/astro-ph/0409513).
- Graff, P. et al. (2014). "SKYNET: an efficient and robust neural network training tool for machine learning in astronomy". In: MNRAS 441, pp. 1741–1759. DOI: [10.1093/mnras/stu642](https://doi.org/10.1093/mnras/stu642). arXiv: [1309.0790 \[astro-ph.IM\]](https://arxiv.org/abs/1309.0790).
- Grillo, C. et al. (2016). "The Story of Supernova 'Refsdal' Told by Muse". In: ApJ 822, 78, p. 78. DOI: [10.3847/0004-637X/822/2/78](https://doi.org/10.3847/0004-637X/822/2/78). arXiv: [1511.04093](https://arxiv.org/abs/1511.04093).
- Gschwend, J. et al. (2018). "DES science portal: Computing photometric redshifts". In: *Astronomy and Computing* 25, pp. 58–80. DOI: [10.1016/j.ascom.2018.08.008](https://doi.org/10.1016/j.ascom.2018.08.008). arXiv: [1708.05643](https://arxiv.org/abs/1708.05643).
- Gunn, J. E. and J. R. Gott III (1972). "On the Infall of Matter Into Clusters of Galaxies and Some Effects on Their Evolution". In: ApJ 176, p. 1. DOI: [10.1086/151605](https://doi.org/10.1086/151605).
- Hamilton, A. J. S. and M. Tegmark (2004). "A scheme to deal accurately and efficiently with complex angular masks in galaxy surveys". In: MNRAS 349, pp. 115–128. DOI: [10.1111/j.1365-2966.2004.07490.x](https://doi.org/10.1111/j.1365-2966.2004.07490.x). eprint: [astro-ph/0306324](https://arxiv.org/abs/astro-ph/0306324).
- Hashimoto, Y., A. Oemler Jr., H. Lin, et al. (1998). "The Influence of Environment on the Star Formation Rates of Galaxies". In: ApJ 499, pp. 589–599. eprint: [astro-ph/9712319](https://arxiv.org/abs/astro-ph/9712319).
- Hasinger, G. et al. (2018). "The DEIMOS 10K Spectroscopic Survey Catalog of the COSMOS Field". In: ApJ 858, 77, p. 77. DOI: [10.3847/1538-4357/aabacf](https://doi.org/10.3847/1538-4357/aabacf). arXiv: [1803.09251](https://arxiv.org/abs/1803.09251).
- Hildebrandt, H. et al. (2010). "PHAT: PHoto-z Accuracy Testing". In: A&A 523, A31, A31. DOI: [10.1051/0004-6361/201014885](https://doi.org/10.1051/0004-6361/201014885). arXiv: [1008.0658](https://arxiv.org/abs/1008.0658).
- Hinton, S. R. et al. (2016). "MARZ: Manual and automatic redshifting software". In: *Astronomy and Computing* 15, pp. 61–71. DOI: [10.1016/j.ascom.2016.03.001](https://doi.org/10.1016/j.ascom.2016.03.001). arXiv: [1603.09438 \[astro-ph.IM\]](https://arxiv.org/abs/1603.09438).
- Hogg, D. W. (1999). "Distance measures in cosmology". In: *arXiv Astrophysics e-prints*. eprint: [astro-ph/9905116](https://arxiv.org/abs/astro-ph/9905116).
- Honscheid, K. et al. (2008). "The Dark Energy Camera (DECam)". In: *ArXiv e-prints*. arXiv: [0810.3600](https://arxiv.org/abs/0810.3600).
- Hoyle, B. et al. (2018). "Dark Energy Survey Year 1 Results: redshift distributions of the weak-lensing source galaxies". In: MNRAS 478, pp. 592–610. DOI: [10.1093/mnras/sty957](https://doi.org/10.1093/mnras/sty957). arXiv: [1708.01532](https://arxiv.org/abs/1708.01532).
- Ilbert, O. et al. (2005). "The VIMOS-VLT deep survey. Evolution of the galaxy luminosity function up to $z = 2$ in first epoch data". In: A&A 439, pp. 863–876. DOI: [10.1051/0004-6361:20041961](https://doi.org/10.1051/0004-6361:20041961). eprint: [astro-ph/0409134](https://arxiv.org/abs/astro-ph/0409134).
- (2006). "Accurate photometric redshifts for the CFHT legacy survey calibrated using the VIMOS VLT deep survey". In: A&A 457, pp. 841–856. DOI: [10.1051/0004-6361:20065138](https://doi.org/10.1051/0004-6361:20065138). eprint: [astro-ph/0603217](https://arxiv.org/abs/astro-ph/0603217).
- (2009). "Cosmos Photometric Redshifts with 30-Bands for 2-deg 2 ". In: ApJ 690, pp. 1236–1249. DOI: [10.1088/0004-637X/690/2/1236](https://doi.org/10.1088/0004-637X/690/2/1236). arXiv: [0809.2101](https://arxiv.org/abs/0809.2101).
- Ilbert, O. et al. (2004). "Bias in the estimation of global luminosity functions". In: MNRAS 351.2, pp. 541–551. DOI: [10.1111/j.1365-2966.2004.07796.x](https://doi.org/10.1111/j.1365-2966.2004.07796.x). arXiv: [astro-ph/0402202 \[astro-ph\]](https://arxiv.org/abs/astro-ph/0402202).
- Ilbert, O. et al. (2013). "Mass assembly in quiescent and star-forming galaxies since $z \approx 4$ from UltraVISTA". In: A&A 556, A55, A55. DOI: [10.1051/0004-6361/201321100](https://doi.org/10.1051/0004-6361/201321100). arXiv: [1301.3157 \[astro-ph.CO\]](https://arxiv.org/abs/1301.3157).

- Ivezić, Ž. et al. (2008). "LSST: from Science Drivers to Reference Design and Anticipated Data Products". In: *ArXiv e-prints*. arXiv: 0805.2366.
- Jarvis, Matt (2012). "The VISTA Deep Extragalactic Observations (VIDEO)". In: *Science from the Next Generation Imaging and Spectroscopic Surveys*, p. 13.
- Johnston, R. (2011). "Shedding light on the galaxy luminosity function". In: *A&A Rev.* 19, 41, p. 41. DOI: 10.1007/s00159-011-0041-9. arXiv: 1106.2039 [astro-ph.CO].
- Jones, D. H. et al. (2009). "The 6dF Galaxy Survey: final redshift release (DR3) and southern large-scale structures". In: *MNRAS* 399, pp. 683–698. DOI: 10.1111/j.1365-2966.2009.15338.x. arXiv: 0903.5451.
- Kaiser, N. et al. (2010). "The Pan-STARRS wide-field optical/NIR imaging survey". In: *Ground-based and Airborne Telescopes III*. Vol. 7733. Proc. SPIE, 77330E. DOI: 10.1117/12.859188.
- Karman, W. et al. (2017). "MUSE integral-field spectroscopy towards the Frontier Fields cluster Abell S1063. II. Properties of low luminosity Lyman α emitters at $z < 3$ ". In: *A&A* 599, A28, A28. DOI: 10.1051/0004-6361/201629055. arXiv: 1606.01471.
- Kashikawa, Nobunari et al. (2004). "The Subaru Deep Field: The Optical Imaging Data". In: *PASJ* 56, pp. 1011–1023. DOI: 10.1093/pasj/56.6.1011. arXiv: astro-ph/0410005 [astro-ph].
- Kessler, R. et al. (2015). "The Difference Imaging Pipeline for the Transient Search in the Dark Energy Survey". In: *AJ* 150, 172, p. 172. DOI: 10.1088/0004-6256/150/6/172. arXiv: 1507.05137 [astro-ph.IM].
- Knobel, C. et al. (2012). "The zCOSMOS 20k Group Catalog". In: *ApJ* 753, 121, p. 121. DOI: 10.1088/0004-637X/753/2/121. arXiv: 1207.0002 [astro-ph.CO].
- Koposov, S. and O. Bartunov (2006). "Q3C, Quad Tree Cube – The new Sky-indexing Concept for Huge Astronomical Catalogues and its Realization for Main Astronomical Queries (Cone Search and Xmatch) in Open Source Database PostgreSQL". In: *Astronomical Data Analysis Software and Systems XV*. Ed. by C. Gabriel et al. Vol. 351. Astronomical Society of the Pacific Conference Series, p. 735.
- Kormendy, J. (2013). "Secular Evolution in Disk Galaxies". In: *Secular Evolution of Galaxies*. Ed. by J. Falcón-Barroso and J. H. Knapen, p. 1.
- Korytov, Danila et al. (2019). "CosmoDC2: A Synthetic Sky Catalog for Dark Energy Science with LSST". In: *arXiv e-prints*, arXiv:1907.06530, arXiv:1907.06530. arXiv: 1907.06530 [astro-ph.CO].
- Krause, E. et al. (2017). "Dark Energy Survey Year 1 Results: Multi-Probe Methodology and Simulated Likelihood Analyses". In: *ArXiv e-prints*. arXiv: 1706.09359.
- Kron, R. G. (1980). "Photometry of a complete sample of faint galaxies". In: *ApJS* 43, pp. 305–325. DOI: 10.1086/190669.
- Larson, R. B., B. M. Tinsley, and C. N. Caldwell (1980). "The evolution of disk galaxies and the origin of S0 galaxies". In: *ApJ* 237, pp. 692–707. DOI: 10.1086/157917.
- Le Fèvre, O. et al. (2004). "The VIMOS VLT Deep Survey. Public release of 1599 redshifts to $I_{AB} \leq 24$ across the Chandra Deep Field South". In: *A&A* 428, pp. 1043–1049. DOI: 10.1051/0004-6361:20048072. eprint: astro-ph/0403628.
- Li, T. S. et al. (2016). "Assessment of Systematic Chromatic Errors that Impact Sub-1% Photometric Precision in Large-area Sky Surveys". In: *AJ* 151, 157, p. 157. DOI: 10.3847/0004-6256/151/6/157. arXiv: 1601.00117 [astro-ph.IM].
- Lidman, C. et al. (2013). "An Efficient Approach to Obtaining Large Numbers of Distant Supernova Host Galaxy Redshifts". In: *PASA* 30, e001, e001. DOI: 10.1017/pasa.2012.001. arXiv: 1205.1306.
- (2016). "The XXL Survey XIV. AAOmega Redshifts for the Southern XXL Field". In: *PASA* 33, e001, e001. DOI: 10.1017/pasa.2015.52. arXiv: 1512.04662.
- Lilly, S. J. et al. (2009). "The zCOSMOS 10k-Bright Spectroscopic Sample". In: *ApJS* 184, pp. 218–229. DOI: 10.1088/0067-0049/184/2/218.
- Lilly, S. J. et al. (1996). "The Canada-France Redshift Survey: The Luminosity Density and Star Formation History of the Universe to Z approximately 1". In: *ApJ* 460, p. L1. DOI: 10.1086/309975. arXiv: astro-ph/9601050 [astro-ph].

- Lilly, S. J., O. Le Fèvre, A. Renzini, et al. (2007). "zCOSMOS: A Large VLT/VIMOS Redshift Survey Covering $0 \leq z \leq 3$ in the COSMOS Field". In: *ApJS* 172, pp. 70–85. DOI: [10.1086/516589](https://doi.org/10.1086/516589). eprint: [astro-ph/0612291](https://arxiv.org/abs/astro-ph/0612291).
- Lima, M. et al. (2008). "Estimating the redshift distribution of photometric galaxy samples". In: *MNRAS* 390, pp. 118–130. DOI: [10.1111/j.1365-2966.2008.13510.x](https://doi.org/10.1111/j.1365-2966.2008.13510.x). arXiv: [0801.3822](https://arxiv.org/abs/0801.3822).
- Lin, Lihwai et al. (2008). "The Redshift Evolution of Wet, Dry, and Mixed Galaxy Mergers from Close Galaxy Pairs in the DEEP2 Galaxy Redshift Survey". In: *ApJ* 681.1, pp. 232–243. DOI: [10.1086/587928](https://doi.org/10.1086/587928). arXiv: [0802.3004 \[astro-ph\]](https://arxiv.org/abs/0802.3004).
- Loveday, J. et al. (2012). "Galaxy and Mass Assembly (GAMA): ugriz galaxy luminosity functions". In: *MNRAS* 420, pp. 1239–1262. DOI: [10.1111/j.1365-2966.2011.20111.x](https://doi.org/10.1111/j.1365-2966.2011.20111.x). arXiv: [1111.0166](https://arxiv.org/abs/1111.0166).
- Lynden-Bell, D. (1971). "A method of allowing for known observational selection in small samples applied to 3CR quasars". In: *MNRAS* 155, p. 95. DOI: [10.1093/mnras/155.1.95](https://doi.org/10.1093/mnras/155.1.95).
- Madau, P. and M. Dickinson (2014). "Cosmic Star-Formation History". In: *ARA&A* 52, pp. 415–486. DOI: [10.1146/annurev-astro-081811-125615](https://doi.org/10.1146/annurev-astro-081811-125615). arXiv: [1403.0007](https://arxiv.org/abs/1403.0007).
- Madau, P., L. Pozzetti, and M. Dickinson (1998). "The Star Formation History of Field Galaxies". In: *ApJ* 498, pp. 106–116. DOI: [10.1086/305523](https://doi.org/10.1086/305523). eprint: [astro-ph/9708220](https://arxiv.org/abs/astro-ph/9708220).
- Man, Allison and Sirio Belli (2018). "Star formation quenching in massive galaxies". In: *Nature Astronomy* 2, pp. 695–697. DOI: [10.1038/s41550-018-0558-1](https://doi.org/10.1038/s41550-018-0558-1). arXiv: [1809.00722 \[astro-ph.GA\]](https://arxiv.org/abs/1809.00722).
- Mandelbaum, R. et al. (2008). "Precision photometric redshift calibration for galaxy-galaxy weak lensing". In: *MNRAS* 386, pp. 781–806. DOI: [10.1111/j.1365-2966.2008.12947.x](https://doi.org/10.1111/j.1365-2966.2008.12947.x). arXiv: [0709.1692](https://arxiv.org/abs/0709.1692).
- Mao, M. Y. et al. (2012). "The Australia Telescope Large Area Survey: spectroscopic catalogue and radio luminosity functions". In: *MNRAS* 426, pp. 3334–3348. DOI: [10.1111/j.1365-2966.2012.21913.x](https://doi.org/10.1111/j.1365-2966.2012.21913.x). arXiv: [1208.2722](https://arxiv.org/abs/1208.2722).
- Maraston, C. (2005). "Evolutionary population synthesis: models, analysis of the ingredients and application to high-z galaxies". In: *MNRAS* 362, pp. 799–825. DOI: [10.1111/j.1365-2966.2005.09270.x](https://doi.org/10.1111/j.1365-2966.2005.09270.x). eprint: [astro-ph/0410207](https://arxiv.org/abs/astro-ph/0410207).
- Maraston, C. et al. (2009). "Modelling the colour evolution of luminous red galaxies - improvements with empirical stellar spectra". In: *MNRAS* 394, pp. L107–L111. DOI: [10.1111/j.1745-3933.2009.00621.x](https://doi.org/10.1111/j.1745-3933.2009.00621.x). arXiv: [0809.1867](https://arxiv.org/abs/0809.1867).
- Masters, D. C. et al. (2017). "The Complete Calibration of the Color-Redshift Relation (C3R2) Survey: Survey Overview and Data Release 1". In: *ApJ* 841, 111, p. 111. DOI: [10.3847/1538-4357/aa6f08](https://doi.org/10.3847/1538-4357/aa6f08). arXiv: [1704.06665](https://arxiv.org/abs/1704.06665).
- McCracken, H. J. et al. (2003). "The VIRMOS deep imaging survey. II: CFH12K BVRI optical data for the 0226-04 deep field". In: *A&A* 410, pp. 17–32. DOI: [10.1051/0004-6361:20031081](https://doi.org/10.1051/0004-6361:20031081). arXiv: [astro-ph/0306254 \[astro-ph\]](https://arxiv.org/abs/astro-ph/0306254).
- McCracken, H. J. et al. (2012). "UltraVISTA: a new ultra-deep near-infrared survey in COSMOS". In: *A&A* 544, A156, A156. DOI: [10.1051/0004-6361/201219507](https://doi.org/10.1051/0004-6361/201219507). arXiv: [1204.6586 \[astro-ph.CO\]](https://arxiv.org/abs/1204.6586).
- McLean, I. S. et al. (2012). "MOSFIRE, the multi-object spectrometer for infra-red exploration at the Keck Observatory". In: *Ground-based and Airborne Instrumentation for Astronomy IV*. Vol. 8446. Proc. SPIE, 84460J. DOI: [10.1117/12.924794](https://doi.org/10.1117/12.924794).
- Mei, S., B. P. Holden, J. P. Blakeslee, et al. (2009). "Evolution of the Color-Magnitude Relation in Galaxy Clusters at $z \sim 1$ from the ACS Intermediate Redshift Cluster Survey". In: *ApJ* 690, pp. 42–68. DOI: [10.1088/0004-637X/690/1/42](https://doi.org/10.1088/0004-637X/690/1/42). arXiv: [0810.1917](https://arxiv.org/abs/0810.1917).
- Mo, H., F. C. van den Bosch, and S. White (2010). *Galaxy Formation and Evolution*.
- Mohr, J. J. et al. (2008). "The Dark Energy Survey data management system". In: *Observatory Operations: Strategies, Processes, and Systems II*. Vol. 7016. Proc. SPIE, p. 70160L. DOI: [10.1117/12.789550](https://doi.org/10.1117/12.789550). arXiv: [0807.2515](https://arxiv.org/abs/0807.2515).
- (2012). "The Dark Energy Survey data processing and calibration system". In: *Software and Cyberinfrastructure for Astronomy II*. Vol. 8451. Proc. SPIE, p. 84510D. DOI: [10.1117/12.926785](https://doi.org/10.1117/12.926785). arXiv: [1207.3189 \[astro-ph.IM\]](https://arxiv.org/abs/1207.3189).

- Momcheva, I. G. et al. (2016). "The 3D-HST Survey: Hubble Space Telescope WFC3/G141 Grism Spectra, Redshifts, and Emission Line Measurements for $\sim 100,000$ Galaxies". In: *ApJS* 225, 27, p. 27. DOI: [10.3847/0067-0049/225/2/27](https://doi.org/10.3847/0067-0049/225/2/27). arXiv: [1510.02106](https://arxiv.org/abs/1510.02106).
- Monna, A. et al. (2017). "Precise strong lensing mass profile of the CLASH galaxy cluster MACS 2129". In: *MNRAS* 466, pp. 4094–4106. DOI: [10.1093/mnras/stx015](https://doi.org/10.1093/mnras/stx015). arXiv: [1605.08784](https://arxiv.org/abs/1605.08784).
- Morganson, E. et al. (2018). "The Dark Energy Survey Image Processing Pipeline". In: *ArXiv e-prints*. arXiv: [1801.03177 \[astro-ph.IM\]](https://arxiv.org/abs/1801.03177).
- Muzzin, A. et al. (2012). "The Gemini Cluster Astrophysics Spectroscopic Survey (GCLASS): The Role of Environment and Self-regulation in Galaxy Evolution at $z \sim 1$ ". In: *ApJ* 746, 188, p. 188. DOI: [10.1088/0004-637X/746/2/188](https://doi.org/10.1088/0004-637X/746/2/188). arXiv: [1112.3655](https://arxiv.org/abs/1112.3655).
- Nakamura, Osamu et al. (2003). "The Luminosity Function of Morphologically Classified Galaxies in the Sloan Digital Sky Survey". In: *The Astronomical Journal* 125.4, pp. 1682–1688. DOI: [10.1086/368135](https://doi.org/10.1086/368135). arXiv: [astro-ph/0212405 \[astro-ph\]](https://arxiv.org/abs/astro-ph/0212405).
- Nanayakkara, T. et al. (2016). "ZFIRE: A KECK/MOSFIRE Spectroscopic Survey of Galaxies in Rich Environments at $z \sim 2$ ". In: *ApJ* 828, 21, p. 21. DOI: [10.3847/0004-637X/828/1/21](https://doi.org/10.3847/0004-637X/828/1/21). arXiv: [1607.00013](https://arxiv.org/abs/1607.00013).
- Newman, J. A. et al. (2013). "The DEEP2 Galaxy Redshift Survey: Design, Observations, Data Reduction, and Redshifts". In: *ApJS* 208, 5, p. 5. DOI: [10.1088/0067-0049/208/1/5](https://doi.org/10.1088/0067-0049/208/1/5). arXiv: [1203.3192](https://arxiv.org/abs/1203.3192).
- Ngeow, C. C. et al. (2006). "Application of the Dark Energy Survey Data Management System to the Blanco Cosmology Survey Data". In: *American Astronomical Society Meeting Abstracts*. Vol. 38. Bulletin of the American Astronomical Society, p. 929.
- Nord, B. et al. (2016). "Observation and Confirmation of Six Strong-lensing Systems in the Dark Energy Survey Science Verification Data". In: *ApJ* 827, 51, p. 51. DOI: [10.3847/0004-637X/827/1/51](https://doi.org/10.3847/0004-637X/827/1/51). arXiv: [1512.03062](https://arxiv.org/abs/1512.03062).
- Oke, J. B. and A. Sandage (1968). "Energy Distributions, K Corrections, and the Stebbins-Whitford Effect for Giant Elliptical Galaxies". In: *ApJ* 154, p. 21. DOI: [10.1086/149737](https://doi.org/10.1086/149737).
- Oyaizu, H. et al. (2008a). "A Galaxy Photometric Redshift Catalog for the Sloan Digital Sky Survey Data Release 6". In: *ApJ* 674, pp. 768–783. DOI: [10.1086/523666](https://doi.org/10.1086/523666). arXiv: [0708.0030](https://arxiv.org/abs/0708.0030).
- (2008b). "Photometric Redshift Error Estimators". In: *ApJ* 689, pp. 709–720. DOI: [10.1086/592591](https://doi.org/10.1086/592591). arXiv: [0711.0962](https://arxiv.org/abs/0711.0962).
- Parkinson, D. et al. (2012). "The WiggleZ Dark Energy Survey: Final data release and cosmological results". In: *Phys. Rev. D* 86.10, 103518, p. 103518. DOI: [10.1103/PhysRevD.86.103518](https://doi.org/10.1103/PhysRevD.86.103518). arXiv: [1210.2130](https://arxiv.org/abs/1210.2130).
- Polletta, M. et al. (2007). "Spectral Energy Distributions of Hard X-Ray Selected Active Galactic Nuclei in the XMM-Newton Medium Deep Survey". In: *ApJ* 663, pp. 81–102. DOI: [10.1086/518113](https://doi.org/10.1086/518113). eprint: [astro-ph/0703255](https://arxiv.org/abs/astro-ph/0703255).
- Prat, J. et al. (2018). "Dark Energy Survey year 1 results: Galaxy-galaxy lensing". In: *Phys. Rev. D* 98.4, 042005, p. 042005. DOI: [10.1103/PhysRevD.98.042005](https://doi.org/10.1103/PhysRevD.98.042005). arXiv: [1708.01537](https://arxiv.org/abs/1708.01537).
- Press, W. H. and P. Schechter (1974). "Formation of Galaxies and Clusters of Galaxies by Self-Similar Gravitational Condensation". In: *ApJ* 187, pp. 425–438. DOI: [10.1086/152650](https://doi.org/10.1086/152650).
- Prevot, M. L. et al. (1984). "The typical interstellar extinction in the Small Magellanic Cloud". In: *A&A* 132, pp. 389–392.
- Ramos, B. H. F. et al. (2011). "Evolution of Galaxy Luminosity Function Using Photometric Redshifts". In: *AJ* 142, 41, p. 41. DOI: [10.1088/0004-6256/142/2/41](https://doi.org/10.1088/0004-6256/142/2/41). arXiv: [1105.5668](https://arxiv.org/abs/1105.5668).
- Rau, Markus Michael, Simon Wilson, and Rachel Mandelbaum (2019). "Estimating redshift distributions using Hierarchical Logistic Gaussian processes". In: *arXiv e-prints*, arXiv:1904.09988, arXiv:1904.09988. arXiv: [1904.09988 \[astro-ph.CO\]](https://arxiv.org/abs/1904.09988).
- Rest, A. et al. (2014). "Cosmological Constraints from Measurements of Type Ia Supernovae Discovered during the First 1.5 yr of the Pan-STARRS1 Survey". In: *ApJ* 795, 44, p. 44. DOI: [10.1088/0004-637X/795/1/44](https://doi.org/10.1088/0004-637X/795/1/44). arXiv: [1310.3828](https://arxiv.org/abs/1310.3828).
- Robertson, Brant E. et al. (2017). "Large Synoptic Survey Telescope Galaxies Science Roadmap". In: *arXiv e-prints*, arXiv:1708.01617, arXiv:1708.01617. arXiv: [1708.01617 \[astro-ph.GA\]](https://arxiv.org/abs/1708.01617).

- Roukema, B. F., P. J. Quinn, and B. A. Peterson (1993). "Spectral Evolution of Merging/Accreting Galaxies". In: *Observational Cosmology*. Ed. by Guido L. Chincarini et al. Vol. 51. Astronomical Society of the Pacific Conference Series, p. 298.
- Rykoff, E. S., E. Rozo, and R. Keisler (2015). "Assessing Galaxy Limiting Magnitudes in Large Optical Surveys". In: *ArXiv e-prints*. arXiv: [1509.00870 \[astro-ph.IM\]](#).
- Sadeh, I., F. B. Abdalla, and O. Lahav (2016). "ANNz2: Photometric Redshift and Probability Distribution Function Estimation using Machine Learning". In: *PASP* 128.10, p. 104502. DOI: [10.1088/1538-3873/128/968/104502](#). arXiv: [1507.00490](#).
- Samuroff, S. et al. (2018). "Dark Energy Survey Year 1 results: the impact of galaxy neighbours on weak lensing cosmology with IM3SHAPE". In: *MNRAS* 475, pp. 4524–4543. DOI: [10.1093/mnras/stx3282](#). arXiv: [1708.01534](#).
- Sánchez, C., M. Carrasco Kind, H. Lin, et al. (2014). "Photometric redshift analysis in the Dark Energy Survey Science Verification data". In: *MNRAS* 445, pp. 1482–1506. DOI: [10.1093/mnras/stu1836](#). arXiv: [1406.4407 \[astro-ph.IM\]](#).
- Sandage, A., G. A. Tammann, and A. Yahil (1979). "The velocity field of bright nearby galaxies. I. The variation of mean absolute magnitude with redshift for galaxies in a magnitude-limited sample." In: *ApJ* 232, pp. 352–364. DOI: [10.1086/157295](#).
- Sarron, F. et al. (2018). "Evolution of the cluster optical galaxy luminosity function in the CFHTLS: breaking the degeneracy between mass and redshift". In: *A&A* 613, A67, A67. DOI: [10.1051/0004-6361/201731981](#). arXiv: [1712.09481](#).
- Schechter, P. (1976). "An analytic expression for the luminosity function for galaxies." In: *ApJ* 203, pp. 297–306. DOI: [10.1086/154079](#).
- Schlafly, E. F. and D. P. Finkbeiner (2011). "Measuring Reddening with Sloan Digital Sky Survey Stellar Spectra and Recalibrating SFD". In: *ApJ* 737, 103, p. 103. DOI: [10.1088/0004-637X/737/2/103](#). arXiv: [1012.4804 \[astro-ph.GA\]](#).
- Schlegel, D. J., D. P. Finkbeiner, and M. Davis (1998). "Maps of Dust Infrared Emission for Use in Estimation of Reddening and Cosmic Microwave Background Radiation Foregrounds". In: *ApJ* 500, pp. 525–553. DOI: [10.1086/305772](#). eprint: [astro-ph/9710327](#).
- Schmidt, M. (1968). "Space Distribution and Luminosity Functions of Quasi-Stellar Radio Sources". In: *ApJ* 151, p. 393. DOI: [10.1086/149446](#).
- Scolnic, D. et al. (2014). "Systematic Uncertainties Associated with the Cosmological Analysis of the First Pan-STARRS1 Type Ia Supernova Sample". In: *ApJ* 795, 45, p. 45. DOI: [10.1088/0004-637X/795/1/45](#). arXiv: [1310.3824](#).
- Scoville, N. et al. (2007). "COSMOS: Hubble Space Telescope Observations". In: *ApJS* 172, pp. 38–45. DOI: [10.1086/516580](#). eprint: [astro-ph/0612306](#).
- Sevilla, I. et al. (2011). "The Dark Energy Survey Data Management System". In: *ArXiv e-prints*. arXiv: [1109.6741 \[astro-ph.IM\]](#).
- Sevilla-Noarbe, I. et al. (2018). "Star-galaxy classification in the Dark Energy Survey Y1 dataset". In: *MNRAS*. DOI: [10.1093/mnras/sty2579](#).
- Shectman, S. A. et al. (1996). "The Las Campanas Redshift Survey". In: *ApJ* 470, p. 172. DOI: [10.1086/177858](#). eprint: [astro-ph/9604167](#).
- Sheldon, E. S. et al. (2012). "Photometric Redshift Probability Distributions for Galaxies in the SDSS DR8". In: *ApJS* 201, 32, p. 32. DOI: [10.1088/0067-0049/201/2/32](#). arXiv: [1109.5192](#).
- Sheldon, E. S. (2014). "An implementation of Bayesian lensing shear measurement". In: *MNRAS* 444, pp. L25–L29. DOI: [10.1093/mnrasl/slu104](#). arXiv: [1403.7669](#).
- Silva, L. et al. (1998). "Modeling the Effects of Dust on Galactic Spectral Energy Distributions from the Ultraviolet to the Millimeter Band". In: *ApJ* 509, pp. 103–117. DOI: [10.1086/306476](#).
- Silverman, J. D. et al. (2015). "The FMOS-COSMOS Survey of Star-forming Galaxies at z~1.6. III. Survey Design, Performance, and Sample Characteristics". In: *ApJS* 220, 12, p. 12. DOI: [10.1088/0067-0049/220/1/12](#). arXiv: [1409.0447](#).

- Somerville, Rachel S. et al. (2004). "Cosmic Variance in the Great Observatories Origins Deep Survey". In: *ApJ* 600.2, pp. L171–L174. DOI: [10.1086/378628](https://doi.org/10.1086/378628). arXiv: [astro-ph/0309071 \[astro-ph\]](https://arxiv.org/abs/astro-ph/0309071).
- Stalin, C. S. et al. (2010). "Optical identification of XMM sources in the Canada-France-Hawaii Telescope Legacy Survey". In: *MNRAS* 401, pp. 294–306. DOI: [10.1111/j.1365-2966.2009.15636.x](https://doi.org/10.1111/j.1365-2966.2009.15636.x). arXiv: [0909.0464](https://arxiv.org/abs/0909.0464).
- Strateva, Iskra et al. (2001). "Color Separation of Galaxy Types in the Sloan Digital Sky Survey Imaging Data". In: *AJ* 122.4, pp. 1861–1874. DOI: [10.1086/323301](https://doi.org/10.1086/323301). arXiv: [astro-ph/0107201 \[astro-ph\]](https://arxiv.org/abs/astro-ph/0107201).
- Suchyta, E. et al. (2016). "No galaxy left behind: accurate measurements with the faintest objects in the Dark Energy Survey". In: *MNRAS* 457.1, pp. 786–808. DOI: [10.1093/mnras/stv2953](https://doi.org/10.1093/mnras/stv2953). arXiv: [1507.08336 \[astro-ph.GA\]](https://arxiv.org/abs/1507.08336).
- Sullivan, M. et al. (2011). "VizieR Online Data Catalog: Type Ia supernovae luminosities (Sullivan+, 2010)". In: *VizieR Online Data Catalog* 740.
- Swanson, M. E. C. et al. (2008). "Methods for rapidly processing angular masks of next-generation galaxy surveys". In: *MNRAS* 387, pp. 1391–1402. DOI: [10.1111/j.1365-2966.2008.13296.x](https://doi.org/10.1111/j.1365-2966.2008.13296.x). arXiv: [0711.4352](https://arxiv.org/abs/0711.4352).
- Tasca, L. A. M. et al. (2017). "The VIMOS Ultra Deep Survey first data release: Spectra and spectroscopic redshifts of 698 objects up to $z_{spec} \sim 6$ in CANDELS". In: *A&A* 600, A110, A110. DOI: [10.1051/0004-6361/201527963](https://doi.org/10.1051/0004-6361/201527963). arXiv: [1602.01842](https://arxiv.org/abs/1602.01842).
- Taylor, M. B. (2006). "STILTS - A Package for Command-Line Processing of Tabular Data". In: *Astronomical Data Analysis Software and Systems XV*. Ed. by C. Gabriel et al. Vol. 351. Astronomical Society of the Pacific Conference Series, p. 666.
- Treu, T. et al. (2015). "The Grism Lens-Amplified Survey from Space (GLASS). I. Survey Overview and First Data Release". In: *ApJ* 812, 114, p. 114. DOI: [10.1088/0004-637X/812/2/114](https://doi.org/10.1088/0004-637X/812/2/114). arXiv: [1509.00475](https://arxiv.org/abs/1509.00475).
- Troxel, M. A. et al. (2018). "Dark Energy Survey Year 1 results: Cosmological constraints from cosmic shear". In: *Phys. Rev. D* 98.4, 043528, p. 043528. DOI: [10.1103/PhysRevD.98.043528](https://doi.org/10.1103/PhysRevD.98.043528). arXiv: [1708.01538](https://arxiv.org/abs/1708.01538).
- Turner, E. L. (1979). "Statistics of the Hubble diagram. II. The form of the luminosity function and density variations with application to quasars." In: *ApJ* 231, pp. 645–652. DOI: [10.1086/157227](https://doi.org/10.1086/157227).
- Urrutia, T. et al. (2018). "The MUSE-Wide Survey: Survey Description and First Data Release". In: *ArXiv e-prints*. arXiv: [1811.06549](https://arxiv.org/abs/1811.06549).
- van Albada, T. S. (1982). "Dissipationless galaxy formation and the R to the 1/4-power law". In: *MNRAS* 201, pp. 939–955. DOI: [10.1093/mnras/201.4.939](https://doi.org/10.1093/mnras/201.4.939).
- White, S. D. M. and M. J. Rees (1978). "Core condensation in heavy halos - A two-stage theory for galaxy formation and clustering". In: *MNRAS* 183, pp. 341–358. DOI: [10.1093/mnras/183.3.341](https://doi.org/10.1093/mnras/183.3.341).
- Willmer, C. N. A. et al. (2006). "The Deep Evolutionary Exploratory Probe 2 Galaxy Redshift Survey: The Galaxy Luminosity Function to $z \sim 1$ ". In: *ApJ* 647, pp. 853–873. DOI: [10.1086/505455](https://doi.org/10.1086/505455). eprint: [astro-ph/0506041](https://arxiv.org/abs/astro-ph/0506041).
- Wolf, C. et al. (2003). "The COMBO-17 survey: Evolution of the galaxy luminosity function from 25 000 galaxies with $0.2 < z < 1.2$ ". In: *A&A* 401, pp. 73–98. DOI: [10.1051/0004-6361:20021513](https://doi.org/10.1051/0004-6361:20021513). eprint: [astro-ph/0208345](https://arxiv.org/abs/astro-ph/0208345).
- Yamauchi, C. and T. Goto (2004). "Are passive spiral galaxies truly 'passive' and 'spiral'? A near-infrared perspective". In: *MNRAS* 352, pp. 815–822. DOI: [10.1111/j.1365-2966.2004.07966.x](https://doi.org/10.1111/j.1365-2966.2004.07966.x). eprint: [astro-ph/0405562](https://arxiv.org/abs/astro-ph/0405562).
- Yasuda, Naoki et al. (2001). "Galaxy Number Counts from the Sloan Digital Sky Survey Commissioning Data". In: *AJ* 122.3, pp. 1104–1124. DOI: [10.1086/322093](https://doi.org/10.1086/322093). arXiv: [astro-ph/0105545 \[astro-ph\]](https://arxiv.org/abs/astro-ph/0105545).
- York, D. G., J. Adelman, J. E. Anderson Jr., et al. (2000). "The Sloan Digital Sky Survey: Technical Summary". In: *AJ* 120, pp. 1579–1587. DOI: [10.1086/301513](https://doi.org/10.1086/301513). eprint: [astro-ph/0006396](https://arxiv.org/abs/astro-ph/0006396).
- Yuan, F. et al. (2015). "OzDES multifibre spectroscopy for the Dark Energy Survey: first-year operation and results". In: *MNRAS* 452, pp. 3047–3063. DOI: [10.1093/mnras/stv1507](https://doi.org/10.1093/mnras/stv1507). arXiv: [1504.03039](https://arxiv.org/abs/1504.03039).
- Zehavi, I. et al. (2011). "Galaxy Clustering in the Completed SDSS Redshift Survey: The Dependence on Color and Luminosity". In: *ApJ* 736, 59, p. 59. DOI: [10.1088/0004-637X/736/1/59](https://doi.org/10.1088/0004-637X/736/1/59). arXiv: [1005.2413](https://arxiv.org/abs/1005.2413).

- Zucca, E. et al. (2006). "The VIMOS VLT Deep Survey. Evolution of the luminosity functions by galaxy type up to $z = 1.5$ from first epoch data". In: A&A 455, pp. 879–890. DOI: [10.1051/0004-6361:20053645](https://doi.org/10.1051/0004-6361:20053645). eprint: [astro-ph/0506393](https://arxiv.org/abs/astro-ph/0506393).
- (2009). "The zCOSMOS survey: the role of the environment in the evolution of the luminosity function of different galaxy types". In: A&A 508, pp. 1217–1234. DOI: [10.1051/0004-6361/200912665](https://doi.org/10.1051/0004-6361/200912665). arXiv: [0909.4674](https://arxiv.org/abs/0909.4674).
- Zuntz, J. et al. (2018). "Dark Energy Survey Year 1 results: weak lensing shape catalogues". In: MNRAS 481, pp. 1149–1182. DOI: [10.1093/mnras/sty2219](https://doi.org/10.1093/mnras/sty2219). arXiv: [1708.01533](https://arxiv.org/abs/1708.01533).

Appendix A

The DES Science Portal

A.1 The DES Science Portal

The DES Science Portal is an integrated web-based data interface that provides a framework to carry out scientific analysis using big-data. The Portal relies on two databases, a mass storage file system, a web interface, a workflow system, and a cluster of computers, as illustrated in Figure A.1. Both databases uses PostgreSQL¹ object-relational database management system. The catalog database stores the catalogs retrieved from the NCSA database and the catalogs produced by the Portal. The administrative database keeps track of metadata such as available releases, ingested products, product information, such as file and table names, storage location, classification, provenance, etc.

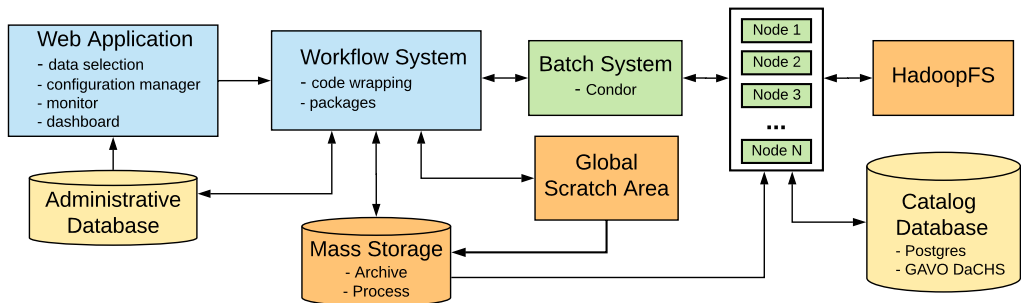


FIGURE A.1: Components of Portal’s infrastructure: software components (in blue), processing systems (in green), and storage systems (databases in yellow, file systems in orange).

The computational tools available in the Portal are organized in pipelines and components. The former are workflows defined in Extensible Markup Language (XML, Bray et al., 2008), which concatenates a chain of tasks performed by components. They determine the order of execution of the tasks and the parallelization strategy, as well as necessary inputs and outputs.

Components are Python scripts, which can both serve as a wrapper for an external code or be an independent algorithm. Scientific codes, which can be written in any programming language, are encapsulated by the wrappers, which are in charge of preparing the inputs in the format expected by the code, calling the code to run, and handling the outputs.

The Portal was conceived as a solution to support complex data processing performed by a large number of people geographically spread and working collaboratively. It provides a controlled environment to organize data and products systematically, enabling the ease testing and comparison of different algorithms, but also addresses the processing requirements by parallelizing the calculation in a transparent way for the user. Figures A.2 and A.3 are examples of the appearance of the Portal’s interface. The first shows the input menu of the pipeline responsible for computing photo-zs for large samples. The second is the product log, i.e., the page where the results of a pipeline are displayed, for the pipeline in charge of doing photo-z training (and validation).

¹<https://www.postgresql.org/>

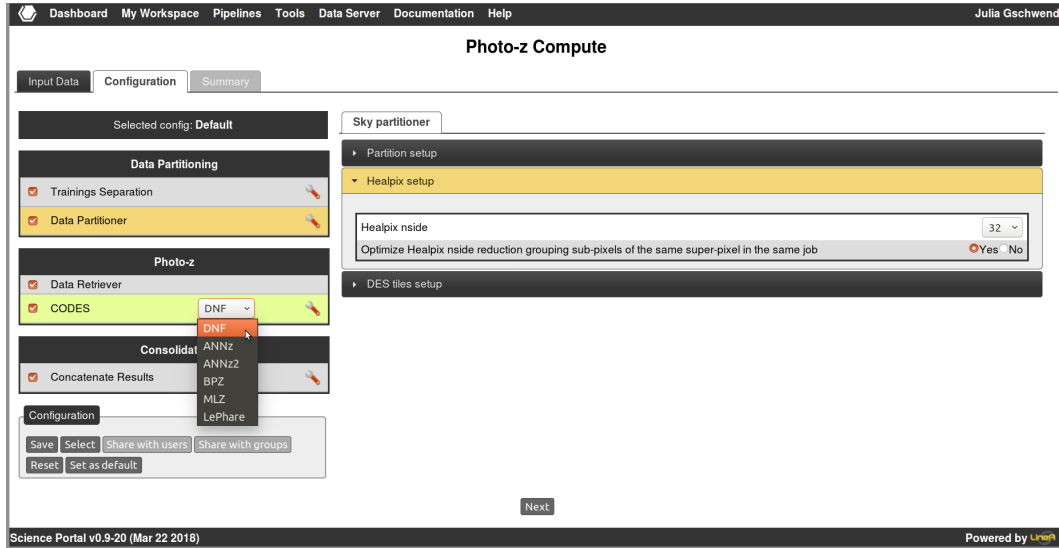


FIGURE A.2: Screenshot of the configuration tab of the *Photo-z Compute* pipeline. On the left, the five photo-z codes available ate the epoch of taking the image. On the right, the choice of the size of each data partition, based on HEALPix pixels.

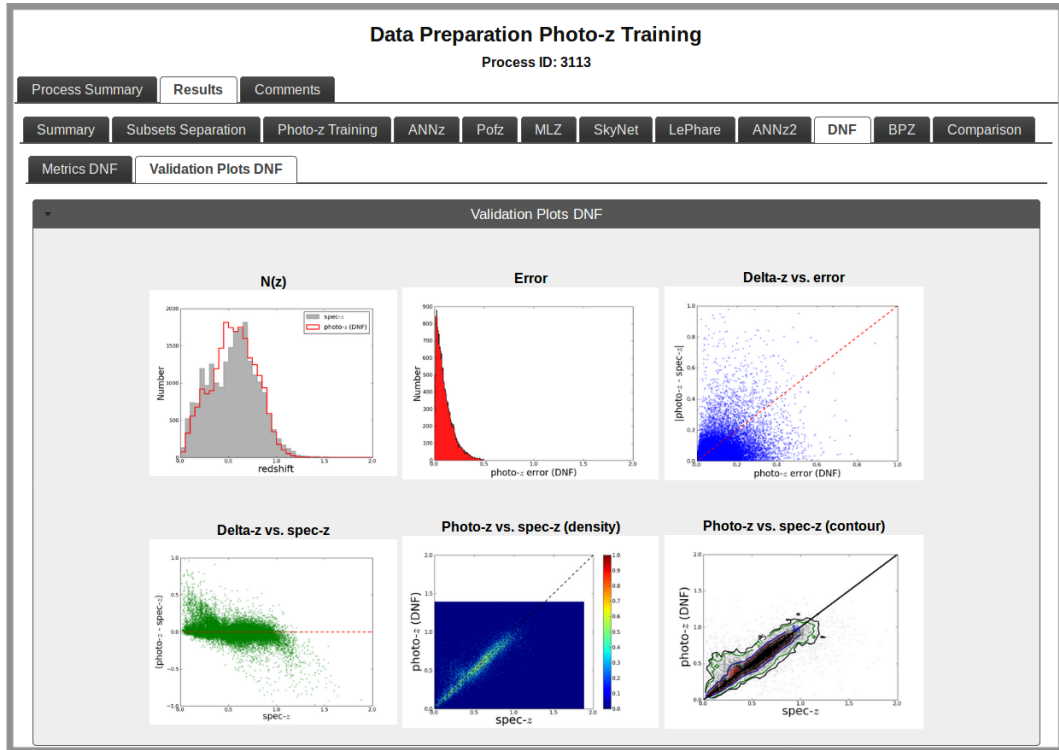


FIGURE A.3: Results from the Photo-z Validation component, organized in tabs by photo-z algorithms. In this example, we present results by DNF on DES Y1A1 data. The three plots on the top are, from left to right, the histograms of redshift and error distributions, and the scatter plot of photo-z error versus the difference between photo-z and spec-z for each object in the validation sample. The plots on the bottom are the scatter plot of photo-z versus the difference between photo-z and spec-z, and the density and contour plots of photo-z versus spec-z.

The pipelines are connected by a system of classes. The output of a given pipeline is registered in the database, and the products are identified by a class, which carried the information about the type

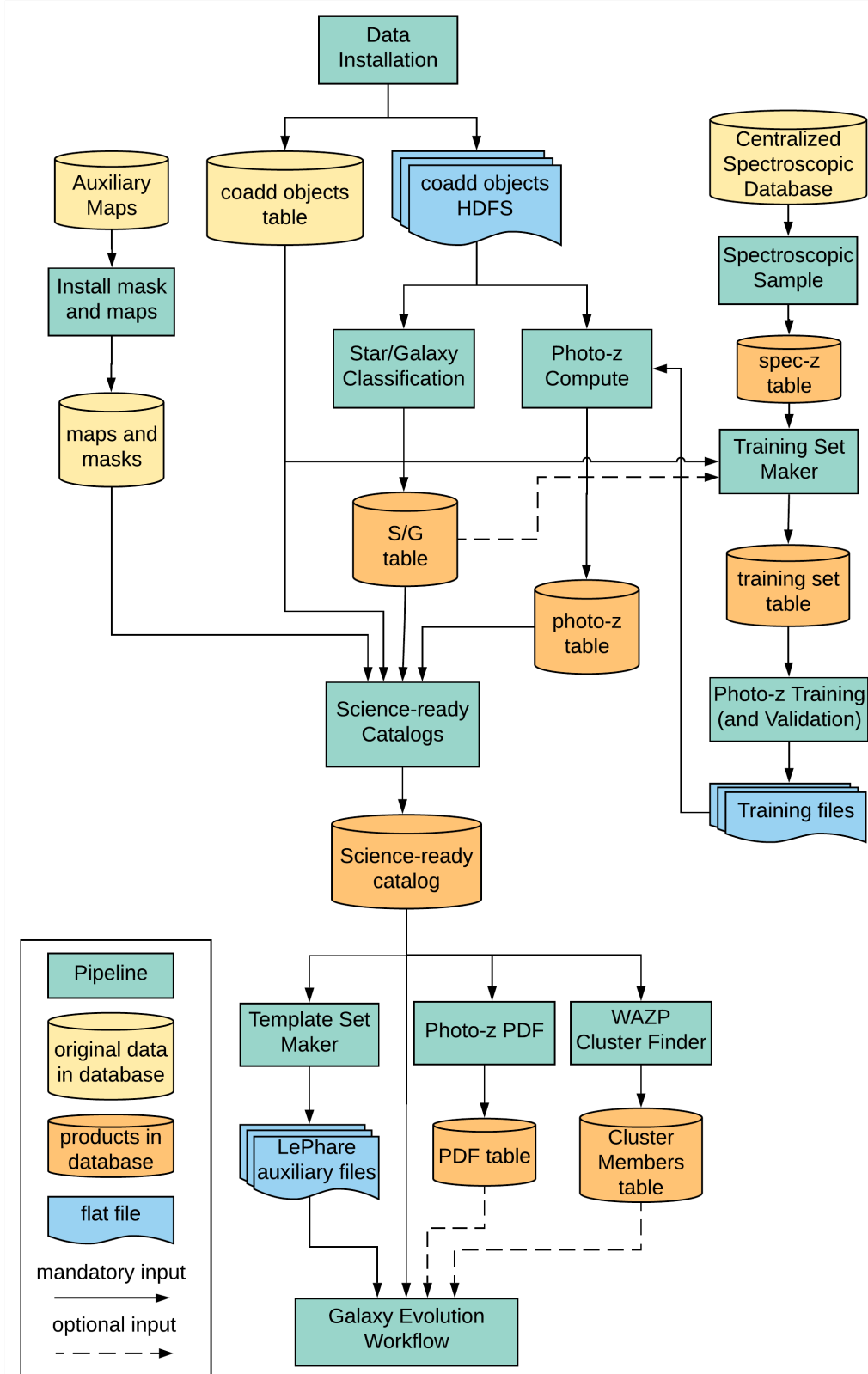


FIGURE A.4: Flowchart of the DES Science Portal E2E.

of data, format, and usage. Once registered, the products become available to the search engine to be selected on the input menu of another pipeline that is expecting the same class as input. After a sequence

of several processes, the Portal keeps track of all steps by a system of provenance control, so that a final product created after passing through several stages can be entirely reproduced. The whole chain of pipelines that is necessary to create science ready catalogs from the raw coadd tables is called the Portal’s end-to-end (E2E).

The complexity of the E2E is illustrated in Figure A.4. The science-ready catalogs are built from the combination of maps and masks created from the observing conditions and external data (the thread on the left side of the figure) and the coadd objects table. In addition, the data is combined with the product of star/galaxy classification, to select only galaxies (or only stars) depending on the science case. For extragalactic studies, it is also necessary to append photo-zs, which requires training and validation using a spectroscopic sample (the thread on the right side of the figure). All steps mentioned above are described in details by Fausti Neto et al. (2018). The particular aspects related to photo-zs are treated separately by Gschwend et al. (2018). Some values are added after the stage of catalog production, such as the set of SED templates for the template-fitting (optimized to cover the color-redshift space of the sample after pruning), the photo-z PDFs (which requires large storage volumes) and the galaxy cluster finder. Finally, all these ingredients are delivered to the Galaxy Evolution Workflows (Luminosity Function, Mass Function, and Halo Occupation Distribution).